Electrochemical and Photocatalytic Flow Strategies for Sustainable Substrate Oxidation

Mark A. Bajada

Department of Chemistry

University of Cambridge

This dissertation is submitted for the degree of
Doctor of Philosophy

St. Edmund's College

January 2020

Abstract

The challenge of relinquishing the use of fossil fuels, and the move to a more sustainable energy model, depends on our ability to effectively and economically capture and store renewable forms of energy. Electro- and photocatalytic techniques present an attractive route towards the respective conversion of renewable electricity and direct sunlight into chemical energy.

Carbon nitride (**CN_x**), a polymeric semiconductor, has recently received much attention, stemming from its successful application as a heterogeneous photocatalyst for solar water splitting and visible light mediated organic transformations, in addition to its nontoxic properties and facile, low-cost synthesis. However, these reactions have mostly been confined to batch reactors, and the advantages offered by continuous flow chemistry vis-à-vis improved light transmission, compatibility with multiphasic systems, and catalyst recyclability, have not been fully explored for this class of materials. In the first part of this thesis, different design strategies are proposed and assembled, in order to carry out **CN_x**-based photocatalysis under continuous flow. An investigation into the aerobic oxidation of a variety of organic substrates was made, and a comparison between the performance of batch and flow **CN_x** photoreactors was conducted. Design of the initial flow prototype involved some computational fluid dynamics analysis and was based on a thin channel device concept. The next iteration was centred around the use of a packed column photoreactor and was tailored towards triphasic flow chemistry.

The second part of the thesis is focused on the development of an anodic system for the electrochemical oxidation of alcohol substrates. It is incentivised by the need to replace the oxygen evolution reaction (OER) within a conventional CO_2 reduction electrolyser, on account of the high energy penalty of the OER and the low commercial value of O_2. A novel hybrid anode was fabricated, featuring a silatrane-modified TEMPO catalyst which was covalently immobilised on a mesoporous indium tin oxide scaffold. The performance of the assembled anode was first optimised towards the oxidation of representative biomass substrates, and then integrated with a precious-metal-free CO_2 reduction electrocatalyst, for coupled alcohol oxidation and CO_2-to-syngas conversion. The system, comprised only of earth-abundant materials, demonstrates the ability to produce chemical feedstocks from sustainable resources, such as biomass-derived alcohols, CO_2, and renewable electricity.

Declaration

I hereby declare that this dissertation the result of my own work and includes nothing which is the outcome of work done in collaboration except as declared in the Preface and specified in the text. It is not substantially the same as any that I have submitted, or, is being concurrently submitted for a degree, diploma or other qualification at the University of Cambridge or any other University or similar institution. I further state that no substantial part of my dissertation has already been submitted, or, is being concurrently submitted for any such degree, diploma or other qualification at the University of Cambridge or any other University or similar institution. This dissertation does not exceed the prescribed word limit of 60,000 words.

Mark A. Bajada

January 2020

Acknowledgments

First of all, I would like to extend my gratitude to my supervisor, Prof. Erwin Reisner, for giving me the great opportunity to join his lab and work on a challenging and stimulating PhD project, and for all the guidance offered during my studies.

The PhD experience of course had its highs and lows, with moments of despair when things just could not seem to work, and (fewer) moments of euphoria when small discoveries were made. I truly savoured the latter, for they were hard to come by but once they did, were instrumental in providing me with the strength and motivation to keep going, to ask more questions and seek more answers.

Nevertheless, during the good times and the bad times, my life over the past four years simply would not have been the same were it not for my colleagues. I feel so privileged to have been a part of this group, and to have been able to meet, interact, and learn from so many great individuals. The groups' sociable attitude, both during work and outside the lab, has been essential in providing support, entertainment, and day-to-day laughs, and I will forever treasure and reminisce the moments we have shared together, and the friendships formed. Special thanks go to Bertrand Reuillard, Charles Creissen, Kristian Dalle, Julian (Javier) Vigil, Daniel Anton Garcia, Esther Moore, Arjun Vijeta, Constantin Sahm, and Andreas Wagner, who were around for a large portion of my PhD and have made my time in Cambridge truly enjoyable.

I would like to extent my gratitude towards Julien Warnan and Souvik Roy, for mentorship and collaboration on challenging, yet exciting, projects. It has been an absolute pleasure to work with them, and am very grateful for their expertise, continued support, and friendship. Fabio Lima and Ricardo Labes from the Ley group were also extremely helpful in providing advice and pieces of flow tech to get our lab started, as I was the first person within the group to work on flow chemistry.

Due to issues arising from the departments dated infrastructure, I had to switch office locations three times. Thankfully there was a bright side, and I did have the pleasure of bonding with different lab members within the various locations. Many thanks to the first office crew, Charles, David Wakerley, Ben Martindale, Tim Rosser, Will Robinson, Hatice Kasap, and Katherine Orchard, for helping me settle in so well, to Nina Heidary

in the second location, and Souvik, Arjun, and Ava Lage in my current spot, who have all been such great company, and have made the office environment all the more pleasant to work in.

A very special thanks of course goes to my family, and in particular my mother, Caroline, who has always been so encouraging of my studies and ambitions. Her enduring love and support have played a key role in helping me to excel and get to where I am today. My brother John was also extremely patient in assisting me to complete a number of illustrative figures – many thanks go to him as well. My childhood friends Rosy, Andrea, Kurt, and David have always tried to support wherever and whenever they can, and their longstanding trust and friendship has always been very special to me.

Finally, I would like to acknowledge my funding bodies, the Endeavour Scholarship Scheme and OMV, for providing the financial support needed to undertake this journey.

List of Publications

This thesis contains results which have been submitted to peer-reviewed journals:

1. M. A. Bajada, A. Vijeta, A. Savateev, G. Zhang, D. Howe, and E. Reisner, 'Visible-Light Flow Reactor Packed with Porous Carbon Nitride for Aerobic Substrate Oxidations', *ACS Appl. Mater. Interfaces*, 2020, **12**, 8176–8182.
2. M. A. Bajada,† S. Roy,† J. Warnan,† K. Abdiaziz, A. Wagner, M. M. Roessler, and E. Reisner, 'A Precious-metal-free Hybrid Electrolyzer for Alcohol Oxidation Coupled to CO_2-to-syngas Conversion', *Angew. Chem. Int. Ed.* 10.1002/anie.202002680 (†denotes equal contribution).

Contributions also made to the following peer-reviewed journal article was not included in this thesis:

1. V. Andrei, R.L.Z. Hoye, M. Crespo-Quesada, M. A. Bajada, S. Ahmad, M. De Volder, R. Friend, and E. Reisner, 'Scalable Triple Cation Mixed Halide Perovskite–$BiVO_4$ Tandems for Bias-free Water Splitting', *Adv. Energy Mater.*, 2018, **8**, 1801403.

Table of Contents

List of Figures

List of Schemes

List of Tables

List of Abbreviations

AcOH	acetic acid
AI	artificial intelligence
AlcOx	alcohol oxidation
b-CN_x	bulk carbon nitride
BET	Brunauer–Emmett–Teller
BPR	back-pressure regulator
CB	conduction band
CE	counter electrode
CFD	computational fluid dynamics
CFL	Courant-Friedrichs-Lewy condition
CNT	carbon nanotubes
Co(P)Pc	(polymeric) cobalt phthalocyanine
CO_2R	CO_2 reduction
Conv	conversion
CP	carbon paper
CPE	controlled potential electrolysis
CV	cycle voltammogram
DSPEC	dye-sensitised photoelectrochemical
EA	electron acceptor
EC	electrochemical
EtOH	ethanol
FE	Faradaic efficiency
FE-EPR	film electrochemical electron paramagnetic resonance spectroscopy
FEP	fluorinated ethylene propylene
FTIR	Fourier-transform infrared spectroscopy
GC	gas chromatography
g-CN_x	graphitic carbon nitride
GlyAd	glyceraldehyde
HER	hydrogen evolution reaction
HMF	hydroxymethylfurfural

HPLC	high performance liquid chromatography
IoT	Internet of Things
IS	internal standard
K-PHI	potassium poly(heptazine imide)
KSCN	potassium thiocyanate
M.B.	mass balance
MBA	4-methylbenyzl alcohol
MBAd	4-methylbenzylaldeyde
MeCN	acetonitrile
*meso*ITO	mesoporous indium tin oxide
MFC	mass flow controller
MO	metal oxide
mpg-CN_x	mesoporous graphitic carbon nitride
MWCNT	multi-walled carbon nanotubes
$^{NCN}CN_x$	cyanamide surface-functionalised carbon nitride
NHE	normal hydrogen electrode
NMR	nuclear magnetic resonance spectroscopy
OER	oxygen evolution reaction
PC	photocatalytic
PCP	packed column photoreactor
PDE	partial differential equation
PDMS	polydimethylsiloxane
PEC	photoelectrochemical
PEG	polyethylene glycol
PET	poly(ethylene terephthalate)
PLA	poly(lactic acid)
PMMA	poly(methyl methacrylate)
PP-ol	2-phenoxy-1-phenylethanol
PTFE	polytetrafluoroethylene
PV	photovoltaic
PVP	polyvinylpyridine
RDS	rate determining step
RE	reference electrode

RHE	reversible hydrogen electrode
SA-to-*V*	surface area-to-volume
Sel	selectivity
SEM	scanning electron microscopy
SET	single-electron transfer
SMBR	serial micro-batch reactor
TAS	transient absorption spectroscopy
TCP	thin channel photoreactor
TEM	transmission electron microscopy
TEMPO	2,2,6,6-tetramethyl-1-piperidinyloxyl
TOF	turnover frequency
TON	turnover number
VB	valence band
WE	working electrode
XPS	X-ray photoelectron spectroscopy
XRD	X-ray diffraction

List of Symbols

A_{anode}, $A_{cathode}$	area of anode and cathode (Chapter 4)
A_{IS}, A_{Sub}	integrated area of IS and substrate NMR peaks (Chapter 3)
c_{sub}	substrate concentration
D	molecular diffusion coefficient
d_{eff}	effective channel diameter
$\lvert E^{o}_{cell} \rvert$	standard thermodynamic cell potential
d_g	interelectrode gap
E	potential (non-standard conditions)
E^o	thermodynamic standard potential
$E_{1/2}$	half-wave potential
E_{app}	applied potential
E_{CE}	potential at counter electrode
E_g	bandgap
E_p	peak potential
F	Faraday constant
i, j	current, and current density (note: symbols used to signify the nodes within the spatial domain in Chapter 2)
i_p	peak current
K_{ads}	equilibrium adsorption coefficient
k_{app}	apparent first order rate constant (Chapter 2); apparent electron transfer rate constant (Chapter 4)
$k_{reaction}$	rate constant for the surface-photocatalysed chemical reaction
L_c, b_c, h_c, A_c	length, breadth, height and cross-sectional area of channel
l_x	characteristic length in the primary direction of flow
n	moles
p	inner cross-sectional perimeter of channel
Pe	Péclet number
Q	charge passed during electrolysis
R	universal gas constant
Re	Reynolds number
R_u	uncompensated resistance
t	time

T	temperature
$\mathbf{u}$	velocity vector profile
u_{avg}	average flow velocity
u_o	velocity at the centre of the laminar flow profile
u_x	x-component of velocity
$\dot{V}$	volumetric flow rate
V_r	photoreactor volume
z	number of electrons involved in a redox process

α	electron-transfer coefficient
Γ_{Co}	surface concentration of electroactive cobalt centres
$\Gamma_{\mathbf{STEMPO}}$	surface concentration of **STEMPO** (determined electrochemically)
$\Gamma_{\mathbf{CN}^*}$	surface concentration of photoactivated $^{\mathbf{NCN}}\mathbf{CN_x}$ sites
Δt	time step in numerical model
Δx, Δy	grid spacing in x- and y- direction of the discretised domain
ε	cell energy efficiency
η	overpotential
κ	conductivity
λ	wavelength
ν	scan rate
ρ_{solv}	solvent density
τ	residence time
υ	kinematic viscosity

Chapter 1

Introduction

1.1 Renewable Energy Sources for Chemical Synthesis

One of the greatest challenges of our generation is to bring about a paradigm shift in the development and implementation of alternative energy technologies, along with more sustainable and “energy smart” chemical manufacturing processes. Wind turbines and photovoltaics have allowed us to tap into essentially inexhaustive and renewable sources of energy, and these have become increasingly prevalent throughout the world. Unfortunately, the time-varying and unpredictable nature of these sustainable, low–carbon emission energy sources has meant that our society still relies on fossil fuel-fired power plants, and a complete transition into a green energy sector is far from complete. Batteries and mechanical energy storage (such as flywheels or compressed air) may provide short-term storage solutions, but there is still a high demand for month-to-month seasonal storage, and a more efficient means to handle excess renewable power generation.[1]

A highly attractive solution to circumvent the intermittency issue associated with renewables and increase their dispatchability and penetration on an even broader scale, is to integrate the energy sector with the chemical sector.[2] In order to make this merger possible, a new generation of synthetic protocols are required that will primarily be based on electrochemical methods and direct solar-to-chemical conversion processes. Electrification via renewable power generation will also assist to decarbonise the chemical industry, which is itself a large energy consumer and currently, a key contributor to greenhouse gas emissions. The prospect of decarbonisation can in addition be realised through the conversion of atmospheric

CO_2 into commodity chemicals and fuels. The electroreduction of CO_2 into more useful carbon-based feedstocks is a highly elegant approach to closing the carbon cycle and in preventing the rise of anthropogenic CO_2 emissions.[3,4] Therefore, using electricity to drive our endergonic synthetic processes, and taking inspiration from natural photosynthesis to store solar energy in the form of chemical bonds, will help in giving us the mix of technologies we need to build a synergistic relationship between the energy and chemical sectors.

1.2 HER and CO_2R

The water splitting reaction and CO_2 reduction (CO_2R) are two of the most investigated approaches for storing sunlight or (excess) renewable electricity in the form of a chemical bond.[5] The H_2 evolution reaction (HER) is most often envisioned as half of the overall water splitting reaction, where the other half, water oxidation (or the oxygen evolution reaction, OER), provides both the protons and the electrons required to evolve H_2 (Table 1-1). Water splitting is a thermodynamically uphill process, which requires a theoretical cell voltage of 1.23 V. However in reality, the applied value is higher, as the kinetic hurdles of a four-electron process in addition to driving force, demand for a large overpotential (η) beyond the ideal threshold.[6,7] CO_2 is the thermodynamically stable end product of numerous chemical and biological oxidation reactions, and thus the reverse processes in converting CO_2 back to fuels is also an endergonic process.[8] In a similar manner to HER, the electron source for carrying out electrochemical CO_2 reduction is typically supplied from water oxidation. Common products from the reductive half-reaction include carbon monoxide (CO) and formate (HCO_2H), and the associated standard potentials are highlighted in Table 1-1.

The oxidation of organics at the anode as a means to source the electrons required for HER and CO_2R, has emerged as a viable alternative to the OER and is attractive from both an energetic and commercial perspective.[9] The standard thermodynamic cell potential ($\left|E^{o}_{cell}\right|$, in V) represents the theoretical minimum energy requirement to drive the HER or CO_2R reaction in a particular cell configuration. Comparing this parameter for two electrolyser configurations, in which the OER or substrate (e.g. glycerol) oxidation is coupled to CO_2-to-CO reduction, highlights the theoretical energy savings achievable upon replacing water oxidation (see Table 1-1). With the OER in-

place, a theoretical $|E^{o}_{cell}|$ value of 1.33 V is computed, while for the organic oxidation, this value is drastically lower (0.50 V). In addition, the ability to synthesise value-added chemicals at the anode in place of O_2 generation can greatly improve the economics of the overall process.[10] This concept forms a central part of the thesis (particularly for the second project, Chapter 4), and shall be discussed in further detail in Section 1.5.1.

Although the potentials for the CO_2 reduction pathways shown in Table 1-1 appear to be fairly moderate, there are a number of kinetic barriers in place which raise the energy requirements for the overall process.[11] Catalysts lower this overpotential by stabilising the intermediate transition states between the linear CO_2 molecules and the intended product. However, hurdles regarding energy efficiency, reaction selectivity between various carbon-based products, and the overall conversion rates, still need to be overcome if electrochemical CO_2 reduction is to become a commercially viable option for chemical energy storage, to replace the fuels derived from petrochemical sources.[4,12] In aqueous solution, CO_2R is typically accompanied by the competing HER, primarily as a result of the presence of protons and the lower overpotential for this half-reaction. CO is arguably the most important C1-building block, and the mixture of CO and H_2 is itself of high commercial interest as it can be employed as 'syngas' for large industrial processes such as the Fischer–Tropsch synthesis of hydrocarbons.[13]

Table 1-1: Standard potentials for anodic and cathodic half-reactions.[9,14,15]

Half-reaction	**Thermodynamic standard potential (V *vs*. RHE)**
Possible anode reactions:	
Water → Oxygen	
$2H_2O \rightarrow O_{2(g)} + 4H^+ + 4e^-$	$E^o = 1.23$
Glycerol → Glyceraldehyde	
$C_3H_8O_{3(aq)} + 2OH^- \rightarrow C_3H_6O_{3(aq)} + 2H_2O + 2e^-$	$E^o = -0.40$
Benzyl alcohol → Benzaldehyde	
$PhCH_2OH_{(aq)} \rightarrow PhCHO_{(aq)} + 2H^+ + 2e^-$	$E^o = -0.20$
Typical cathode reactions:	
$4H^+ + 4e^- \rightarrow H_{2(g)}$	$E^o = 0$
$CO_2 + 2H^+ + 2e^- \rightarrow CO_{(g)} + H_2O$	$E^o = -0.10$
$CO_2 + 2H^+ + 2e^- \rightarrow HCO_2H_{(aq)}$	$E^o = -0.12$

1.3 Technical Strategies for Solar-to-Chemical Conversion

In accordance with the literature, I will introduce the three main architectures which have been described for solar-to-chemical conversion, namely: photocatalytic (PC) systems, photovoltaic–electrochemical (PV–EC) cells, and photoelectrochemical (PEC) cells (Figure 1.1). These strategies however, can be encased under the broader label of ‘renewable energy-to-chemical’ conversion to encompass other approaches which do not use solar irradiation directly, but fulfil a similar outcome by converting a form of renewable energy into a chemical bond. This was exemplified in Section 1.1, with the introduction of the concept of excess renewable electricity to drive synthetically useful electrochemical reactions, and shall be discussed further in Section 1.5.1. A brief description of the three ‘classical’ approaches, along with some technical merits and drawbacks which affect broader scale implementation are provided below. This will then be used as a platform to delve into the specific areas which are of relevance to this overall PhD project.

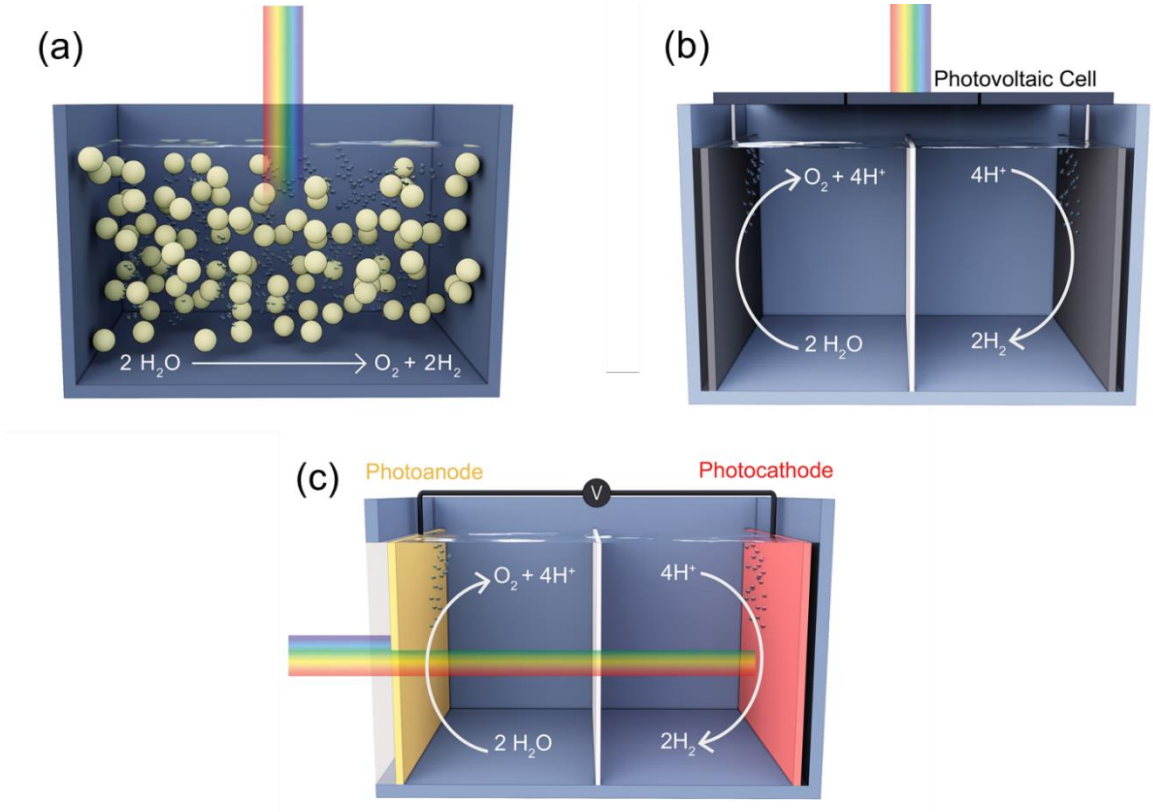

Figure 1.1: Schematic diagrams for solar-to-chemical device configurations, exemplified through the water splitting reaction: (a) PC, (b) PV–EC, and (c) PEC systems.

1.3.1 Photocatalytic Systems

This approach encompasses the so-termed “one-pot” reactor design, which typically features a colloidal suspension of semiconductor nanoparticles and co-catalysts in a single medium, that can be used to directly split water.[16] Thermodynamic constraints require that the band levels of the semiconductor lie at a suitable potential in order to drive the two half-reactions involved in the overall water splitting process (i.e. the conduction band (CB) minimum must be more cathodic than the H^+/H_2 potential, while valence band (VB) maximum should be more anodic than the O_2/H_2O energy level; c.f. Table 1-1).[17] However, the utilisation of a PC system driven by a one-step photoexcitation has been impeded due to the lack of a suitable compound which can satisfy all the necessary requirements for overall water splitting by visible light irradiation, namely: (i) a band gap narrower than 3 eV, (ii) band-edge potentials suitable for overall water splitting, and (iii) stability in the photocatalytic reaction environment.[18,19]

Inspired by the natural photosynthetic pathways in green plants, an alternative, two-stage, double-excitation approach was proposed (known as a “Z-scheme”) in order to circumvent issues arising with the single-excitation system.[20] In natural photosynthesis, chlorophyll *a* pigments in the reaction centre P680 of the enzyme photosystem II (PSII), absorb photons with $\lambda \leq 680$ nm, leading to the generation of electron–hole pairs (Figure 1.2).

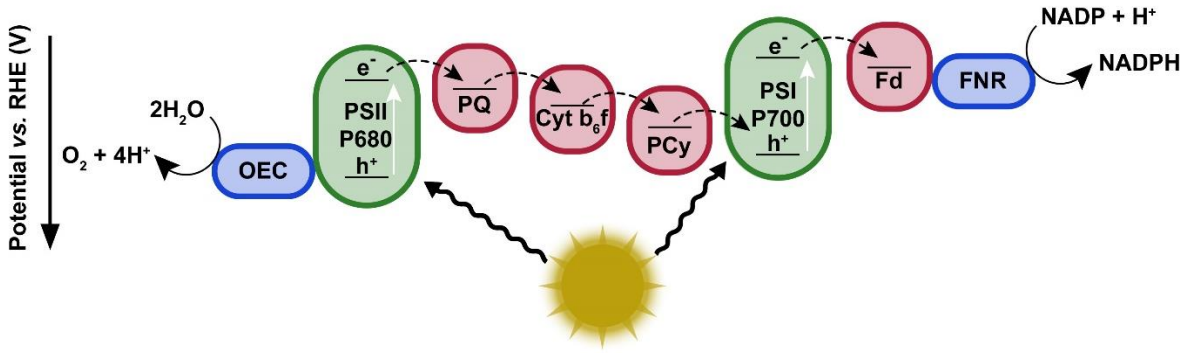

Figure 1.2: Schematic illustration of natural photosynthesis, where the arrows represent the direction of electron (e^-) flow through the system. (Abbreviations: OEC = oxygen-evolving complex, PSII = photosystem II, PQ = plastoquinone, Cyt b_6f = cytochrome b_6f complex, PCy = plastocyanin, PSI = photosystem I, Fd = ferredoxin, FNR = ferredoxin-$NADP^+$ reductase, NADP = nicotinamide adenine dinucleotide phosphate).

Photoinduced holes oxidise water, producing O_2 and protons at the catalytic Mn_4CaO_5 cluster of the oxygen-evolving complex (OEC).[21] The photoexcited electrons enter an electron transport chain passing through plastoquinone (PQ), cytochrome b_6f, and plastocyanin (PCy) to photosystem I (PSI). Here, in the reaction centre P700, electrons are further excited by photons with $\lambda \leq 700$ nm. These energised electrons are used by ferredoxin-$NADP^+$ reductase (FNR) to reduce nicotinamide adenine dinucleotide phosphate (NADP) into NADPH, which, together with adenosine triphosphate (ATP), provides the reductive power and energy for the conversion of CO_2 to sugars (via the Calvin cycle).[22,23] A schematic illustration of an inorganic-based Z-scheme for overall water splitting is depicted in Figure 1.3. This approach has been shown to utilise visible light more efficiently than a single photocatalyst water splitting system, on account of the lower energy requirement to drive each half-reaction involved.[24]

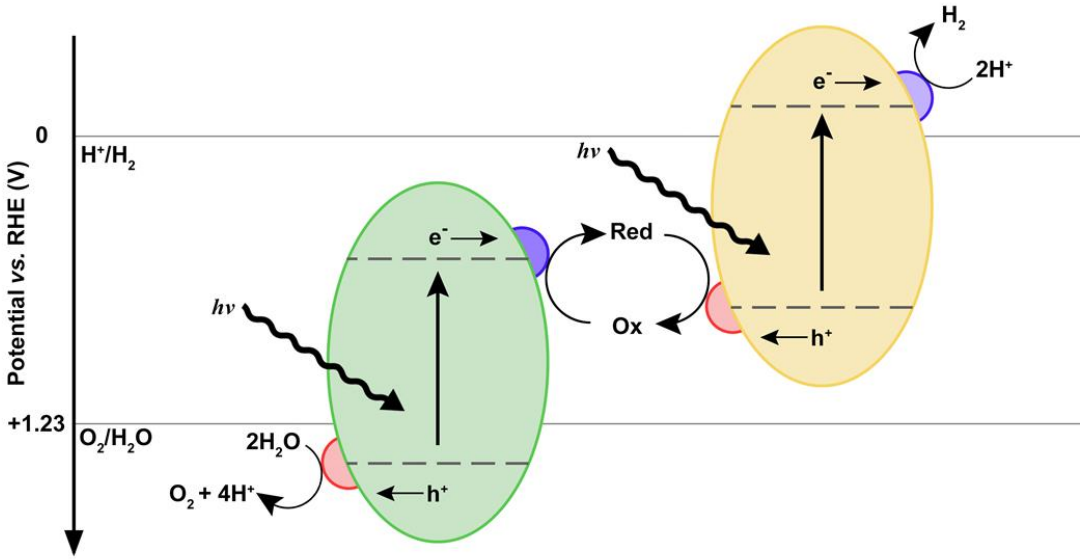

Figure 1.3: Schematic illustration of "one pot" photocatalysis in a Z-scheme configuration (artificial photosynthesis). 'Red' and 'Ox' denote the reduced and oxidised forms of the mediator species, respectively; e^- = electrons, h^+ = holes; dashed lines are representative of conduction and valence band positions.

The PC design benefits greatly from its simplicity, in which no electrical wiring is required, and hence could potentially translate to low scalability costs. Some of the downsides to this technology are related to the fact that H_2 and O_2 are generated together in the same compartment. Having both products in the same phase complicates downstream processing and raises a concern for safety due to the accumulation of this explosive mixture in the reactor headspace. Finally, combining all elements in a single vessel can limit the components which can be used together, as

all will be required to function under the same conditions. As per the case of electrochemical CO_2R, current research efforts in the field of photocatalysis are also targeting liquid-based oxidative reactions in place of the OER, ranging from organic transformations, to lignocellulosic and even plastic photoreforming.[25–30] Some key examples of this line of research shall be described in Section 1.4, and are closely related to the first project included in this thesis (Chapter 2 and Chapter 3).

1.3.2 PV–EC

Today, photovoltaics (PVs) are produced on a commercial scale and can effectively convert solar energy directly into electricity. Crystalline Si cells are able to achieve an efficiency close to 27%,[31] while III-V multijunction cells can reach even higher values (e.g. GaInP/GaAs/Si, efficiency = 36%).[32] To make the best use of the solar energy harvested by PV devices, it would be suitable to couple the technology with a good energy-storage system, such as an external battery pack. Unfortunately, with the current infrastructure, we only have the capacity to store ~1% of the energy consumed worldwide, most of which is through pumped-storage hydroelectricity, with stationary batteries only accounting for 0.01% of energy storage demands.[33] In a photovoltaic–electrochemical (PV–EC) cell, light harvesting via the PV module and electrocatalysis are spatially decoupled. This means that existing, state of the art PV cells can be combined with an electrolyser, thereby providing a solar-to-chemical storage pathway. The act of combining the two mostly presents a number of engineering and technoeconomic challenges, particularly related to reducing the costs of large-scale implementation,[34,35] better integration with the grid electricity,[36] and minimising large efficiency losses as the cell size is increased. However, there is still a lot to be offered from the scientific community with regards to the electrocatalysts employed within the electrolyser module, and the continual improvement of the efficiency of multijunction methods within the PV field. The second part of the PhD project delves into the EC aspect of this technological strategy and will be described further in Section 1.5.

1.3.3 PEC

Photoelectrochemical (PEC) systems are typically comprised of two semiconductor photoelectrodes, absorbing complementary portions of the solar spectrum, immersed in an electrolyte solution and separated by an exchange membrane (e.g. proton

exchange membrane (PEM) for the case of acidic media).[37] Cells featuring one photoelectrode and a counter electrode that is operated in the dark, are also included within the PEC category.[38] In a tandem PEC cell, the oxidation half-reaction takes place at the photoanode, generating electrons that travel through an external circuit to reach the photocathode, where the reduction half-reaction takes place (see Figure 1.1c). The spatial separation of the two half-reactions into different compartments prevents the build-up of potentially explosive gas mixtures and facilitates product collection. A further advantage of the separation of the photoelectrodes, is that the individual half-reactions can be studied and optimised independently in a three-electrode set up with a reference and counter electrode.

Examples of n-type semiconductors used as photoanodes within PEC devices include TiO_2, Fe_2O_3, $BiVO_4$, and WO_3,[39–42] while p-type semiconductors such as Cu_2O, NiO, $CuCrO_2$, and p-Si[43–46] have been utilised for the photocathodic side. The use of low-cost metal oxides is appealing for renewable energy devices, however, the low efficiency of PEC cells and stability issues of certain semiconductors in aqueous conditions, have so far hindered commercial application.[47] To improve the efficiency of tandem PEC cells, efforts have been devoted towards optimising the performance of individual photoelectrodes, through interfacing them with protection layers to enhance photostability and by integrating electrocatalysts to provide for more efficient fuel forming pathways.[48–51]

1.4 PC Approach Towards Organic Transformations and Fuel Production

1.4.1 Overview

Advancements in the field of photocatalysis have been made possible through research efforts from different communities. Although extensively applied in the field of solar fuels, primarily for solar water splitting and CO_2 reduction reactions, the synthetic organic community has begun to strongly engage in this arena and develop novel synthetic methodologies which make use of the photocatalytic mechanism. A key factor leading to this recent, yet rapid, growth has been the recognition that readily accessible polypyridyl complexes of either Ru(II) or Ir(III), and organic dyes can bring

about the conversion of visible light into chemical energy under extremely mild conditions.[52]

Organic substrate molecules typically do not contain visible light-absorbing chromophore units, and hence, electronically excited states are often only available upon irradiation with UV light. However, such short wavelength photons can result in uncontrolled photodecomposition processes, limiting the applicability of UV-driven photochemical synthesis for the creation of more complex organic compounds. On the other hand, photocatalysts are conceptually very useful for synthetic applications, as they absorb light with greater efficiency at wavelengths which are longer than the absorption range of these organic substrate molecules. Upon visible light photoexcitation, such photocatalysts can engage in single-electron transfer (SET) events with organic substrates, thereby generating reactive organic radicals.[53] Such species play a vital role in organic synthesis, and often, cannot readily be generated using nonphotochemical strategies. Traditionally, radical generation is associated with non-selective UV irradiation, high temperature conditions, or highly reactive radical initiators.[54] Visible-light photocatalysis by-passes the need for such harsh, energy-intensive, and sometimes toxic methods, and can be seen as a *green* and *sustainable* approach to conducting organic synthesis.

The application of PC for synthetic organic chemistry was largely non-existent before 2008, with only a few, but seminal publications present in the literature. The pioneering work by Kellogg in 1978 on reductive desulfuration,[55] Cano-Yelo and Deronzier in 1984 on the photocatalytic Pschorr reaction,[56] and by Okada in the early 1990s on reductive decarboxylation of redox-active esters, laid the foundations for the recent developments in the field of modern photoredox catalysis.[57,58] In 2008 MacMillan and co-workers developed a dual photoredox–organocatalytic protocol to resolve the asymmetric α-carbonyl alkylation challenge.[59] At the same time, Yoon and co-workers reported a photoredox-catalysed intramolecular [2 + 2] enone cycloaddition.[60] Shortly afterward, Stephenson and co-workers devised a mild, tin-free protocol for the reductive dehalogenation of benzylic and α-acyl halides.[60]

These three reports collectively led to the so-called “rebirth” of photoredox catalysis, as evidenced by the exponential increase in the number of associated publications since the late 2000s.[61] A broad range of transformations in organic synthesis have

been developed using this valuable catalysis platform, including C–C and C–X bond forming reactions (where X = heteroatom), cycloadditions, oxidations, and reductions with applications in natural product synthesis and even late-stage functionalisation of pharmaceutical compounds.[62,63] The majority of the studies carried out to-date have employed homogeneous iridium- or ruthenium-based transition metal complexes as photocatalysts (such as $[Ru(bpy)_3]^{2+}$ and *fac*-$Ir(ppy)_3$, where bpy = 2,2′-bipyridine and ppy = 2-phenylpyridine respectively; Figure 1.4).[54,59,61] Despite the promises offered by these remarkable photocatalysts, they still present a number of hurdles for wider applications in industry. In particular, these issues are related to the toxicity of the photocatalyst itself, for which industry must comply with residual transition metal limits in final products (e.g. oral permitted daily exposure for iridium ≤ 100 μg per day),[64] and the high-cost of the precious-metal-containing complex (e.g. *fac*-$Ir(ppy)_3$ ~ €1000 g^{-1}; source: Sigma-Aldrich). Further adding to the price of the photocatalyst are the costly purification protocols which must be carried out following the light-driven synthesis, to ensure that transition metal levels are kept within safe limits.

Although polypyridyl complexes of iridium and ruthenium are still very much in use due to their long excited state lifetimes and useful redox windows, research efforts are being placed on developing the next generation of synthetic protocols, which use alternative, organic-based, homogeneous and heterogeneous photocatalysts.[65,66] Many of the homogeneous examples in the literature feature organic dyes, for example eosin Y,[67] acridinium salts,[65] perylene,[68] Rhodamine 6G,[69] or riboflavines[70] (see Figure 1.4 for some exemplary structures).

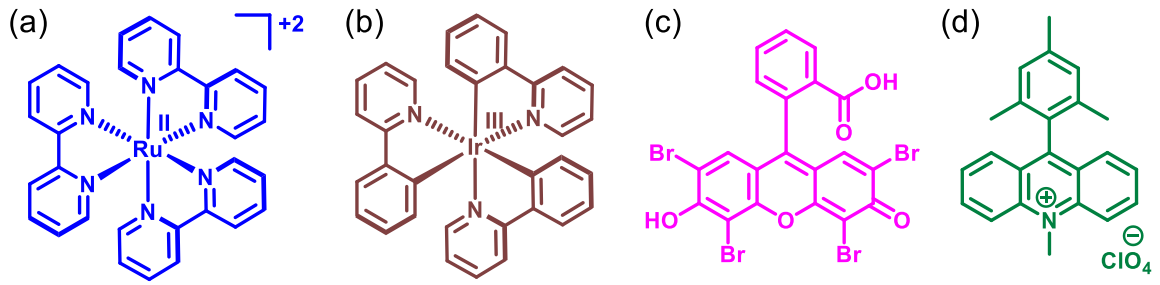

Figure 1.4: Examples of commonly employed homogeneous photocatalysts: (a) $[Ru(bpy)_3]^{2+}$, (b) *fac*-$Ir(ppy)_3$, (c) eosin Y, and (d) the acridinium salt 9-mesityl-10-methylacridinium perchlorate.

The organic-based material for complementary heterogeneous photocatalytic studies is carbon nitride. This polymeric, metal-free material has gained widespread attention as a low-cost and sustainable photocatalyst for artificial photosynthesis and organic

transformations, following Antonietti and Domen's seminal publication in 2009 regarding the use of carbon nitride to generate H_2 from water under visible light irradiation in the presence of a sacrificial donor.[71] Carbon nitride is central to the first part of this PhD project and the next section will therefore focus on this material, featuring discussions on its photophysical properties, and applications in photoredox catalysis.

1.4.2 Carbon Nitride

The first synthesis of a polymeric carbon nitride was reported by Berzelius and Liebig in 1834, and was given the name "*melon*".[72] It is thus regarded to be one of the oldest synthetic polymers. Graphitic carbon nitride (**g-CN_x**) is the most stable allotrope of carbon nitride,[73] and is easily fabricated by thermal polymerisation (temperatures in excess of 500 °C) of abundant nitrogen-rich precursors, such as melamine,[74,75] dicyandiamide,[76,77] cyanamide,[71,78] urea,[79,80] and thiourea.[81,82] The triazine (C_3N_3) and tri-*s*-triazine/heptazine (C_6N_7) rings have been suggested as the two possible basic tectonic units which could yield the graphic carbon nitride allotropes.[83] However, experimental works,[84,85] supported by first-principle density functional theory calculations,[86] have demonstrated that the tri-*s*-triazine-based polymer is energetically more stable, and thus, the heptazine unit is generally recognised as the connection pattern in **g-CN_x** (Figure 1.5a). It should be mentioned that graphitic carbon nitride synthesised via this route does not yield the ideal fully condensed carbon nitride structure (with C_3N_4 stoichiometry), but rather a partially condensed, 'N-bridged poly-heptazine' polymer.[87,88] Defects sites within the polymeric structure therefore arise from these secondary amine bridging groups and primary amine end-groups, which in-turn facilitate hydrogen bonding between the poly-heptazine strands to form quasi 2D arrays or 'sheets' which can then stack through π–π interactions.[89] The sheets which comprise the graphitic carbon nitride structure however, are not aligned with an 'A–A' configuration but present an offset with respect to each other. The structure therefore adopts an 'A–B' configuration, wherein the poly-heptazine sheets are alternated, minimising the repulsive forces of the π-clouds of adjacent layers (as highlighted schematically in Figure 1.5a (inset)).[90]

With regards to the physical properties of **g-CN_x**, the heptazine ring structure and high degree of condensation provides the polymer with high thermal stability (up to 600 °C

in air).[87] Additionally, the optimised van der Waals interactions between single **CN_x** layers gives the polymer a strong chemical resistance, making it insoluble in conventional solvents such as water, alcohols, DMF, THF, diethyl ether and toluene.[91] The sp^2 hybridization of the carbon and nitrogen in the respective heptazine units leads to the formation of a π-conjugated electronic structure. **g-CN_x** exhibits the lowest bandgap among its allotropes,[92] and has an absorption pattern typical to that of an organic semiconductor, with an absorption peak in the blue region of the visible spectrum (λ_{max} ~ 400 nm).[93] Besides the magnitude of the bandgap, it is also important to investigate the potential of the VB and CB of the material, in assessing its suitability for photoredox catalysis. **g-CN_x** has a CB minimum located at –0.88 V *vs*. RHE and a VB maximum at +1.82 V *vs*. RHE (Figure 1.5b).[94] From a thermodynamic perspective, it can therefore engage in controlled substrate oxidation or reduction reactions, and in principle, can also drive the water-splitting reaction. In addition to all these beneficial properties, the cost to synthesise carbon nitride is extremely low, about 10 € kg^{-1},[95] which is ~100,000 times cheaper than precious-metal containing photocatalysts, such iridium-based complexes.

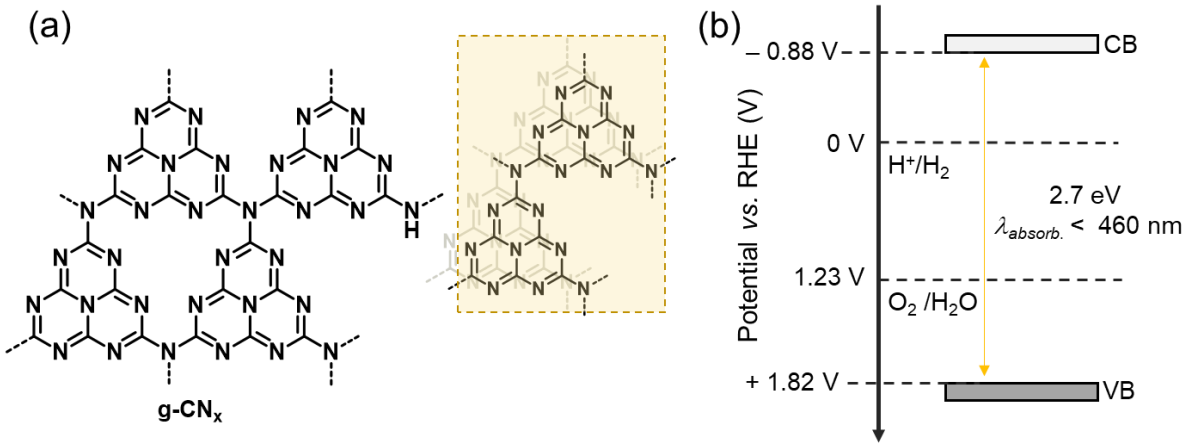

Figure 1.5: Properties of **g-CN_x**: (a) heptazine-based polymeric structure (inset: the misaligned stacking motif, 'A–B' configuration); (b) band positions.

Although from a thermodynamic basis, **g-CN_x** is a suitable heterogenous photocatalyst, the active surface area of the bulk carbon nitrides is too low (typically < 10 m^2 g^{-1}) for practical applications.[87] To circumvent this issue, a mesoporous graphitic carbon nitride (**mpg-CN_x**) was designed and synthesised using a nanocasting ('hard-template') technique.[73,96,97] In the reported method, the carbon nitride precursor was thermally condensed into the polymer in the presence of silica nanoparticles, which in-turn acted as the mesoporous template. The **mpg-CN_x**

material obtained after removal of the silica had a higher surface area (ranging from 100 to 400 $m^2 g^{-1}$) and showed enhanced photocatalytic activity relative to the bulk material, thus highlighting the importance of morphology control.[98]

Chemical modification can influence the local structure, the packing, and the defect sites within the carbon nitride material; it is therefore an effective strategy for tuning the physicochemical (optical, electronic, luminescent) properties of the parent **g-CN$_x$** material in order to extends its applications and/or improve its photocatalytic activity.[87] Some of the possible chemical approaches include the copolymerisation of different precursor building blocks,[99–101] the construction of heterojunctions (featuring either p–n or Schottky junctions),[102–105] and doping (typically in-situ).[106–109] For example, a blue-shift of carbon nitride's absorption edge can be induced via post-functionalisation protonation[106] or sulfur doping,[110] while boron or fluorine doping[111] and copolymerisation with barbituric acid[99] would tend to cause a red-shift in the absorption profile. The **mpg-CN$_x$**/MoS_2 composite is a good example of an organic–inorganic hybrid layered heterojunction, which shows higher rates of photocatalytic H_2 evolution in comparison to **mpg-CN$_x$** alone and an **mpg-CN$_x$**/Pt hybrid material.[104] MoS_2 is an effective electrocatalyst for HER,[112] and typically lowers the activation barrier for H_2 evolution. However, when simply mixed with **mpg-CN$_x$**, a poor activity was still recorded. Wang *et al.*[104] therefore ascribe the enhancement of the **mpg-CN$_x$**/MoS_2 composite to the thin, effective interfacial 2D junctions between MoS_2 and **mpg-CN$_x$**, which in-turn leads to improved charge separation and an increase in the lifetime of the photogenerated electron–hole pair.

There are several other examples in the literature concerning such chemical modifications to carbon nitride, resulting in altered physicochemical and photocatalytic properties. A number of recent reviews summarising the different categories, such as morphological tuning, heterojunction formation, and doping, are available in the literature.[87,113–115] In this introductory section, it is of greater interest to discuss a few key '**g-CN$_x$**' derivatives which have shown great promise within the field of organic photoredox catalysis and/or solar fuel production. The first of these derivatives, which has already been mentioned above, is the morphologically refined **mpg-CN$_x$** material, which has been utilised as a photocatalyst for several organic transformations. Some notable examples include the oxidation of primary and secondary benzylic alcohols to aldehydes and ketones, respectively, at temperatures of around 100 °C and an O_2

pressure of 8 bar (Scheme 1.1a).[116] In the case of primary alcohols, a lower selectivity was reported due to further oxidation of the product aldehyde to the corresponding carboxylic acid upon depletion of the starting material. According to the literature, O_2 is reduced to the superoxide radical anion via the photogenerated electrons in **mpg-CN$_x$**, and can partake in the oxidative mechanism via H-radical abstraction.[116–118] O_2 is therefore believed to act as both an electron acceptor and a co-oxidant, enhancing the rate of substrate oxidation. Other organic transformations conducted under an aerobic atmosphere were hypothesised to proceed via a photocatalytic mechanism that involved the superoxide radical anion. Examples include the oxidation of secondary amines to imines (Scheme 1.1b),[117] the oxidative coupling of two primary benzyl amines to a dibenzylic secondary (*E*)-imine (Scheme 1.1c),[117] and the Diels–Alder cycloaddition reaction (Scheme 1.1d).[119] Most recently, Antonietti and König employed **mpg-CN$_x$** as the photocatalyst for the direct C-H functionalisation of arenes and heteroarenes, with examples including C-H trifluoromethylation, difluoromethylation, and perfluoroarylation of such substrates (Scheme 1.1e).[120]

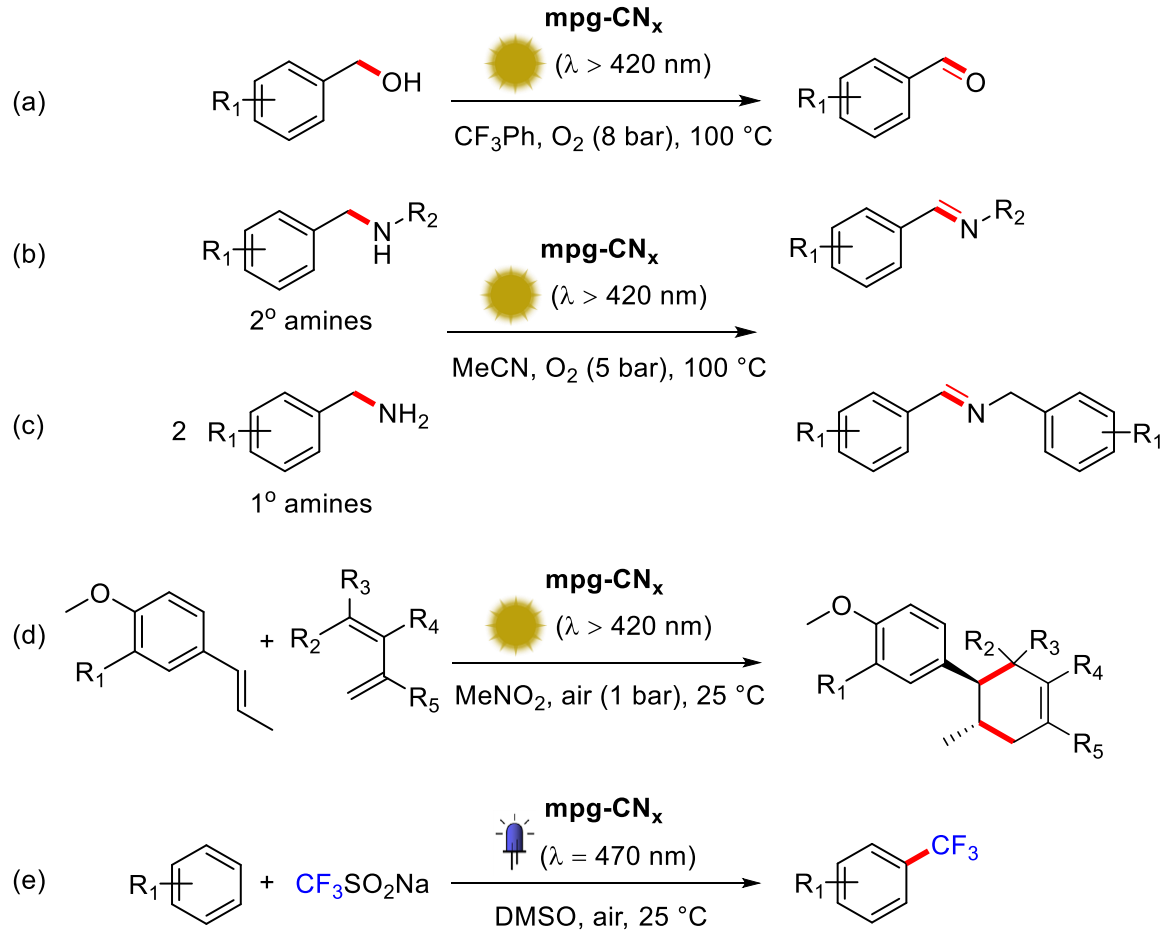

Scheme 1.1: Examples of organic transformations photocatalysed by **mpg-CN$_x$**. In (e), only the trifluoromethylation reaction is shown.

Potassium poly(heptazine imide) (K-PHI) is a newly reported carbon nitride-based material, that is synthesised by the heat treatment of 5-aminotetrazole or triazole in an LiCl/KCl eutectic salt melt, at temperatures close to 600 °C.[94] Similar to **g-CN$_x$**, K-PHI is also built from heptazine rings, but varies in the way that the heptazine units covalently bond together which thus gives rise to a different repeating motif. In K-PHI, six heptazine molecules are arranged in a hexagonal fashion with a metal cation at the core.[121] This structural difference affects the redox properties of K-PHI, and the material was found to have a VB maximum at +2.54 V *vs.* RHE, equating to an anodic shift of 720 mV relative to the VB of **g-CN$_x$**.[122] The more anodic VB potential, and the consequently higher thermodynamic driving force of the photogenerated holes within K-PHI, thus permitted the exploration of alternative organic transformations and oxidations. Some examples of transformations photocatalysed by K-PHI include C-H thiolation of methylarenes to form dibenzyldisulfane derivatives (Scheme 1.2a),[123] the assembly of thioamides from primary aromatic, heterocyclic, and aliphatic amines (Scheme 1.2b),[124] and the oxidative cyclisation of hydrazides to 1,3,4-oxadizoles (Scheme 1.2c).[125] In all these cases, elemental sulfur (S_8) was used as the electron acceptor, and some of the listed examples demonstrate the incorporation of S atoms into the final product to yield organosulfur compounds (as per Scheme 1.2a and 1.2b). For the oxidative cyclisation mechanism (Scheme 1.2c), the authors report a higher selectivity for the desired product in the presence of S_8 in comparison to other conventional electron scavengers such as O_2, therefore highlighting the advantages of using sulfur as a low-cost, widely abundant starting material.

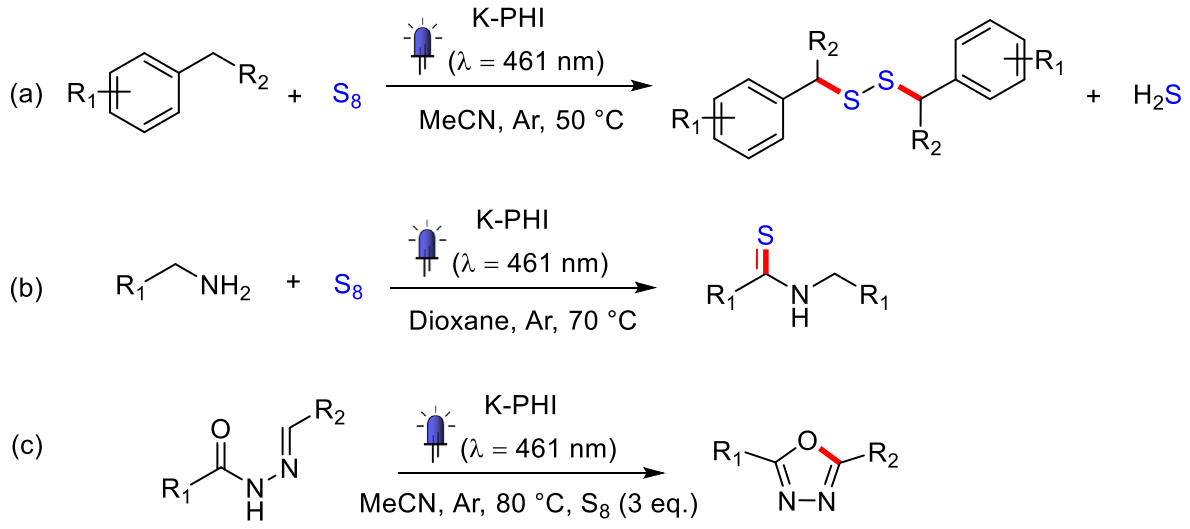

Scheme 1.2: Examples of organic transformations photocatalysed by K-PHI.

The final strategy that will be discussed here was one pioneered by Lotsch *et al.* wherein, based on the accepted postulate that surface terminations and defects seem to be the real active sites within carbon nitride materials,[87] they looked towards modifying such sites in bulk **g-CN$_x$** in an attempt to tailor the material's intrinsic photocatalytic activity.[126] After an initial screening process they illustrated this concept by converting the primary amine termination groups of **g-CN$_x$** into anionic cyanamides, through a post-synthetic salt melt treatment with potassium thiocyanate (KSCN). This resulted in a material (henceforth denoted as **^{NCN}CN$_x$**) that outperformed the rate of H_2 evolution of (unfunctionalised) **g-CN$_x$** by over 12 times at optimum Pt loading.[126] Through post-photocatalysis characterisation of the material and computational modelling, they attributed the improvement to (i) an enhanced interaction between the cyanamide moieties and the co-catalyst, which can facilitate interfacial electron transfer to the Pt centres, and (ii) an improved separation of the photoexcited charges through the built-in electrostatic potential differences across the polymer, stemming from the spatial distribution of the K^+ cations.

Although only a recently discovered carbon nitride variant, **^{NCN}CN$_x$** has already been used in a variety of photocatalytic reactions. Our group demonstrated, for the first time, the ability to use a carbon nitride-based photocatalyst to couple solar H_2 generation with a value-added substrate oxidation reaction.[25] Here, **^{NCN}CN$_x$** was used as a photocatalyst to selectively oxidise 4-methylbenzyl alcohol (MBA) to the corresponding aldehyde, 4-methylbenzylaldeyde (MBAd), under solar irradiation conditions, using a molecular phosphonic acid-modified nickel(II) bisdiphosphine complex (**NiP**) as the proton reduction catalyst (Scheme 1.3a). Prior to this work, carbon nitride-based photocatalytic systems were only used to evolve a solar fuel (H_2) under sacrificial conditions. Sacrificial electron donors (and acceptors) are extensively used to isolate half-reactions in photocatalytic processes, since it is typically challenging to couple oxidative and reductive catalysts in a full photoredox cycle under the same conditions.[127] However, common sacrificial electron donors (such as triethanolamine (TEOA), triethylamine (TEA), and ethylenediaminetetraacetic acid (EDTA)) typically undergo 1 e^- oxidations resulting in a mixture of potentially destructive and non-innocent radical species,[128] which can in-turn decompose the catalytic components of the system.[129] The potential damage to the system caused by these reactive radicals has prompted the community to search for electron donors that

result in a stable, well-defined oxidation product. There is also a financial incentive to replace the sacrificial 'waste' input with a 'clean', selective oxidation pathway, that could result in the generation of some value-added product. The **$^{NCN}CN_x$–NiP** system described herein is a fantastic example of this pioneering concept, and demonstrates a fully sustainable photocatalytic redox cycle, with value added products (an aldehyde and H_2) generated from both the oxidative and reductive half-reactions.

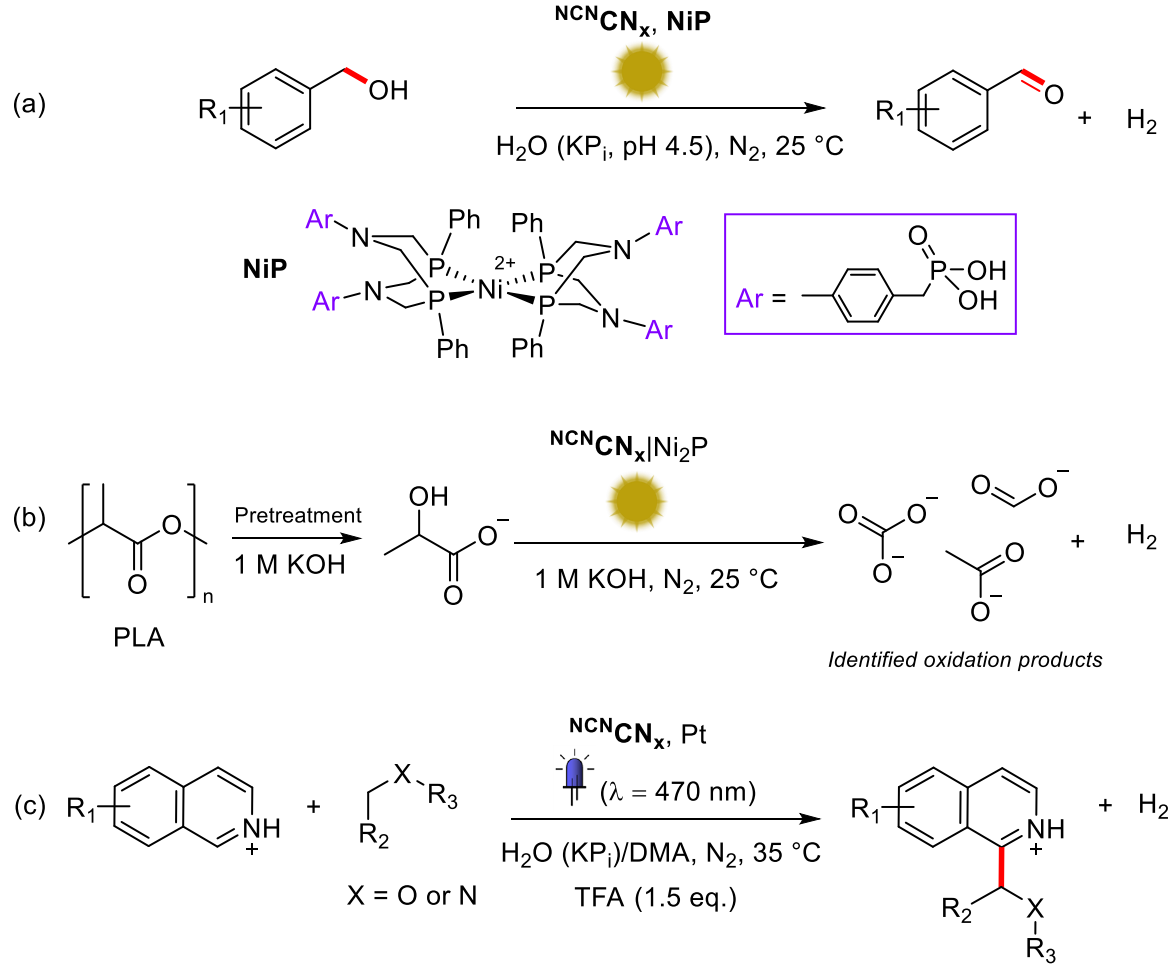

Scheme 1.3: Fuel-generating reactions coupled to organic transformations, photocatalysed by **$^{NCN}CN_x$**. In (a) and (c), 'KP_i' denotes phosphate buffer. In (b), the authors acknowledge that some other unidentified products are also forming in the reactor.[30]

At a similar time, another intriguing property about **$^{NCN}CN_x$** was also realised. Upon light excitation and extraction of the photogenerated holes, the material was able to accumulate the photogenerated electrons in the form of stable π-radicals.[130] Under an inert atmosphere, the "trapped", ultra-long-lived (> 10 h) radicals, which can be visually discerned by the dispersion's colour change (from yellow to blue), maintain a reducing potential, and are therefore thermodynamically capable of converting H^+ to H_2. Recent works have in fact demonstrated the applicability of this temporal decoupling of the

two half-reactions of the photoredox system, with the absorption of solar energy and substrate oxidation taking place in the 'light-phase' of the cycle, and the generation of H_2, via addition of a suitable catalyst, in the 'dark' on demand.[25,130] The development of this viable photoredox cycle for solar fuel and chemical generation, and the discovery of the ability to temporally decouple the two half-reactions, has prompted the research community to explore further applications involving $^{NCN}\mathbf{CN_x}$.

Some recent examples include the use of ultrasonicated $^{NCN}\mathbf{CN_x}$ in the presence of the molecular **NiP** HER catalyst, to photoreform solubilised monomers stemming from purified lignocellulosic components and raw biomass substrates to H_2, under benign conditions (25 °C, and an aqueous medium at pH 4.5).[28] The ultrasonication technique led to the breakdown and exfoliation of the $^{NCN}\mathbf{CN_x}$ aggregates, thereby increasing the active surface area towards lignocellulosic oxidation. This strategy was later adopted for the photoreforming of representative plastic polymers (namely poly(ethylene terephthalate) (PET) and poly(lactic acid) (PLA)), as an alternative choice to naturally occurring polymers such as α-cellulose.[30] In this case, a composite $^{NCN}\mathbf{CN_x}$ / nickel phosphide ($^{NCN}\mathbf{CN_x}$|Ni_2P) heterogeneous catalyst was employed where the role of Ni_2P was to act as the H_2 evolution co-catalyst (see Scheme 1.3b for photoreforming reaction of PLA). In order to achieve reasonable H_2 yields, the plastic substrates were pre-treated to initiate polymer breakdown (24 h in aqueous KOH at 40 °C, with stirring) prior to being added into the batch photoreactor. The conditions during the actual photoreforming process were also more alkaline (1 M KOH) when compared to biomass conversion, and this was deemed necessary to allow for the continual degradation of the plastic polymers. Nonetheless, the system conditions were greatly improved in terms of cost, safety, and sustainability, in comparison to previous reports in the literature for plastic photoreforming, which required much higher alkaline conditions (10 M KOH) and a highly toxic photocatalyst (CdS/CdO_x quantum dots).[29] Additionally, with the $^{NCN}\mathbf{CN_x}$|Ni_2P system the authors identified a variety of oxidation products (such as acetate, formate, glycolate, and glyoxal) from the photoreforming of PET and PLA, demonstrating that potentially valuable organics could be recovered from the input plastic waste feed, particularly if the selectivity of the oxidation half-reaction is improved and tailored toward a single product. Although still in its early days, the system shows signs of robustness and versatility, exemplified through its

ability to photoreform real-world waste samples, including polyester microfibers and oil-contaminated PET, making it an attractive option for future industrial applications.

Alternative organic transformations to substrate oxidation have also been achieved with $^{NCN}CN_x$, wherein this material was used to photocatalyse a visible light-mediated Minisci coupling of N-heteroarenes with ethers, alcohols and amides in the presence of aerobic O_2 as the oxidant.[26] Furthermore, under anaerobic conditions and in the presence of Pt nanoparticles as a proton reduction co-catalyst, the Minisci reaction was coupled to the generation of H_2, thereby demonstrating the ability to integrate more complex organic synthesis with fuel production under visible light irradiation (Scheme 1.3c). Lotsch *et al*. took a different approach altogether and decided to exploit the 'charge storage' properties of $^{NCN}CN_x$ by devising a solar battery anode (operating as a pseudocapacitor). Through this system, they showed that the absorption of light, the consequent storage of photoinduced electrons, and the eventual release of the stored charge in the form of electrical energy, could take place within a single monolithic device.[131]

This discussion does not provide an exhaustive list of all the carbon-nitride based applications which have been published in the past decade, but helps give an overview of the diverse capabilities of this class of materials within the fields of heterogeneous photoredox catalysis, solar fuels, biomass and plastic photoreformation, and solar batteries. What has been perhaps most lacking in the literature, is the development of more appropriate reactor designs in order to facilitate this type of heterogeneous photocatalysis. Conventionally, batch photoreactors tend to be comprised of a simple tube or flask and therefore suffer from a lack of design specificity towards light driven transformations. For reactions with heterogeneous catalysts, flow conditions are more ideal since an immobilised or stationary catalyst phase simulates a high loading that interacts with the mobile reagent phase; this setup reduces reaction times and performs especially well under triphasic conditions.[132] It is well understood that photochemistry in general relies on efficient irradiation of the reaction mixture. However, at the point of incidence, starting materials, products, and the photocatalyst itself, can all filter or scatter the light, thereby attenuating its intensity and reducing the available photons for the rest of the reactor vessel (as described by the Beer–Lambert–Bouguer law). Therefore, reaction mixtures will experience more uniform irradiation in flow because of the small dimensions of the tube reactor design typically

used to conduct such experiments.[133] A carbon nitride-based system, falling under the categories of both “heterogeneous catalysis” and “photocatalysis”, should be highly amenable to incorporation within a continuous flow reaction environment. Electrochemistry can also benefit from the advantages of flow reactors, and so the positive attributes of continuous flow chemistry will be considered in Section 1.6, following the discussion of electrochemical-based approaches to fuel generation and organic transformations (commonly grouped under the heading ‘electrosynthetic techniques’).

1.5 EC Techniques for Substrate Oxidation and Fuel Generation

1.5.1 Electrosynthesis of Chemicals and Fuels

Currently, there is a revival of electrochemistry in the organic synthetic chemistry community.[134] A recent review by Baran has very neatly categorised several of the electrosynthetic advancements made in the past 15 years, with regards to functional group transformations and electrochemical techniques.[135] It delves into various chemistries which can be applied at the anode and cathode, or used in a complete electrolytic cell, and complements other recent reviews within this field which focus on different subject matter. Examples of the latter include the developments made in mediated electrolysis by Little,[134] the reaction engineering aspects of organic electrochemistry by Yoshida,[136] and the environmental impact of electrochemistry vis-à-vis sustainability by Frontana-Uribe/Little[137] and Schäfer.[138] A thorough discussion of electrosynthetic methods is beyond the scope of this introductory chapter, but recognition of this line of work is important for appreciating the direction in which the chemical sector is heading.

The Chemistry 4.0 and Industry 4.0 initiatives aim to improve the energy efficiency and sustainability of the chemical industry, through use of disruptive technologies such as the Internet of Things (IoT), Cloud computing, and Big Data.[139] Such implementations will strive to digitalise the industrial chemical environment, and effectively promote automation, optimisation, and real-time data acquisition (Figure 1.6). Artificial intelligence (AI) is also seeing renewed interest amongst the chemistry and drug-

discovery communities, as cutting-edge in silico technologies are put to the challenge of automating retrosynthetic analysis and in identifying new reaction pathways.[140–143] Such advancements will assist bench chemists with recognising patterns and correlations in data, and offer solutions to problems that are otherwise intractable for humans. Besides the advancements which will be brought about from the continual improvement of computing power,[144] IT infrastructure, and sophisticated machine-learning algorithms,[145] another strategy relies on the electrification and decarbonisation of the chemical industry as a means to reduce its carbon footprint.[2]

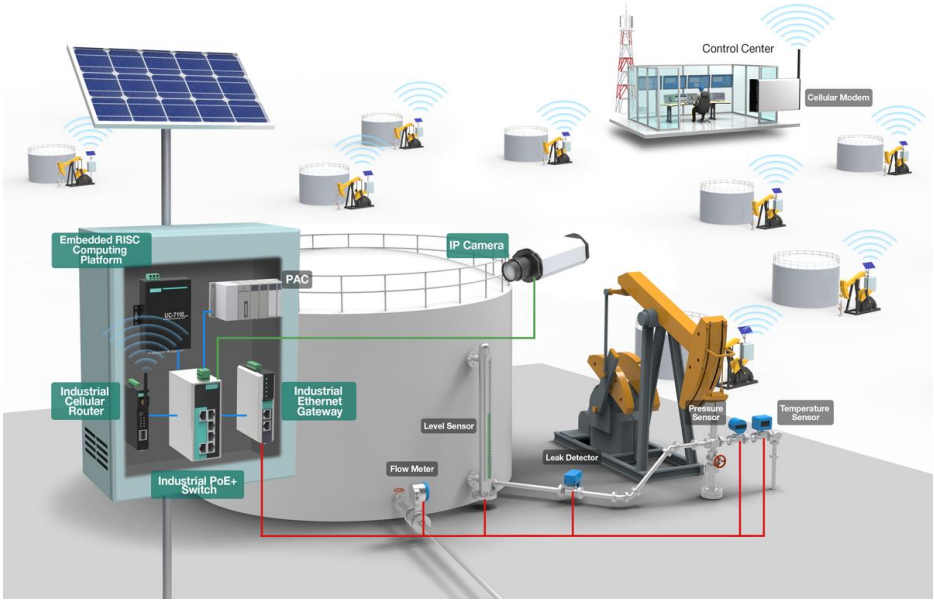

Figure 1.6: Illustration of the industrial IoT, showing on-site connections, often made via a local intranet, and offsite connections, usually made through the Internet. These higher level software platforms provide users with better control and monitoring, and allow for more specialised data-analysis. Figure taken from reference 146.

It is therefore quite clear as to why electrochemical processes are being viewed as such an attractive option in the 21st century over the more conventional thermochemical production routes (such as the Haber-Bosch process for the synthesis of ammonia,[147] the reverse water-gas shift reaction for CO_2 reduction to CO,[148] amongst many others). Electrification of the chemical industry by coupling renewable sources of energy (solar, wind, hydroelectric) with electrochemical-based reactions, such as organic transformations and CO_2R, could lead to the greener production of chemical commodities and fuels.[1] As highlighted in Section 1.1, the merger between renewables and electrosynthesis could: (i) provide storage in the form of chemical bonds, and (ii) further contribute to the decarbonisation of the chemical industry as a whole, by utilising CO_2 as a feedstock (Figure 1.7).

At present, direct air CO_2 capture is far from industrially mature, but recent works are showing promise.[149] The concept of storing energy within a chemical bond is an extremely important concept when it comes to discussing the dispatchability of renewable sources. Existing electricity grid infrastructure is not well designed to absorb excess renewable power generation, resulting in a mismatch of supply and demand.[150] Electrosynthesising fuels and chemicals is a possible solution to the intermittency problem of renewable sources, whereby during periods of peak generation, excess supply could be directed to a stable chemical-forming process (be it a commodity chemical or a fuel, Figure 1.7), rather than leading to negative electricity prices. In a similar manner, renewably derived fuels can then be used during periods of low power generation in order to balance the grid.

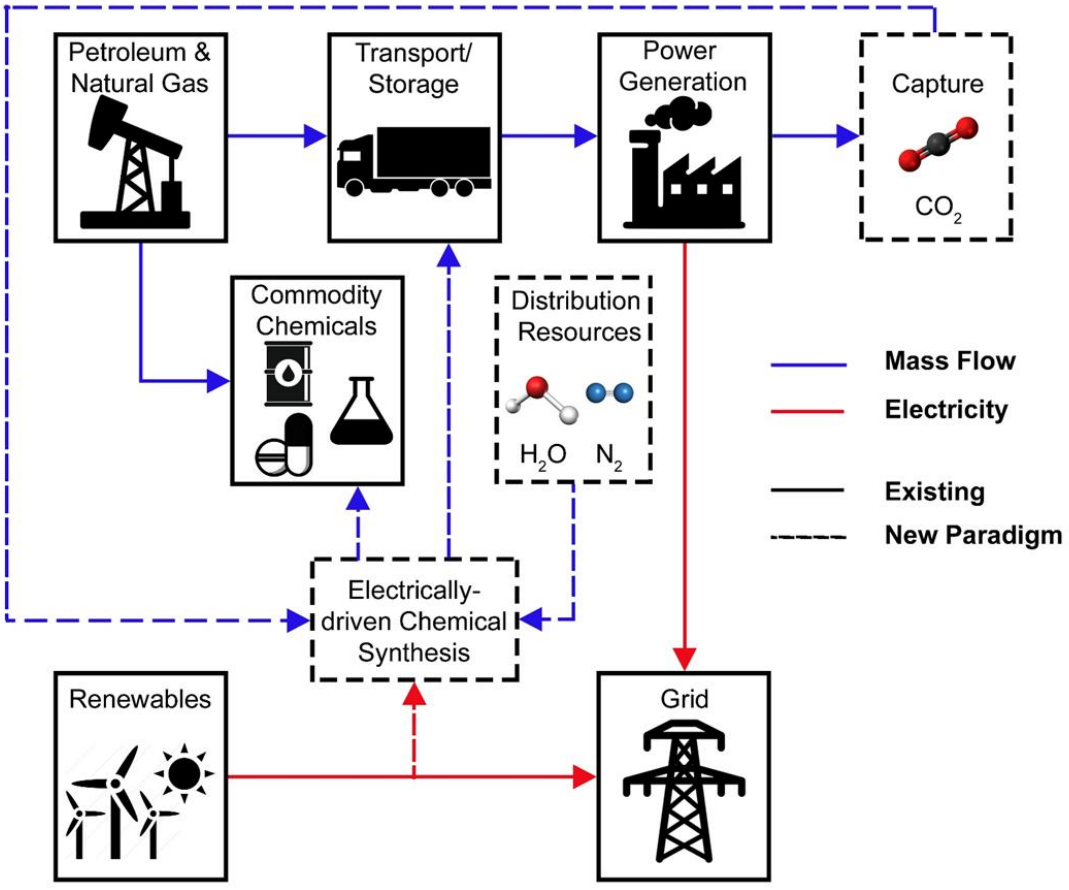

Figure 1.7: Integration of the chemical and energy industries. Blue and red lines indicate mass flow and electrical energy transport, respectively. Solid lines denote existing infrastructure, while dashed lines indicate pathways for electrification and decarbonisation of the aforementioned industries. An electrosynthesis device could be driven by renewable electricity to generate chemicals, which could in-turn be used as energy carriers, or as feedstocks in the manufacturing of other products. Figure adapted from reference 2.

These ambitious directives, to electrify the chemical industry and couple it to the energy sector, are important in providing that “bigger picture” application, and an industrially-relevant spin to much of the research that is carried out on the science of CO_2R and electrochemical synthesis. Nonetheless, to better integrate the respective sectors, we will probably rely on a diverse portfolio of technologies. PC systems for instance can also be envisioned to operate in an analogous manner to electrosynthetic methods during periods of surplus renewable power. This arises from the fact that photocatalysts will typically experience an absorption maximum depending on their bandgap (as exemplified by **g-CN$_x$** in Section 1.4), and hence, will only use a portion of the solar spectrum. Highly efficient and/or low-cost photoredox catalysts can be applied on a more industrial level using wavelength-specific LEDs that are powered using a variety of low-carbon energy sources. This would alleviate the dependence of the technology to be operated via a single renewable source, therefore leading to improvements in terms of practicality and applicability.

Conventional fuel-generating electrolysers typically couple a reductive half-reaction, such as HER or CO_2R, with water oxidation, evolving O_2 gas as a by-product at the anode.[7,151] However, as introduced in Section 1.2, there is an increasing interest to replace this anodic reaction with more synthetically attractive and facile organic transformations.[14,152–157] This strategy is appealing as it not only offers the possibility to reduce the energy requirements of a fuel-forming electrolyser (by avoiding the OER), but imperatively offers the formation of a more valuable product from the oxidative half-reaction too. This is a key concept in the design of the system and will play a role in facilitating the transition to an electrified chemical industry, that is more closely integrated with the energy sector.

Technoeconomic studies by Kenis[9] have highlighted that as much ~90% of the overall energy requirements for current commercial CO_2R electrolysers come from the OER. Through combining theory (thermodynamics) and experiment (electroanalysis), the anodic oxidation of glycerol, which is one of the top biomass-derived platform chemicals and a surplus by-product from the production of biodiesel and soap,[158,159] was identified as a potentially attractive, alternative half-reaction for coupling to CO_2R. This reaction could significantly lower the cell potential for CO_2 electroreduction by ~0.85 V (c.f. Table 1-1), and thus greatly improve the commercial feasibility of the overall redox process.

The works from Sun[153], Zhang[157], Berlinguette[155], and Meyer[14] represent some recent examples from the literature of groups pioneering this novel line of research, in coupling organic-based oxidative reactions with fuel-forming reductive chemistry. Sun[153] made use of a bi-functional, porous Ni_3S_2/Ni foam electrocatalyst, and probed the oxidation of representative biomass substrates at the anode and the subsequent production of H_2 at the cathode. On a similar note, Zhang[157] adopted a bi-functional Ni_2P nanosheet electrode, but extended the anode reaction to include the selective semi-dehydrogenation of tetrahydroisoquinolines to dihydroisoquinolines, which have potential applications in the pharmaceutical industry,[160,161] coupled to the stoichiometric production of H_2 in the cathodic compartment.

Berlinguette's[155] and Meyer's[14] approach is more in-line with the analysis published by Kenis, and present a tandem electrolyser for coupling alcohol oxidation (AlcOx) to CO_2R. The published systems, which made use of molecular catalysts (in-part, or fully for the case of Meyer's system) to conduct the respective half-reactions, suffered two main drawbacks, in that precious metal-containing components were employed in the electrolytic cells, and homogeneous catalysts and mediators were incorporated within the electrocatalytic cycle (the advantages brought about by catalyst immobilisation will be discussed in Section 1.5.3). Specifically, the system by Berlinguette employed a Cu/In cathode for CO_2 reduction, and a Pt anode in the presence of a diffusional redox mediator to facilitate alcohol oxidation. In Meyer's system, Ru-based molecular catalysts were used in tandem, so as to generate syngas at the cathode and carry out benzyl alcohol oxidation at the anode. The Ru-based catalyst for alcohol oxidation was modified with a phosphonic acid anchor for immobilisation on a mesoporous ITO (*meso*ITO) electrode, but a homogeneous Ru complex was adopted for the cathodic half-reaction.

Part of my PhD project is centred on developing a robust and precious-metal-free anodic assembly, for conducting electrocatalytic substrate oxidations, that could then be applied within a tandem AlcOx–CO_2R electrolyser. I chose to work with the organic nitroxyl radical '2,2,6,6-tetramethyl-1-piperidinyloxyl', typically known by its simpler acronym, 'TEMPO', due to the extensive history of this nitroxyl compound as a highly effective (electro)catalyst for the selective oxidation of organic substrates.[162] The next sections of this chapter will therefore be based on TEMPO and its corresponding catalytic cycle, the advantages of catalyst immobilisation for electrocatalytic

applications, the main methods used to-date for TEMPO immobilisation on electrode surfaces, and finally, the choice of anchor for the TEMPO-based anodic assembly developed in my PhD.

1.5.2 TEMPO

The powerful organic redox mediator TEMPO was popularised in the 1980s,[163] during a similar period when the principles of indirect electrolysis were being formalised by Steckhan,[164] and is a promising alternative (electro)catalyst to precious metals. Under electrochemical conditions, this remarkable nitroxyl-based radical can be oxidised into the corresponding oxoammonium cation (the reactive species), which can in turn catalytically oxidise a wide range of alcohols, aldehydes, and amines at room temperature under mild conditions.[165–167]

Earlier mechanistic works by Semmelhack[168] on the oxidation of alcohols via the electrochemically generated oxoammonium cation (**T**$^+$) proposed that, in the presence of base (B), a reactive complex is formed by the nucleophilic attack of an alkoxide anion on either the nitrogen atom or the oxygen atom of **T**$^+$ (see Scheme 1.4, which shows the case of attack on the nitrogen position of **T**$^+$). Intramolecular proton transfer within either intermediate complex would serve to deliver the carbonyl product and a molecule of the hydroxylamine (**TH**). At the time, Semmelhack favoured the route involving alkoxide attack on nitrogen, but based on the data they gathered, could not exclude the alternative pathway. Further studies by Bobbitt[169] however, ruled out attack on the oxygen atom, hence formation of a nitrogen centred complex has since been accepted as the plausible route to generate the pre-oxidation intermediate.

The general mechanism for the electrocatalytic oxidation of alcohols by TEMPO is thus thought to proceed through two electro-oxidative steps: the first, as described above, is needed to produce the catalytically active site (i.e. **T**$^+$), while the second electro-oxidative step is required in order to regenerate TEMPO from **TH** (Scheme 1.4). A recent study by Sigman and Minteer tracked the pH-dependence of the anodic peak potential for the **TH**/TEMPO redox couple relative to that of the pH-invariant TEMPO/**T**$^+$ couple, and helped shed some light on this regeneration step within the reaction mechanism.[170] The observed trend highlighted a shift in potential: from a value more positive to that of the TEMPO/**T**$^+$ couple at acidic pH, to a lower anodic

peak potential at higher pH. This decrease in the peak potential when operating in basic conditions illustrates both a thermodynamic and kinetic effect – the proton-coupled redox process to regenerate TEMPO is thus more favourable and more facile at higher pH.

The increased rate of oxidation of primary versus secondary alcohols was also explained through the proposed mechanism highlighted in Scheme 1.4. Bobbitt *et al*.[169] ascribe the more facile oxidation of the former versus the latter in basic solution to be due to the appreciable decrease in the Gibbs free energy change (ΔG) for complex formation as the steric bulk of the alkoxide is increased. Moreover, at a given pH, primary alkoxide concentration will exceed that of the secondary alkoxide, owing to the slightly more acidic nature of primary versus secondary alcohols.

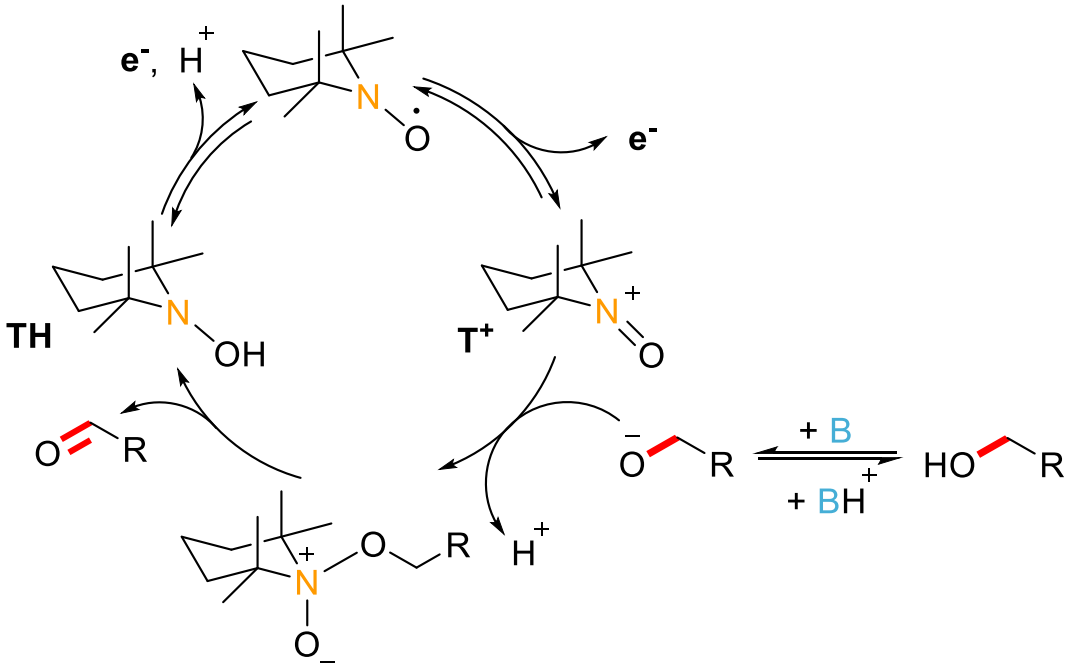

Scheme 1.4: Proposed TEMPO-mediated oxidation mechanism in basic solution.

The catalytic cycle depicted in Scheme 1.4 however could not account for the variation in chemoselectivity with pH, for which it was observed that in basic solution, primary alcohols are oxidised more rapidly than secondary alcohols, whereas in acidic medium the trend is reversed.[171] In general, oxidations of alcohols by $\mathbf{T^+}$ in acidic solution are significantly slower processes than oxidations at higher pH, due to the negligible concentration of alkoxide in the highly protic environment.[172] However, as the pH falls below 4, the oxidation rate of the secondary alcohol by $\mathbf{T^+}$ exceeds that of the primary. Bobbitt *et al*.[169] elaborated on the reason behind this switch and proposed a different

reaction pathway, featuring a bimolecular transfer of a hydride from the α-carbon of alcohol to the oxygen of **T**$^+$ (Scheme 1.5). Although slower than the oxidative reaction in base, this process has a lower activation energy for secondary versus primary alcohols, therefore favouring the rate of oxidation of the former over the latter, as is observed experimentally.

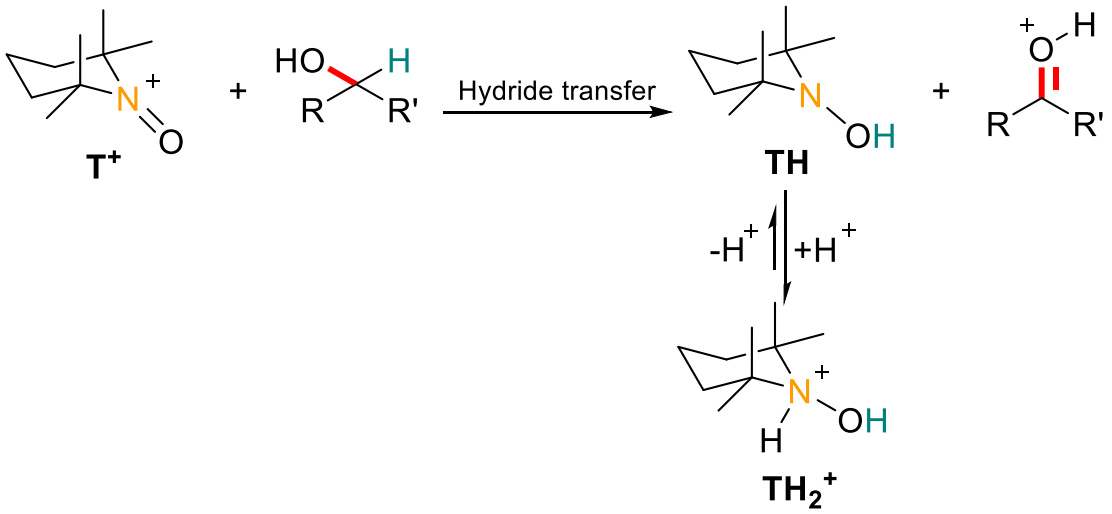

Scheme 1.5: Suggested TEMPO-mediated oxidation mechanism in acidic media. Under such conditions, protonation of the nitrogen atom of **TH** occurs in order to afford the hydroxylammonium species (**TH**$_2^+$), with a corresponding pK_a value of ~7.1.[173–175]

1.5.3 Immobilising Molecular Catalysts

The use of molecular electrocatalysts in solution presents a number of challenges in electrosynthesis, primarily stemming from the fact that the catalyst is only active while in the diffusion layer close to the electrode surface. A large portion of the catalyst is present in the bulk solution, and thus, is inactive at any given time. Having solubilised catalysts also complicates downstream processing of the post-reaction mixture, since additional treatment is required to recover the catalytic components. This issue is all the more relevant as we shift towards the electrosynthesis of liquid products. Molecular catalyst immobilisation has been deemed as a suitable strategy to circumvent such challenges,[176,177] and has become an area of extreme importance in the field of (semi-)artificial photosynthesis, which relies on the efficient connectivity and electronic communication between various system components (such as catalysts, redox-active polymers, and photosensitisers) and the electrode surface or semiconductor powder, in order to improve charge transfer.[178–180]

Immobilising molecular catalysts on solid-state supports, either through physical or chemical means, can allow the system to undergo single-site catalysis, which can enhance the selectivity for a desired product, and simplify identification of the active species.[177] Having the catalyst localised on the electrode surface is also beneficial for maintaining direct electronic communication between the electrode and the catalyst, implying that the latter is constantly undergoing catalytic turnover under the application of a suitable bias, and is not impeded by mass transfer limitations.[181] Metrics used to assess catalyst performance, in terms of system stability and rate of product generation, include the turnover number (TON) and turnover frequency (TOF).[182] These quantities become more meaningful for benchmarking purposes vis-à-vis immobilised catalysts, since as mentioned, for the majority of an experiment, catalyst molecules in a homogeneous system are inactive within the bulk solution.[183] In contrast to homogeneous systems, product isolation and catalyst recyclability are greatly facilitated through the immobilisation procedure, which in-turn promotes the integration of such systems within continuous flow electrochemical devices and more industrially relevant processes. Another benefit provided by immobilisation is that it has allowed water-insoluble catalysts to be used under aqueous conditions. More generally, this implies that catalyst solubility in any reaction medium is no longer a requirement. Reports have indeed emerged where the catalyst was not operable in homogeneous aqueous conditions but was able to demonstrate catalytic activity within the same aqueous medium once immobilised on the electrode surface.[184–186]

Some examples from the literature help illustrate some of these benefits, with regards to the enhancement in the catalytic performance recorded upon surface immobilisation. Artero and co-workers grafted a proton reduction diimine–dioxime cobalt complex onto the surface of a multi-walled carbon nanotube (MWCNT) electrode.[184] When operated in solution, the complex showed significant degradation after just 50 turnovers,[187] whereas upon heterogenization, the catalyst's lifetime and performance were dramatically improved and a corresponding TON of ~33,000 was recorded after a 4 hour electrolysis experiment. The inactivation of the solution-based complex is thought to originate from dimer formation, where the new metal coordination sphere is believed to be unsuitable for catalysis.[188] The authors propose that upon grafting, the molecular complexes become isolated from one another, and this therefore suppresses the reductive homocoupling pathway (which typically leads

to dimer formation) from occurring. Our group synthesised a pyrene-anchored manganese bipyridine CO_2R catalyst, and effectively immobilised it onto a MWCNT scaffold for aqueous operation.[185] The surface loading of the Mn complex was found to have a distinct effect on the selectivity of the CO_2R pathway; at low surface concentrations, the catalyst was observed to remain mostly in its monomeric form and favoured the reduction of CO_2 to formate, whereas a higher surface loading seemed to yield a dimeric Mn^0 species which favoured the formation of CO. In contrast to Artero's system, dimer formation did not cause any adverse effects to the catalytic performance, and only affected the product distribution. This system is therefore an important example of the advantages gained by integrating molecular catalysts onto electrode surfaces, where in this case, the product selectivity was fine-tuned by simply controlling the surface loading of the catalyst, without the need for any synthetic modifications of the catalytic site or the electrode itself.

Cobalt phthalocyanine (**CoPc**) is a well-known molecular CO_2R catalyst,[189–191] and when adsorbed onto a graphite electrode, can produce CO with only modest selectivity, due to the significant co-generation of H_2 stemming from proton reduction in aqueous media. McCrory and co-workers reported an intriguing system, in which they incorporated **CoPc** into a poly-4-vinylpyridine (P4VP) film, prior to assembling onto an electrode, and observed a dramatic enhancement in the CO selectivity (Faradaic efficiency (FE) for CO ~90%).[192] Their work highlighted two key synergistic properties of P4VP which are believed to have contributed towards supressing the competing HER catalytic pathway while simultaneously improving its performance for CO_2R. First, is the ability of the individual pyridine residues of P4VP to coordinate to the square planar cobalt centre of **CoPc**, wherein axial coordination of pyridine has been implicated in enhanced CO_2R activity for this class of compounds.[193–195] Second, is the high concentration of uncoordinated pyridine residues throughout the P4VP film that, upon protonation in acidic electrolyte, may enable secondary coordination sphere effects, such as hydrogen bonding interactions which stabilise activated intermediates, in addition to outer sphere effects, such as proton availability around catalytically active sites.

1.5.4 TEMPO Immobilisation

Various approaches have been adopted for TEMPO immobilisation on an electrode surface, with most using a polymer-based method. Initial investigations into TEMPO immobilisation on carbon felt electrodes were pioneered primarily by Moutet[196] and Bobbitt[197,198] in the late 1980's. The approach by Moutet[196] involved the surface electropolymerisation of a nitroxyl-based monomer containing covalently linked pyrrole groups, while that of Bobbitt[197,198] featured the coupling of 4-NH_2-TEMPO with the acid functionalities on a polyacrylic acid-coated electrode. Some other examples feature TEMPO embedded into an external Nafion® matrix, and immobilised on graphite electrodes,[199] and the formation of poly-(4-methacryloyloxy-TEMPO), starting from the TEMPO methacrylate monomer and subsequent deposition onto aluminium foil by means of a graphite-based slurry.[200] Using a similar strategy, Minteer *at al.* synthesised a TEMPO-modified linear poly-(ethylenimine) polymer, which was combined with carboxylated MWCNTs and glutaraldehyde to form a 'film solution', that was then coated onto a glassy carbon electrode.[201,202] The immobilised, polymeric-TEMPO anode experienced a dramatic increase in the catalytic current density (around an order of magnitude) in the presence of substrate alcohols like methanol and glycerol, relative to the homogeneous TEMPO analogue. They also coupled their novel anode to an enzymatic biocathode to construct a hybrid biofuel cell that was able to generate a maximum current density of ~400 $\mu A\ cm^{-2}$ and power density of 8 $\mu W\ cm^{-2}$, in the presence of methanol at pH 5.0. Despite a low overall cell potential, their results demonstrated both the application of a TEMPO derivative as an organic electrocatalyst within the context of a fuel cell, and the improvement in catalytic activity upon surface immobilisation.

Recently, Stahl developed a pyrene–TEMPO derivative,[203] which was successfully immobilised on a carbon-cloth electrode impregnated with MWCNTs. The noncovalent immobilisation was afforded through the π–π stacking interactions between the pyrene linker and the MWCNT surface[204] – this is one of the few examples that does not involve a polymeric approach towards immobilising the nitroxyl species for electrocatalytic purposes. Further, they highlighted their system for potential electrosynthetic applications by evaluating the oxidation of one of the precursor alcohol compounds that forms part of the synthetic route to rosuvastatin, an active

pharmaceutical ingredient. Replacing traditional oxidising and reducing chemical agents with such an approach is well aligned with the principles outlined in the Green Agenda for organic synthesis,[137,205,206] and also complements earlier discussions on the electrification of the chemical industry, where new technologies are required to improve the sustainability of chemical manufacturing processes and provide better integration with the energy sector.

The covalent immobilisation of TEMPO onto metal oxide (MO) electrodes however, has remained largely underexplored. MOs present an interesting platform for the immobilisation of electrocatalysts and offer a range of alternative advantages over carbon-based electrodes. Firstly, they can be easily synthesised using low-cost solution processing techniques, and can exhibit different electronic properties, as demonstrated by the metallic behaviour of indium tin oxide (ITO) and the semiconducting properties of TiO_2. ITO is thus a suitable choice for electrochemical applications, unlike TiO_2 which does not allow for efficient electronic conduction within its bandgap. TiO_2 however, is commonly used as a charge collector and separator in dye-sensitised PEC cells.[207,208] Moreover, the surfaces of MOs can be nanostructured to introduce a higher surface area-to-volume (*SA*-to-*V*) ratio which consequently allows for an increased loading of catalytic species.[38,209–211] The surface morphology can also be tuned to give rise to more complex hierarchical MO structures, with one such example featuring an electrode composed of a macroporous inverse opal architecture and a mesoporous skeleton.[212] This design was applied to both ITO and TiO_2,[180,213] and was developed to maximise enzyme loading, wherein the macroporosity allowed for enhanced penetration of enzymes and substrate/s, while the mesoporosity increased the effective surface area for enzyme interactions and electronic coupling with the MO surface, and facilitated stable anchoring.[214,215]

ITO and TiO_2 have the additional advantage of being (semi)transparent, and hence, can be incorporated as protection layers and molecular scaffolds for photoelectrochemical applications.[216] Particularly, thin *meso*ITO electrodes combine optical transparency with both a high conductivity and molecular loading ability, making it an ideal platform to conduct *in operando* characterisation via transmission-mode spectroelectrochemical techniques.[217,218] This strategy allows users to probe the surface-bound species and gain mechanistic insights about the catalytic process, which can assist with optimising system performance.[219] Carbon nanotubes are a

relatively inert and stable conducting material and have been successfully utilised as high surface area scaffolds for molecular catalyst immobilisation, either through direct grafting or noncovalent attachment to the carbon surfaces.[220–222] However, the carbon nanotubes have typically been deposited on carbon cloth electrodes or gas diffusion layers, which have therefore precluded *in operando* transmission spectroscopic studies of the reactive intermediates due to a lack of any optical transmission through the assembled electrodes. As will be discussed in more detail in Chapter 4, ITO-based electrodes are suitable for carrying out 'film electrochemical electron paramagnetic resonance' (FE-EPR) studies,[223] due to its aforementioned advantages combined with the EPR silent response (clean background) of the unfunctionalised electrode. Carbon-based supports on the other hand tend to give rise to large radical signals and hence, are unsuitable for such studies.

A derivatised TEMPO compound, amenable to immobilisation on different MO surfaces would therefore make for a versatile catalyst that could either be implemented on an ITO surface for electrochemical applications, or co-immobilised with a dye on a TiO_2 scaffold for photodriven substrate oxidation studies. The aforementioned reasons for replacing the OER at the anode in traditional electrolysers with more facile oxidative chemistry, is also applicable to the conventional water splitting PEC assembly. Originally designed for dye immobilisation in dye-sensitised solar cells, a number of chemical functionalities have been employed for anchoring molecular components to MO surfaces, including carboxylic acids,[224,225] phosphonic acids,[226–228] silatranes,[229–233] hydroxamic acids,[234–236] acetylacetonate anchors,[237] and catechol anchors[238] (some examples are shown in Figure 1.8).

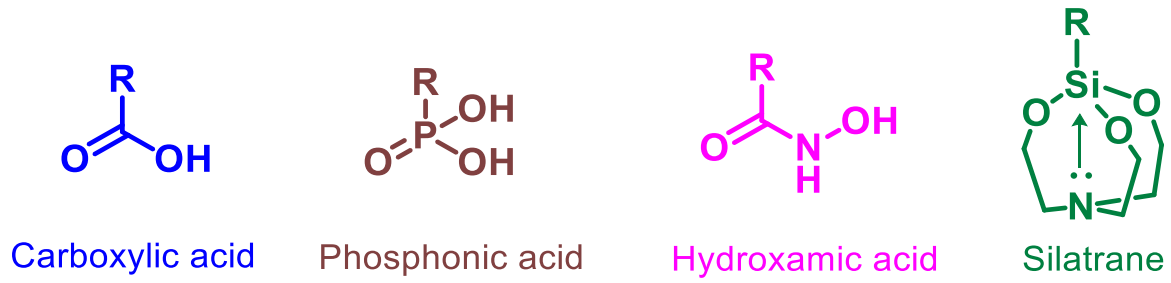

Figure 1.8: Possible anchors for immobilising molecular catalysts onto metal oxide surfaces**.**

To develop a robust, hybrid anode, comprised of an immobilised compound featuring the TEMPO moiety, the anchor must satisfy three important criteria, and must: (i) be stable under oxidative conditions, hence it should have a formal oxidation potential

that is more positive than that of TEMPO to avoid desorption during operation, (ii) be stable in aqueous media, for integration within a coupled AlcOx–CO_2R electrolyser, and (iii) be stable under alkaline pH (pH > 7), in accordance with the proposed TEMPO-mediated electrocatalytic mechanism for substrate alcohol oxidation, for which the rate of oxidation increases with increasing pH.[162,163,169]

Thus, the catechol and acetylacetonate anchors can be ruled out on the grounds that the former is readily oxidised and hence, unstable under the required operating conditions, while the latter is prone to deacetylation in aqueous media.[239] For both carboxylates and phosphonates, anchoring onto MOs is thought to occur via condensation reactions involving the incoming acid moiety and hydroxyl groups that exist on the surface of the MO, resulting in a covalent interaction between the material surface and the molecule.[230] Although this form of chemisorption is stable under oxidative potentials and in aqueous solution, i.e. satisfying both criteria (i) and (ii) above, the stability window for the carboxylate and phosphonate anchors lies within the acidic pH range (pH stability < 4 and 7, respectively),[239] and thus both fail to satisfy criterion (iii). Recently, Brudvig *et al.* reported a broad pH stability range (2 < pH < 11) for silatrane-functionalised ruthenium complexes covalently attached to *meso*ITO electrodes,[231] and attribute this behaviour to the strong siloxane bonds formed upon hydrolysis of the caged moiety to the MO surface. They applied a similar methodology to a pentamethylcyclopentadienyl-based iridium water-oxidation catalyst, and demonstrated that the heterogenized system could perform electrochemically driven water oxidation under a positive applied potential (1.35 V *vs.* NHE, at pH 5.8).[232] These promising reports are well aligned with the system requirements for a robust, TEMPO-based anode assembly, and satisfy all three of the prerequisite criteria for the choice of anchor. This rationale, in addition to the fact that silatranes are among one of the least explored surface anchors and thus merit further research and investigation into catalytic applications,[233] provided the incentive to design a ‘silatrane modified TEMPO analogue’ for immobilisation onto a MO surface.

1.6 Continuous Flow Chemistry

1.6.1 Fundamental Properties of Flow Reactors

The renewed interest in photocatalytic and electrochemical processes has also raised questions regarding the design and efficiency of the reactors used to carry out such reactions. Typically, a batch reactor design is employed, but this tends to suffer from a lack of design specificity towards its intended application. For instance, scalability in batch photoreactors is hampered by the rapid attenuation of the incident photon beam, as governed by the Beer–Lambert–Bouguer law, implying that minimal light intensity would reach the central part of the mixture. The non-uniform distribution of the incident radiation could have consequences on by-product formation stemming from over-irradiated zones in the reactor.[240] With regards to a batch electrochemical cell, scaling up the reactor volume would lead to an increase in the relative distance between the two electrodes (the interelectrode gap, d_g), consequently giving rise to a higher ohmic drop (iR_u). The ohmic potential drop is a result of the additional resistance encountered by the flow of charge (i.e. the current, i) through the solution between the two electrodes, and can represented through Equation 1.1:

$$iR_u = i\frac{d_g}{\kappa A} \qquad 1.1$$

where R_u is the uncompensated resistance, A the electrode surface area, and κ the solution conductivity. Hence in batch, large amounts of supporting electrolyte (to increase κ) are usually employed. This makes the electrochemical process more complicated as the supporting electrolyte needs to be separated from the product after the reaction, and can also lead to surmounting costs for the overall process if the electrolyte is not recycled.

One of the most effective techniques to circumvent these issues is through the implementation of continuous flow reactor technologies, in which the flow devices can be fabricated to have a high *SA*-to-*V* ratio. This would, for a photoreactor, guarantee an extensive transmission of light throughout the reaction mixture,[133] or in the case of an electrochemical set-up, entail a narrow interelectrode spacing and therefore, lower ohmic drop.[241] In addition to photon attenuation and ohmic drop considerations, mass

transport phenomena and electron transfer kinetics are also crucial in the design of an appropriate reactor.[242] Immobilised photocatalytic and electrochemical systems can be regarded as heterogeneous processes, in which the substrate/s need to be transported from the bulk of the solution to the active surface; narrow channel dimensions and a corresponding high *SA*-to-*V* ratio is therefore beneficial from a mass transfer perspective too. For this reason, flow reactors for such applications have been designed to have relatively small channel dimensions, with 'microreactors' and 'mesoreactors' being classified as having channel dimensions below and above 1 mm, respectively.[243,244]

A laminar flow pattern is present within a microreactor,[245–247] and hence, the fluid flows along in parallel laminae. The transport of species, and therefore mixing between laminae, is primarily through the process of diffusion, which stems from the concentration gradients developed as a result of substrate consumption at the interface. The smaller channel dimension defining the microreactor facilitates the rate of the heterogeneous reaction due to the short diffusion paths of the reagent species.[248] This design approach, with optimal *SA*-to-*V* characteristics, also offers a high thermal transfer efficiency, reducing the risk of runaway reactions from exothermic pathways,[249–251] enabling energetic materials to be synthesised in a more controlled manner.[252]

Flow reactor design also facilitates efficient mixing for multiphase reactions,[132] such as in biphasic (gas–liquid, solid–liquid, liquid–liquid) and triphasic (gas–liquid–solid) systems, where phase transfer across the interfacial area can play an important role in governing the rate of reaction. Continuous flow has been exploited to enhance heterogeneous catalysis, by essentially combining the reaction and separation into one step using a packed bed reactor, which is characterised by the solid catalyst being immobilised in the entire column or channel in order to restrict particle movement. Gas–liquid–solid reactions, such as hydrogenation reactions, are exceptionally valuable transformations and comprise the majority of heterogeneous catalysis reactions in flow, wherein the packed bed offers both a large interfacial area and simulates high local catalyst loading.[249,253–255] Many different flow regimes can exist for gas–liquid and liquid–liquid mixtures; however, segmented flow (also known as Taylor flow or slug flow) and annular flow (sometimes referred to as pipe flow) are most commonly described for reactions in micro- and tube reactors.[244] Segmented

flow is characterised by liquid slugs and elongated bubbles of an immiscible phase (which could be gas or liquid), such that the bubble is separated from the reactor walls by a thin liquid film (Figure 1.9). Toroidal vortices are established which promote mixing and intensify mass transport from one phase to the other.[256] Of course, the segmented flow-approach in microreactors can also be extended to include triphasic reactions, such as for heterogeneous photochemical applications. In this case, the photocatalyst can be immobilised on the reactor wall, and the maximal *SA*-to-*V* characteristics of the device would permit extensive contact between all three phases and the incident photons.[257] Another popular approach for gas–liquid flow chemistry, pioneered by Ley and co-workers, is the tube-in-tube rector.[258] This is a form of membrane reactor that consists of a pair of concentric capillaries in which pressurised gas, flowing through an outer (impermeable) tube, permeates through an inner Teflon tube which houses the liquid flow.

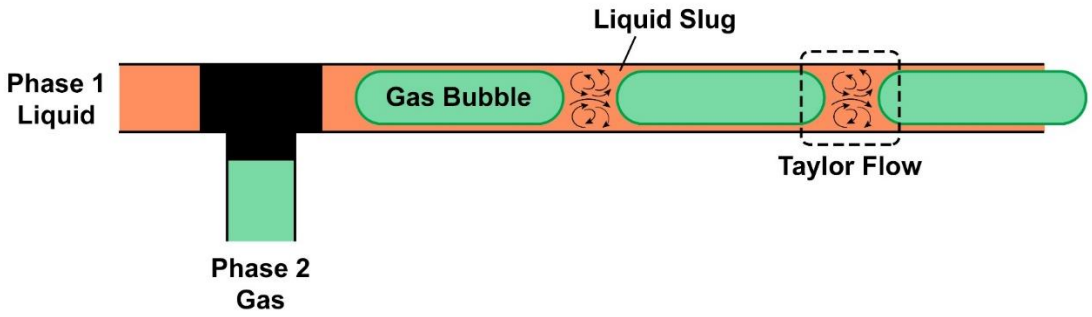

Figure 1.9: Segmented flow pattern for a gas–liquid mixture in a microfluidic channel, and the resultant Taylor flow within the liquid phase.

Besides from a reactor design perspective, there are several other benefits offered through the continuous flow process when compared to the conventional batch approach. The continuous operation allows for accurate control of the residence time via the flow rate,[259] which is an indispensable tool for preventing secondary reactions or product decomposition by rapidly removing the mixture from the reactive area (be it a photo- or electroactive zone). For photochemical transformations, photocatalyst immobilisation within the reactor can assist with downstream processing of the reaction mixture, as it avoids catalyst separation and thereby facilitates reusability and recyclability.[260] Combining multiple synthetic steps into a single, uninterrupted, continuous flow process circumvents the need to isolate intermediate products after each reaction step (Figure 1.10).[261,262] This not only improves the synthetic efficiency,[263] but also means that volatile or hazardous intermediates can be better

contained, therefore improving the overall safety of the process.[264,265] Continuous flow technologies have also facilitated the handling of slurries,[266] and low temperature reaction protocols.[266]

Another appealing quality of a continuous flow system is the potential to couple this technology with in-line detection and analytical methods. The acquired data would provide insight regarding system performance as a function of the input reactor parameters (such as substrate concentration, temperature, and flow rate, among others), in close to real time.[267] Integration of continuous in-line monitoring techniques with feedback control units, allows for synthetic procedures to become automated, and by linking the data with machine learning algorithms, makes it possible to design autonomously self-optimising systems.[268–275]

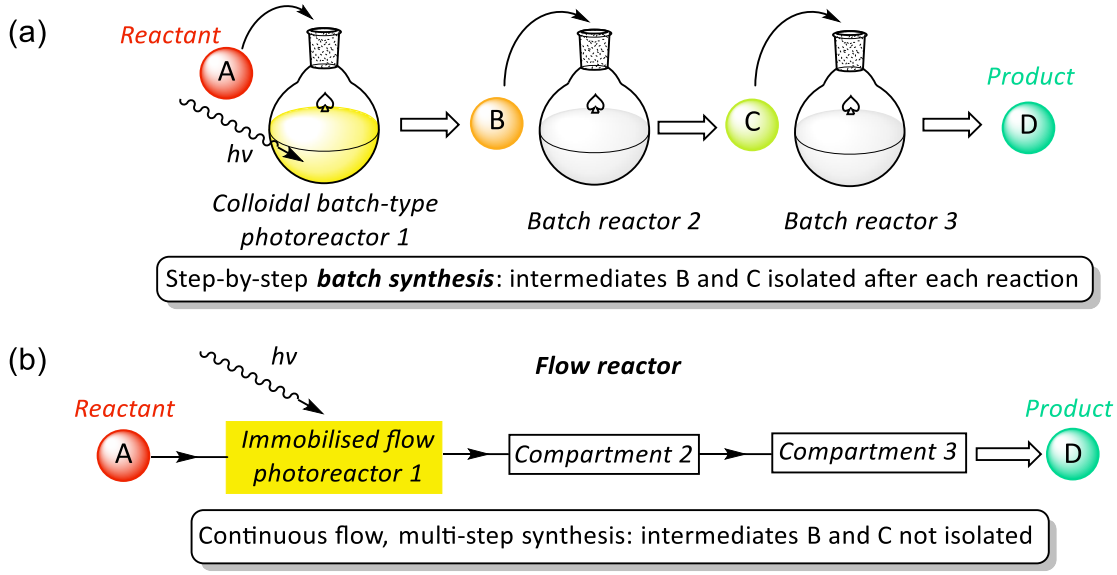

Figure 1.10: Multi-step synthetic strategy with the first step being photocatalysed, for (a) batch versus (b) flow.

Such advancements in continuous flow chemistry will play a key role in the modernisation of the chemical industry, and complement the trends outline by the Chemistry 4.0 and Industry 4.0 initiatives, as previously highlighted (c.f. Section 1.5.1). Reports in the literature have already described the ability to harness the Cloud in order to remotely initiate, monitor, and control self-optimisation reactions across international borders.[276,277] The progress stemming from the continuous flow community regarding in-line analysis,[278] real-time data acquisition on reactor performance, and automated feedback optimisation,[279] is being met with the development of AI and machine learning algorithms, especially targeted towards Big

Data analytics.[280] This has inspired pioneering research into a new generation of robotic platforms for machine-augmented drug and chemical synthesis, and for the discovery of novel chemistries.[281–283]

1.6.2 Heterogeneous Photocatalysis in Flow

Despite the broad range of carbon nitride photocatalysed chemistries that have emerged in recent years (Section 1.4.2), and the clear advantages gained by implementing heterogeneous catalysis in-flow, there have only been a few reports regarding continuous flow applications with this material. Blechert *et al.* developed a continuous-flow protocol for the photocatalytic radical cyclisation of 2-bromomalonates in the presence of **mpg-CN$_x$**.[284] Their set-up was comprised of a fluorinated ethylene propylene (FEP) tube, that was packed with a silica gel, glass bead, and **mpg-CN$_x$** mixture, which was in-turn irradiated with blue LEDs (λ = 425 nm) when the substrate solution was being pumped through the packed column (Figure 1.11a). For this biphasic (liquid–solid) flow reaction, the authors reported a dramatic improvement in selectivity and a six-fold increase in the rate of substrate conversion, when compared with the batch analogue.

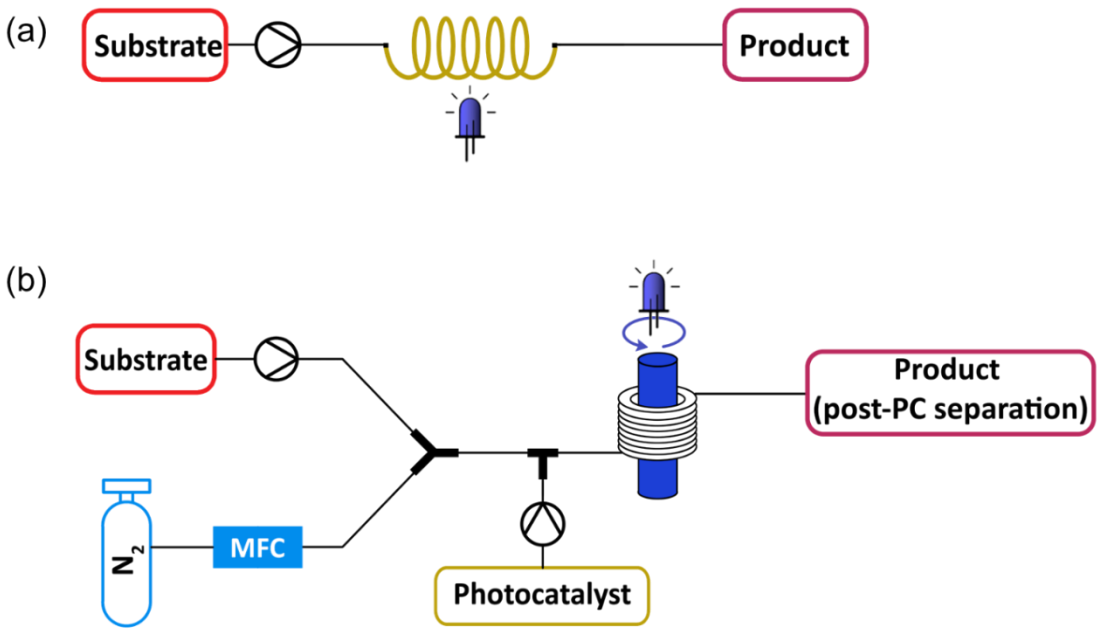

Figure 1.11: Continuous flow systems incorporating carbon nitride materials: (a) packed column approach, and (b) simplified reaction schematic to generate the SMBR (PC = photocatalyst).

Recently, Seeberger and Antonietti designed a serial micro-batch reactor (SMBR), to pursue triphasic flow photochemistry with carbon nitride in a continuous flow environment (flow schematic depicted in Figure 1.11b).[285] The SMBR is comprised of a series of small liquid-solid suspensions ('batch reactors') that are separated by an inert gas spacer. The aforementioned toroidal vortices stemming from the segmented flow pattern assist with 'stirring' the locally confined micro suspensions, therefore providing well-mixed reaction environments, which are irradiated in a uniform fashion. To minimise settling of the carbon nitride during operation, a viscous component (in their case an imidazolium ionic liquid) was added to the substrate input feed. The decarboxylative fluorination of phenoxyacetic acid using Selectfluor® was chosen in order to assess the performance of the carbon-nitride-based SMBR, and the authors report nearly full conversion with a residence time of only 14 minutes. The carbon nitride was also recovered and reused without loss of catalytic activity. When a homogeneous Ru-based catalyst was used in place of carbon nitride within the SMBR, not only were the conversions lower, but the Ru complex also led to fouling of the reactor, thus limiting its recyclability. One of the few downsides of the set-up was the slightly tedious downstream process (three-step extraction protocol) required to recover the photocatalyst, ionic liquid, and the organofluorine product.

1.7 Thesis Aims and Outline

From the discussion made in this chapter, it is evident that: (i) continuous flow chemistry offers numerous advantages over batch reactors and is very appealing for heterogeneous photocatalytic applications; however, it has been particularly underexplored for the carbon nitride materials. (ii) More synthetically attractive and facile oxidative processes are needed in place of the OER, to lower applied cell potentials for coupling to fuel-generating chemistries, such as CO_2R.

The aim of this work was thus to utilise organic substrate oxidations as a substitute for the OER, and (i) develop a method to conduct such transformations in-flow using a carbon nitride photocatalyst, and (ii) construct a novel anodic assembly featuring the TEMPO electrocatalyst, for implementation within an electrolyser device that couples value-added substrate oxidation with CO_2R. The focus of the PhD is therefore split into two main sections. The first part falls under the general category of

‘photocatalysis’, and delves into the modelling, design, and assessment of some continuous flow configurations involving carbon nitride materials, namely ^{NCN}**CN$_x$** (Chapter 2) and **mpg-CN$_x$** (Chapter 3). Chapter 2 includes a computational fluid dynamics (CFD) model for a *thin channel flow device* incorporating a stationary ^{NCN}**CN$_x$** photocatalyst sheet. The aim of such was to gain a parametric understanding of the device configuration, which also served to lay the groundwork for building the initial prototype photoreactor. Chapter 3 builds on the lessons learnt from the proof-of-concept flow design. The setup needed to conduct triphasic (gas–liquid–solid) flow photochemistry with carbon nitride materials is discussed. The final configuration featured a packed column photoreactor, incorporating **mpg-CN$_x$** as the photocatalyst, and was operated under continuous flow conditions with aerobic O_2 as one of the input streams. Alcohol and amine oxidations were investigated as a means to assess reactor performance compared to an analogous batch setup.

The second part of this PhD project is reflected in Chapter 4. The emphasis of this chapter is on ‘electrochemical’ approaches to substrate oxidations, which can be coupled to fuel-generating reductive chemistry. The advantageous properties of utilising the organic electrocatalyst TEMPO to conduct oxidative chemistry, and the benefits that could be achieved through immobilisation on a MO scaffold, have been addressed in Chapter 1. In Chapter 4, a robust metal oxide-based anode featuring the TEMPO moiety was developed. More synthetic details regarding our approach to modify TEMPO with a silatrane anchor, and the requirements needed to immobilise this compound on a *meso*ITO electrode are presented, followed by complementary optimisation studies on the performance of the assembled anode towards the oxidation of representative substrate alcohols. Having demonstrated the applicability of the TEMPO-based anode architecture, the hybrid was combined with a CO_2R electrocatalyst to create a coupled electrolyser. A carbon nanotube cathode modified with a polymeric cobalt phthalocyanine was used as the CO_2R electrocatalyst. This was the first example in the literature of a precious-metal-free, fully molecular electrolyser for stoichiometrically coupling alcohol-to-aldehyde oxidation and CO_2-to-syngas conversion. The system was exemplified using both the model substrate MBA, and the more commercially viable and abundant resource glycerol.

Finally, in Chapter 5, the main conclusions and key messages derived from the investigations conducted throughout the course of the PhD are presented. Future

prospects stemming from this thesis, including the next generation of carbon nitride-based flow reactors, and the plans to transform our TEMPO-based anode into a photoanode for visible light-driven substrate oxidation, are also discussed.

1.8 References

1 P. De Luna, C. Hahn, D. Higgins, S. A. Jaffer, T. F. Jaramillo and E. H. Sargent, *Science*, 2019, **364**, eaav3506.

2 Z. J. Schiffer and K. Manthiram, *Joule*, 2017, **1**, 10–14.

3 O. S. Bushuyev, P. De Luna, C. T. Dinh, L. Tao, G. Saur, J. van de Lagemaat, S. O. Kelley and E. H. Sargent, *Joule*, 2018, **2**, 825–832.

4 Y. Y. Birdja, E. Pérez-Gallent, M. C. Figueiredo, A. J. Göttle, F. Calle-Vallejo and M. T. M. Koper, *Nat. Energy*, 2019, **4**, 732–745.

5 S. C. Roy, O. K. Varghese, M. Paulose and C. A. Grimes, *ACS Nano*, 2010, **4**, 1259–1278.

6 N. S. Lewis and D. G. Nocera, *Proc. Natl. Acad. Sci. U. S. A.*, 2006, **103**, 15729–15735.

7 C. C. L. McCrory, S. Jung, I. M. Ferrer, S. M. Chatman, J. C. Peters and T. F. Jaramillo, *J. Am. Chem. Soc.*, 2015, **137**, 4347–4357.

8 E. E. Benson, C. P. Kubiak, A. J. Sathrum and J. M. Smieja, *Chem. Soc. Rev.*, 2009, **38**, 89–99.

9 S. Verma, S. Lu and P. J. A. Kenis, *Nat. Energy*, 2019, **4**, 466–474.

10 L. M. Reid, T. Li, Y. Cao and C. P. Berlinguette, *Sustain. Energy Fuels*, 2018, **2**, 1905–1927.

11 B. Kumar, M. Llorente, J. Froehlich, T. Dang, A. Sathrum and C. P. Kubiak, *Annu. Rev. Phys. Chem.*, 2012, **63**, 541–569.

12 M. G. Kibria, J. P. Edwards, C. M. Gabardo, C. T. Dinh, A. Seifitokaldani, D. Sinton and E. H. Sargent, *Adv. Mater.*, 2019, **1807166**, 1–24.

13 M. E. Dry, *Catal. Today*, 2002, **71**, 227–241.

14 Y. Wang, S. Gonell, U. R. Mathiyazhagan, Y. Liu, D. Wang, A. J. M. Miller and T. J. Meyer, *ACS Appl. Energy Mater.*, 2019, **2**, 97–101.

15 S. Nitopi, E. Bertheussen, S. B. Scott, X. Liu, A. K. Engstfeld, S. Horch, B. Seger, I. E. L. Stephens, K. Chan, C. Hahn, J. K. Nørskov, T. F. Jaramillo and I. Chorkendorff, *Chem. Rev.*, 2019, **119**, 7610–7672.

16 S. Chen, T. Takata and K. Domen, *Nat. Rev. Mater.*, 2017, **2**, 1–17.

17 A. Kudo and Y. Miseki, *Chem. Soc. Rev.*, 2009, **38**, 253–278.

18 K. Maeda and K. Domen, *J. Phys. Chem. C*, 2007, **111**, 7851–7861.

19 K. Maeda, *ACS Catal.*, 2013, **3**, 1486–1503.

20 K. Sayama, R. Yoshida, H. Kusama, K. Okabe, Y. Abe and H. Arakawa, *Chem. Phys. Lett.*, 1997, **277**, 387–391.

21 Y. Umena, K. Kawakami, J. R. Shen and N. Kamiya, *Nature*, 2011, **473**, 55–60.

22 N. Nelson and A. Ben-Shem, *Nat. Rev. Mol. Cell Biol.*, 2004, **5**, 971–982.

23 J. Barber and P. D. Tran, *J. R. Soc. Interface*, DOI:10.1098/rsif.2012.0984.

24 Y. Wang, H. Suzuki, J. Xie, O. Tomita, D. J. Martin, M. Higashi, D. Kong, R. Abe and J. Tang, *Chem. Rev.*, 2018, **118**, 5201–5241.

25 H. Kasap, C. A. Caputo, B. C. M. Martindale, R. Godin, V. W.-H. Lau, B. V. Lotsch, J. R. Durrant and E. Reisner, *J. Am. Chem. Soc.*, 2016, **138**, 9183–9192.

26 A. Vijeta and E. Reisner, *Chem. Commun.*, 2019, **55**, 14007–14010.

27 D. W. Wakerley, M. F. Kuehnel, K. L. Orchard, K. H. Ly, T. E. Rosser and E. Reisner, *Nat. Energy*, 2017, **2**, 17021.

28 H. Kasap, D. S. Achilleos, A. Huang and E. Reisner, *J. Am. Chem. Soc.*, 2018, **140**, 11604–11607.

29 T. Uekert, M. F. Kuehnel, D. W. Wakerley and E. Reisner, *Energy Environ. Sci.*, 2018, **11**, 2853–2857.

30 T. Uekert, H. Kasap and E. Reisner, *J. Am. Chem. Soc.*, 2019, **141**, 15201–15210.

31 K. Yoshikawa, H. Kawasaki, W. Yoshida, T. Irie, K. Konishi, K. Nakano, T. Uto, D. Adachi, M. Kanematsu, H. Uzu and K. Yamamoto, *Nat. Energy*, , DOI:10.1038/nenergy.2017.32.

32 S. Essig, C. Allebé, T. Remo, J. F. Geisz, M. A. Steiner, K. Horowitz, L. Barraud, J. S. Ward, M. Schnabel, A. Descoeudres, D. L. Young, M. Woodhouse, M. Despeisse, C. Ballif and A. Tamboli, *Nat. Energy*, 2017, **2**, 17144.

33 D. Larcher and J. M. Tarascon, *Nat. Chem.*, 2015, **7**, 19–29.

34 J. Newman, P. G. Hoertz, C. A. Bonino and J. A. Trainham, *J. Electrochem. Soc.*, 2012, **159**, 1722–1729.

35 M. R. Shaner, S. J. Davis, N. S. Lewis and K. Caldeira, *Energy Environ. Sci.*, 2018, **11**, 914–925.

36 S. Ardo, D. Fernandez Rivas, M. A. Modestino, V. Schulze Greiving, F. F. Abdi, E. Alarcon Llado, V. Artero, K. Ayers, C. Battaglia, J. P. Becker, D. Bederak, A. Berger, F. Buda, E. Chinello, B. Dam, V. Di Palma, T. Edvinsson, K. Fujii, H. Gardeniers, H. Geerlings, S. M. Hashemi, S. Haussener, F. Houle, J. Huskens, B. D. James, K. Konrad, A. Kudo, P. P. Kunturu, D. Lohse, B. Mei, E. L. Miller, G. F. Moore, J. Muller, K. L. Orchard, T. E. Rosser, F. H. Saadi, J. W. Schüttauf, B. Seger, S. W. Sheehan, W. A. Smith, J. Spurgeon, M. H. Tang, R. Van De Krol, P. C. K. Vesborg and P. Westerik, *Energy Environ. Sci.*, 2018, **11**, 2768–

2783.

37 K. Sivula and R. van de Krol, *Nat. Rev. Mater.*, 2016, **1**, 15010.

38 T. E. Rosser, M. A. Gross, Y.-H. Lai and E. Reisner, *Chem. Sci.*, 2016, **7**, 4024–4035.

39 A. Wolcott, W. A. Smith, T. R. Kuykendall, Y. Zhao and J. Z. Zhang, *Small*, 2009, **5**, 104–111.

40 S. D. Tilley, M. Cornuz, K. Sivula and M. Grätzel, *Angew. Chem. Int. Ed.*, 2010, **49**, 6405–6408.

41 S. K. Cho, H. S. Park, H. C. Lee, K. M. Nam and A. J. Bard, *J. Phys. Chem. C*, 2013, **117**, 23048–23056.

42 Y. H. Lai, T. C. King, D. S. Wright and E. Reisner, *Chem. Eur. J.*, 2013, **19**, 12943–12947.

43 A. Paracchino, V. Laporte, K. Sivula, M. Grätzel and E. Thimsen, *Nat. Mater.*, 2011, **10**, 456–461.

44 Z. Ji, M. He, Z. Huang, U. Ozkan and Y. Wu, *J. Am. Chem. Soc.*, 2013, **135**, 11696–11699.

45 C. E. Creissen, J. Warnan and E. Reisner, *Chem. Sci.*, 2018, **9**, 1439–1447.

46 J. R. McKone, E. L. Warren, M. J. Bierman, S. W. Boettcher, B. S. Brunschwig, N. S. Lewis and H. B. Gray, *Energy Environ. Sci.*, 2011, **4**, 3573–3583.

47 M. S. Prévot and K. Sivula, *J. Phys. Chem. C*, 2013, **117**, 17879–17893.

48 T. W. Kim and K.-S. Choi, *Science*, 2014, **343**, 990–994.

49 J. R. McKone, N. S. Lewis and H. B. Gray, *Chem. Mater.*, 2014, **26**, 407–414.

50 A. Kargar, J. S. Cheung, C.-H. Liu, T. K. Kim, C. T. Riley, S. Shen, Z. Liu, D. J. Sirbuly, D. Wang and S. Jin, *Nanoscale*, 2015, **7**, 4900–4905.

51 Y. H. Lai, D. W. Palm and E. Reisner, *Adv. Energy Mater.*, 2015, **5**, 1–11.

52 C. K. Prier, D. A. Rankic and D. W. C. MacMillan, *Chem. Rev.*, 2013, **113**, 5322–5363.

53 N. A. Romero and D. A. Nicewicz, *Chem. Rev.*, 2016, **116**, 10075–10166.

54 K. L. Skubi, T. R. Blum and T. P. Yoon, *Chem. Rev.*, 2016, **116**, 10035–10074.

55 D. M. Hedstrand, W. H. Kruizinga and R. M. Kellogg, *Tetrahedron Lett.*, 1978, **19**, 1255–1258.

56 H. Cano-Yelo and A. Deronzier, *J. Photochem.*, 1987, **37**, 315–321.

57 K. Okada, K. Okubo, N. Morita and M. Oda, *Tetrahedron Lett.*, 1992, **33**, 7377–7380.

58 K. Okada, K. Okubo, N. Morita and M. Oda, *Chem. Lett.*, 1993, 22, 2021–2024.

59 D. A. Nicewicz and D. W. C. MacMillan, *Science*, 2008, **322**, 77–80.

60 M. A. Ischay, M. E. Anzovino, J. Du and T. P. Yoon, *J. Am. Chem. Soc.*, 2008, **130**, 12886–12887.

61 M. H. Shaw, J. Twilton and D. W. C. MacMillan, *J. Org. Chem.*, 2016, **81**, 6898–6926.

62 J. W. Tucker and C. R. J. Stephenson, *J. Org. Chem.*, 2012, **77**, 1617–1622.

63 L. Marzo, S. K. Pagire, O. Reiser and B. König, *Angew. Chem. Int. Ed.*, 2018, 10034–10072.

64 F. Lima, L. Grunenberg, H. B. A. Rahman, R. Labes, J. Sedelmeier and S. V Ley, *Chem. Commun.*, 2018, **54**, 5606–5609.

65 A. Joshi-Pangu, F. Lévesque, H. G. Roth, S. F. Oliver, L. C. Campeau, D. Nicewicz and D. A. DiRocco, *J. Org. Chem.*, 2016, **81**, 7244–7249.

66 A. Savateev, I. Ghosh, B. König and M. Antonietti, *Angew. Chem. Int. Ed.*, 2018, **57**, 15936–15947.

67 D. P. Hari and B. König, *Chem. Commun.*, 2014, **50**, 6688–6699.

68 I. Ghosh, T. Ghosh, J. I. Bardagi and B. Konig, *Science*, 2014, **346**, 725–728.

69 I. Ghosh and B. König, *Angew. Chem. Int. Ed.*, 2016, **55**, 7676–7679.

70 R. Lechner, S. Kümmel and B. König, *Photochem. Photobiol. Sci.*, 2010, **9**, 1367–1377.

71 X. Wang, K. Maeda, A. Thomas, K. Takanabe, G. Xin, J. M. Carlsson, K. Domen and M. Antonietti, *Nat. Mater.*, 2009, **8**, 76–80.

72 J. Liebig, *Ann. der Pharm.*, 1834, **10**, 1–47.

73 A. Thomas, A. Fischer, F. Goettmann, M. Antonietti, J.-O. Müller, R. Schlögl and J. M. Carlsson, *J. Mater. Chem.*, 2008, **18**, 4893.

74 J. Fang, H. Fan, M. Li and C. Long, *J. Mater. Chem. A*, 2015, **3**, 13819–13826.

75 C. Caputo, L. Wang, R. Beranek and E. Reisner, *Chem. Sci.*, 2015, **6**, 5690.

76 Y. Wang, H. Li, J. Yao, X. Wang and M. Antonietti, *Chem. Sci.*, 2011, **2**, 446.

77 K. Schwinghammer, B. Tuffy, M. B. Mesch, E. Wirnhier, C. Martineau, F. Taulelle, W. Schnick, J. Senker and B. V. Lotsch, *Angew. Chem. Int. Ed.*, 2013, **52**, 2435–2439.

78 J. Liu, H. Wang, Z. P. Chen, H. Moehwald, S. Fiechter, R. Van De Krol, L. Wen, L. Jiang and M. Antonietti, *Adv. Mater.*, 2015, **27**, 712–718.

79 J. Liu, T. Zhang, Z. Wang, G. Dawson and W. Chen, *J. Mater. Chem.*, 2011, **21**, 14398–14401.

80 D. J. Martin, K. Qiu, S. A. Shevlin, A. D. Handoko, X. Chen, Z. Guo and J. Tang, *Angew. Chem. Int. Ed.*, 2014, **53**, 9240–9245.

81 G. Zhang, J. Zhang, M. Zhang and X. Wang, *J. Mater. Chem.*, 2012, **22**, 8083–8091.

82 J. Yu, K. Wang, W. Xiao and B. Cheng, *Phys. Chem. Chem. Phys.*, 2014, **16**, 11492–11501.

83 B. Jürgens, E. Irran, J. Senker, P. Kroll, H. Müller and W. Schnick, *J. Am. Chem. Soc.*, 2003, **125**, 10288–10300.

84 B. V. Lotsch and W. Schnick, *Chem. Mater.*, 2006, **18**, 1891–1900.

85 M. J. Bojdys, J. O. Müller, M. Antonietti and A. Thomas, *Chem. Eur. J.*, 2008, **14**, 8177–8182.

86 E. Kroke, M. Schwarz, E. Horath-Bordon, P. Kroll, B. Noll and A. D. Norman, *New J. Chem.*, 2002, **26**, 508–512.

87 Y. Wang, X. Wang and M. Antonietti, *Angew. Chem. Int. Ed.*, 2012, **51**, 68–89.

88 J. Liu and M. Antonietti, *Energy Environ. Sci.*, 2013, **6**, 1486.

89 V. S. Vyas, V. W. H. Lau and B. V. Lotsch, *Chem. Mater.*, 2016, **28**, 5191–5204.

90 F. Fina, S. K. Callear, G. M. Carins and J. T. S. Irvine, *Chem. Mater.*, 2015, **27**, 2612–2618.

91 E. G. Gillan, *Chem. Mater.*, 2000, **12**, 3906–3912.

92 K. Maeda, X. Wang, Y. Nishihara, D. Lu, M. Antonietti and K. Domen, *J. Phys. Chem. C*, 2009, **113**, 4940–4947.

93 M. Deifallah, P. F. McMillan and F. Corà, *J. Phys. Chem. C*, 2008, **112**, 5447–5453.

94 D. Dontsova, S. Pronkin, M. Wehle, Z. Chen, C. Fettkenhauer, G. Clavel and M. Antonietti, *Chem. Mater.*, 2015, **27**, 5170–5179.

95 A. Savateev and M. Antonietti, *ACS Catal.*, 2018, **8**, 9790–9808.

96 M. Groenewolt and M. Antonietti, *Adv. Mater.*, 2005, **17**, 1789–1792.

97 F. Goettmann, A. Fischer, M. Antonietti and A. Thomas, *Angew. Chem. Int. Ed.*, 2006, **45**, 4467–4471.

98 X. Wang, K. Maeda, X. Chen, K. Takanabe, K. Domen, Y. Hou, X. Fu and M. Antonietti, *J. Am. Chem. Soc.*, 2009, **131**, 1680–1681.

99 J. Zhang, X. Chen, K. Takanabe, K. Maeda, K. Domen, J. D. Epping, X. Fu, M. Antonietti and X. Wang, *Angew. Chem. Int. Ed.*, 2010, **49**, 441–444.

100 M. Zhang and X. Wang, *Energy Environ. Sci.*, 2014, **7**, 1902–1906.

101 Y. Ishida, L. Chabanne, M. Antonietti and M. Shalom, *Langmuir*, 2014, **30**, 447–451.

102 Q. Xiang, J. Yu and M. Jaroniec, *J. Phys. Chem. C*, 2011, **115**, 7355–7363.

103 X.-H. Li, X. Wang and M. Antonietti, *Chem. Sci.*, 2012, **3**, 2170.

104 Y. Hou, A. B. Laursen, J. Zhang, G. Zhang, Y. Zhu, X. Wang, S. Dahl and I. Chorkendorff, *Angew. Chem. Int. Ed.*, 2013, **52**, 3621–3625.

105 F. Dong, Z. Zhao, T. Xiong, Z. Ni, W. Zhang, Y. Sun and W. K. Ho, *ACS Appl.*

Mater. Interfaces, 2013, **5**, 11392–11401.

106 Y. Zhang, A. Thomas, M. Antonietti and X. Wang, *J. Am. Chem. Soc.*, 2009, **131**, 50–51.

107 Y. Wang, J. Zhang, X. Wang, M. Antonietti and H. Li, *Angew. Chem. Int. Ed.*, 2010, **49**, 3356–3359.

108 Y. Zhang, T. Mori, J. Ye and M. Antonietti, *J. Am. Chem. Soc.*, 2010, **132**, 6294–6295.

109 L. F. Gao, T. Wen, J. Y. Xu, X. P. Zhai, M. Zhao, G. W. Hu, P. Chen, Q. Wang and H. L. Zhang, *ACS Appl. Mater. Interfaces*, 2016, **8**, 617–624.

110 G. Liu, P. Niu, C. Sun, S. C. Smith, Z. Chen, G. Q. (Max) Lu and H.-M. Cheng, *J. Am. Chem. Soc.*, 2010, **132**, 11642–11648.

111 Y. Wang, Y. Di, M. Antonietti, H. Li, X. Chen and X. Wang, *Chem. Mater.*, 2010, **22**, 5119–5121.

112 A. B. Laursen, S. Kegnæs, S. Dahl and I. Chorkendorff, *Energy Environ. Sci.*, 2012, **5**, 5577–5591.

113 J. P. Paraknowitsch and A. Thomas, *Energy Environ. Sci.*, 2013, **6**, 2839–2855.

114 Z. Zhao, Y. Sun and F. Dong, *Nanoscale*, 2015, **7**, 15–37.

115 P. Kumar, R. Boukherroub and K. Shankar, *J. Mater. Chem. A*, 2018, **6**, 12876–12931.

116 F. Su, S. C. Mathew, G. Lipner, X. Fu, M. Antonietti, S. Blechert and X. Wang, *J. Am. Chem. Soc.*, 2010, **132**, 16299–16301.

117 F. Su, S. C. Mathew, L. Möhlmann, M. Antonietti, X. Wang and S. Blechert, *Angew. Chem. Int. Ed.*, 2011, **50**, 657–660.

118 X. H. Li, X. Wang and M. Antonietti, *ACS Catal.*, 2012, **2**, 2082–2086.

119 Y. Zhao and M. Antonietti, *Angew. Chem. Int. Ed.*, 2017, **56**, 9336–9340.

120 I. Ghosh, J. Khamrai, A. Savateev, N. Shlapakov, M. Antonietti and B. König, *Science*, 2019, **365**, 360–366.

121 Z. Chen, A. Savateev, S. Pronkin, V. Papaefthimiou, C. Wolff, M. G. Willinger, E. Willinger, D. Neher, M. Antonietti and D. Dontsova, *Adv. Mater.*, 2017, **29**, 1–8.

122 A. Savateev, S. Pronkin, J. D. Epping, M. G. Willinger, C. Wolff, D. Neher, M. Antonietti and D. Dontsova, *ChemCatChem*, 2017, **9**, 167–174.

123 A. Savateev, B. Kurpil, A. Mishchenko, G. Zhang and M. Antonietti, *Chem. Sci.*, 2018, **9**, 3584–3591.

124 B. Kurpil, B. Kumru, T. Heil, M. Antonietti and A. Savateev, *Green Chem.*, 2018, **20**, 838–842.

125 B. Kurpil, K. Otte, M. Antonietti and A. Savateev, *Appl. Catal. B Environ.*, 2018, **228**, 97–102.

126 V. W. Lau, I. Moudrakovski, T. Botari, S. Weinberger, M. B. Mesch, V. Duppel, J. Senker, V. Blum and B. V. Lotsch, *Nat. Commun.*, 2016, **7**, 12165.

127 A. Harriman, *A. Phil. Trans. R. Soc.*, 2013, **371**, 20110415.

128 J. Schneider and D. W. Bahnemann, *J. Phys. Chem. Lett.*, 2013, **4**, 3479–3483.

129 B. C. M. Martindale, E. Joliat, C. Bachmann, R. Alberto and E. Reisner, *Angew. Chem. Int. Ed.*, 2016, **55**, 9402–9406.

130 V. W. Lau, D. Klose, H. Kasap, F. Podjaski, M.-C. Pignié, E. Reisner, G. Jeschke and B. V. Lotsch, *Angew. Chem. Int. Ed.*, 2017, **56**, 510–514.

131 F. Podjaski, J. Kröger and B. V. Lotsch, *Adv. Mater.*, 2018, **30**, 1705477.

132 M. B. Plutschack, B. Pieber, K. Gilmore and P. H. Seeberger, *Chem. Rev.*, 2017, **117**, 11796–11893.

133 K. Loubière, M. Oelgemöller, T. Aillet, O. Dechy-Cabaret and L. Prat, *Chem. Eng. Process.*, 2016, **104**, 120–132.

134 A. Wiebe, T. Gieshoff, S. Möhle, E. Rodrigo, M. Zirbes and S. R. Waldvogel, *Angew. Chem. Int. Ed.*, 2018, **57**, 5594–5619.

135 M. Yan, Y. Kawamata and P. S. Baran, *Chem. Rev.*, 2017, **117**, 13230–13319.

136 J. I. Yoshida, K. Kataoka, R. Horcajada and A. Nagaki, *Chem. Rev.*, 2008, **108**, 2265–2299.

137 B. A. Frontana-Uribe, R. D. Little, J. G. Ibanez, A. Palma and R. Vasquez-Medrano, *Green Chem.*, 2010, **12**, 2099–2119.

138 H. J. Schäfer, *Comptes Rendus Chim.*, 2011, **14**, 745–765.

139 V. Alcácer and V. Cruz-Machado, *Eng. Sci. Technol. an Int. J.*, 2019, **22**, 899–919.

140 J. N. Wei, D. Duvenaud and A. Aspuru-Guzik, *ACS Cent. Sci.*, 2016, **2**, 725–732.

141 C. W. Coley, W. H. Green and K. F. Jensen, *Acc. Chem. Res.*, 2018, **51**, 1281–1289.

142 M. H. S. Segler, M. Preuss and M. P. Waller, *Nature*, 2018, **555**, 604–610.

143 A. F. de Almeida, R. Moreira and T. Rodrigues, *Nat. Rev. Chem.*, 2019, **3**, 589–604.

144 A. Aspuru-Guzik, R. Lindh and M. Reiher, *ACS Cent. Sci.*, 2018, **4**, 144–152.

145 S. Ekins, A. C. Puhl, K. M. Zorn, T. R. Lane, D. P. Russo, J. J. Klein, A. J. Hickey and A. M. Clark, *Nat. Mater.*, 2019, **18**, 435–441.

146 Bluechip Infocorp, Industrial Internet of Things, https://medium.com/@jaydev_21091/industrial-internet-of-things-74a4ffb44679, (accessed 1 December 2019).

147 J. W. Erisman, M. A. Sutton, J. Galloway, Z. Klimont and W. Winiwarter, *Nat. Geosci.*, 2008, **1**, 636–639.

148 Y. A. Daza and J. N. Kuhn, *RSC Adv.*, 2016, **6**, 49675–49691.

149 D. W. Keith, G. Holmes, D. St. Angelo and K. Heidel, *Joule*, 2018, **2**, 1573–1594.

150 Y. Parag and B. K. Sovacool, *Nat. Energy*, , DOI:10.1038/nenergy.2016.32.

151 P. Kang, Z. Chen, A. Nayak, S. Zhang and T. J. Meyer, *Energy Environ. Sci.*, 2014, **7**, 4007–4012.

152 H. G. Cha and K.-S. Choi, *Nat. Chem.*, 2015, **7**, 328–333.

153 B. You, X. Liu, N. Jiang and Y. Sun, *J. Am. Chem. Soc.*, 2016, **138**, 13639–13646.

154 E. J. Horn, B. R. Rosen, Y. Chen, J. Tang, K. Chen, M. D. Eastgate and P. S. Baran, *Nature*, 2016, **533**, 77–81.

155 T. Li, Y. Cao, J. He and C. P. Berlinguette, *ACS Cent. Sci.*, 2017, **3**, 778–783.

156 T. Li, T. Kasahara, J. He, K. E. Dettelbach, G. M. Sammis and C. P. Berlinguette, *Nat. Commun.*, 2017, **8**, 390.

157 C. Huang, Y. Huang, C. Liu, Y. Yu and B. Zhang, *Angew. Chem. Int. Ed.*, 2019, **58**, 12014–12017.

158 S. S. Yazdani and R. Gonzalez, *Curr. Opin. Biotechnol.*, 2007, **18**, 213–219.

159 C. Dai, L. Sun, H. Liao, B. Khezri, R. D. Webster, A. C. Fisher and Z. J. Xu, *J. Catal.*, 2017, **356**, 14–21.

160 M. Chaumontet, R. Piccardi and O. Baudoin, *Angew. Chem.*, 2009, **121**, 185–188.

161 J. Ziemska, A. Guśpiel, J. Jarosz, A. Nasulewicz-Goldeman, J. Wietrzyk, R. Kawęcki, K. Pypowski, M. Jarończyk and J. Solecka, *Bioorganic Med. Chem.*, 2016, **24**, 5302–5314.

162 J. M. Bobbitt, C. BrüCkner and N. Merbouh, *Org. React.*, 2010, 103–424.

163 M. F. Semmelhack, C. S. Chou and D. A. Cortes, *J. Am. Chem. Soc.*, 1983, **105**, 4492–4494.

164 E. Steckhan, *Angew. Chem. Int. Ed. Engl.*, 1986, **25**, 683–701.

165 M. F. Semmelhack and C. R. Schmid, *J. Am. Chem. Soc.*, 1983, **105**, 6732–6734.

166 T. Miyazawa, T. Endo, S. Shiihashi and M. Okawara, *J. Org. Chem.*, 1985, **50**, 1332–1334.

167 T. Miyazawa and T. Endo, *J. Org. Chem.*, 1985, **50**, 3930–3931.

168 M. F. Semmelhack, C. R. Schmid and D. A. Cortés, *Tetrahedron Lett.*, 1986, **27**, 1119–1122.

169 W. F. Bailey, J. M. Bobbitt and K. B. Wiberg, *J. Org. Chem.*, 2007, **72**, 4504–4509.

170 D. P. Hickey, D. A. Schiedler, I. Matanovic, P. V. Doan, P. Atanassov, S. D.

Minteer and M. S. Sigman, *J. Am. Chem. Soc.*, 2015, **137**, 16179–16186.

171 N. Merbouh, J. M. Bobbitt and C. Brückner, *Org. Prep. Proced. Int.*, 2004, **36**, 1–31.

172 A. E. J. de Nooy, A. C. Besemer and H. van Bekkum, *Synthesis (Stuttg).*, 1996, **1996**, 1153–1176.

173 Y. Kato, Y. Shimizu, L. Yijing, K. Unoura, H. Utsumi and T. Ogata, *Electrochim. Acta*, 1995, **40**, 2799–2802.

174 A. Israeli, M. Patt, M. Oron, A. Samuni, R. Kohen and S. Goldstein, *Free Radic. Biol. Med.*, 2005, **38**, 317–324.

175 J. B. Gerken, Y. Q. Pang, M. B. Lauber and S. S. Stahl, *J. Org. Chem.*, 2018, **83**, 7323–7330.

176 R. M. Bullock, A. K. Das and A. M. Appel, *Chem. Eur. J.*, 2017, **23**, 7626–7641.

177 K. E. Dalle, J. Warnan, J. J. Leung, B. Reuillard, I. S. Karmel and E. Reisner, *Chem. Rev.*, 2019, **119**, 2752–2875.

178 N. M. Muresan, J. Willkomm, D. Mersch, Y. Vaynzof and E. Reisner, *Angew. Chem. Int. Ed.*, 2012, **51**, 12749–12753.

179 J. Willkomm, K. L. Orchard, A. Reynal, E. Pastor, J. R. Durrant and E. Reisner, *Chem. Soc. Rev*, 2016, **45**, 9–23.

180 K. P. Sokol, W. E. Robinson, J. Warnan, N. Kornienko, M. M. Nowaczyk, A. Ruff, J. Z. Zhang and E. Reisner, *Nat. Energy*, 2018, **3**, 944–951.

181 J.-M. Saveant, *Chem. Rev.*, 2008, **108**, 2348–2378.

182 V. S. Thoi, Y. Sun, J. R. Long and C. J. Chang, *Chem. Soc. Rev.*, 2013, **42**, 2388–2400.

183 C. D. Windle and E. Reisner, *Chimia (Aarau).*, 2015, **69**, 435–441.

184 E. S. Andreiadis, P. A. Jacques, P. D. Tran, A. Leyris, M. Chavarot-Kerlidou, B. Jousselme, M. Matheron, J. Pécaut, S. Palacin, M. Fontecave and V. Artero, *Nat. Chem.*, 2013, **5**, 48–53.

185 B. Reuillard, K. H. Ly, T. E. Rosser, M. F. Kuehnel, I. Zebger and E. Reisner, *J. Am. Chem. Soc.*, 2017, **139**, 14425–14435.

186 M. F. Kuehnel, K. L. Orchard, K. E. Dalle and E. Reisner, *J. Am. Chem. Soc.*, 2017, **139**, 7217–7223.

187 P. A. Jacques, V. Artero, J. Pécautb and M. Fontecave, *Proc. Natl. Acad. Sci. U. S. A.*, 2009, **106**, 20627–20632.

188 E. B. Hulley, P. T. Wolczanski and E. B. Lobkovsky, *J. Am. Chem. Soc.*, 2011, **133**, 18058–18061.

189 C. M. Lieber and N. S. Lewis, *J. Am. Chem. Soc.*, 1984, **106**, 5033–5034.

190 K. Kusuda, R. Ishihara, H. Yamaguchi and I. Izumi, *Electrochim. Acta*, 1986, **31**, 657–663.

191 J. H. Zagal, *Coord. Chem. Rev.*, 1992, **119**, 89–136.

192 W. W. Kramer and C. C. L. McCrory, *Chem. Sci.*, 2016, **7**, 2506–2515.

193 T. Yoshida, K. Kamato, M. Tsukamoto, T. Iida, D. Schlettwein, D. Wöhrle and M. Kaneko, *J. Electroanal. Chem.*, 1995, **385**, 209–225.

194 T. Abe, T. Yoshida, S. Tokita, F. Taguchi, H. Imaya and M. Kaneko, *J. Electroanal. Chem.*, 1996, **412**, 125–132.

195 A. Hirohide, A. Aramata and Y. Hisaeda, *J. Electroanal. Chem.*, 1997, **437**, 111–118.

196 A. Deronzier, D. Lìmosin and J.-C. Moutet, *Electrochim. Acta*, 1987, **32**, 1643–1647.

197 T. Osa, U. Akiba, I. Segawa and J. M. Bobbitt, *Chem. Lett.*, 1988, **17**, 1423–1426.

198 T. Osa, Y. Kashiwagi, K. Mukai, A. Ohsawa and J. M. Bobbitt, *Chem. Lett.*, 1990, **19**, 75 – 78.

199 E. M. Belgsir and H. J. Schäfer, *Electrochem. commun.*, 2001, **3**, 32–35.

200 L. Bugnon, C. J. H. Morton, P. Novak, J. Vetter and P. Nesvadba, *Chem. Mater.*, 2007, **19**, 2910–2914.

201 D. P. Hickey, R. D. Milton, D. Chen, M. S. Sigman and S. D. Minteer, *ACS Catal.*, 2015, **5**, 5519–5524.

202 F. C. Macazo, D. P. Hickey, S. Abdellaoui, M. S. Sigman and S. D. Minteer, *Chem. Commun.*, 2017, **53**, 10310–10313.

203 A. Das and S. S. Stahl, *Angew. Chem. Int. Ed.*, 2017, **56**, 8892–8897.

204 C. Backes and A. Hirsch, *Chem. Nanocarbons*, 2010, **42**, 1–48.

205 P. T. Anastas and M. M. Kirchhoff, *Acc. Chem. Res.*, 2002, **35**, 686–694.

206 R. A. Sheldon, *Chem. Soc. Rev.*, 2012, **41**, 1437–1451.

207 A. Mills and S. Le Hunte, *J. Photochem. Photobiol. A Chem.*, 1997, **108**, 1–35.

208 M. K. Brennaman, R. J. Dillon, L. Alibabaei, M. K. Gish, C. J. Dares, D. L. Ashford, R. L. House, G. J. Meyer, J. M. Papanikolas and T. J. Meyer, *J. Am. Chem. Soc.*, 2016, **138**, 13085–13102.

209 Z. Chen, J. J. Concepcion, J. F. Hull, P. G. Hoertz and T. J. Meyer, *Dalt. Trans.*, 2010, **39**, 6950.

210 P. G. Hoertz, Z. Chen, C. A. Kent and T. J. Meyer, *Inorg. Chem.*, 2010, **49**, 8179–8181.

211 S. Morra, F. Valetti, S. J. Sadeghi, P. W. King, T. Meyer and G. Gilardi, *Chem. Commun.*, 2011, **47**, 10566–10568.

212 K. R. Phillips, G. T. England, S. Sunny, E. Shirman, T. Shirman, N. Vogel and J. Aizenberg, *Chem. Soc. Rev.*, 2016, **45**, 281–322.

213 D. Mersch, C. Y. Lee, J. Z. Zhang, K. Brinkert, J. C. Fontecilla-Camps, A. W. Rutherford and E. Reisner, *J. Am. Chem. Soc.*, 2015, **137**, 8541–8549.

214 M. Kato, T. Cardona, a W. Rutherford and E. Reisner, *J. Am. Chem. Soc.*, 2012, **134**, 8332–8335.

215 M. Kato, T. Cardona, A. W. Rutherford and E. Reisner, *J. Am. Chem. Soc.*, 2013, **135**, 10610–10613.

216 J. J. Leung, J. Warnan, D. H. Nam, J. Z. Zhang, J. Willkomm and E. Reisner, *Chem. Sci.*, 2017, **8**, 5172–5180.

217 T. E. Rosser and E. Reisner, *ACS Catal.*, 2017, **7**, 3131–3141.

218 N. Kornienko, K. H. Ly, W. E. Robinson, N. Heidary, J. Z. Zhang and E. Reisner, *Acc. Chem. Res.*, 2019, **52**, 1439–1448.

219 J. J. Leung, J. Warnan, K. H. Ly, N. Heidary, D. H. Nam, M. F. Kuehnel and E. Reisner, *Nat. Catal.*, 2019, **2**, 354–365.

220 A. Le Goff, V. Artero, B. Jousselme, P. D. Tran, N. Guillet, R. Metaye, A. Fihri, S. Palacin and M. Fontecave, *Science*, 2009, **326**, 1384–1387.

221 P. D. Tran, A. Le Goff, J. Heidkamp, B. Jousselme, N. Guillet, S. Palacin, H. Dau, M. Fontecave and V. Artero, *Angew. Chem. Int. Ed.*, 2011, **50**, 1371–1374.

222 N. Queyriaux, N. Kaeffer, A. Morozan, M. Chavarot-Kerlidou and V. Artero, *J. Photochem. Photobiol. C Photochem. Rev.*, 2015, **25**, 90–105.

223 K. Abdiaziz, E. Salvadori, K. P. Sokol, E. Reisner and M. M. Roessler, *Chem. Commun.*, 2019, **55**, 8840–8843.

224 R. Ernstorfer, L. Gundlach, S. Felber, W. Storck, R. Eichberger and F. Willig, *J. Phys. Chem. B*, 2006, **110**, 25383–25391.

225 G. F. Moore, J. D. Blakemore, R. L. Milot, J. F. Hull, H. E. Song, L. Cai, C. A. Schmuttenmaer, R. H. Crabtree and G. W. Brudvig, *Energy Environ. Sci.*, 2011, **4**, 2389–2392.

226 P. H. Mutin, G. Guerrero and A. Vioux, *J. Mater. Chem.*, 2005, **15**, 3761–3768.

227 L. Wang, D. L. Ashford, D. W. Thompson, T. J. Meyer and J. M. Papanikolas, *J. Phys. Chem. C*, 2013, **117**, 24250–24258.

228 Y. Gao, L. Zhang, X. Ding and L. Sun, *Phys. Chem. Chem. Phys.*, 2014, **16**, 12008–12013.

229 B. J. Brennan, A. E. Keirstead, P. A. Liddell, S. A. Vail, T. A. Moore, A. L. Moore and D. Gust, *Nanotechnology*, 2009, **20**, 505203.

230 B. J. Brennan, M. J. Llansola Portolés, P. A. Liddell, T. A. Moore, A. L. Moore and D. Gust, *Phys. Chem. Chem. Phys.*, 2013, **15**, 16605–16614.

231 K. L. Materna, B. J. Brennan and G. W. Brudvig, *Dalt. Trans.*, 2015, **44**, 20312–20315.

232 K. L. Materna, B. Rudshteyn, B. J. Brennan, M. H. Kane, A. J. Bloomfield, D. L. Huang, D. Y. Shopov, V. S. Batista, R. H. Crabtree and G. W. Brudvig, *ACS*

Catal., 2016, **6**, 5371–5377.

233 K. L. Materna, J. Jiang, R. H. Crabtree and G. W. Brudvig, *ACS Appl. Mater. Interfaces*, 2019, **11**, 5602–5609.

234 W. R. McNamara, R. C. Snoeberger, G. Li, C. Richter, L. J. Allen, R. L. Milot, C. A. Schmuttenmaer, R. H. Crabtree, G. W. Brudvig and V. S. Batista, *Energy Environ. Sci.*, 2009, **2**, 1173–1175.

235 W. R. McNamara, R. L. Milot, H. E. Song, R. C. Snoeberger, V. S. Batista, C. A. Schmuttenmaer, G. W. Brudvig and R. H. Crabtree, *Energy Environ. Sci.*, 2010, **3**, 917–923.

236 T. P. Brewster, S. J. Konezny, S. W. Sheehan, L. A. Martini, C. A. Schmuttenmaer, V. S. Batista and R. H. Crabtree, *Inorg. Chem.*, 2013, **52**, 6752–6764.

237 L. A. Martini, G. F. Moore, R. L. Milot, L. Z. Cai, S. W. Sheehan, C. A. Schmuttenmaer, G. W. Brudvig and R. H. Crabtree, *J. Phys. Chem. C*, 2013, **117**, 14526–14533.

238 C. R. Rice, M. D. Ward, M. K. Nazeeruddin and M. Grätzel, *New J. Chem.*, 2000, **24**, 651–652.

239 K. L. Materna, R. H. Crabtree and G. W. Brudvig, *Chem. Soc. Rev.*, 2017, **46**, 6099–6110.

240 M. Oelgemoeller, *Chem. Eng. Technol.*, 2012, **35**, 1144–1152.

241 A. Ziogas, G. Kolb, M. O'Connell, A. Attour, F. Lapicque, M. Matlosz and S. Rode, *J. Appl. Electrochem.*, 2009, **39**, 2297–2313.

242 R. L. Hartman, J. P. McMullen and K. F. Jensen, *Angew. Chem. Int. Ed.*, 2011, **50**, 7502–7519.

243 B. P. Mason, K. E. Price, J. L. Steinbacher, A. R. Bogdan and D. T. McQuade, *Chem. Rev.*, 2007, **107**, 2300–2318.

244 D. Cambié, C. Bottecchia, N. J. W. Straathof, V. Hessel and T. Noël, *Chem. Rev.*, 2016, **116**, 10276–10341.

245 K. Jähnisch, V. Hessel, H. Löwe and M. Baerns, *Angew. Chem. Int. Ed.*, 2004, **43**, 406–446.

246 N.-T. Nguyen and Z. Wu, *J. Micromech. Microeng.*, 2005, **15**, R1–R16.

247 D. Horii, T. Fuchigami and M. Atobe, *J. Am. Chem. Soc.*, 2007, **129**, 11692–11693.

248 J. Yoshida, H. Kim and A. Nagaki, *J. Flow Chem.*, 2017, **7**, 60–64.

249 S. G. Newman and K. F. Jensen, *Green Chem.*, 2013, **15**, 1456–1472.

250 B. Gutmann, D. Cantillo and C. O. Kappe, *Angew. Chem. Int. Ed.*, 2015, **54**, 6688–6728.

251 Gemoets, Y. Su, M. Shang, V. Hessel, R. Luque and T. Noel, *Chem. Soc. Rev.*, 2016, **45**, 83–117.

252 C. Wiles and P. Watts, *Chem. Comm.*, 2011, **47**, 6512–6535.

253 M. Irfan, T. N. Glasnov and C. O. Kappe, *ChemSusChem*, 2011, **4**, 300–316.

254 R. Munirathinam, J. Huskens and W. Verboom, *Adv. Synth. Catal.*, 2015, **357**, 1093–1123.

255 R. Ricciardi, J. Huskens and W. Verboom, *ChemSusChem*, 2015, **8**, 2586–2605.

256 P. Angeli and A. Gavriilidis, in *Encyclopedia of Microfluidics and Nanofluidics*, ed. D. Li, Springer, Boston, MA, 2008, p. 1971−1976.

257 S. In, M. G. Nielsen, P. C. K. Vesborg, Y. Hou, B. L. Abrams, T. R. Henriksen, O. Hansen and I. Chorkendorff, *Chem. Commun.*, 2011, **47**, 2613–2615.

258 M. Brzozowski, M. O'Brien, S. V. Ley and A. Polyzos, *Acc. Chem. Res.*, 2015, **48**, 349–362.

259 J. J. Douglas, M. J. Sevrin and C. R. J. Stephenson, *Org. Process Res. Dev.*, 2016, **20**, 1134–1147.

260 J. P. Knowles, L. D. Elliott and K. I. Booker-Milburn, *Beilstein J. Org. Chem.*, 2012, **8**, 2025–2052.

261 D. Webb and T. F. Jamison, *Chem. Sci.*, 2010, **1**, 675.

262 J. C. Pastre, D. L. Browne and S. V. Ley, *Chem. Soc. Rev.*, 2013, **42**, 8849–8869.

263 J. Wegner, S. Ceylan and A. Kirschning, *Adv. Synth. Catal.*, 2012, **354**, 17–57.

264 L. J. Martin, A. L. Marzinzik, S. V. Ley and I. R. Baxendale, *Org. Lett.*, 2011, **13**, 320–323.

265 C. J. Smith, C. D. Smith, N. Nikbin, S. V. Ley and I. R. Baxendale, *Org. Biomol. Chem.*, 2011, **9**, 1927–1937.

266 J. Sedelmeier, S. V. Ley, I. R. Baxendale and M. Baumann, *Org. Lett.*, 2010, **12**, 3618–3621.

267 K. S. Elvira, X. Casadevall i Solvas, R. C. R. Wootton and A. J. de Mello, *Nat. Chem.*, 2013, **5**, 905–15.

268 J. P. McMullen, M. T. Stone, S. L. Buchwald and K. F. Jensen, *Angew. Chem. Int. Ed.*, 2010, **49**, 7076–7080.

269 A. J. Parrott, R. A. Bourne, G. R. Akien, D. J. Irvine and M. Poliakoff, *Angew. Chem. Int. Ed.*, 2011, **50**, 3788–3792.

270 V. Sans, L. Porwol, V. Dragone and L. Cronin, *Chem. Sci.*, 2015, **6**, 1258–1264.

271 S. V. Ley, D. E. Fitzpatrick, R. J. Ingham and R. M. Myers, *Angew. Chem. Int. Ed.*, 2015, **54**, 3449–3464.

272 D. C. Fabry, E. Sugiono and M. Rueping, *React. Chem. Eng.*, 2016, **1**, 129–133.

273 D. Cortés-Borda, E. Wimmer, B. Gouilleux, E. Barré, N. Oger, L. Goulamaly, L. Peault, B. Charrier, C. Truchet, P. Giraudeau, M. Rodriguez-Zubiri, E. Le

Grognec and F. X. Felpin, *J. Org. Chem.*, 2018, **83**, 14286–14289.

274 M. Baumann, *Org. Biomol. Chem.*, 2018, **16**, 5946–5954.

275 A. D. Clayton, J. A. Manson, C. J. Taylor, T. W. Chamberlain, B. A. Taylor, G. Clemens and R. A. Bourne, *React. Chem. Eng.*, 2019, **4**, 1545–1554.

276 D. E. Fitzpatrick, C. Battilocchio and S. V Ley, *Org. Process Res. Dev.*, 2016, **20**, 386–394.

277 D. E. Fitzpatrick, T. Maujean, A. C. Evans and S. V. Ley, *Angew. Chem. Int. Ed.*, 2018, **57**, 15128–15132.

278 V. Sans and L. Cronin, *Chem. Soc. Rev.*, 2016, **45**, 2032–2043.

279 K. F. Jensen, *AIChE J.*, 2017, **63**, 858–869.

280 D. E. Fitzpatrick, C. Battilocchio and S. V. Ley, *ACS Cent. Sci.*, 2016, **2**, 131–138.

281 J. M. Granda, L. Donina, V. Dragone, D. L. Long and L. Cronin, *Nature*, 2018, **559**, 377–381.

282 C. W. Coley, D. A. Thomas, J. A. M. Lummiss, J. N. Jaworski, C. P. Breen, V. Schultz, T. Hart, J. S. Fishman, L. Rogers, H. Gao, R. W. Hicklin, P. P. Plehiers, J. Byington, J. S. Piotti, W. H. Green, A. J. Hart, T. F. Jamison and K. F. Jensen, *Science*, 2019, **365**, eaax1566.

283 S. Steiner, J. Wolf, S. Glatzel, A. Andreou, J. M. Granda, G. Keenan, T. Hinkley, G. Aragon-Camarasa, P. J. Kitson, D. Angelone and L. Cronin, *Science*, 2019, **363**, eaav2211.

284 M. Woźnica, N. Chaoui, S. Taabache and S. Blechert, *Chem. Eur. J.*, 2014, **20**, 14624–14628.

285 B. Pieber, M. Shalom, M. Antonietti, P. H. Seeberger and K. Gilmore, *Angew. Chem. Int. Ed.*, 2018, **57**, 9976–9979.

Chapter 2

Proof-of-concept Photoreactor Design and Fabrication

2.1 Introduction

As discussed in Chapter 1, carbon nitride is a low-cost, robust, and transition-metal-free semiconductor, which has a suitable electronic band structure that enables both visible light absorption and the controlled oxidation and reduction of substrates, thus making it a suitable candidate for photoredox catalytic applications.[1,2] Due to its heterogeneous nature, it also makes for an interesting candidate to immobilise and study within a continuous flow setting, rather than in a traditional batch-type photoreactor. We chose to work with the cyanamide-functionalised carbon nitride ($^{NCN}CN_x$), following the exciting research conducted by our group which effectively showed the ability to: (i) selectively oxidise 4-methylbenzyl alcohol (MBA) to the corresponding aldehyde, 4-methylbenzylaldeyde (MBAd), while generating stoichiometric amounts of H_2 in the presence of a HER catalyst under solar irradiation, and (ii) to decouple the oxidative and reductive half-reactions, via the accumulation and storage of the photogenerated electrons within $^{NCN}CN_x$ under an inert atmosphere.

The aim of this chapter is to model a proof-of-concept flow device for the photocatalysed oxidation of MBA using a stationary $^{NCN}CN_x$ phase and gain a parametric understanding of the system in order to develop an initial prototype. For simplicity, the reduction of protons to generate H_2 is omitted from this analysis, and the system is considered to operate under aerobic conditions, i.e. with dissolved O_2 acting as the terminal electron acceptor.

A number of objectives were therefore devised in order to accomplish this task. Computational fluid dynamics (CFD) was first used to model the chemical flow within

a thin channel photoreactor (TCP), in which $^{NCN}CN_x$ was taken to be coated on the base of the channel. The *thin channel* flow concept was selected as it offers a high surface area-to-volume (*SA-to-V*) ratio, and, from a design perspective, was a suitable starting point for conducting the study of the heterogeneous flow system. The parametric study was needed in order to obtain a series of experimental and design trends that will facilitate the fabrication stage of the prototype. A prototype flow device was then constructed, based on the trends obtained from the CFD model. A modular design approach for the reactor was selected to allow for facile interchangeability of system components. A $^{NCN}CN_x$ sheet was finally formulated, using a variety of deposition techniques (as outlined in Experimental Section 2.5), and incorporated as the stationary phase in the prototype device. A continuous flow test-rig was set up to acquire empirical data and assess the similarity between the modelling and experimental exercises.

2.2 The Numerical Model

2.2.1 Criteria for the Model Flow System

The list below details the criteria employed for designing and modelling the prototype flow device:

i) The design should resemble that of a thin channel flow device, wherein the *height of the channel* should be less < 1 mm to comply with the definition of a microreactor.[3,4]

ii) The optical windows incorporated into the flow device should have minimal absorbance in the near UV and visible range.

iii) The dimensions of the irradiated cross-sectional area must be comparable to the illuminated area that is generated by the solar light simulator (i.e. ~20 cm^2).

iv) A modular design approach must be applied to ensure a degree of flexibility during the testing phases; primarily, to be able to alter the channel height, and to test $^{NCN}CN_x$ samples prepared through different deposition techniques.

A discussion with regards to the fundamental layout of the model, the computational algorithm, and some of the results procured shall be provided herein, and in

Section 2.3.1. The fabrication and testing of the flow device within the assembled test-rig shall be described in Section 2.3.2.

2.2.2 Photochemical Reaction Scheme

A kinetic model is needed in order to describe the reactive aspect of the flow within the CFD code, to be able to derive the reactant concentration profile at the output of the flow device. To deduce such a kinetic model however, we must first rationalise the photocatalytic process occurring between the stationary $^{NCN}\mathbf{CN_x}$ phase, and the mobile substrate phase. The heterogeneous photocatalytic reaction can thus be broken down into the following steps:

(1) Photoexcitation of $^{NCN}\mathbf{CN_x}$ (photoexcited state denoted by an asterisk)
(2) Mass transfer of the substrate from the bulk fluid to the stationary photocatalyst
(3) Donor-acceptor association; surface adduct formation
(4) Charge-transfer complex formation; electron transfer between the associated pair
(5) Product desorption from the surface
(6) Mass transfer of the product from photocatalyst to the bulk fluid
(7) Transfer of the 'trapped' photoexcited electrons in $^{NCN}\mathbf{CN_x}$ to a terminal electron acceptor.

For the chemical system under investigation, the kinetic framework incorporating steps (3) – (5) and (7) can be described by Scheme 2.1:

$$\left(^{NCN}\mathbf{CN_x}\right)^{*} + \mathrm{MBA} \rightleftharpoons \left(^{NCN}\mathbf{CN_x}\right)^{*}\mathrm{MBA} \qquad (3)$$

$$\left(^{NCN}\mathbf{CN_x}\right)^{*}\mathrm{MBA} \xrightarrow{-H^+} \left(^{NCN}\mathbf{CN_x}\right)^{\bullet -}\mathrm{MBA}^{\bullet} \qquad (4.i)$$

$$\mathrm{MBA}^{\bullet} + h_s{}^{+} \xrightarrow{-H^+} \mathrm{MBAd} \qquad (4.ii), (5)$$

$$\left(^{NCN}\mathbf{CN_x}\right)^{\bullet -} + \mathrm{EA} \longrightarrow {}^{NCN}\mathbf{CN_x} + \mathrm{EA}^{-} \qquad (7)$$

Scheme 2.1: Elemental steps within the reductive quenching mechanism, involving $^{NCN}\mathbf{CN_x}$ in the presence of light, MBA, and a terminal electron acceptor (EA). The benzylic radical ion generated in step (4.i) can react with a surface bound hole ($h_s{}^{+}$) to give the corresponding benzaldehyde product (MBAd) upon desorption.

In the work by our group,[5] the hydrogen evolution catalyst **NiP** (c.f. Scheme 1.3a) assumed the role of the terminal electron acceptor (EA), wherein aqueous proton reduction to hydrogen was the final step in the transfer process. Electron transfer to **NiP** is kinetically slower than charge transfer between (^{NCN}**CN**$_x$)* and MBA**,** as highlighted by Transient Absorption Spectroscopy (TAS) studies,[5] implying that the reductive quenching scheme was a suitable fit for the system. It was also observed that due to this difference in reaction rates, a build-up of negative charge accumulated on the ^{NCN}**CN**$_x$ material, making it appear blue in colour.

However, to simplify the model and deal with a liquid-phase product output, only the products of the oxidative half-reaction were to be assessed (i.e. the MBA to MBAd conversion); hence the **NiP** component was omitted from the system. Thus, the EA species in Scheme 2.1 had to be replaced with a different molecular species. In practice, aerobic O_2 is often employed as a terminal electron acceptor, as it is readily available and its kinetics for electron transfer are typically fast or unhindered.[6]

The reduction of O_2 can lead to a superoxide radical anion formation, which can also provide an oxidative pathway for the MBA starting material.[7] Additionally, since its electron transfer kinetics are faster than **NiP**, it can reverse the quenching mechanism, from *reductive* (as portrayed in Scheme 2.1) to *oxidative*. Nonetheless, in theory, the role of the 'EA species' was taken to be analogous to that of **NiP**, without the subsequent generation of H_2 gas. This assumption simplifies the computational aspect of the model without altering any of the physical properties of the system; i.e. that the photoredox reaction is confined along a stationary/immobilised phase at the base of the flow channel.

Hence, if we simply take step (7) in Scheme 2.1 to be a facile pathway for the photoexcited electrons to discharge from the activated material, then we can take step (4) in Scheme 2.1 to be the *rate determining step* (RDS). The kinetics of the photocatalytic transformation of MBA can therefore be modelled through application of the Langmuir–Hinshelwood framework.[8] Scheme 2.2 groups steps (4.1), (4.ii), and (5) into one overall process in accordance with the described framework, where $k_{reaction}$ represents the kinetic rate constant of the surface-photocatalysed chemical reaction:

$$\left({}^{\mathbf{NCN}}\mathbf{CN_x}\right)^{*} + \text{MBA} \rightleftharpoons \left({}^{\mathbf{NCN}}\mathbf{CN_x}\right)^{*}\text{MBA} \xrightarrow{k_{reaction}} \text{MBAd} + \left({}^{\mathbf{NCN}}\mathbf{CN_x}\right)^{\bullet -}$$

Scheme 2.2: Overview of the physical processes and reaction term related to the $^{\mathbf{NCN}}\mathbf{CN_x}$ and MBA system under investigation.

The overall rate law which describes the transformation of MBA is given by:

$$\frac{\mathrm{d}c_{MBA}}{\mathrm{d}t} = -\frac{k_{reaction} K_{ads} \Gamma_{\mathbf{CN}^*} c_{MBA}}{1 + K_{ads} c_{MBA}} \qquad 2.1$$

where c_{MBA} is the molar concentration of MBA, K_{ads} denotes the equilibrium adsorption coefficient describing surface adduct formation (donor-acceptor association), and $\Gamma_{\mathbf{CN}^*}$ represents the surface concentration of photoactivated $^{\mathbf{NCN}}\mathbf{CN}_x$ sites. Since $^{\mathbf{NCN}}\mathbf{CN}_x$ is stationary within the system, then as $c_{MBA} \rightarrow 0$, Equation 2.1 can be simplified to a *pseudo first-order rate equation*:[9]

$$\frac{\mathrm{d}c_{MBA}}{\mathrm{d}t} \approx -k_{app} c_{MBA} \qquad 2.2$$

where the *apparent* first-order rate constant, k_{app}, is given by:

$$k_{app} \equiv k_{reaction} K_{ads} \Gamma_{\mathbf{CN}^*} \qquad 2.3$$

A dimensional analysis of k_{app} yields units of 's^{-1}'. Thus, in Equation 2.2 the rate law is solely written in terms of the concentration of the substrate and an *apparent* rate of reaction.

2.2.3 Computational Fluid Dynamics (CFD)

A mass transport equation coupled to a chemical rate law forms the foundation of the CFD code. It is needed in order to describe the variations in the reactant concentration as the flow traverses through the TCP, and thus provides an output concentration profile. Based on the selective conversion of MBA to the corresponding aldehyde, we can derive a numerical value for the reactant conversion based on the depletion of starting material.

Since the chemical reaction is confined to the stationary $^{\mathbf{NCN}}\mathbf{CN}_x$ | liquid interface, depletion of MBA only occurs at a boundary condition (detailed below), and not in the bulk solution (i.e. within the channel volume). The mass transport equation to describe the volumetric flow through the channel can be expressed (in vector notation) as:

$$\frac{\partial c_{MBA}}{\partial t} = D\nabla^2 c_{MBA} - \mathbf{u}\cdot\nabla c_{MBA} \qquad 2.4$$

where t is time, D denotes the concentration-independent molecular diffusion coefficient of MBA, and **u** describes the velocity profile of the chemical flow. ∇ is the gradient operator, and ∇^2 is the Laplacian operator for molecular transport. The first term on the left-hand-side of Equation 2.4 describes the diffusive part of the flow, while the second term, the convective aspect.

Some fundamental rationales necessary to construct the CFD code are described below.[10] A schematic illustration of the channel cross-section (taken along the channel length) is depicted in Figure 2.1.

i) Since the photoactive material is immobilised on the bottom surface, we can model the flow device as a quasi-two-dimensional (quasi-2D) system. In rectangular coordinates, the concentration of MBA is thus a function of only two spatial coordinates; in accordance with Figure 2.1: $c_{MBA} = c_{MBA}(x,y)$.

ii) The mass transport and chemical reaction process occurs isothermally. This implies that heat transport processes within the reactor can be neglected. Additionally, other physical parameters such as the fluid density, fluid viscosity, molecular diffusion coefficient, and the surface kinetic rate constant can be treated as constants within the framework of the model.

iii) Molecular diffusion in the primary direction of flow (i.e.: the x-direction) is negligible compared to convective mass transport, and hence the diffusive term in Equation 2.4 only applies transverse to the direction of flow (i.e.: the y-direction). This assumption holds for large values of the mass transfer Péclet number ($\mathrm{Pe} \gg 1$); this number describes the ratio of mass transport via convection to that via diffusion:

$$\mathrm{Pe} = \frac{l_x u_{avg}}{D} \qquad 2.5$$

l_x is the characteristic length in the primary direction of flow (typically taken to be equal to the grid-spacing within a numerical model), and u_{avg} is the average flow velocity.

iv) Fluid flow within the channel is incompressible and Newtonian. The Reynolds number (Re), a dimensionless parameter used to describe whether a flow stream is laminar or turbulent, is expressed as:

$$\mathrm{Re} = \frac{d_{eff} u_{avg}}{\upsilon} \qquad 2.6$$

where υ is the kinematic viscosity of the fluid, and d_{eff} is the effective channel diameter (defined in Equation 2.7). For a rectangular channel cross-section, the latter is given by:

$$d_{eff} = \frac{4A_c}{p} = \frac{2h_c b_c}{h_c + b_c} \qquad 2.7$$

where A_c is the cross-sectional area, p the inner perimeter, h_c the height, and b_c the breadth of the channel. The flow is *laminar* in the device for Re < 100, *turbulent* for Re > 10^4, and for the intermediate range the flow is *transitional*.[11] Within the applicable design and experimental range (i.e.: h_c < 1 mm; volumetric flow rate < 0.5 mL min^{-1}), the flow within the photoreactor device is *laminar* and can thus be described by the Hagen-Poiseuille flow.[12] The solution to the velocity profile is parabolic, and takes the form:

$$u_x = 4u_o\left(\frac{y}{h_c} - \left(\frac{y}{h_c}\right)^2\right) \qquad 2.8$$

u can therefore be simplified to u_x, and is thus represented by a flow that travels in the *x*-direction (in accordance to the reference frame defined in Figure 2.1), for which the velocity at the centre of the channel is maximal, and equal to u_o.

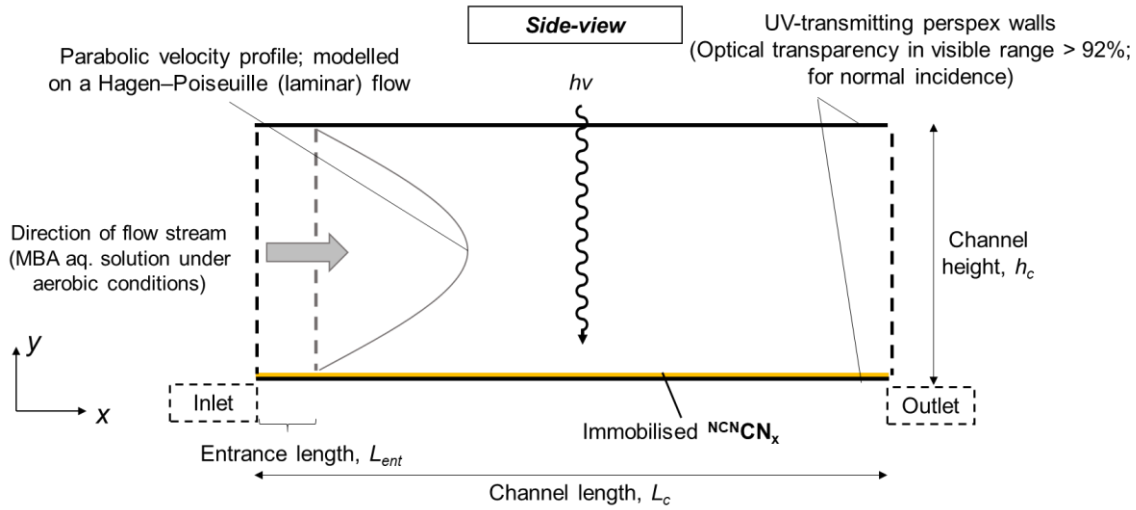

Figure 2.1: Schematic illustration of the flow channel. The von Kármán laminar momentum boundary layer approach is adopted for estimating the entrance length (L_{ent}) in a parallel plate set-up, and is approximated via the following: $L_{ent}/h_c \approx \mathrm{Re}/40$. This parameter provides an estimate for the length at which the flow acquires a fully developed parabolic profile, as highlighted in the figure.

Applying rationales (i) – (iv), Equation 2.4 can be simplified to yield the following second order, homogeneous and parabolic partial differential equation (PDE):

$$\frac{\partial c_{MBA}}{\partial t} = D\frac{\partial^2 c_{MBA}}{\partial y^2} - u_x\frac{\partial c_{MBA}}{\partial x} \qquad 2.9$$

A numerical method was required to solve the PDE, and compute $c_{MBA}(x,y)$ throughout the flow channel, for which the reaction term was only applied at the photoactive surface. To accomplish this, the domain was first discretised into several grid points, and c_{MBA} was computed at each point via a finite-difference approximation of the first and second order derivatives in Equation 2.9. A brief outline of the adopted computational method entailing the d*iscretisation* of the PDE, analysis of the *boundary conditions* (BCs), description of the *stability criteria*, and *quantification* of reactor design effectiveness, is provided on the subsequent pages.

Discretisation of the PDE

For the discretisation, a Forward-Time-Centred-Space (FTCS) explicit upwind scheme was implemented, in which a *first-order approximation* was used for the *time derivative* and a *second order approximation* was used for the *spatial derivative*. Ideally, the distribution of nodes within the discretised domain (i.e. the grid) should mimic the concentration distribution of species in the channel. Steep concentration gradients occur in the flow region above the photoactive surface (due to the reactivity within that zone of the device); hence, closely-packed nodes near this surface improve the model accuracy. This requirement can be incorporated into the numerical solution by means of an *expanding grid* along the *y*-direction (equidistant node spacing is used for the *x*-direction). This mathematical function controls the distribution of nodes within the domain allowing grid points to be closer to one another near the region of interest, and further apart at the nonreactive boundary. The discretised version of Equation 2.9 is given by:

$$\frac{c_{i,j}^{n+1} - c_{i,j}^{n}}{\Delta t} \approx D\left(\frac{\left(\frac{c_{i,j+1}^{n} - c_{i,j}^{n}}{\Delta y_+}\right) - \left(\frac{c_{i,j}^{n} - c_{i,j-1}^{n}}{\Delta y_-}\right)}{\frac{1}{2}\left(\Delta y_+ + \Delta y_-\right)}\right) - u_{x,j}\left(\frac{c_{i+1,j}^{n} - c_{i-1,j}^{n}}{2\Delta x}\right) \qquad 2.10$$

where *i* and *j* are indices to signify the nodes within the spatial domain (*x* and *y* respectively), whilst *n* corresponds to the current time-level within the simulation.

c denotes the concentration of MBA (MBA subscript omitted for clarity), and is represented as a function of space and time (i.e. $c = f(x,y,t)$). Δt is the time step of the numerical integration, Δx is the grid spacing in the *x*-direction, and $\Delta y_{+/-}$ represents the unequal grid spacing in the *y*-direction, centralised around the node '*i*,*j*'.

Boundary Conditions

For a stationary photocatalyst, it is mathematically feasible to account for the chemical reaction on the defined photocatalytic "flat" surface which contacts the flow regime. The description of the boundary condition is based on a steady-state mass balance over a differential surface element. Since convective transport vanishes on the stationary surface (*no-slip* condition), the boundary condition at the photoactive layer can be derived by equating the contributions arising from diffusion, and chemical reactivity (Equation 2.2). Quantitatively, this can be expressed in the following manner:

$$flux|_{y=0} = -k_{app} c_{MBA}|_{y=0} \qquad 2.11$$

where the '$y = 0$' subscript represents the photoactive surface. Substituting the 'flux' term for Fick's first law of diffusion yields:

$$-D\frac{\partial c_{MBA}}{\partial y}\Big|_{y=0} = -k_{app} c_{MBA}|_{y=0} \qquad 2.12$$

The term on the left-hand side refers to the rate of reactant transport toward the catalytic surface via molecular mass transfer (transverse to the flow direction), whereas the right-hand term describes the rate of depletion of MBA via the $^{NCN}\mathbf{CN_x}$ photocatalysed pathway (the minus sign on the left and right hand side of Equation 2.12 are kept for clarity).

Stability Criteria

Two primary stability criteria must be satisfied in order for the *convection-diffusion-chemical reaction* equation to converge.[13] The first of which is the Courant-Friedrichs-Lewy (CFL) condition:

$$CFL \equiv \frac{u_o \Delta t}{\Delta x} \leq 1 \qquad 2.13$$

and the second is the ‘Diffusion Number’:

$$\frac{D\Delta t}{(\Delta y_{min})^2} \leq {}^1/_2 \qquad 2.14$$

where u_o (the velocity at the centre of the channel) is equivalent to the maximum velocity of the flow in the x-direction, and Δy_{min} is the minimum distance between two nodes within the expanding grid. These criteria govern the maximum size of the time step Δt that would result in the convergence of the numerical approximation, and hence, which would yield a stable solution. From a physical point of view, these conditions ensure that the propagation speed of the physical perturbation under investigation is always smaller than the numerical propagation. From a mathematical perspective, this implies that the physical domain of dependence lies within the numerical domain of dependence.

Quantification of Reactor Design Effectiveness

The final requirement in order to implement the numerical model is a metric to govern and quantify the ‘effectiveness’ of a set of design parameters and flow conditions. The *conversion* of starting material (denoted as ***Conv***) was selected as a suitable metric, and is calculated by means of the following:

$$\boldsymbol{Conv} = \frac{c_{MBA}|_{bulk,\, x=0} - c_{MBA}|_{bulk,\, x=L_c}}{c_{MBA}|_{bulk,\, x=0}} \qquad 2.15$$

where ‘$c_{MBA}|_{bulk,\ x\ =\ 0}$’ and ‘$c_{MBA}|_{bulk,\ x\ =\ Lc}$’ signify the inlet and outlet concentration respectively. The latter can be computed by means of the following equation:

$$c_{MBA}|_{bulk,\, x=L_c} \equiv \frac{\int_0^{h_c} c_{MBA}|_{x=L_c} u_x \mathrm{d}y}{\int_0^{h_c} u_x \mathrm{d}y} \qquad 2.16$$

2.3 Results and Discussion

2.3.1 Trends Deduced from CFD

As an initial exercise, it was beneficial to deduce some basic trends from the model, to ascertain the effect and sensitivity of the design, flow, and reaction parameters on

the conversion of starting material inside the TCP. The explicit scheme incorporated for the purpose of this study was however found to be *conditionally stable*, meaning that certain input parameters would cause instabilities to develop within the numerical model. This is related to the *stability criteria*, as defined by Equations 2.13 and 2.14, which essentially place a constraint on the broader applicability of the code. For instance, a high-resolution grid, needed to model a kinetically fast reaction occurring at the boundary, would require too much memory and typically cause the simulation to crash. Use of an expanding grid would not be able to circumvent this issue, since the Diffusion Number criteria is dependent on the minimum distance between two nodes within the expanding grid. Hence, the latter places an upper bound with regards to how compact the nodes can be within the vicinity of the reactive surface. On a similar note, the time step Δt adopted for a numerical simulation must also lie within the stable region. i.e.: $\Delta t \leq \Delta t_{stability}$. Therefore, such explicit schemes typically take a long time to converge and reach a steady state, as a result of the infinitesimally small Δt required. An implicit scheme would therefore be more suitable as it would avoid the use of the CFL and Diffusion Number criteria. Nevertheless, with the devised model, a number of parameters were varied successfully, and a stable, steady solution was obtained for each case.

Some exemplary results are depicted in Figure 2.2, where it is clear that both a decrease in channel height, and an increase in channel length, improve the conversion of the starting benzylic alcohol to the corresponding aldehyde, with the former exhibiting a more pronounced effect than the latter (Figure 2.2a). A decrease in the volumetric flow rate, $\dot{V}$, which ties into the code via the residence time (τ, Equation 2.17 in Experimental Section 2.5), had a marked improvement on the conversion of starting material (Figure 2.2b). Changes in the apparent rate of reaction appeared to have a much less significant effect on the conversion factor, until $k_{app} \equiv k_{reaction} K_{ads} \Gamma_{\mathbf{CN}^*} \longrightarrow 0$ (Figure 2.2c). Although values for $k_{reaction}$ for this system can be appreciable,[5] the product of these three terms can yield a correspondingly low value that reflects poorly on the overall apparent rate of reaction at the heterogeneous photoactive surface.

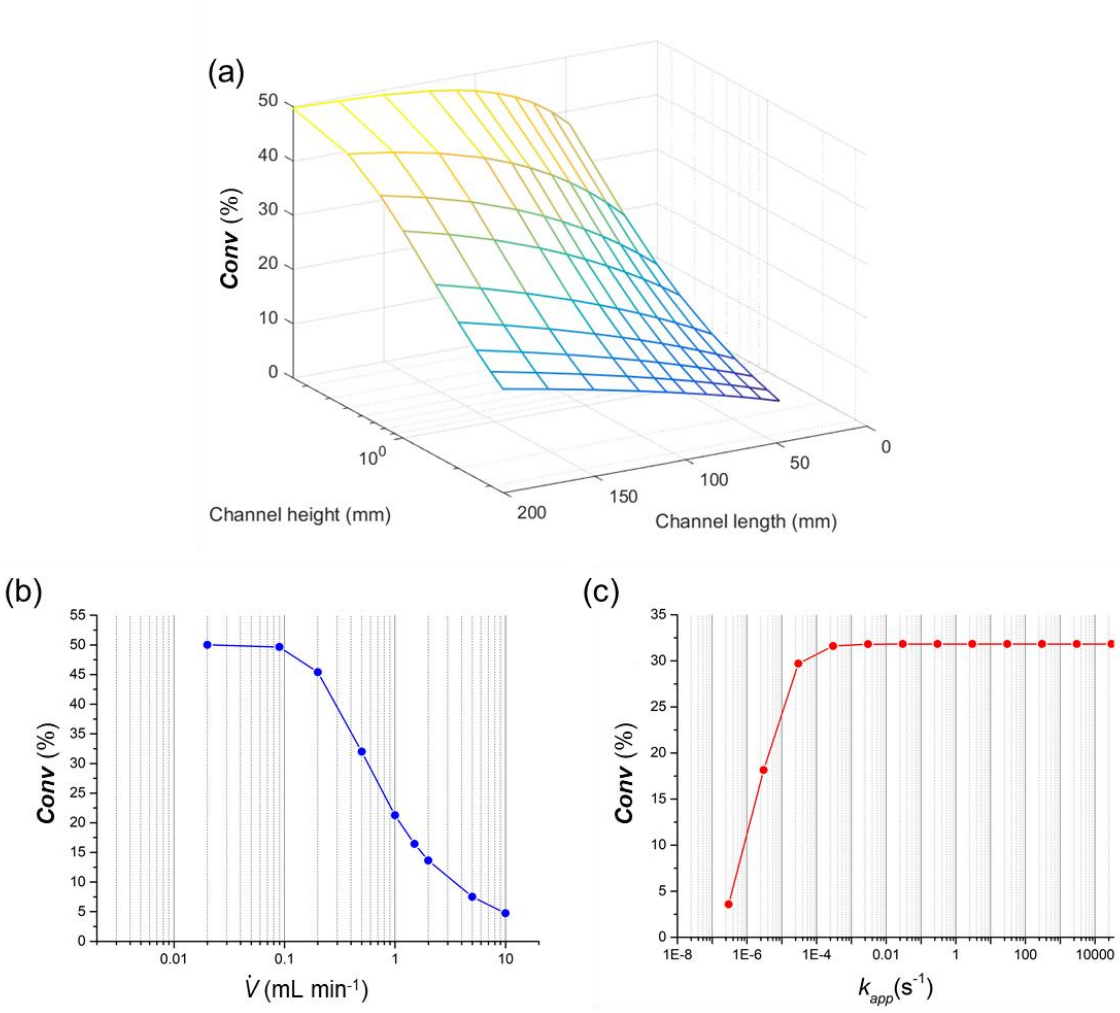

Figure 2.2: Output trends from the numerical model, showing the variation in the ***Conv*** against: (a) the channel height and length of the TCP, (b) the volumetric flow rate, and (c) the apparent rate of reaction, thus highlighting the effect of design, flow, and reaction parameters on the conversion metric, respectively.

2.3.2 TCP Prototype Test-rig

The TCP was designed and fabricated based on the preliminary trends deduced from the numerical model, in combination with the four criteria specified in Section 2.2.1. Full details regarding the fabrication are provided in Experimental Section 2.5. A rendered image of the TCP prototype is illustrated in Figure 2.3. Utilising a channel height < 1 mm was an important design parameter in ensuring higher conversion (Figure 2.2a). For this reason, a commercial polytetrafluoroethylene (PTFE) sheet (thickness = 0.5 mm) was chosen for preliminary testing and was used to define the microfluidic channel. For the device to fall within the spot size of the solar light simulator, a channel length < 70 mm was required. Thus, a standard microscope slide

provided a suitable template for coating with the photocatalyst to yield the photoactive sheet, and the length and breadth of the prototype were based on its dimensions.

A flow set-up was constructed to begin testing the TCP, and a schematic illustration of this is shown in Figure 2.4. Three $^{NCN}CN_x$ coating techniques were initially attempted (see Experimental Section 2.5), and the stability of the respective sheet under continuous flow conditions was tested by securing it in the TCP and then flowing an aqueous electrolyte solution through the channel for a duration of 1 h, at a flow rate of 0.1 mL min^{-1}. The Nafion®-based dispersion method proved to be most stable, and hence, was used for photocatalytic flow experiments.

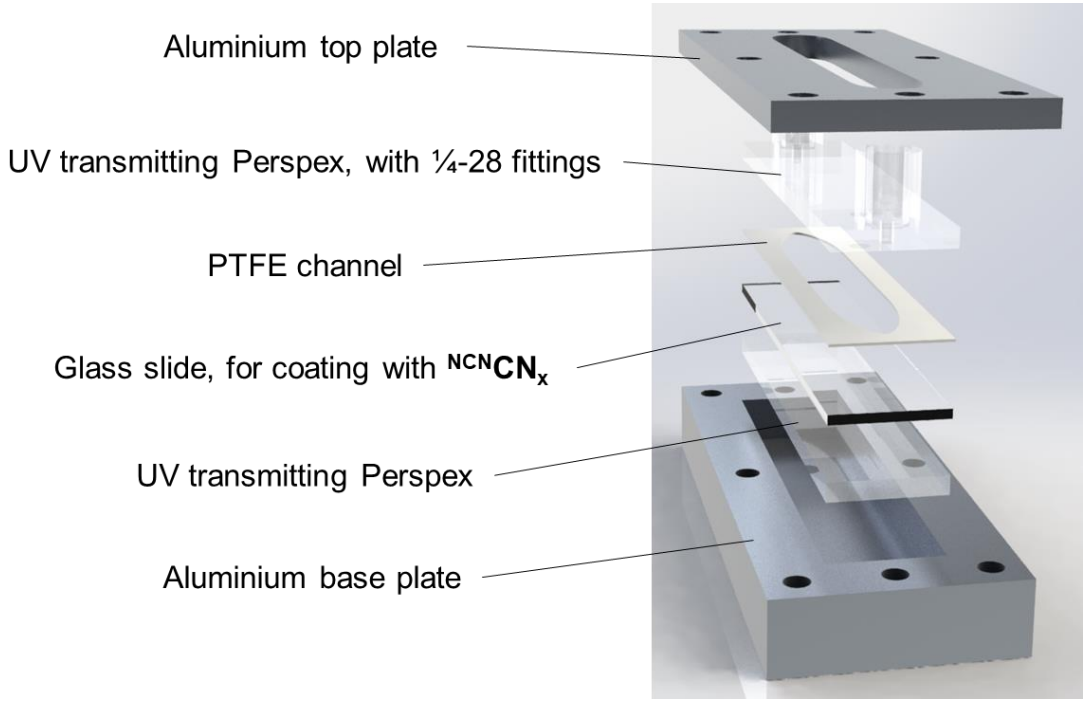

Figure 2.3: Rendered image (exploded view) of the TCP prototype design. (*Note*: the PTFE channel dimensions are: $L_c \times b_c \times h_c = 68 \times 15 \times 0.5$ mm).

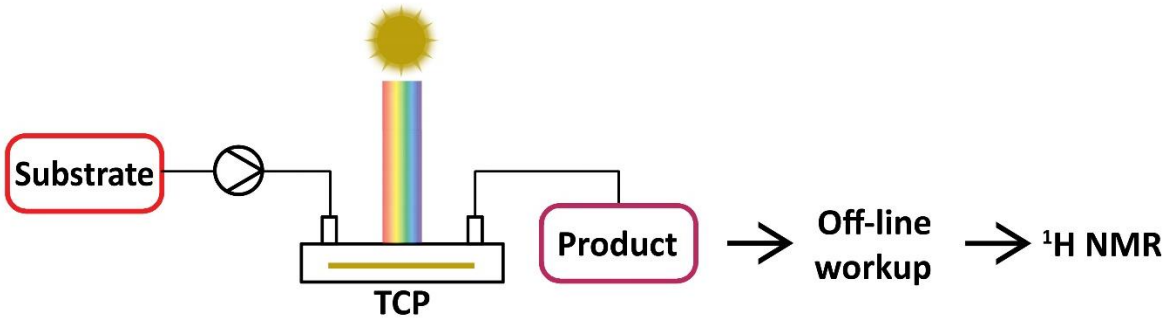

Figure 2.4: Schematic diagram of the TCP setup, incorporating $^{NCN}CN_x$ as the stationery phase. Irradiation is carried out via a solar light simulator (100 mW cm^{-2}, AM 1.5G, IR filtration).

To assess the performance of the TCP under solar irradiation, an MBA solution (20 mM) prepared in aqueous phosphate electrolyte (under ambient conditions) was pumped though the photoreactor at a volumetric flow rate of 0.05 mL min^{-1}. Following an off-line work-up of the reaction mixture, an NMR-based alcohol-to-aldehyde conversion of 17% was measured (quantified by addition of an internal standard (IS), DMSO).

Decreasing the height of the channel and/or increasing the effective pathlength over the photoactive surface, were two possible design alterations envisioned to improve the experimental performance of the TCP. For this reason, a polydimethylsiloxane (PDMS) microfluidic device, with a serpentine shaped channel of length 1.2 m, and a corresponding breadth and height of 100 μm, was fabricated using conventional photolithographic techniques. However, complications arose after attempting to plasma bind the PDMS device to the photocatalyst sheet. Although a thin layer of the $^{NCN}CN_x$-Nafion composite was doctor bladed onto the glass, the coating itself was not perfectly flat, and some irregularities were present. This led to the formation of small gaps between the glass slide and the PDMS device, making the flow system susceptible to leakage and thus, unusable for photocatalytic flow applications.

Comparison Between the Numerical and Experimental Results

When inputting the straight-cut channel dimensions into the numerical code ($L_c \times b_c \times h_c$ = 68 × 15 × 0.5 mm, Figure 2.3 and Figure 2.6) along with the flow rate used in TCP experiment, a conversion of 32% was computed, based on the outflow concentration profile (Figure 2.5a, c.f. Equation 2.15), wherein Δt, Δx, and Δy were varied accordingly (within the stable region) to ascertain convergence of the numerical solution. The corresponding simulated concentration profile throughout the full length of the channel is presented in Figure 2.5b.

Although the experimental and numerical conversions were not too dissimilar from one another, discrepancies between the two were expected. Firstly, in the model, it was assumed that the bottom boundary was completely reactive towards MBA photocatalysed oxidation. In practice, the fractional coverage of $^{NCN}CN_x$ over the glass slide was neither completely homogeneous nor equal to unity. Additionally, at times, there could have been poor contact between the $^{NCN}CN_x$-Nafion composite coating

and the liquid flow, thus impeding mass transfer of the benzyl alcohol to the catalytically active sites. The extremities of the TCP also lied just outside the illuminated area (spot size) of the solar light simulator, and thus, were effectively unreactive. From an experimental perspective, loss of product during the work-up, and insufficient O_2 dissolved in solution to mediate electron transfer from the photoexcited carbon nitride sheet, could both contribute to a decrease in the conversion metric.

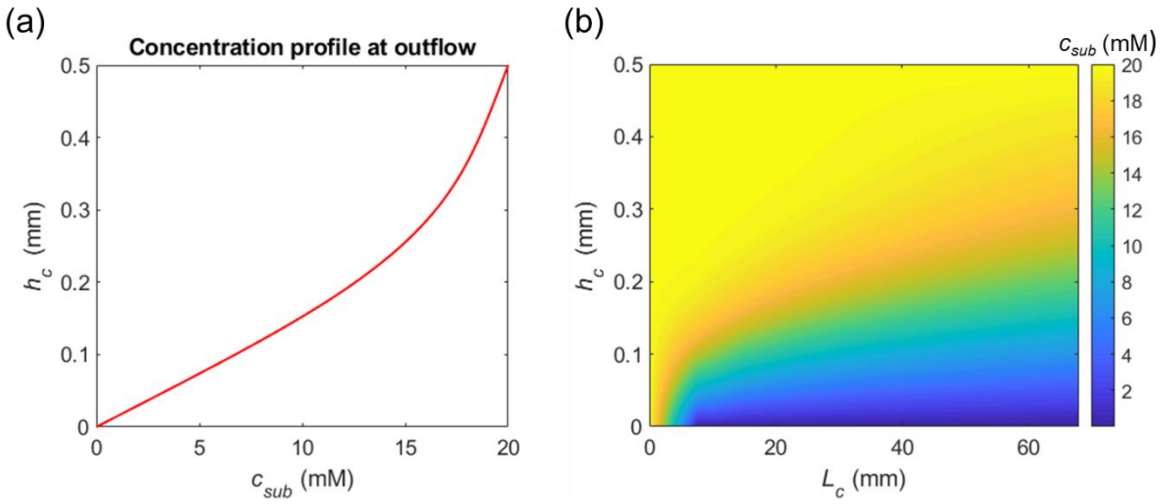

Figure 2.5: Concentration profiles calculated via the numerical model; (a) outflow concentration profile, and (b) concentration profile throughout the TCP channel. *Simulation conditions*: substrate concentration, c_{sub} = 20 mM, channel dimensions: $L_c \times b_c \times h_c$ = 68 × 15 × 0.5 mm, $\dot{V}$ = 0.05 mL min^{-1}, k_{app} = 3×10^3 s^{-1}.

For this comparative study, the k_{app} value incorporated into the numerical model was rationally derived from the TAS findings of the **^{NCN}CN$_x$–NiP** system.[5] However, not all the kinetic elements of the immobilised heterogeneous photocatalytic system were probably captured by the approximation for k_{app}, leading to inconsistencies between numerical and empirical findings. The predicted ***Conv*** metric does tend to zero for low values of k_{app}, as highlighted in Figure 2.2c, and hence a more detailed understanding of this parameter will be beneficial for improving comparative studies between the experimental and computational approaches. On a similar note, the exact molecular diffusion coefficient for MBA within a phosphate electrolyte medium was unknown, and a value for D for benzyl alcohol was extrapolated from the literature.[14] In a similar manner to the variation in k_{app}, the error in D (as implemented within the algorithm) could further contribute towards discrepancies between the two methods.

2.4 Conclusion

In conclusion, we have modelled, designed and fabricated a thin channel photoreactor incorporating a $^{NCN}\mathbf{CN_x}$-Nafion composite as the photocatalyst sheet, in order to conduct the oxidation of MBA under continuous flow conditions. This proof-of-concept device provided the data to support, and further investigate, the use of carbon nitride materials in a continuous flow environment. Building a numerical model for the immobilised, heterogeneous flow photoreactor, was a beneficial exercise in visualising the impact of certain parameters (such as L_c, h_c, $\dot{V}$, and k_{app}) on the photocatalysed conversion of the alcohol substrate. In addition, the trends deduced facilitated in the design and fabrication stages of the TCP prototype.

From the coating methods considered, the $^{NCN}\mathbf{CN_x}$-Nafion composite was found to be a suitable technique for the formation of the photocatalyst sheet, and when incorporated in the TCP, a MBA-to-aldehyde conversion of 17% was measured under solar light irradiation (at a flow rate of 0.05 mL min^{-1}). The discrepancy between the experimentally determined value and the numerical prediction was hypothesised to stem from a combination of factors. Some of the issues that were discussed include the inhomogeneity of the coating and poorly exposed $^{NCN}\mathbf{CN_x}$ active sites in the experimental setup (which were unaccounted for in the model), along with any errors originating from estimations made in the numerical model, particularly for the molecular diffusion coefficient of MBA and the apparent first-order rate constant for the surface-photocatalysed chemical reaction.

Substituting the PTFE channel for a PDMS microfluidic device, with the aim of improving the *SA-to-V* characteristics of the flow reactor, was unsuccessful, on account of the surface roughness of the photocatalyst sheet. Although in theory, the TCP offers some attractive features for conducting photocatalytic substrate oxidations under continuous flow conditions, limitations with regards to system improvement (vis-à-vis the conversion metric) demanded for an alternative photoreactor design. The TCP therefore laid the groundwork for the next generation of carbon nitride-based flow devices, which will be the topic of discussion in Chapter 3.

2.5 Experimental Section

2.5.1 Construction of the TCP

A layered, modular design was implemented to allow for facile replacement of the $^{NCN}CN_x$ sheet within the TCP. An aluminium casing was used to support the stresses induced from sealing the device (via M2.5 × 8 mm screws) to prevent leakage of the reaction mixture. A PTFE gasket of the desired thickness was used to mimic a flow channel and was selected due to its pliable characteristics. The windows of the device were constructed from UV transmitting Plexiglas® (GS Clear 2458), a commercially available poly(methyl methacrylate) (PMMA) based material, which has an optical transmission of 92% in the visible range (400 – 780 nm) and permits UVA and UVB radiation with a transmission of ~80%. The size of a standard microscope glass slide (25 × 75 mm) suited the overall dimension specifications for the device, and hence, was used for coating with $^{NCN}CN_x$ in order to form the photocatalyst sheet. Schematic projections of the designed prototype are presented in Figure 2.6.

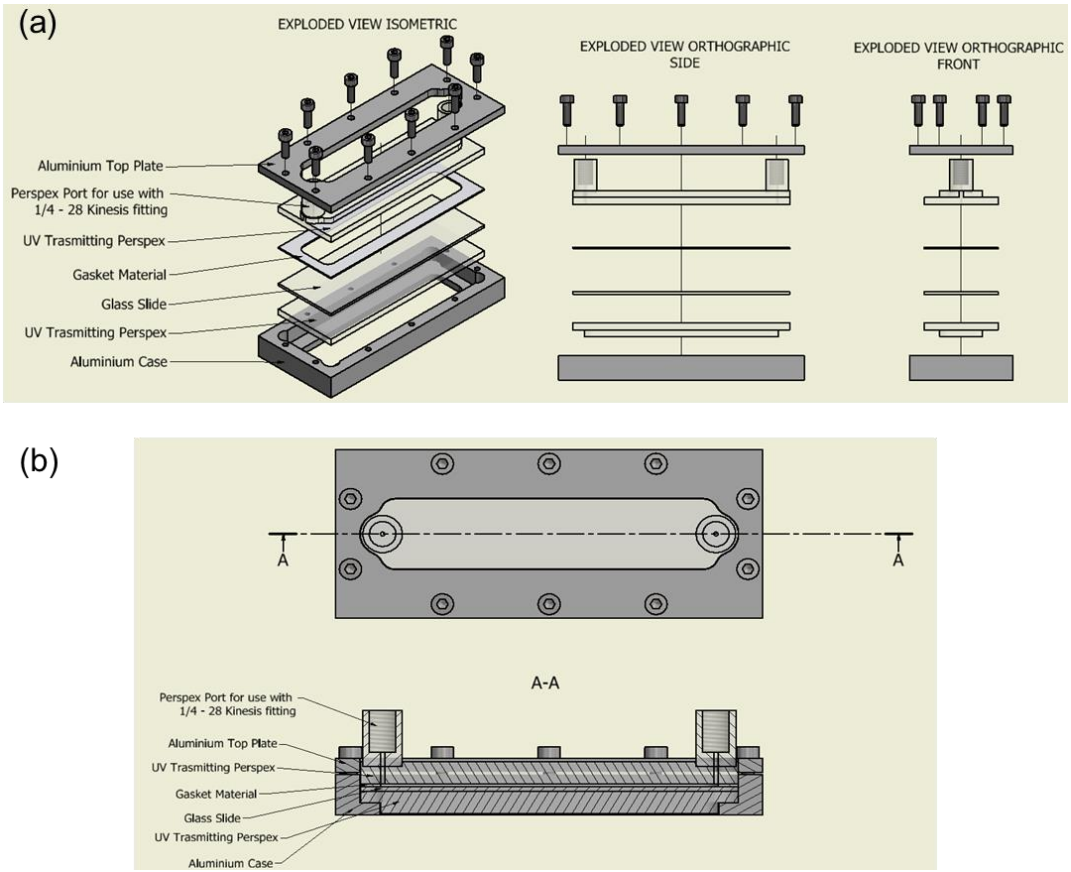

Figure 2.6: Schematic diagram of the TCP, portraying (a) the exploded isometric and orthographic projections of the design. (b) Orthographic projection of the top of the device, along with a cross-section view through the A-A plane.

2.5.2 Synthesis and Immobilisation of $^{NCN}CN_x$

$^{NCN}CN_x$ was synthesised following a reported procedure.[15] Briefly, graphitic carbon nitride was first prepared by heating melamine to 550 °C for 4 h under air. The yellow solid obtained was thoroughly ground using a pestle and mortar, then mixed with potassium thiocyanate (KSCN) (1:2 w/w; dried overnight at 140 °C under vacuum), and heated at 400 °C for 1 h and then at 500 °C for 30 min under Ar.[16] After cooling to room temperature, the residual KSCN was removed by washing with water, and the yellow product was dried under vacuum at 60 °C.

Three $^{NCN}CN_x$-coating methods were tested for incorporation within the TCP for continuous flow studies. For all three methods, a Scotch tape mask was placed on the glass slide to define the surface area of the channel (15 × 68 mm), and was always removed shortly after the deposition method, in order to prevent cracking of the resultant carbon nitride coating.

(i) *Polyethylene glycol dispersion*

Polyethylene glycol (PEG) was dissolved in absolute ethanol (60 mg mL^{-1}). $^{NCN}CN_x$ (5 mg) was added to 50 µL of the PEG mixture to produce a slurry, which was then sonicated for 45 min. The resultant dispersion was transferred to the glass slide and spread evenly over the entire surface by using the doctor blading method. The fabricated slide was dried at 100 °C for 2 h.

(ii) *Nafion dispersion*

$^{NCN}CN_x$ (5 mg), absolute ethanol (50 µL) and Nafion® (20 µL) were mixed, and the composition was sonicated for 15 min. The resultant dispersion was deposited onto a glass slide using the doctor blading method, and the slide was then dried at 100 °C for 30 min.

(iii) *Epoxy resin technique*

A 3:1 w/w adhesive mixture of epoxy resin to Aradur® hardener was first prepared. A 12:1 w/w ratio of adhesive to $^{NCN}CN_x$ (using 5 mg of $^{NCN}CN_x$) was then weighed out, and the resultant paste was mixed thoroughly and coated onto the unmasked surface of the glass slide. The $^{NCN}CN_x$ films were left to dry overnight at room temperature.

2.5.3 Continuous Flow TCP Test-rig

A schematic of the devised flow configuration is portrayed in Figure 2.4, and an actual image of the photocatalyst sheet loaded within the TCP is shown in Figure 2.7. The substrate solution was housed in Luer-Lock terminated syringe, and was pumped into the reactor via a syringe pump (Legato 110 series). The electrolyte solution was comprised of a pH 4.5 phosphate buffer (0.1 M), and the concentration of MBA used for the flow experiments was 20 mM. PTFE tubing (1.6 mm o.d. × 1 mm i.d.) was used to connect the syringe to the entrance point of the TCP. A Newport Oriel Xenon 150 W solar light simulator (100 mW cm^{-2}, AM 1.5G, containing infrared water filter) was used as the light source to irradiate the TCP during operation. The value for $\dot{V}$ set on the syringe pump was used to control the residence time, τ, of the reactant species inside the TCP, as the reactor volume, V_r, was kept constant (Equation 2.17):

$$\tau = \frac{V_r}{\dot{V}} \qquad 2.17$$

3 mL of the MBA solution was pumped through the TCP. The accumulated reaction mixture was collected at the output, and then extracted three times with dichloromethane (DCM). The combined organic layers were dried over anhydrous $MgSO_4$, filtered, and concentrated to dryness under reduced pressure. Quantification of MBA and MBAd was afforded by ^1H NMR spectroscopy on a Bruker DPX 400 spectrometer at 25 °C, by addition of an IS (DMSO).

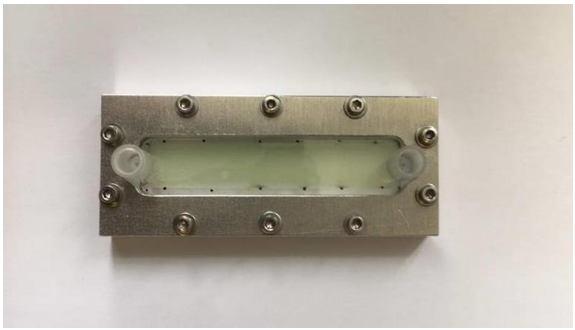

Figure 2.7: Photograph of the $^{NCN}CN_x$ sheet prepared via the Nafion dispersion method, loaded within the TCP flow device.

2.6 References

1 A. Savateev, I. Ghosh, B. König and M. Antonietti, *Angew. Chem. Int. Ed.*, 2018, **57**, 15936–15947.

2 A. Savateev and M. Antonietti, *ACS Catal.*, 2018, **8**, 9790–9808.

3 B. P. Mason, K. E. Price, J. L. Steinbacher, A. R. Bogdan and D. T. McQuade, *Chem. Rev.*, 2007, **107**, 2300–2318.

4 D. Cambié, C. Bottecchia, N. J. W. Straathof, V. Hessel and T. Noël, *Chem. Rev.*, 2016, **116**, 10276–10341.

5 H. Kasap, C. A. Caputo, B. C. M. Martindale, R. Godin, V. W.-H. Lau, B. V. Lotsch, J. R. Durrant and E. Reisner, *J. Am. Chem. Soc.*, 2016, **138**, 9183–9192.

6 J. a Imlay, *Annu. Rev. Microbiol.*, 2003, **57**, 395–418.

7 X. H. Li, X. Wang and M. Antonietti, *ACS Catal.*, 2012, **2**, 2082–2086.

8 C. S. Turchi and D. F. Ollis, *J. Catal.*, 1990, **122**, 178.

9 I. K. Konstantinou and T. A. Albanis, *Appl. Catal. B Environ.*, 2004, **49**, 1–14.

10 L. A. Belfiore, John Wiley & Sons, Inc., Hoboken, NJ, 1st edn., 2003, pp. 611–653.

11 R. L. Hartman, J. P. McMullen and K. F. Jensen, *Angew. Chem. Int. Ed.*, 2011, **50**, 7502–7519.

12 A. C. Fisher and R. G. Compton, *Electroanalysis*, 1992, **4**, 311–315.

13 O. Zikanov, *Essential Computational Fluid Dynamics*, John Wiley & Sons, Inc., Hoboken, NJ, 1st edn., 2010.

14 T. Autrey, P. Kandanarachchi and J. a Franz, *J. Phys. Chem. A*, 2001, **105**, 5948–5953.

15 C. A. Caputo, M. A. Gross, V. W. Lau, C. Cavazza, B. V. Lotsch and E. Reisner, *Angew. Chem. Int. Ed.*, 2014, **53**, 11538–11542.

16 V. W. Lau, I. Moudrakovski, T. Botari, S. Weinberger, M. B. Mesch, V. Duppel, J. Senker, V. Blum and B. V. Lotsch, *Nat. Commun.*, 2016, **7**, 12165.

Chapter 3

Visible Light Flow Reactor Packed with a Porous Carbon Nitride Photocatalyst for Aerobic Substrate Oxidations

The contents of this chapter have been published in a peer-reviewed article: ACS Appl. Mater. Interfaces, 2020, **12**, 8176–8182*. Results presented were obtained solely by the author of this thesis, with contributions from others as outlined here: Arjun Vijeta assisted with obtaining the batch photoreactor measurements. Aleksandr Savateev, Guigang Zhang, and Tobias Heil from the Department of Colloid Chemistry at the Max Planck Institute of Colloids and Interfaces synthesised* ***mpg-CN$_x$*** *and obtained TEM images of the material. Duncan Howe from the NMR spectroscopy suite at the Department of Chemistry helped devise the acetonitrile suppression ^{1}H NMR programme.*

3.1 Introduction

A proof-of-concept thin channel flow device featuring the cyanamide-functionalised carbon nitride (^{NCN}**CN$_x$**) material was developed in Chapter 2. Certain limitations with regards to the design, assembly, and performance were acknowledged, and thus, it was of interest to pursue alternative carbon nitride-based photocatalytic reactors for conducting organic transformations, and particularly, substrate oxidation reactions, under continuous flow conditions.

In the literature, carbon nitride is starting to find applications in early-stage flow photochemical reactors. To-date, as introduced in Chapter 1 (c.f. Figure 1.11), two main approaches for carbon nitride-based flow photochemistry have been adopted: (i) featuring a stationary carbon nitride phase within a packed bed reactor,[1] and (ii) using a suspension in-flow, that is divided into smaller sub-units by means of an inert

gas spacer (termed the serial micro-batch reactor, SMBR).[2] The former approach is perhaps more conventionally utilised when heterogeneous catalysis is needed for continuous chemical transformations,[3,4] and is ideal since the carbon nitride material is effectively immobilised and so the overall setup can be re-used with minimal effort to recover the photocatalyst. The configuration however was limited to liquid-only flow applications, and the authors did not pursue any triphasic (gas–liquid–solid) flow chemistry. The innovative design of the SMBR made use of toroidal vortices in the segmented flow pattern to produce 'well-stirred' micro-suspensions containing the carbon nitride photocatalyst. This internal mixing phenomenon was therefore responsible for homogenising the mixture and resulted in the formation of uniformly irradiated suspensions in the flow sequence. However, the separation strategy for product isolation, and recovery of the catalyst and ionic liquid was quite tedious (featuring filtration, liquid extraction, and solid extraction stages), and hence offered some additional complexity to the reaction protocol in comparison to the packed column design. It was also noted that the authors reported using inert gas conditions (N_2) in order to generate the SMBR flow pattern, and hence, their study precluded the use of a reactive atmosphere.

Demand from industry for aerobic oxidation catalysts is in fact growing.[5] O_2 can be considered as an ideal oxidant, as it is readily abundant and usually generates water as a benign by-product. This is especially advantageous for the production of active pharmaceutical ingredients, where impurities are strongly regulated.[6] A review of large-scale oxidation processes concluded that O_2 gas has the advantage of being a cost-effective and readily available oxidant, but the safety issues surrounding its use make it one of the least frequently used reagents (mixtures of O_2 and organic solvents can potentially be highly flammable).[7] The recent revival in the development of catalytic systems for aerobic substrate oxidations is testimony to the commitment from industry to pursue the application of aerobic O_2. However, such systems are either confined to a small scale,[8] feature catalysts containing precious metals,[9] make use of a homogeneous photocatalyst that hinders downstream processing and separation,[10,11] or are unsuitable for a continuous flow platform.[12] Successful implementation of a carbon nitride-based flow photoreactor, tailored towards aerobic oxidation chemistry, could thus have further-reaching applications on a more industrially relevant level.

In this chapter, I therefore look towards adapting the approach of Blechert *et al*.[1], to develop a packed column photoreactor (**PCP**) for immobilisation of the carbon nitride material, in order to probe the oxidation of substrate alcohols and amines in-flow, under visible light irradiation, and in the presence of an aerobic atmosphere. For reasons which will be described herein, mesoporous graphitic carbon nitride (**mpg-CN$_x$**), rather than a bulk carbon nitride (such as ^{NCN}**CN$_x$**) is incorporated as the stationary photocatalyst. O_2 acts as the terminal electron acceptor and co-oxidant for this class of reactions (refer to Scheme 3.1),[13–15] and thus the flow system is specifically designed to be compatible with triphasic (gas–liquid–solid) conditions, employing aerobic O_2 (air) as one of the input reagents. In accordance with the Beer–Lambert–Bouguer law, photon absorption will mostly be limited to the outer region of the reactor, and hence, a small diameter (~2 mm) packed column is beneficial for this kind of heterogeneous catalysis.

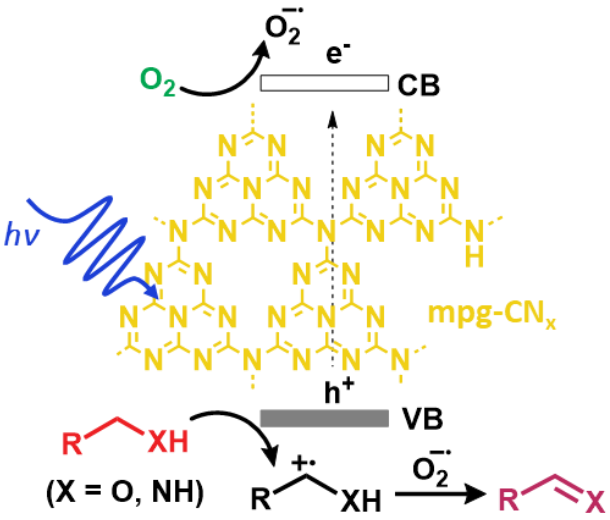

Scheme 3.1: Proposed photocatalytic cycle for the aerobic oxidation of benzyl alcohol/amine to the corresponding aldehyde/imine. According to the literature, O_2 is reduced to the superoxide radical anion via the photogenerated electrons in **mpg-CN$_x$**. The **mpg-CN$_x$** surface bound superoxide species is believed to react with the benzylic intermediate to enhance the rate of substrate oxidation (note that the involvement of H_2O_2 cannot be excluded).[13–15] CB and VB denote the conduction and valence band, respectively.

The previously proposed carbon nitride-photocatalysed oxidation mechanism of alcohols and amines suggests that photoactivated **mpg-CN$_x$** oxidises the benzyl alcohol/amine to the corresponding aldehyde/imine and reduces O_2 to hydrogen peroxide and water (Scheme 3.1).[13] Aldehydes and imines are commonly used synthetic building blocks for the pharmaceutical industry,[14] and thus, tailoring a synthetic procedure that excludes the use of any toxic heavy metals, makes use of

visible light as one of the “reagents”, and is facilitated by continuous flow techniques, will permit this kind of chemistry to be conducted in a more sustainable and efficient manner. This in essence also ties in with some of the themes presented in Chapter 1, where the modernisation of chemical manufacturing processes, and the ability to utilise renewable energy sources for synthetic purposes, will contribute to bridging the gap between the energy and chemical sectors.

3.2 Results and Discussion

3.2.1 Triphasic Flow Photoreactor Setup

A flow setup was constructed to generate a stable gas–liquid segmented (slug) flow pattern (Figure 3.1). This pattern formed downstream of a 4-port 3-way valve, where the substrate and air fronts meet and mix. The resultant segmented flow feeds into the **PCP**, which was comprised of a flexible, transparent fluorinated ethylene propylene (FEP) tube (*l* = 75 cm, i.d. = 2 mm), which was packed with the carbon nitride material (3.5 wt.% in a glass bead mixture). The **PCP** was coiled around a reflective support, and then irradiated in a 360° fashion with a blue LED setup (14.4 W at λ = 470 nm). Typically, 2.5 mL of the substrate solution (concentration in the range of 50 – 100 mM) was first injected into the reactor, followed by 2.5 mL of pure solvent. The residence time of the starting material, τ, within the photoactive zone was varied by changing the flow rate as the reactor volume was kept fixed at ~1 mL (see Experimental Section 3.4 for more details regarding the flow setup).

We observed that the morphology of the carbon nitride greatly impacts the flow performance of the **PCP**. In preliminary tests, both **mpg-CN$_x$** and conventional bulk carbon nitride (**b-CN$_x$**) were individually incorporated within the **PCP**. Transmission electron microscopy (TEM) images show the nonporous, flat morphology of **b-CN$_x$** (Figure 3.2a), which is in stark contrast to the mesoporous network of **mpg-CN$_x$** (Figure 3.2b). This morphological difference is also corroborated by N_2 sorption measurements (Figure 3.3a), which demonstrate the large Brunauer–Emmett–Teller (BET) surface area of **mpg-CN$_x$** (187 $m^2\ g^{-1}$) in comparison to **b-CN$_x$** (5 $m^2\ g^{-1}$). The pore size distribution gives an average pore size of 5.5 nm for **mpg-CN$_x$** (Figure 3.3b).

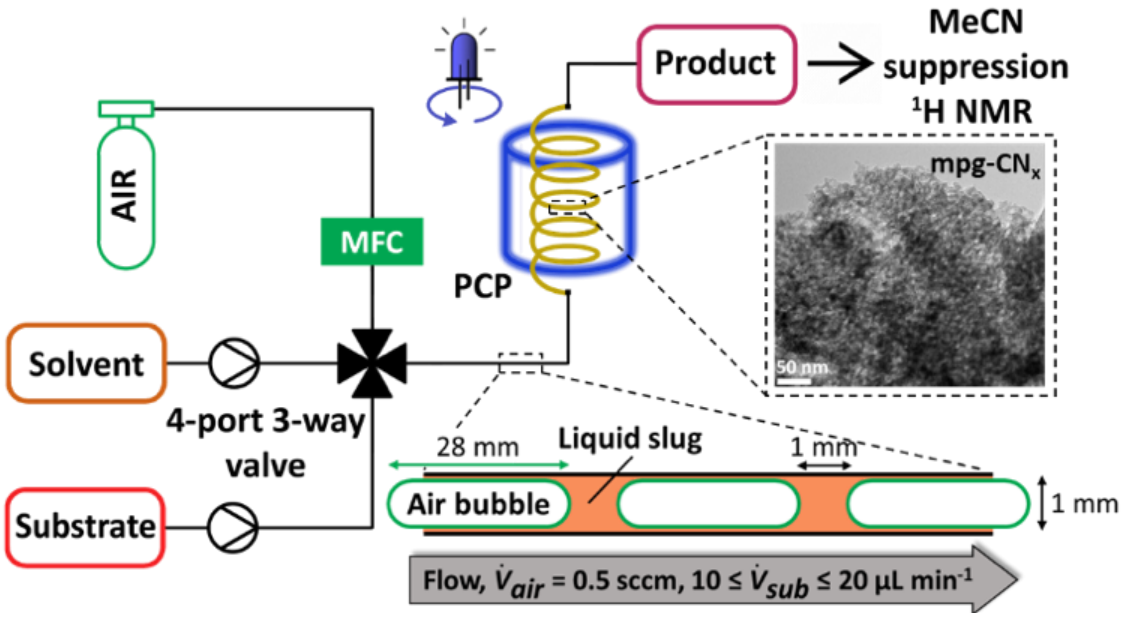

Figure 3.1: Schematic diagram of the triphasic flow photoreactor incorporating **mpg-CN$_x$** within the **PCP**. Irradiation is carried out via 360° blue LEDs (14.4 W at λ = 470 nm) (MFC: mass flow controller). TEM image highlighting the mesoporous morphology of the **mpg-CN$_x$** material and illustration of the gas–liquid flow injected into the **PCP** is also shown.

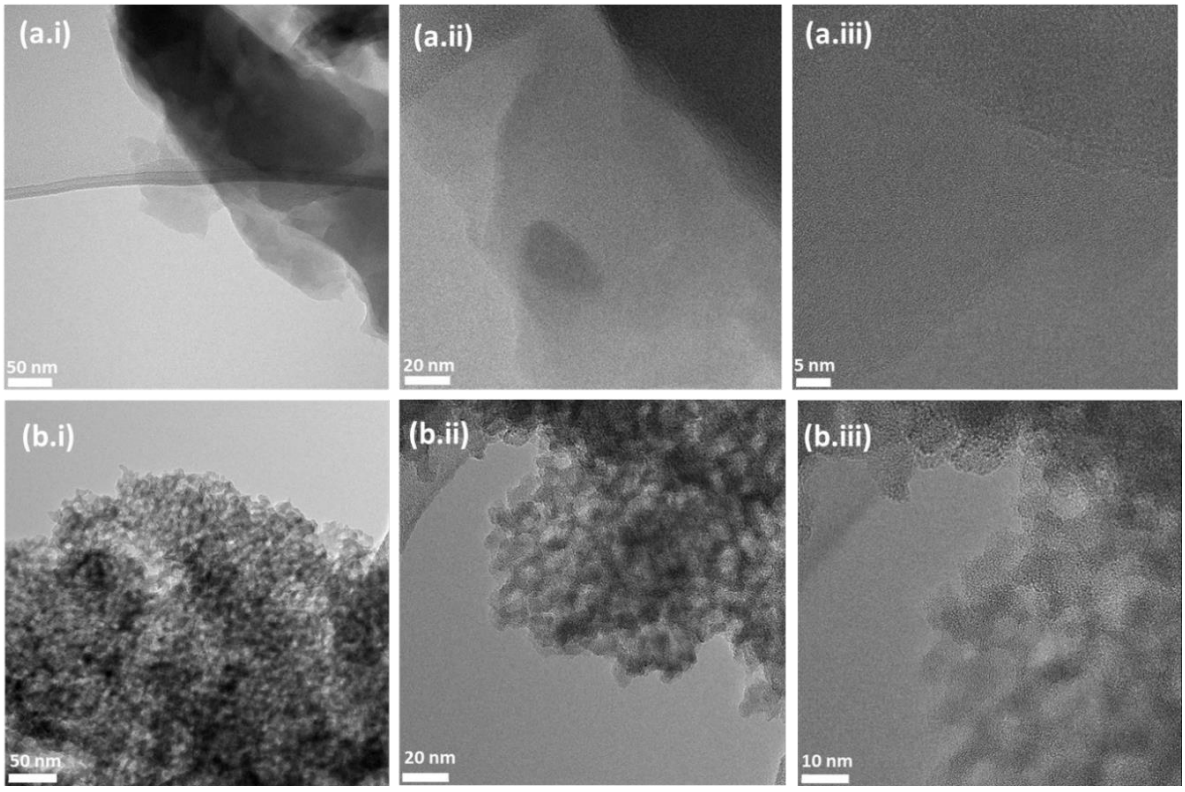

Figure 3.2: TEM images of (a) **b-CN$_x$** and (b) **mpg-CN$_x$**, with different magnifications (i, ii and iii).

The **b-CN$_x$ PCP** could not support the movement of a gas–liquid flow, presumably due to the agglomeration and clustering of the flat **b-CN$_x$** particles, which resulted in a high back-pressure (~1.5 MPa) during operation. On the other hand, the porous framework of **mpg-CN$_x$** allowed for facile gas–liquid permeation, making it suitable for flow applications. The absence of any critical back-pressure issues permitted the use of small diameter reactors, satisfying the high *SA*-to-*V* constraint imposed for photoinduced reactions, and allowing extensive transmission of light to reach the reactive sites. The larger surface area of **mpg-CN$_x$** compared to **b-CN$_x$** gives the additional benefit of improved charge separation and interfacial electron transfer.[15]

The photoreactor assembly allowed for substrate and solvent injection, and the air feed was continuously switched on to ensure the formation of a gas–liquid flow, and to constantly supply aerobic O_2 to the reactive centres. Acetonitrile (MeCN) was the most effective solvent (Figure 3.4), and the heat generated from the LED setup (~55 °C) increased the overall conversion yield. To facilitate downstream processing and to minimise the loss of product and starting material during the work-up stage, an MeCN suppression pulse programme for ^{1}H NMR analysis was designed and implemented. This therefore allowed for direct sampling and measurement of the crude mixture without the need for reaction treatment (see Section 3.4 for more details about how the suppression programme was devised).

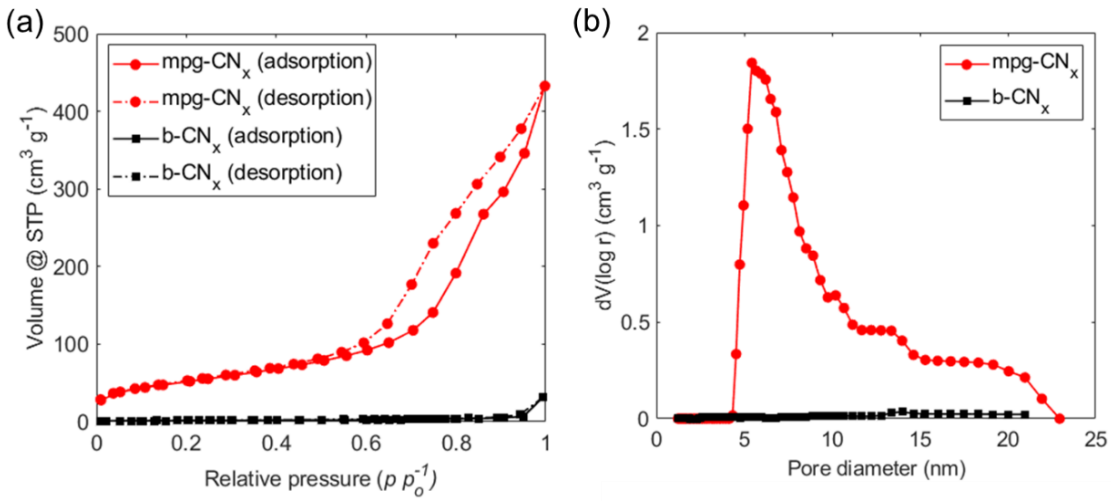

Figure 3.3: Nitrogen sorption data for **mpg-CN$_x$** and **b-CN$_x$**, both prepared using cyanamide as the precursor compound; (a) BET isotherm, (b) pore size distribution.

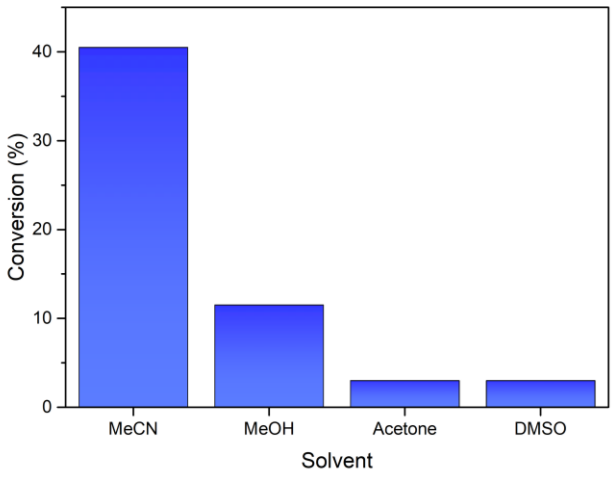

Figure 3.4: Solvent screening experiment performed in batch photoreactor (conditions: 1-naphthalenemethanol concentration = 100 mM (0.6 mL), **mpg-CN$_x$** photocatalyst loading = 2 mg, blue LEDs (14.4 W at λ = 470 nm), *T* = 55 °C, reaction time = 120 min). Deuterated solvents were used.

3.2.2 Photocatalytic Substrate Oxidations In-flow

The system was initially studied using the photocatalysed aerobic oxidation of benzylic alcohols,[13] with 1-naphthalenemethanol selected as the model compound (Scheme 3.2a,). The overall *starting material conversion* (***Conv***), into the resultant aldehyde and carboxylic acid, and *product selectivity* (***Sel***) to the corresponding aldehyde, was controlled by varying the residence time in the **PCP**. The overall ***Conv*** approaches 100% at τ > 90 min, and the formation of the 'overoxidised' product (carboxylic acid) only becomes appreciable at τ > 75 min (Figure 3.5). The significance of this result is that a lower value of τ could be employed to ensure high selectivity for the aldehyde; the starting material can then be separated from the reaction mixture in an in-line manner at the **PCP** exit and recycled back into the photoreactor setup.

The fit applied to the ***Conv*** dataset in Figure 3.5 is of the form: $1 - e^{-k_{PCP}\tau}$, where k_{PCP} represents a form of 'rate constant' (units: min^{-1}) for the triphasic oxidation reaction within the **PCP**. k_{PCP} is therefore expected to vary with both an alteration in the reactor parameters (such as catalyst loading, and diameter of the packed column, amongst others), and a change in substrate. Effectively, it can be used as a design guide to compare the performance of different reactor configurations (in the presence of the same substrate), or to compare the reactivity of different substrates within the same **PCP** design.

The inset in Figure 3.5 highlights the recyclability of the photocatalytic system, which maintains a high level of activity for multiple flow cycles. To compile this plot, a 1-naphthalenemethanol solution in MeCN was injected into reactor (2.5 mL, 100 mM), followed by 2.5 mL of pure MeCN. This procedure was repeated for a total of 25 times, and the ***Conv*** metric was computed after each individual flow reaction. Relative to the initial run, there was only an approximate 10% drop in activity by the 25th flow experiment, most likely due to some sedimentation or aggregation of the **mpg-CN$_x$** particles within the **PCP**, which would effectively lead to a reduction in the active surface area of the photocatalyst.

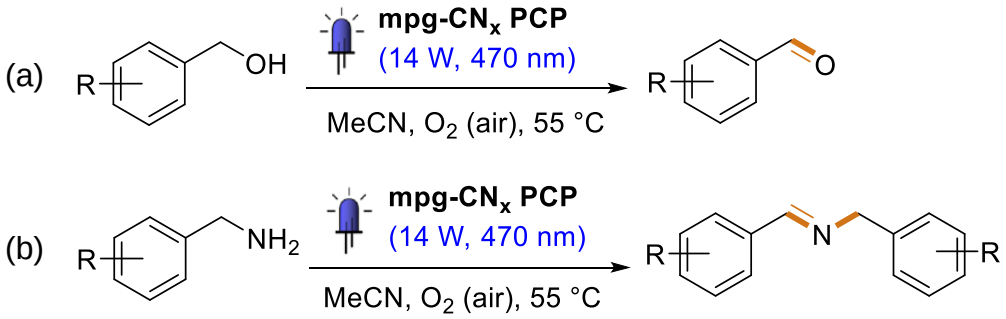

Scheme 3.2: (a) Alcohol and (b) amine oxidation reactions studied under continuous flow conditions.

The benzylic oxidation reaction (Scheme 3.2a) was compared under both batch and flow conditions and the performance was assessed by determining a number of metrics, namely the ***Conv***, ***Sel***, and *mass balance* (***M.B.***). ***M.B.*** evaluates the moles of species exiting the reactor, relative to the amount injected into the system (see Experimental Section 3.4 for further details). For the batch photoreactor, the reaction time was set to 90 min and the optimal **mpg-CN$_x$** loading was established (Figure 3.6). A wide range of *para*-substituted benzyl alcohols were studied, and the **PCP** setup displayed a substantial improvement in ***Conv*** compared to its batch counterpart (Table 3-1). The enhancement of the flow setup compared to batch stems from a higher local loading of the photocatalyst in the light-responsive zone; by directing more of the substrate over the catalyst, and constantly replenishing the O_2 at the reactive sites (by means of the constant airflow), a higher activity is achieved for a given reaction.

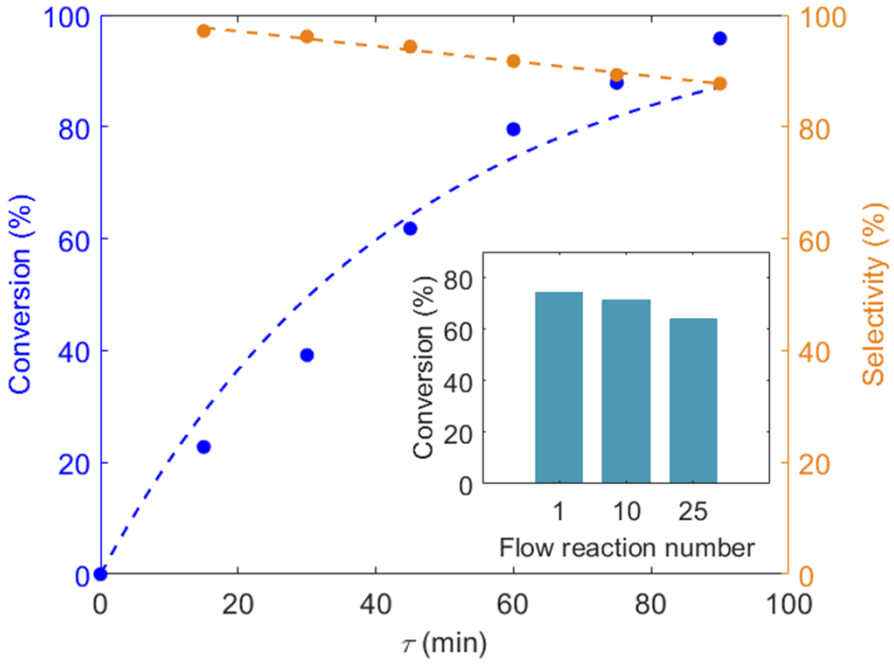

Figure 3.5: Residence time profile with both starting material *conversion* and *selectivity* for aldehyde production (1-naphthalenemethanol concentration = 50 mM in MeCN). Inset: photoreactor re-usability with a total of 25 flow experiments in the **PCP** setup (1-naphthalenemethanol concentration = 100 mM in MeCN, τ = 90 min). General conditions: $\dot{V}_{air}$ = 0.5 sccm, blue LEDs (14.4 W at λ = 470 nm), T = 55 °C.

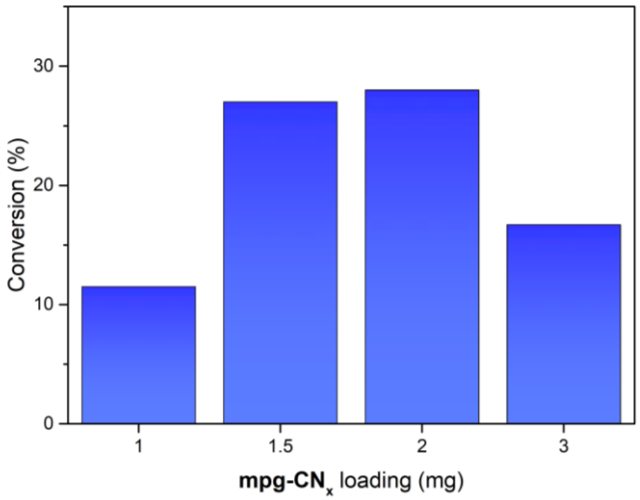

Figure 3.6: Loading optimisation of **mpg-CN$_x$** in the batch photoreactor (conditions: 1-naphthalenemethanol concentration = 75 mM (0.6 mL CD_3CN), blue LEDs (14.4 W at λ = 470 nm), T = 55 °C, reaction time = 90 min). The maximum in the plot stems from the fact that any additional quantities of **mpg-CN$_x$** result in significant photocatalyst sedimentation, which hinder the absorption of photons within the colloidal suspension (where a successful reaction is more likely to occur).

Control experiments with the **PCP** in the absence of light did not result in alcohol conversion (Table 3-1, entry **1.i**). Switching off the air feed or using N_2 purged

substrate and solvent feed stocks resulted in ***Conv*** of 17% and 11%, respectively (Table 3-1, entry **1.ii**, **iii**). The low, but significant, conversion of entry **1.iii** (Table 3-1) is most likely the result of O_2 trapped within the **mpg-CN$_x$** mesoporous network.[15] These results highlight the advantage of using a gas–liquid, rather than a liquid-only, flow in which O_2 acts as both an electron acceptor and a subsequent reagent in the overall oxidation process.

Table 3-1: Alcohol oxidation scope under batch and flow conditions, featuring control experiments performed in flow, based on Scheme 3.2a.

Entry	Substrate[a]	Flow[b]		Batch[c]	
		Conv [d]	***Sel*** [e]	***Conv*** [d]	***Sel***
		[%]			
1	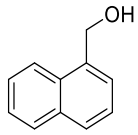	80	93	39	94
1.i	No light	0	N.A.	-	-
1.ii	No air flow[f]	17	100	-	-
1.iii	No air flow, N_2 purged[g]	11	100	-	-
2	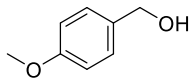	100	76	63	94
3	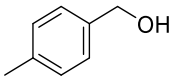	76	88	32	94
4	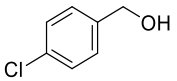	46	93	25	91
5	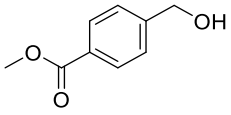	44	93	12	100
6	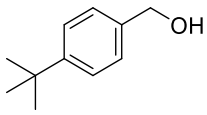	55	92	25	94

[a] General conditions: substrate concentration 75 mM in MeCN (CD_3CN in batch), blue LEDs (14.4 W at λ = 470 nm), T = 55 °C. Control flow experiments detailed as sub-entries within the table. [b] Flow conditions: τ = 90 min, $\dot{V}_{air}$ = 0.5 sccm. [c] Batch conditions: *reaction time* = 90 min, **mpg-CN$_x$** photocatalyst loading = 2 mg. [d] ***Conv*** calculated using 1,3,5-trimethoxybenzene as internal standard. [e] ***Sel*** for corresponding aldehyde. [f] Residual O_2 (from ambient air) still present in liquid feeds. [g] Solvent and solution feeds purged with N_2 for 15 min prior to use.

Para-substituents with the lowest Hammett parameter (σ) generally achieved the highest conversions, as they are more effective in stabilising the radical intermediate (Table 3-1, entries **2** and **3**, versus **4** and **5**; Figure S1).[16] 4-*tert*-butylbenzyl alcohol displays a lower than expected ***Conv***, which is presumably due to unfavourable steric effects (Table 3-1, entry **6**). A higher ***Conv*** was achieved for all substrates under continuous flow compared to batch, as a consequence of the higher throughput efficiency provided by the **PCP** environment. The slightly higher ***Sel*** metric of the batch photoreactor is a consequence of the lower ***Conv***. As discussed above (Figure 3.5), formation of the overoxidation product only becomes considerable once the concentration of the starting material decreases substantially, such that the oxidation of aldehyde begins to take place. Some variance in the ***M.B.*** between batch and flow was observed (average of 94% and 90%, respectively), which is most likely due to the volatility of the aldehyde, which can escape from the flow reactor via the gas output stream. Thus, in reality, ***Conv*** and ***Sel*** for the flow **PCP** system are likely higher than reported in Table 3-1, and system improvements are currently being made to increase the ***M.B*.**

Upon replacing the alcohol by a primary benzyl amine, a dibenzylic secondary (*E*)-imine was obtained as the major product (Scheme 3.2b). This resulted from the cascade condensation reaction between the primary aldimine intermediate with the starting material in the presence of **mpg-CN$_x$**.[14] Preliminary batch studies revealed that the oxidation of benzylic amines proceeds at a faster rate than that of benzylic alcohols – hence a lower value for τ was selected (60 min) for the continuous flow experiments. Analogous to the aerobic alcohol oxidations, an enhanced performance of the **PCP** in comparison to the batch photoreactor was recorded (Table 3-2). We observe that the **PCP** setup does not impede the condensation step following the initial amine oxidation, and thus highlights the versatility of the flow configuration to be able to accommodate and improve the reaction rates of various aerobic oxidation processes.

Table 3-2: Amine reaction scope under batch and flow conditions, featuring control experiments performed in flow, based on Scheme 3.2b.

Entry	Substrate[a]	Flow[b]		Batch[c]	
		Conv [d]	***Sel*** [e]	***Conv*** [d]	***Sel***
		[%]			
1	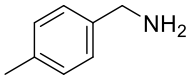	85	99	56	100
2	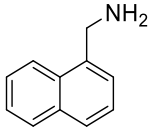	84	99	36	100
3	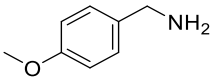	92	95	64	100
4	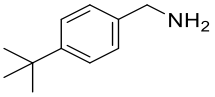	84	100	40	100
5	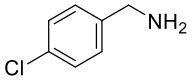	92	99	69	100
6	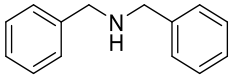	63	78	32	89
6.i	No air flow[f]	16	88	-	-
6.ii	No light	0.8	93	-	-

[a] General conditions: substrate concentration 75 mM in MeCN (CD_3CN in batch), blue LEDs (14.4 W at λ = 470 nm), T = 55 °C. Control flow experiments detailed as sub-entries within the table. [b] Flow conditions: τ = 60 min, $\dot{V}_{air}$ = 0.5 sccm. [c] Batch conditions: *reaction time* = 60 min, **mpg-CN_x** photocatalyst loading = 2 mg. [d] ***Conv*** calculated as per Table 3-1. [e] ***Sel*** is for the dibenzylic secondary (*E*)-imine; minor impurity due to presence of primary benzyl imine. [f] Residual O_2 (from ambient air) still present in the liquid feeds.

However, there was a discrepancy in the ***M.B.*** metric when comparing the primary amine oxidation in the **PCP** setup and in-batch. The ***M.B.*** for the primary amines in-flow was on average ~75% (Table 3-2, entries **1** – **5**), whereas a ***M.B.*** of ~98% was obtained in batch. Flow experiments using 1,3,5-trimethoxybenzene as a tracer molecule (which was added to the amine solution and pumped simultaneously into the **PCP**, but was unreactive towards light activated **mpg-CN_x**) gave complete ***M.B.*** for the tracer compound (DMSO was used as internal standard in this case). Secondary amines faced no such issue (Table 3-2, entry **6**) and a ***M.B.*** of 95% was achieved in-flow. This implied that a side-product from the reaction with the primary amine may

have deposited within the **PCP**, and hence could not be accounted for during downstream liquid analysis.

High concentrations of benzylic primary amines are known to react with aerobic CO_2 to form a carbamic acid/carbamate salt mixture, which consists of a white precipitate that is insoluble in a number of organic solvents.[17,18] We therefore propose that the mass imbalance could originate from the formation of a carbamic acid precipitate in the **PCP**. To verify this hypothesis, $^{13}CO_2$ was bubbled into a primary benzyl amine solution in MeCN (100 mM), which rapidly resulted in the formation of a white precipitate within the vial. An infrared spectrum of this solid revealed the appearance of a single sharp band at 3380 cm^{-1}, indicative of the loss of a primary amine. Characteristic peaks centred at 1650 cm^{-1} and 1620 cm^{-1}, which can be attributed to the asymmetric (C=O) stretch of the COOH moiety of the carbamic acid and the carboxylate anion, respectively, were also noted (Figure 3.7).[19] Furthermore, a strong peak at ~158 ppm was observed for the carbamic acid carbon atom in the ^{13}C NMR spectrum (Figure 3.8).[19] Finally, continuous flow experiments under alkaline conditions increased the ***M.B.*** by 12%, as the hydroxide ions facilitate hydrolysis of the carbamic acid/carbamate salt.[20]

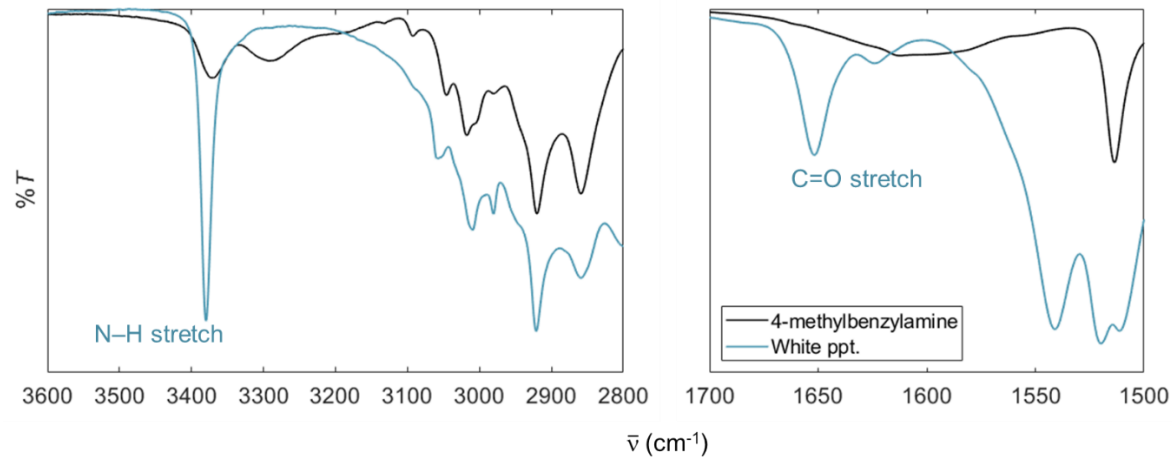

Figure 3.7: FTIR spectra of 4-methylbenzylamine, and the white precipitate formed upon bubbling a solution of 4-methylbenzylamine in MeCN with $^{13}CO_2$.

Our rational understanding of the flow reaction shown in Scheme 3.2b is that some degree of solvent evaporation occurs upon passing the solution through the heated zones of the **PCP**, causing the local concentration of amine to increase at such points. Here, the low pressure of CO_2 from the compressed air feed is sufficient to react with the locally concentrated starting material to yield the carbamic acid/carbamate salt.

Due to the insolubility of this mixture in MeCN, it precipitates from the solution and settles in the **PCP** during operation. This kind of reaction environment is not experienced within the batch reactor, and hence, could explain the difference in the ***M.B.*** metric. The **PCP** flow setup is therefore being investigated as a potential tool to explore other organic transformations, as it could potentially lead to a product distribution that differs from that obtained in a typical batch setup.

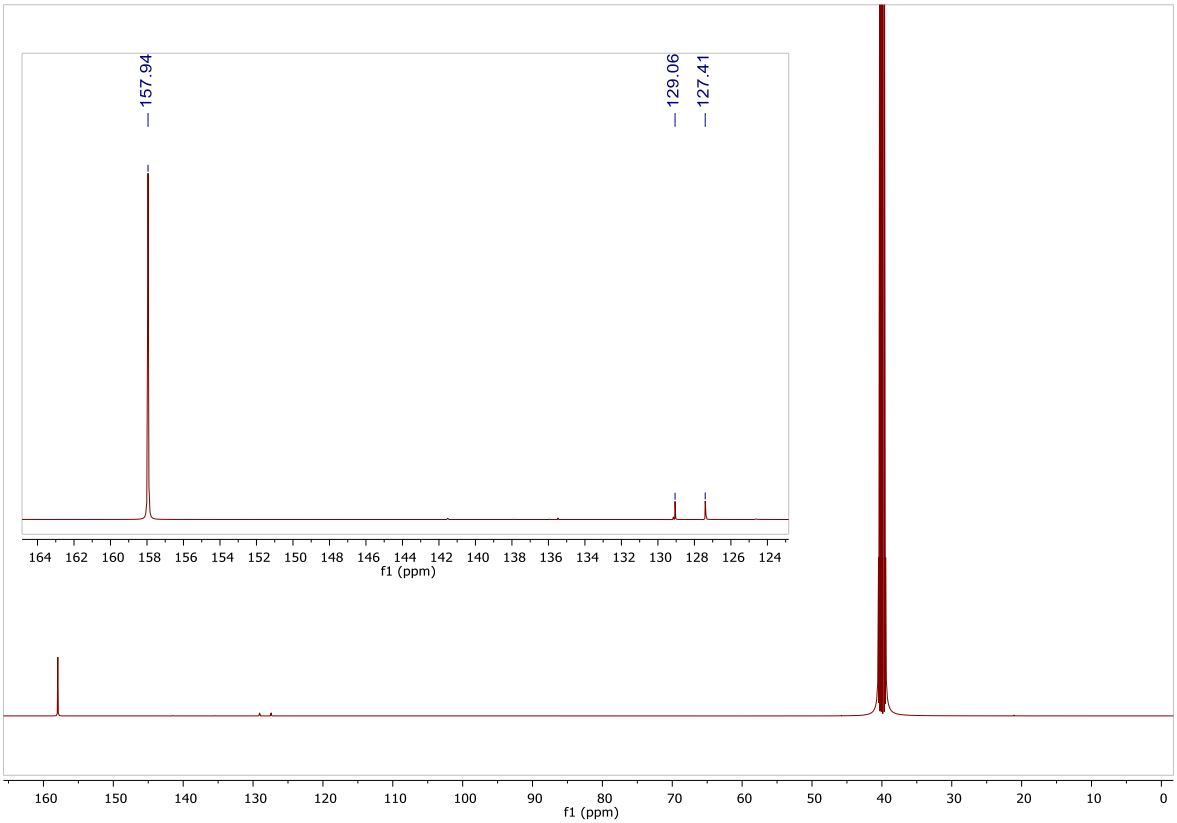

Figure 3.8: ^{13}C NMR (DMSO-d_6) spectroscopy of the white precipitate formed upon bubbling a solution of 4-methylbenzylamine in MeCN with $^{13}CO_2$.

3.3 Conclusions

In conclusion, we have developed a triphasic (gas–liquid–solid) packed column photoreactor featuring **mpg-CN$_x$**, to explore aerobic substrate oxidations and reactions in-flow under benign conditions. The impact of the morphology of the carbon nitride material within the **PCP** under a continuous flow environment was first investigated, and it was established that the mesoporosity plays a vital role with regards to the gas–liquid dynamics through the heterogeneous catalytic reactor. The alcohol and amine oxidation reactions presented herein demonstrated the versatility of the **mpg-CN$_x$**–based continuous flow system, along with its improved performance

(for the conversion of starting material) and practicality (in circumventing photocatalyst recovery) relative to a conventional batch photoreactor. Improvements vis-à-vis the performance were also achieved for this flow setup, in comparison to the prototype thin channel flow device described in Chapter 2. The low decrease in activity of the **PCP** over multiple flow cycles (~9% by the 25th flow experiment) further highlighted the facile reusability of the photocatalytic system. The overall low-cost of the setup, due to the lack of any precious-metal-containing components or expensive reagents, makes it an attractive choice for adopting as a potential tool in multistep organic flow synthesis.

This photocatalytic flow reactor can conduct oxidative transformations using more benign conditions when compared to previously reported **mpg-CN$_x$**–based batch photoreactors, which required temperatures and O_2 pressures in the range of 80–100 °C and 5–8 bar, respectively (c.f. Scheme 1.1 in Chapter 1).[13,14] The use of a well-controlled air feed, rather than high O_2 pressures, makes our technique more compatible with the safety restrictions surrounding the use of O_2 for industrial applications, making it an attractive option for carrying out sustainable substrate oxidations in flow. Efforts are now being placed to utilise the overall visible light activated **mpg-CN$_x$ PCP** setup to investigate the improvement in performance of other known aerobic reactions,[14,21,22] and to probe novel organic transformations under continuous flow operation.

3.4 Experimental Section

3.4.1 Materials

All chemicals purchased from commercial suppliers were of the highest available purity and used without further purification unless otherwise noted. Cyanamide, Ludox SM colloidal silica (40 wt.% dispersion in water), 4-methoxybenzyl alcohol, tetrabutylammonium hydroxide 30-hydrate, and $^{13}CO_2$ (> 99 atom % ^{13}C) were purchased from Sigma Aldrich. 4-Methylbenzyl alcohol, 4-*tert*-butylbenzyl alcohol, 1-naphthalenemethanol, and 1-naphthalenemethylamine were purchased from Alfa Aesar, and 4-chlorobenzyl alcohol, methyl 4-(hydroxymethyl)benzoate,

dibenzylamine, 4-methoxybenzylamine, 4-chlorobenzylamine, 4-methylbenzylamine, and 4-*tert*-butylbenzylamine from Acros Organics.

3.4.2 Physical Characterisation

^{1}H and ^{13}C NMR spectra were recorded on a Bruker AVIII HD+ console at 500 MHz, with a dual $^{13}C/^{1}H$ cryoprobe, at room temperature. FTIR (ATR) spectra were recorded on a Thermo Scientific Nicolet iS50 spectrometer. Nitrogen adsorption/desorption measurements were performed after degassing the samples at 150 °C for 20 h, using a Quantachrome Quadrasorb SI-MP porosimeter at 77.4 K. The TEM measurements were acquired using a double-corrected Jeol ARM200F, equipped with a cold field emission gun and a Gatan GIF Quantum. The acceleration voltage was set to 200 kV, and the emission was set to 10 µA to reduce beam damage. An objective aperture with a diameter of 60 µm was introduced into the beam to improve the contrast.

3.4.3 b-CN_x and mpg-CN_x fabrication

b-CN_x and **mpg-CN_x** were synthesised and characterised by FTIR, XRD, and UV-Vis as previously reported.[23] For **b-CN_x**, cyanamide (3 g) was placed in a crucible with a cover and heated at 550 °C with a heating rate of 2.3 °C min^{-1} for 4 h under an N_2 flow. For **mpg-CN_x,** cyanamide (3 g) was dissolved in a 40 wt.% dispersion of SiO_2 (7.5 g, Ludox SM) in water, with stirring at 60 °C overnight. The resultant transparent mixture was then heated at a rate of 2.3 °C min^{-1} over 4 h to reach a temperature of 550 °C, and then kept at this temperature for a further 4 h. The resulting brown-yellow powder was treated with 4 M NH_4HF_2 for 24 h in order to remove the silica template. The powders were then centrifuged at 9000 rpm and washed three times with distilled water and twice with ethanol. Finally, the powders were dried overnight at 70 °C under vacuum.

3.4.4 Photocatalytic Methods

Batch Setup

An organic substrate (0.045 mmol), **mpg-CN_x** (2 mg), CD_3CN (0.6 mL, 75 mM), and a small magnetic stirrer bar were transferred into an NMR tube, which in-turn functioned as the batch photoreactor. Since O_2 was required as the terminal electron acceptor,

the tubes were left open to atmosphere during the duration of the experiment. Photocatalytic batch experiments were carried out using a coiled blue LED setup (1 m, from Ledxon, λ = 470 nm) with a total power output of 14.4 W, to provide the samples with 360° irradiation. The temperature was maintained at 55 °C due to the heat produced by the LED setup. An initial ^{1}H NMR was recorded at time t = 0 h. The photoreaction was initiated, and a ^{1}H NMR spectrum was recorded at the end of the reaction following the addition of 0.1 mL of 1,3,5-trimethoxybenzene internal standard (IS) solution (200 mM, CD_3CN). All final products identified were found to be identical to previously reported characterisations.

Flow Setup

(i) PCP Preparation

A 3.5 wt.% **mpg-CN$_x$** mixture was prepared by gently grinding 100 mg of **mpg-CN$_x$** and 2.8 g of a 1:1 mixture of 212-300 µm and 250-500 µm diameter glass beads in an agate mortar,[1] followed by more vigorous stirring via a vortex generator for 30 s. One end of a 75 cm long FEP tube (3 mm o.d. × 2 mm i.d.) was plugged with Celite and filled approximately up to a height of 5 cm with 212-300 µm diameter glass beads. The photocatalyst containing mixture was packed into the tube, and the other end was then equipped with a cotton filter. The entry and exit point of the reactor were connected to 1/8” o.d. 1/4”-28 flat bottom flangeless fittings, for facile in-line connection. The volume of the photoreactor, V_r, was calculated using the difference in mass of the packed ‘dry’ reactor (m_{PCP}) and the mass of the packed reactor when filled with the solvent of choice ($m_{PCP\,+\,solv.}$) (Equation 3.1).

$$V_r = \frac{\Delta m}{\rho_{solv.}} = \frac{(m_{PCP+solv.} - m_{PCP})}{\rho_{solv.}} \qquad 3.1$$

where ρ_{solv} denotes the solvent density.

(ii) Assembly of Continuous Flow Test-rig

A schematic of the devised flow configuration is portrayed in Figure 3.1, and an actual image of the **mpg-CN$_x$** continuous flow test-rig is shown in Figure 3.9. The amount of air, and hence O_2, entering the flow photoreactor was controlled by means of the mass flow controller (MFC). The liquid feeds were housed in gas-tight syringes (Hamilton

1000 series, Luer-Lock termination), and were pumped into the reactor via syringe pumps (Legato 110 series). The liquid stream and gas stream met at the 4-port 3-way valve and generated a gas–liquid segmented (slug) flow prior to entering the **PCP**. PTFE tubing (1.6 mm o.d. × 1 mm i.d.) was used to connect the syringes to the 4-port 3-way valve, and from the valve to the **PCP** entrance point.

A back-pressure regulator (BPR) was not included in the finalised flow configuration, since the back-pressure generated by the packed column was found to be sufficient for the generation of the gas–liquid flow. The **PCP** was mounted onto a reflective support in a coiled fashion and was irradiated by means of a 360° blue LED setup (14.4 W at λ = 470 nm). The flow setup had two modes of injection: substrate, and pure solvent injection. The latter was required to purge out the reaction mixture following substrate injection. When conducting a typical flow experiment, 2.5 mL of the substrate solution (concentration in the range of 50 – 100 mM) was injected into the reactor, followed by 2.5 mL of pure MeCN.

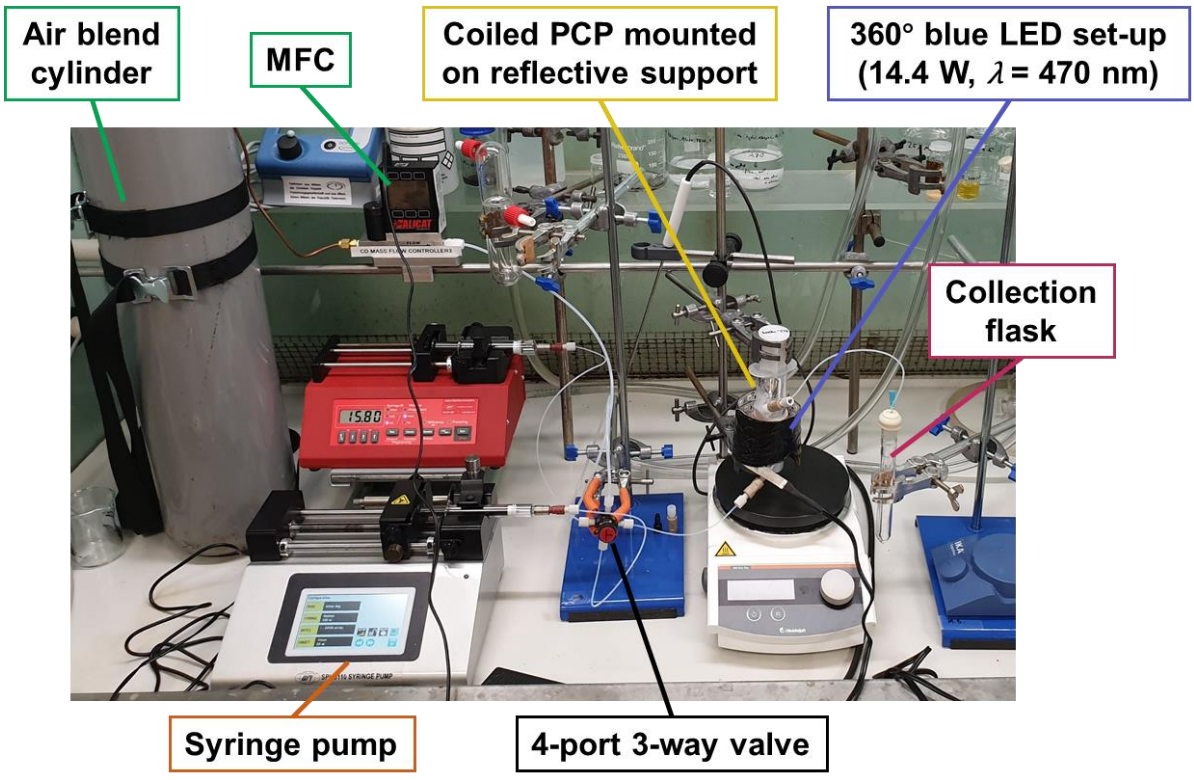

Figure 3.9: Actual image of the test-rig for triphasic photocatalytic experiments using the **PCP** design.

The substrate volume flow rate, $\dot{V}_{sub}$, set on the syringe pump was used to control the residence time of the reactant species inside the **PCP**, as the reactor volume was kept constant (Equation 3.2):

$$\tau = \frac{V_r}{\dot{V}_{sub}} \qquad 3.2$$

3.4.5 Product Analysis and Quantification

Acetonitrile Suppression ^{1}H NMR: Choice of Suppression Methodology and Experimental Parameters

All the experimental work was done on a Bruker AVIII HD+ console at 500 MHz, with a dual ^{13}C/^{1}H cryoprobe, controlled by Topspin 3.5 pl7.

The suppression methods utilising presaturation,[24] WATERGATE (w5),[25] and WATERGATE with excitation sculpting and a perfect echo scheme,[26] were investigated. WATERGATE with excitation sculpting and a perfect echo scheme was selected, as it provided a narrow irradiation bandwidth and produced "clean" spectra which were free from any artefacts that might prevent accurate peak integration.

The Bruker standard pulse sequence for excitation sculpting was modified to add ^{13}C decoupling (utilising the Bruker standard 'garp.p31' sequence) to remove the residual sidebands of acetonitrile. A range of samples were run at varying concentrations to test the accuracy and reproducibility of the method. An appropriate relaxation delay of 60 s was chosen, after observing a signal maximum at ~30 s for the test samples.

To find an appropriate suppression bandwidth, the carbon decoupling power levels were set to zero so that the ^{13}C satellite peaks could be observed. The pulse programme contains a 'cnst12' parameter which the user can adjust. This is used as a basis to calculate the power of the shaped pulse and hence, the width of the suppression region. The value of cnst12 was progressively increased from 1 to 16 ms, until the ^{13}C satellites could first be seen; their intensity was then maximised. On the instrument used, a value of 9 ms was found to be optimum – i.e. the MeCN peak was suppressed effectively, the ^{13}C satellites were visible (proving the irradiation is specific to a narrow region), and minimal distortions to the rest of the spectrum were induced.

Past 9 ms, distortions due to proton-proton coupling become apparent, the intensity of which depends on the strength of the coupling.

For the analytical routine, the primary excitation pulse of 14 W was applied for about 10.2 µs. The shaped 'sinc' suppression pulse of 9 ms used around 70.32 µW, as the pulse tended to vary slightly from one sample to the next. A relaxation delay of 60 s was used between each scan. The gradient pulses were set to the pulse-programme default of 31%, 11% and 5% of the maximum strength of the probe (which corresponds to 6.02 G cm^{-1} A^{-1} for the probe used). ^{13}C decoupling used 0.967 W for 160 µs with the 'garp.p31' decoupling scheme. An exemplary ^{1}H NMR spectrum depicting the output before and after application of the devised acetonitrile suppression routine is presented in Figure 3.10.

Finally, to test the protocol, calibration curves were produced using known concentrations of three chosen substrates (1-naphthalenemethanol, 4-methylbenzylalcohol, and 4-methylbenzylamine). The curves were prepared by mixing a 600 µL aliquot of the substrate with 100 µL of the IS solution (1,3,5-trimethoxybenzene prepared in CD_3CN, 100 mM), and recording the acetonitrile suppression ^{1}H NMR for each sample using the optimised routine.

The *normalised relative area* ($\tilde{A}_{rel}$), as defined in Equation 3.3 below, was determined for each dilution, of each substrate:

$$\text{Normalised relative area: } \tilde{A}_{rel} = \frac{A_{Sub}}{A_{IS}} \cdot \frac{N_{IS}}{N_{Sub}} \qquad 3.3$$

where N_{IS} and N_{Sub} denote the number of H atoms associated with the IS peak and the substrate peak, respectively, whilst A_{IS} and A_{Sub} represent the integrated peak areas of the former and latter.

The average of this parameter was calculated and plotted against the substrate concentration to yield a standard curve (Figure 3.11). The quantitative technique was validated by the linear relationship between the normalised parameter and the substrate concentration ($R^2 = 0.999$). This meant that the technique could be used on test samples, to determine the number of moles of species *i* within the reaction mixture.

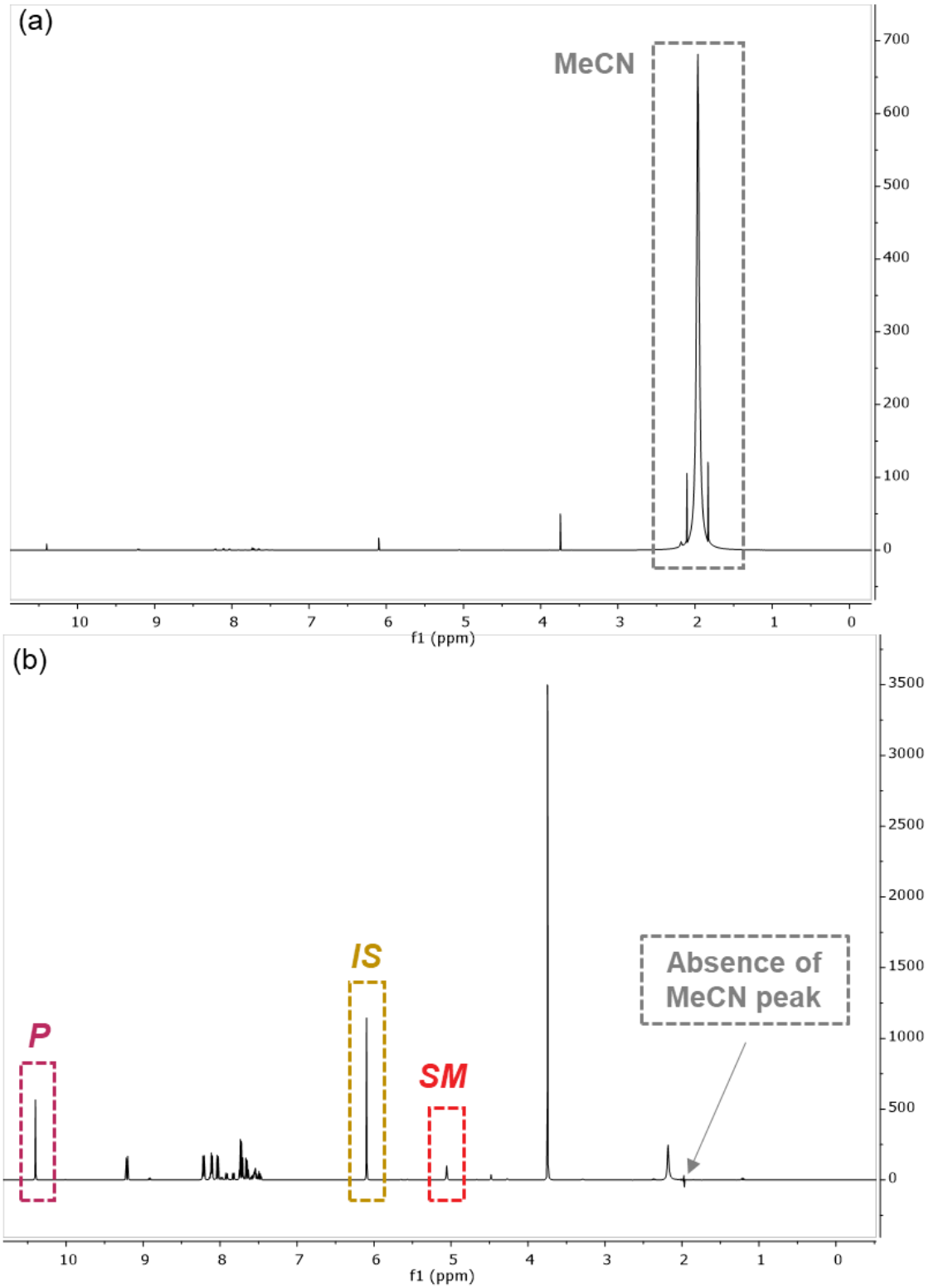

Figure 3.10: ^{1}H NMR spectrum of crude reaction mixture exiting the **PCP** setup, before (a) and after (b) the application of the MeCN suppression pulse programme (experimental conditions: 1-naphthalenemethanol concentration = 75 mM (in MeCN), blue LEDs (14.4 W at λ = 470 nm), T = 55 °C, τ = 90 min, $\dot{V}_{air}$ = 0.5 sccm). In figure, representative peaks denoting starting material (*SM*), internal standard (*IS*), and product (*P*) are highlighted. IS solution: 1,3,5-trimethoxybenzene prepared in CD_3CN, 100 mM.

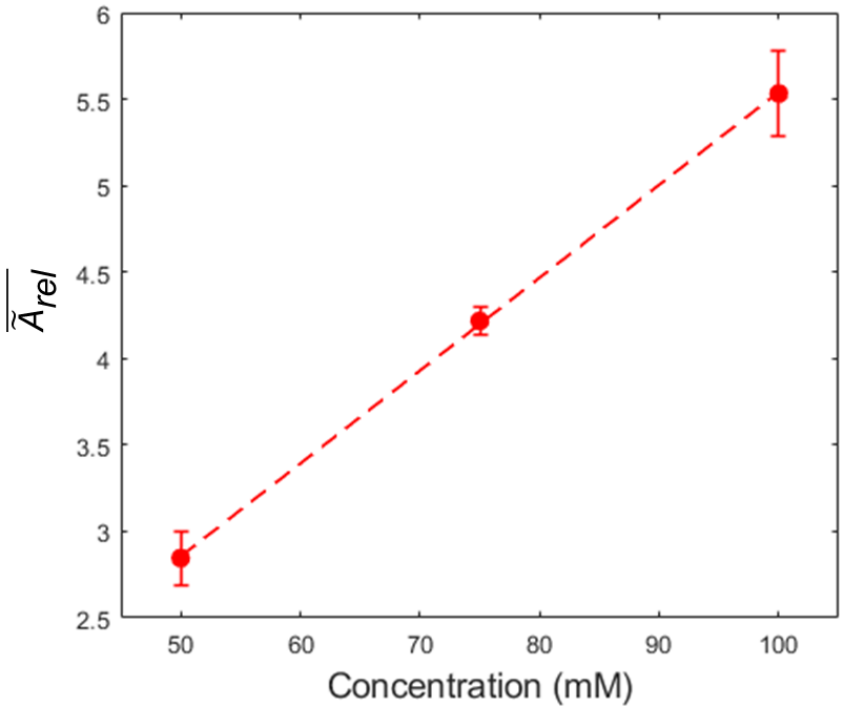

Figure 3.11: Normalised standard curve compiled using 1-naphthalenemethanol, 4-methylbenzylalcohol, and 4-methylbenzylamine as substrate materials (1,3,5-trimethoxybenzene as IS). The plot portrays the linear response between the average normalized relative area of the integrated ^{1}H NMR peaks (obtained via the optimised acetonitrile suppression pulse programme) and the substrate concentration.

Hence, for a reaction mixture collected in the receiver flask of the flow test-rig, a 600 µL aliquot was spiked with 100 µL of the aforementioned IS solution, and then analysed via the acetonitrile suppression pulse programme. The total number of moles of species *i*, n_i, was then calculated via Equation 3.4.

$$n_i = \frac{A_i}{A_{IS}} \cdot \frac{N_{IS}}{N_i} \cdot \frac{V_{rxn}}{V_{aliquot}} \cdot n_{IS} \qquad 3.4$$

V_{rxn} and $V_{aliquot}$ correspond to the volume of the reaction mixture collected in the receiver flask, and the volume of the aliquot taken for analysis respectively. N_{IS} and N_i denote the number of H atoms associated with the IS peak and the species peak of interest, respectively, whilst A_{IS} and A_i represent the integrated peak areas of the former and latter. n_{IS} denotes the number of moles of IS added to the reaction mixture aliquot. Hence the metrics needed to understand the chemistry within the **PCP** and the performance of the experimental setup (i.e. *starting material conversion*, *product selectivity*, and *mass balance*) could be determined accordingly. All final products identified via the acetonitrile suppression ^{1}H NMR routine were found to be identical to previously reported characterisations.

The ***M.B.*** metric is needed in order to evaluate the moles of species exiting the reactor, relative to the amount injected into the system. This parameter was determined through Equation 3.5.

$$\boldsymbol{M.B.} = \frac{n_{out}}{n_{in}} = \frac{\sum_i \left\{ \chi_i \int_{t_{rxn}} \dot{n}_i \, \mathrm{d}t \right\}}{n_{in}}; \text{ where } \dot{n} = \lim_{\Delta t \to 0} \frac{\Delta n}{\Delta t} = \frac{\mathrm{d}n}{\mathrm{d}t} \qquad 3.5$$

n_{out} is the total number of moles exiting the reactor. The mass balance is thus quantified by comparing this value to the number of moles of substrate, n_{in}, injected into the reactor. $\dot{n}_i$ is the molar flow rate of species *i* out of the reactor; once integrated over the complete time course of the flow reaction, t_{rxn}, it yields the total number of moles for species *i*. Summing over all detectable species *i* provides a value for the total number of moles exiting the reactor.

3.5 References

1 M. Woźnica, N. Chaoui, S. Taabache and S. Blechert, *Chem. Eur. J.*, 2014, **20**, 14624–14628.

2 B. Pieber, M. Shalom, M. Antonietti, P. H. Seeberger and K. Gilmore, *Angew. Chem. Int. Ed.*, 2018, **57**, 9976–9979.

3 C. G. Frost and L. Mutton, *Green Chem.*, 2010, **12**, 1687–1703.

4 R. Munirathinam, J. Huskens and W. Verboom, *Adv. Synth. Catal.*, 2015, **357**, 1093–1123.

5 Z. Guo, B. Liu, Q. Zhang, W. Deng, Y. Wang and Y. Yang, *Chem. Soc. Rev.*, 2014, **43**, 3480.

6 A. Gavriilidis, A. Constantinou, K. Hellgardt, K. K. (Mimi) Hii, G. J. Hutchings, G. L. Brett, S. Kuhn and S. P. Marsden, *React. Chem. Eng.*, 2016, **1**, 595–612.

7 S. Caron, R. W. Dugger, S. G. Ruggeri, J. A. Ragan and D. H. Brown Ripin, *Chem. Rev.*, 2006, **106**, 2943–2989.

8 K. Marui, A. Nomoto, H. Akashi and A. Ogawa, *Synth.*, 2016, **48**, 31–42.

9 G. Wu, E. Cao, P. Ellis, A. Constantinou, S. Kuhn and A. Gavriilidis, *Chem. Eng. J.*, 2018, 1–9.

10 N. Emmanuel, C. Mendoza, M. Winter, C. R. Horn, A. Vizza, L. Dreesen, B. Heinrichs and J. M. Monbaliu, *Org. Process Res. Dev.*, 2017, **21**, 1435–1438.

11 K. Liu, S. Jiang, L. Lu, L.-L. Tang, S.-S. Tang, H.-S. Tang, Z. Tang, W. He and

X. Xu, *Green Chem.*, 2018, **20**, 3038–3043.

12 W. Schilling, D. Riemer, Y. Zhang, N. Hatami and S. Das, *ACS Catal.*, 2018, **8**, 5425–5430.

13 F. Su, S. C. Mathew, G. Lipner, X. Fu, M. Antonietti, S. Blechert and X. Wang, *J. Am. Chem. Soc.*, 2010, **132**, 16299–16301.

14 F. Su, S. C. Mathew, L. Möhlmann, M. Antonietti, X. Wang and S. Blechert, *Angew. Chem. Int. Ed.*, 2011, **50**, 657–660.

15 X. H. Li, X. Wang and M. Antonietti, *ACS Catal.*, 2012, **2**, 2082–2086.

16 D. H. McDaniel and H. C. Brown, *J. Org. Chem.*, 1958, **23**, 420–427.

17 A. Patchornik and Y. Shalitin, *Anal. Chem.*, 1961, **33**, 1887–1889.

18 G. Richner, G. Puxty, A. Carnal, W. Conway, M. Maeder and P. Pearson, *Chem. Eng. J.*, 2015, **264**, 230–240.

19 A. H. Liu, R. Ma, C. Song, Z. Z. Yang, A. Yu, Y. Cai, L. N. He, Y. N. Zhao, B. Yu and Q. W. Song, *Angew. Chem. Int. Ed.*, 2012, **51**, 11306–11310.

20 L. W. Dittert and T. Higuchi, *J. Pharm. Sci.*, 1963, **52**, 852–857.

21 T. Song, B. Zhou, G.-W. Peng, Q.-B. Zhang, L.-Z. Wu, Q. Liu and Y. Wang, *Chem. Eur. J.*, 2014, **20**, 678–682.

22 Y. Zhao and M. Antonietti, *Angew. Chem. Int. Ed.*, 2017, **56**, 9336–9340.

23 X. Wang, K. Maeda, X. Chen, K. Takanabe, K. Domen, Y. Hou, X. Fu and M. Antonietti, *J. Am. Chem. Soc.*, 2009, **131**, 1680–1681.

24 H. D.I, *J. Magn. Reson.*, 1976, **21**, 337–347.

25 M. Liu, X. A. Mao, C. Ye, H. Huang, J. K. Nicholson and J. C. Lindon, *J. Magn. Reson.*, 1998, **132**, 125–129.

26 R. W. Adams, C. M. Holroyd, J. A. Aguilar, M. Nilsson and G. A. Morris, *Chem. Commun.*, 2013, **49**, 358–360.

Chapter 4

Precious-metal-free, Molecular Hybrid Electrolyser for Alcohol Oxidation Coupled to CO_2-to-syngas Conversion

The contents of this chapter have been published in a peer-reviewed article: Angew. Chem. Int. Ed. 10.1002/anie.202002680*. Results presented were obtained solely by the author of this thesis, with contributions from others as outlined here: Souvik Roy fabricated the* ***CoPc****-based electrodes and shared the coupled electrolyser experiments with the author. Kaltum Abdiaziz carried out the FE-EPR measurements at Imperial College and the University of Oxford. Andreas Wagner is acknowledged for setting up the continuous flow GC instrument.*

4.1 Introduction

Renewable electrosynthesis of fuels is being pursued as a potential solution to the intermittency of energy sources such as wind and solar,[1] and, as highlighted in Chapter 1, better integration of the energy and chemical sectors will be crucial in allowing this transition to take place. Conventional electrolysers for fuel-generating reductive chemistry, such as HER or CO_2R, are typically coupled to the OER at the anode.[2,3] However, this anodic half-reaction exhibits a two-fold problem; the first point is related to the sluggish kinetics of the four-electron transfer process of the OER, which requires a high overpotential and consequently, a high energy input to drive water oxidation.[4,5] Secondly, the product from this 'energy-intensive' process, O_2, has a low commercial value and therefore reflects poorly on the technoeconomic benefits of the electrolyser approach. Indeed, this research directive is spurring interest in the field to couple more synthetically attractive and facile organic electrooxidation chemistry, such as alcohol oxidation (AlcOx), to fuel-generating reductive chemistry, primarily HER and CO_2R.[6–12] Bringing down the energy requirements of the overall

electrolyser, and also providing a value-added product at the anode, could potentially be key to promoting the broader adoption and application of renewable electricity to drive such electrocatalytic processes. However, as highlighted in Section 1.5.1 of Chapter 1, there is much work to be done in constructing a system that is comprised of earth-abundant components, and that can effectively oxidise a variety of cheap and abundant alcohol substrates.

In this study, we first fabricate a new anodic assembly, featuring a silatrane-modified TEMPO electrocatalyst (henceforth denoted as **STEMPO**) covalently immobilised on a mesoporous indium tin oxide (*meso*ITO) scaffold (*meso*ITO|**STEMPO**), for the efficient oxidation of a wide range of alcohols under mild conditions. The silatrane group appeared to satisfy the necessary criteria for it to be considered a suitable anchor for immobilising the TEMPO moiety onto a MO-based electrode (c.f. Section 1.5.4). Reports in the literature suggest that the silatrane anchor hydrolyses on the MO surface to form strong, water-stable, siloxane surface bonds which are resistant to desorption over a broad pH range ($2 < pH < 11$).[13] The silicon atom in a silatrane cage is less susceptible to nucleophilic attack than silicon in the open-chain analogue (such as in trialkoxysilane) and thus, silatranes are known to be relatively unreactive during a synthetic procedure, allowing them to be dissolved in aqueous solutions and even purified by column chromatography.[14] Trialkoxysilanes on the other hand, are prone to silane polymerisation, which can easily complicate and interfere with the synthesis of the desired compound. The enhanced stability offered by the silatrane cage is due to both the cyclic nature of the molecule and the coordination of nitrogen's lone-pair of electrons to the silicon.[15,16] This interaction results in the formation of a trans-annular dative bond, thereby producing an electron-rich pentacoordinate silicon species, as depicted in Scheme 4.1.

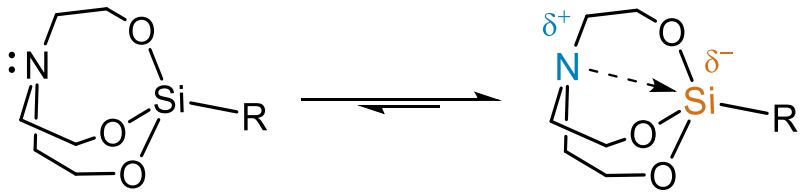

Scheme 4.1: Trans-annular dative bonding within the silatrane cage.

The second aspect of this study involves the integration of the hybrid anodic assembly within a coupled electrolyser. Conversion of CO_2-to-syngas as the cathodic half-reaction in the electrolyser was deemed as an attractive strategy to utilise the electrons

from alcohol oxidation by *meso*ITO|**STEMPO**. To facilitate a cost-efficient redox cycle, use of robust, earth-abundant catalysts for selective CO_2R is essential. While many 3d transition metal-based molecular catalysts have been developed over the years,[17] cobalt phthalocyanine (**CoPc**) has emerged as one of the most promising catalysts for CO_2-to-CO reduction. This is primarily due to its enhanced performance upon immobilisation onto polymers and carbon-based electrodes, particularly with regards to the improved selectivity to produce CO in pure aqueous conditions, in addition to the fact that it lacks a precious-metal centre and hence, has an appealingly low cost.[18–21] In the coupled electrolyser, we therefore employed a **CoPc**-based electrocatalyst polymerised onto carbon nanotubes (CNT) to form the CNT-polymeric **CoPc** composite (CNT-**CoPPc**; where **CoPPc** denotes *polymeric cobalt phthalocyanine*).[22] This was then deposited onto porous carbon paper (CP) to yield the cathode assembly, henceforth denoted as CP|CNT-**CoPPc** (Figure 4.1), which catalyses the electrochemical reduction of CO_2 to syngas, with a $CO:H_2$ ratio that is dependent on the applied potential.[22,23] The constructed device is thus the first report of a fully molecular, precious-metal-free, hybrid electrolyser for coupled alcohol oxidation and CO_2-to-syngas conversion. A concept illustration of the AlcOx–CO_2R electrolyser, along with the chemical structures of the molecular catalysts involved, is depicted in Figure 4.1.

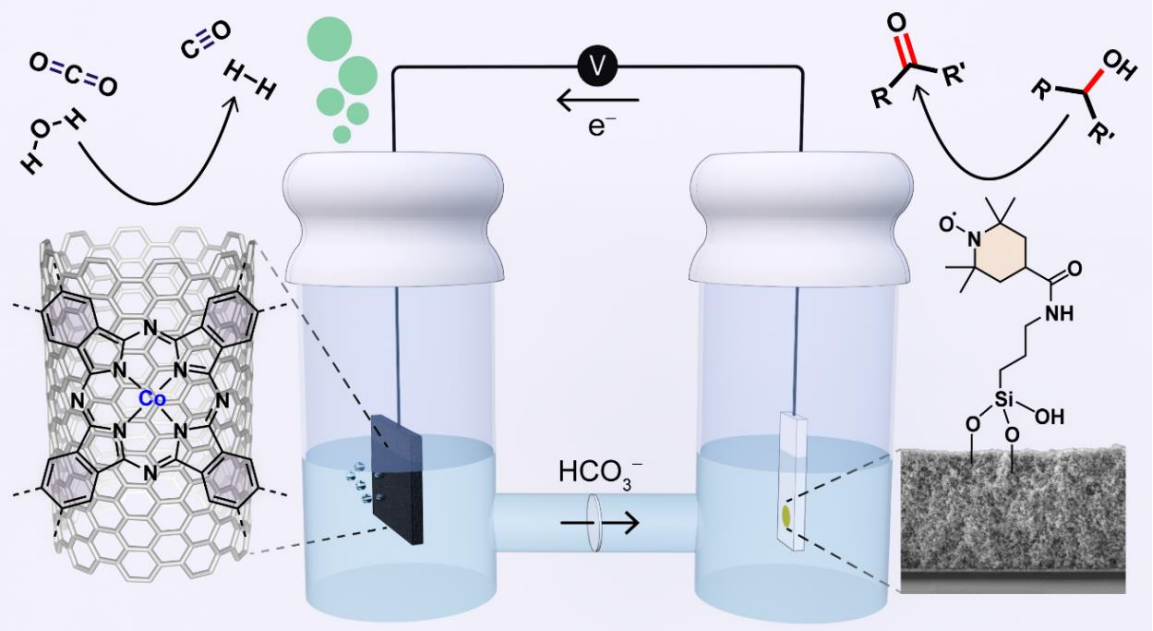

Figure 4.1: Coupled AlcOx–CO_2R electrolyser. The setup features a *meso*ITO|**STEMPO** anode (right-hand compartment) and a CP|CNT-**CoPPc** cathode. An SEM cross-section image of the *meso*ITO electrode is shown on the right (film thickness ~4.5 µm).

To facilitate the presentation of the results, this chapter is divided into three parts. The first of which discusses the synthesis of **STEMPO**, and the subsequent attempts to activate this compound towards surface hydrolysation, and therefore immobilisation, on a *meso*ITO surface. This is followed by an overview of the physical and electrochemical properties of the hybrid anode, assembled under *optimised* conditions, along with a description of its catalytic capabilities towards substrate (alcohol) oxidation. Finally, the integration of this hybrid anode with the CP|CNT-**CoPPc** cathode, for coupled alcohol oxidation and CO_2R, will be presented.

4.2 Results and Discussion

4.2.1 STEMPO Synthesis and Electrode Assembly

STEMPO was synthesised in good yield by reacting the acyl chloride of 4-carboxy-TEMPO with 3-aminopropylsilatrane. The synthetic procedure and corresponding characterisation (high-resolution mass spectrometry, infrared spectroscopy and elemental analysis) are provided in the Experimental Section 4.4. The ATR-FTIR spectra of **STEMPO** (Figure 4.2) showed intense bands at 1456 cm^{-1} for $\delta(CH_2)$ groups, while bands at 1646 and 1547 cm^{-1} were attributed to the secondary amide group. Marker bands of the silatrane cage from the ν(C-O) and ν(Si-O) were also observed at 1178 cm^{-1} and from 1130 to 1080 cm^{-1}, respectively.[24]

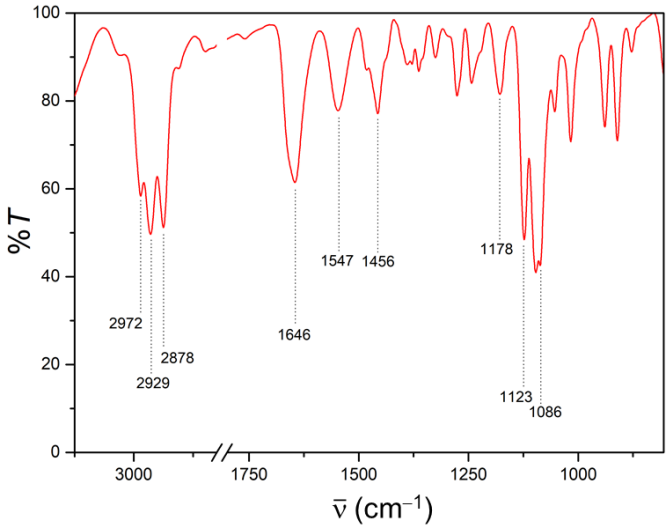

Figure 4.2: ATR-FTIR spectrum for **STEMPO**.

Although the relative stability of the silatranes in comparison to the non-caged silane analogues has been clearly described in the literature, the conditions required to activate the silatrane in order to react with the MO surface, such as TiO_2 or ITO, are not completely well-understood. Recent works regarding the modification of dyes and catalysts for photoelectrochemical and electrochemical applications, tend to immobilise silatrane-functionalised inorganic compounds by heating a solution of the latter in the presence of the MO.[24–27] However, the conditions required to catalyse or facilitate this hydrolysation process (such as the temperature, incubation time, and solvent) are far from standardised, and seem to differ from one system to the next.

Initial attempts to assemble the *meso*ITO|**STEMPO** anode involved incubating the *meso*ITO electrode (film thickness ~4.5 µm, Figure 4.3) in a **STEMPO** solution (2 mM) in anhydrous acetonitrile (MeCN), and heating to 70 °C under a nitrogen atmosphere for a duration of 6 h. However, this did not result in any significant loading of the **STEMPO** species, as evidenced by the unstable redox couple observed on the multi-scan cycle voltammogram (CV) measurement (Figure 4.4). Variants of this method, by increasing the temperature to 100 °C, and the incubation time to 24 h, yielded similarly poor results.

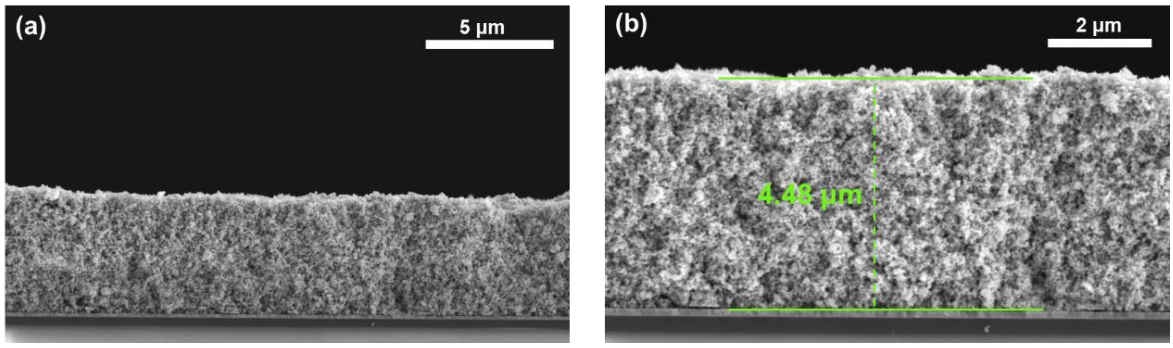

Figure 4.3: Scanning electron microscopy (SEM) cross-section image of the *meso*ITO electrode, at (a) 10.0 kx magnification, and (b) 20.0 kx magnification.

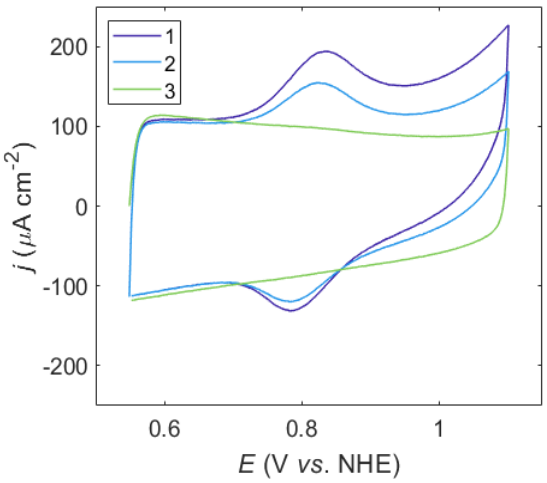

Figure 4.4: CV for *meso*ITO|**STEMPO**, assembled in anhydrous MeCN solvent (70 °C, N_2 overpressure, 6 h). *Conditions*: pH 8 aq. HCO_3^-/CO_3^{2-} (0.2 M), ν = 50 mV s^{-1}, N_2 (the legend denotes scan number).

It has recently been reported that the addition of a *hydrolysing agent*, comprised of a mixture of acetic acid (AcOH) and water in ethanol, accelerated the cleavage of the silatrane cage on a glass surface.[28] This approach was used as a basis to devise a study to probe the conditions required to facilitate surface immobilisation of the **STEMPO** compound onto the *meso*ITO surface. Three anhydrous organic solvents were initially chosen to begin the investigation: ethanol (polar and protic), MeCN (polar and aprotic), and toluene (non-polar and aprotic). Solutions of each (2 mM **STEMPO**, 2.8 mL), containing 0.2% v/v AcOH, were prepared, and the *meso*ITO electrodes were submerged in the solution in a capped vial, and heated at 70 °C under a N_2 overpressure for a duration of 6 h.

Multi-scan CV measurements were used to analyse and assess the effect of the incubation conditions on the surface coverage/loading of **STEMPO** ($\Gamma_{\mathbf{STEMPO}}$), wherein the latter was determined through the integration of the oxidation wave in the CV scan (Equation 4.1):

$$\Gamma_{\mathbf{STEMPO}} = \frac{Q}{zFA_{anode}} \qquad 4.1$$

where Q is the total integrated charge, z is the number of electrons involved in the oxidation of the nitroxyl radical to the oxoammonium cation (i.e. z = 1), F is the Faraday constant, and A_{anode} is the geometrical area of the anode (0.25 cm^2). Plotting $\Gamma_{\mathbf{STEMPO}}$ as a function of the scan number in the multi-CV scan revealed that MeCN offered better stability in comparison to ethanol and toluene (Figure 4.5), and hence was the

solvent of choice for further optimisation. The combined effect of the AcOH and H_2O was then probed by varying the AcOH/H_2O ratio, and heating in an analogous manner to as previously described, until the **STEMPO** surface loading was both maximal, and stable over scan number (Figure 4.6). These two criteria were best satisfied by the '2% v/v AcOH and 1% v/v H_2O' combination in MeCN, and thus, all further *meso*ITO|**STEMPO** electrodes were assembled using these 'optimised' conditions (*note*: the measured CVs used to produce the plots in Figure 4.5 and Figure 4.6 are presented in Appendix A; Figure A.1 and Figure A.2, respectively).

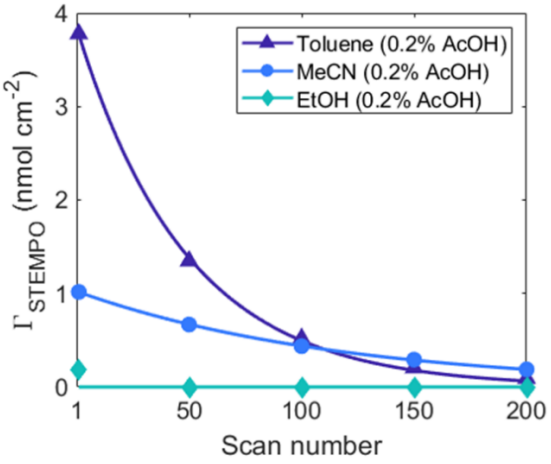

Figure 4.5: Γ_{STEMPO} *vs.* scan number; effect of solvent on *meso*ITO|**STEMPO** assembly. The data points were fitted to a mono-exponential decay.

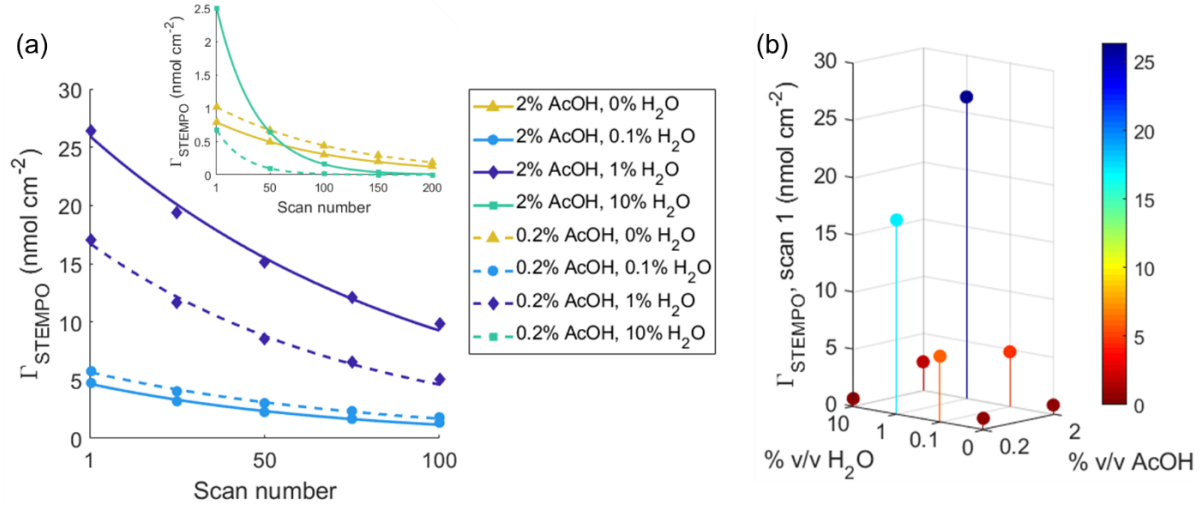

Figure 4.6: Combined effect of AcOH and H_2O concentration on Γ_{STEMPO}; (a) Γ_{STEMPO} *vs.* scan number (data points fitted to a mono-exponential decay), and (b) Γ_{STEMPO} for scan 1, as a function of % v/v AcOH and % v/v H_2O.

4.2.2 Hybrid Anode Characterisation and Catalytic Performance

Hybrid Anode Characterisation

When *meso*ITO|**STEMPO** electrodes were assembled under optimised conditions, $\Gamma_{\mathbf{STEMPO}}$ was typically found to be equal to 20–25 nmol cm^{-2}, which is in the expected range for these nanostructured ITO surfaces.[24,29,30] X-ray photoelectron spectroscopy (XPS) showed binding signals in the Si_{2p} and N_{1s} regions (Figure 4.7), where the Si_{2p} signal corresponds well with XPS reference spectra for the siloxane-bearing group.[31]

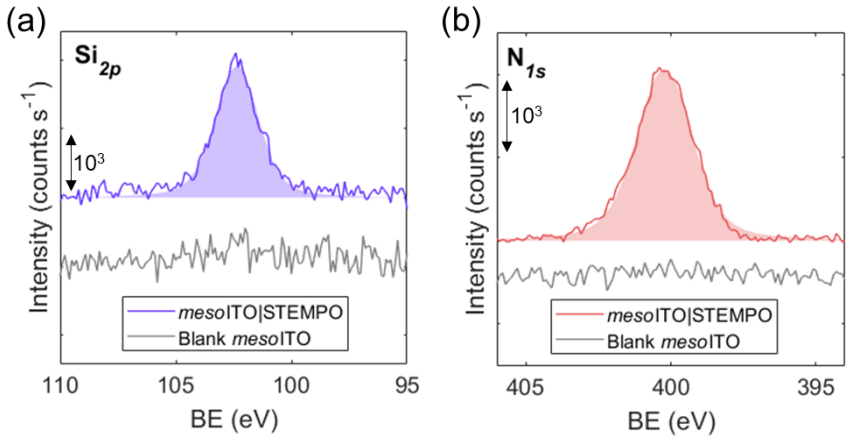

Figure 4.7: XPS spectra of freshly prepared *meso*ITO|**STEMPO** under optimised conditions, for (a) Si_{2p} and (b) N_{1s} regions. Respective spectra for the blank electrode are also shown.

A multi-scan cyclic voltammogram of the *meso*ITO|**STEMPO** electrode assembled under optimised conditions (Figure 4.8), reveals a reversible redox wave at $E_{1/2}$ = 0.83 V *vs.* NHE corresponding to the nitroxide/oxoammonium species, and is only slightly more positive than that of diffusional TEMPO ($E_{1/2}$ = 0.74 V *vs.* NHE, Figure 4.9a). The full width at half-maximum for *meso*ITO|**STEMPO**, measured at low scan rates (10 mV s^{-1}), is 116 mV (Figure 4.9b), slightly broader than the theoretically predicted value of around 90 mV for a 1 e$^-$ process in an ideally adsorbed system (at 25 °C).[32] This could be attributed to multilayer formation,[33,34] stemming from the cross-polymerisation of Si-O-Si bonds between adjacent anchoring units in the mesoporous scaffold.

A deeper analysis of the electron-transfer dynamics of the *meso*ITO|**STEMPO** system was inferred using the Laviron method,[35] which relies on the change in the peak potential (ΔE_p) with scan rate (ν). The resultant trumpet plot for the *meso*ITO|**STEMPO**

assembly is portrayed in Figure 4.9c. The intercepts of the linear regions of the plot can be used to deduce the critical scan rate (ν_c) and the apparent electron transfer rate constant (k_{app}) for the system (see Calculations Section 4.5 for further details regarding the necessary equations). Values for ν_c and k_{app} were determined to be equal to 72.2 ± 1.7 mV s^{-1} and 0.679 ± 0.018 s^{-1}, respectively. The rate of electron transfer appears to be sluggish (hence the low value for ν_c) but is comparable with other covalently linked redox species described in the literature.[36] The linear relationship between the peak current (i_p) and ν, for $\nu < \nu_c$ (Figure 4.9d) is characteristic for a surface-immobilised redox entity.[32] Figure 4.10 depicts the CVs measured over the range of scan rates (as required to conduct the Laviron analysis), so as to highlight the change in the peak-to-peak separation for the **STEMPO** redox wave as the applied scan rate exceeds ν_c.

The pH stability of the *meso*ITO|**STEMPO** assembly was investigated using the multi-scan CV approach, whereby the electrode was subjected to several redox cycles in solutions of differing pH (Figure 4.11; measured CVs presented in Figure A.3). Very good stability was obtained after 200 scans at pH 7 and 8, and the decay curve only began to be more severe at pH 10. These results were a promising indication that the electrode assembly is well suited to operate under the basic conditions which facilitate the TEMPO catalytic cycle.

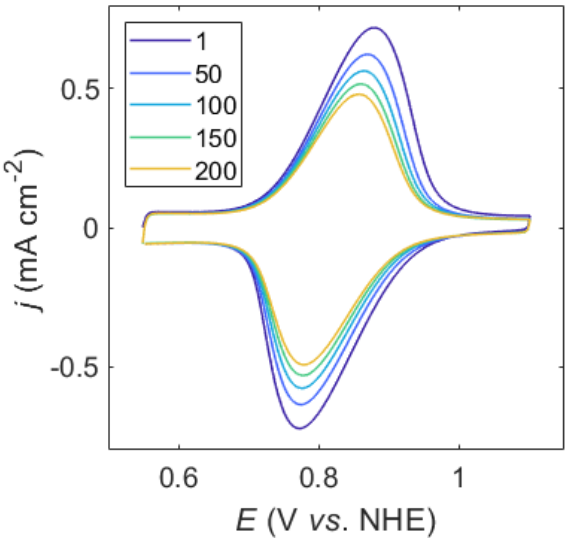

Figure 4.8: Multi-scan CV for optimised *meso*ITO|**STEMPO** assembly. *Conditions*: pH 8 aq. HCO_3^-/CO_3^{2-} (0.2 M), ν = 50 mV s^{-1}, N_2 (the legend denotes scan number).

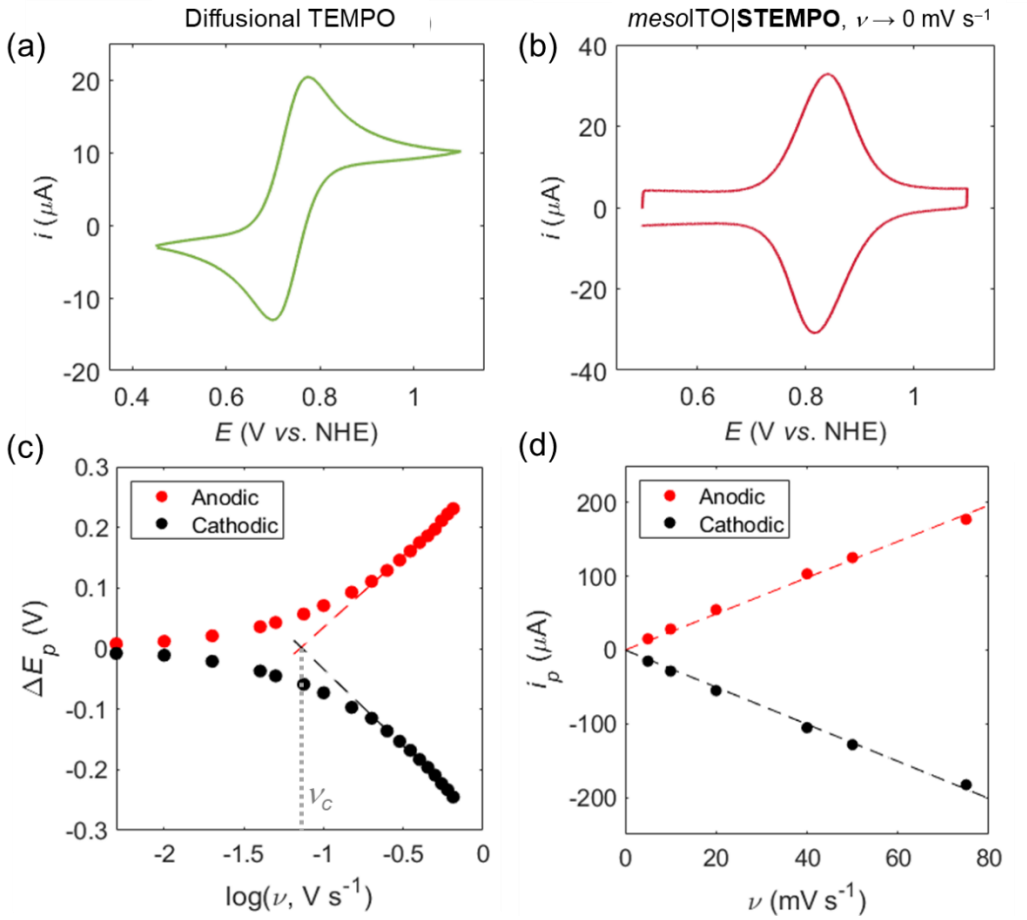

Figure 4.9: Further electrochemical characterisation of *meso*ITO|**STEMPO**. CVs recorded at low scan rate (10 mV s^{-1}) for (a) diffusional TEMPO (5 mM, glassy carbon working electrode), and (b) *meso*ITO|**STEMPO**. (c) Trumpet plot deduced for *meso*ITO|**STEMPO** from the variable scan rate CV measurements, (d) i_p *vs.* ν plot, for $\nu < \nu_c$. *Conditions*: pH 8 aq. HCO_3^- /CO_3^{2-} (0.5 M), N_2.

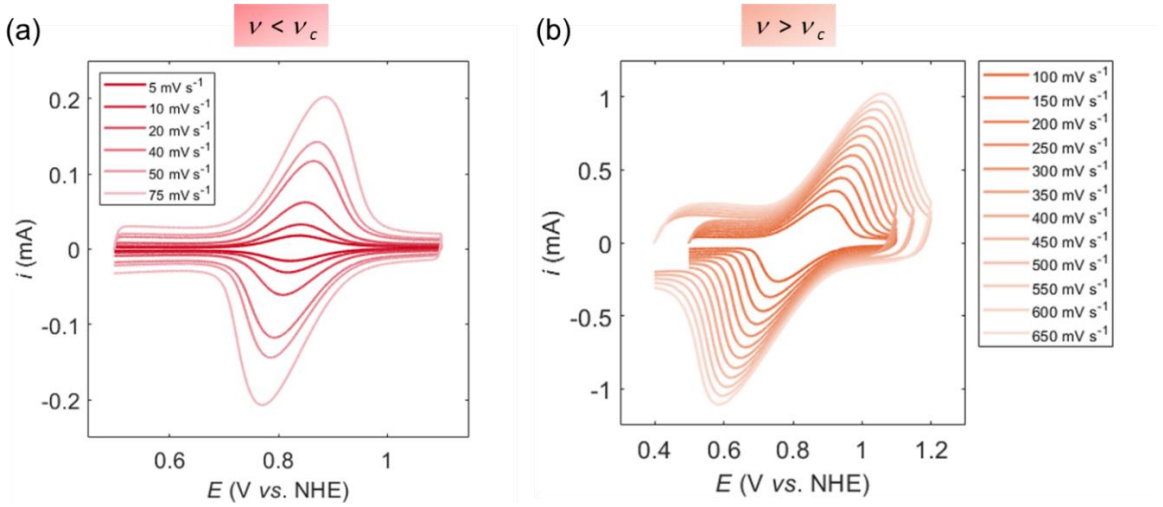

Figure 4.10: Variable scan rate CV measurements, (a) below, and (b) above the critical scan rate. The variable scan rate assessment is required to be able to carry out the Laviron analysis and determine electron-transfer parameters for the *meso*ITO|**STEMPO** system.

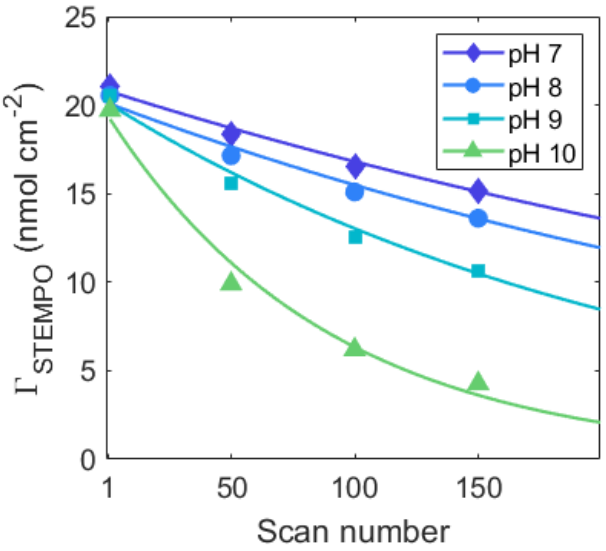

Figure 4.11: Stability curves as a function of pH (data points fitted to a mono-exponential decay), formulated by tracing the change in $\Gamma_{\mathbf{STEMPO}}$ (Equation 4.1) over scan number in the multi-scan CV experiment.

Immobilisation and direct wiring of **STEMPO** to the *meso*ITO electrode was confirmed via electron paramagnetic resonance (EPR) spectroscopy and film electrochemical-EPR (FE-EPR) spectroscopy (details provided in Experimental Section 4.4).[37] The combined FE-EPR spectroelectrochemical technique allows for the appearance and disappearance of paramagnetic species to be monitored as a function of the applied potential. It therefore provides a useful method for investigating redox active paramagnetic states, for the purposes of physical characterisation or to elucidate the mechanism behind a radical-containing electrocatalytic reaction. The high electrical conductivity combined with the surface-modification properties of ITO make it a suitable platform for carrying out FE-EPR spectroscopy. Carbon-based electrodes tend to give rise to large radical signals and thus, are unsuitable for such studies.[37]

For FE-EPR spectroscopy, cylindrical *meso*ITO (*C-meso*ITO) electrodes were required in order to fit inside the EPR spectroelectrochemical cell. The unpaired electron in the TEMPO moiety is delocalised around the nitrogen and oxygen atoms with nuclear spins (I) of 1 and 0, respectively, and thus only couples with nitrogen nuclei. This interaction gives rise to a triplet pattern in which the peaks, for the case of a diffusional species tumbling rapidly in solution at room temperature, are all the same intensity (EPR spectrum for diffusional NH_2-TEMPO in Figure 4.12a, black trace). A triplet pattern is also discernible for the *C-meso*ITO|**STEMPO** assembly, however in this case, the peak intensities are distorted (Figure 4.12a, red trace). This change in

the line-shape of the EPR spectrum relative to the diffusional TEMPO species, arises from a slower tumbling rate which can be a consequence of the impaired mobility of the TEMPO moiety upon **STEMPO** surface immobilisation.[38]

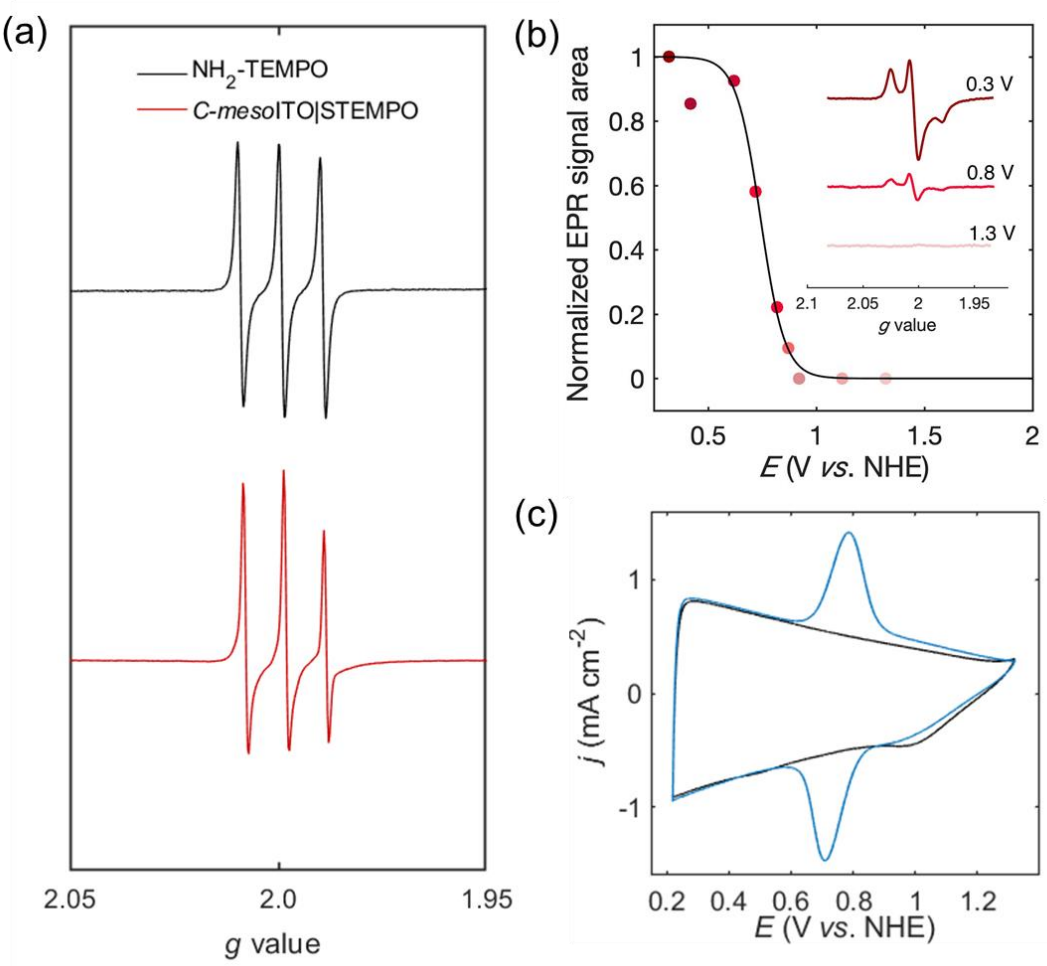

Figure 4.12: Results from EPR and FE-EPR spectroscopy. (a) X-band EPR spectra of diffusional NH_2-TEMPO and *C-meso*ITO|**STEMPO**; *conditions*: temperature = 298 K, 20.02 mW microwave power, 9 scans, and 1 G modulation amplitude. (b) FE-EPR potentiometric titration of *C-meso*ITO|**STEMPO**. Peak area of the **STEMPO** EPR signal as a function of potential (coloured dots), fitted to 1 e^- Nernst equation (solid line). Inset: X-band (9.5 GHz) EPR spectra of STEMPO at different applied potentials. Measurements were performed at 100 K, 2 mW microwave power, 100 KHz modulation frequency and 2 G modulation amplitude. (c) CV for blank *C-meso*ITO (black trace) and *C-meso*ITO|**STEMPO** (blue trace); *conditions*: ν = 10 mV s^{-1}, air, temperature = 298 K. Note: pH 8 aq. HCO_3^-/CO_3^{2-} (0.2 M) was used in all cases, (a) – (c).

Figure 4.12b highlights the results from the FE-EPR investigation. *C-meso*ITO|**STEMPO** samples were poised at a particular potential, using a 3-electrode setup, and then flash-frozen to allow for low temperature EPR characterisation. Exemplary EPR spectra, at three different potentials, are presented in Figure 4.12b (inset) (full range is shown in Figure A.4), where an increase in the

applied bias is accompanied by a clear drop in signal intensity, that eventually vanishes due to the oxidation of the radical to EPR-silent **STEMPO**$^{+}$. The shape of the EPR spectra for $E < 1$ V *vs*. NHE are typical of nitroxide radicals measured at low temperatures (100 K).[39] The normalised signal area of each individual EPR spectrum was plotted as a function of the potential, and is a close fit to the anticipated 1 e^- Nernst equation (solid line in Figure 4.12b). The mid-point potential deduced from the potentiometric titration (0.75 V *vs*. NHE) is in agreement with the $E_{1/2}$ value measured via CV for the *C-meso*ITO|**STEMPO** electrode (Figure 4.12c).

Hybrid Anode Electrocatalytic Performance

Next, we investigated the catalytic performance of the *meso*ITO|**STEMPO** assembly. Figure 4.13a depicts the catalytic behaviour of the system as a function of the solution pH, where 4-methylbenzylalcohol (MBA) was chosen as a model substrate. It is the first example in the literature of an electrocatalytic response from a TEMPO-based compound immobilised on a MO surface. The current density increases with increasing pH, accompanied by a lower onset potential for catalysis (from 0.75 V at pH 7.3, to 0.68 V at pH 10, *vs*. NHE), and is not too dissimilar from other reports for immobilised TEMPO compounds on carbon-based electrodes.[40,41] This observation is in-line with the established TEMPO-mediated oxidation mechanism, whereby alcohol deprotonation leads to formation of a pre-oxidation complex via nucleophilic attack of the alkoxide on the electrophilic nitrogen of the oxidised TEMPO moiety (i.e. the oxoammonium cation), prior to aldehyde formation (c.f. Chapter 1, Section 1.5.2).[41–44] However, the enhancement starts to plateau between pH 9 and pH 10, contrary to what is observed for TEMPO, and related nitroxyl derivatives, in solution.[44] The plateau witnessed in Figure 4.13a for the *meso*ITO|**STEMPO** system could be due to a combination of factors, and we rationalise this behaviour to stem from the relatively slow electron transfer between the ITO electrode and immobilised **STEMPO**, as well as from mass transport limitations of the substrate alcohol in the mesoporous network.

Controlled potential electrolysis (CPE) was then conducted at an applied potential (E_{app}) of 1 V *vs.* NHE at room temperature, to further probe the effect of pH on the *meso*ITO|**STEMPO** system. From Figure 4.11, we observed that the *stability* of the assembly shares an inverse relation with pH, while the TEMPO-mediated catalysis,

and hence reaction *kinetics*, are favoured under more alkaline conditions (Figure 4.13a). To compare the *meso*ITO|**STEMPO** performance as a function of pH, the turnover number (TON) and Faradaic efficiency (FE) (see Equations 4.5 and 4.6 in Calculations Section 4.5, respectively) were calculated after a 3 h CPE experiment with MBA (30 mM) as the substrate, at the four different pH values (Figure 4.13b; chronoamperometric traces shown in Figure A.5).

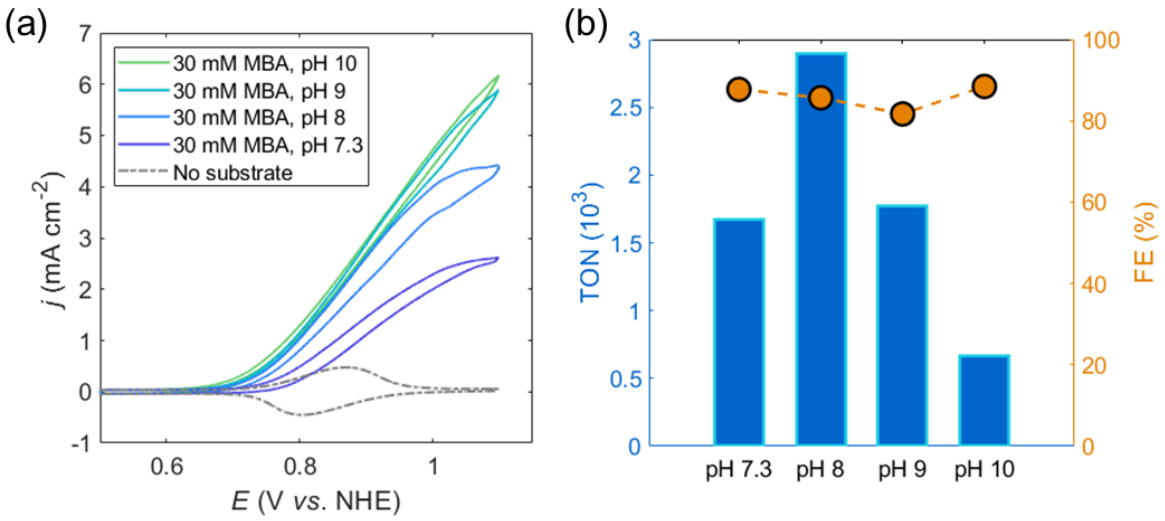

Figure 4.13: Effect of pH on the *meso*ITO|**STEMPO** performance. (a) pH dependent CVs measured for the *meso*ITO|**STEMPO** system, in the presence of 30 mM MBA (CV in the absence of any substrate is also shown). (b) TON and FE metrics compiled from the CPE experiment under a range of pH values. *Conditions*. pH 7.3: CO_2 saturated aq. HCO_3^-/CO_3^{2-} (0.5 M); pH 8 – 10: aq. HCO_3^-/CO_3^{2-} (0.5 M) titrated under ambient conditions to the correct pH; *for CVs*: ν = 20 mV s^{-1}; *for CPE*: E_{app} = 1 V *vs.* NHE, t_{CPE} = 3 h, MBA (30 mM). Product quantification (via HPLC) at the 3 h time-point, was used for TON and FE calculation (see Equations 4.5 and 4.6).

The moles of product, 4-methylbenzylaldehyde (n_{MBAd}), originating from selective MBA oxidation, was quantified by high performance liquid chromatography (HPLC) (HPLC parameters detailed in Experimental Section 4.4). The TON metric for **STEMPO** experiences a clear maximum at pH 8, reaching a value close to 3000, highlighting the fine balance between immobilisation stability and catalytic reactivity for long-term electrolysis experiments. On either side of the maximum, there is a corresponding decrease in the TON; at lower pH, this can be attributed to a slower rate of substrate oxidation thereby resulting in less n_{MBAd}, while higher pH adversely affects the stability of the *meso*ITO|**STEMPO** assembly, likely leading to a loss of the catalytic sites on the electrode over the course of the reaction. Post-electrolysis (at pH 8) XPS conducted on the *meso*ITO|**STEMPO** electrode reveal peaks in the Si_{2p} and N_{1s} regions (Figure A.6), similar to those observed on a freshly assembled electrode

(Figure 4.7). This indicates that the gradual drop in activity could be primarily due to hydrolysis of the amide bond, and subsequent loss of the TEMPO moiety from the assembly. On the other hand, the FE metric is invariant with the pH (average of 86 ± 3% as calculated across the pH range, Figure 4.13b), implying that the electrode|catalyst assembly retains its selectivity towards substrate oxidation throughout the tested pH range.

The versatility of the hybrid electrode was demonstrated by extending the substrate scope to include an aliphatic alcohol, a different primary benzylic alcohol, and a secondary benzylic alcohol. Three representative biomass substrates were therefore selected based on these criteria, namely glycerol, hydroxymethylfurfural (HMF), and a lignin-model compound, 2-phenoxy-1-phenylethanol (PP-ol).[45] The rationale outlined by Costentin and Savéant[46] was adopted in order to conduct a turnover frequency (TOF) analysis, based on the sigmoidal catalytic response of the **STEMPO** system in the presence of the different substrates (see Calculations Section 4.5 for a summary of the TOF analysis technique employed). Figure 4.14 depicts the concentration profiles obtained for MBA, glycerol and HMF, along with the corresponding 'maximum current density *vs.* concentration' plots.

PP-ol was poorly soluble in pure aqueous electrolyte, and thus, a CV trace for this compound was recorded in an MeCN-water mixture (Figure 4.15). The estimated TOFs for the four compounds, and the relevant experimental conditions, are summarised in Table 4-1. The results show that the *meso*ITO|**STEMPO** system can be used to oxidise a variety of alcohol-based substrates, with the primary benzylic alcohols MBA and HMF showing highest activity (TOF = 0.677 and 0.680 s^{-1}, respectively), followed by the aliphatic triol glycerol (0.557 s^{-1}). The results from this analysis therefore signify the use of low-cost and abundant alcohols like glycerol for electrocatalytic applications with the *meso*ITO|**STEMPO** electrode. PP-ol gave the lowest TOF (0.268 s^{-1}), consistent with previous reports which showed that primary alcohols are oxidised more rapidly than secondary alcohols by TEMPO in basic solution.[42]

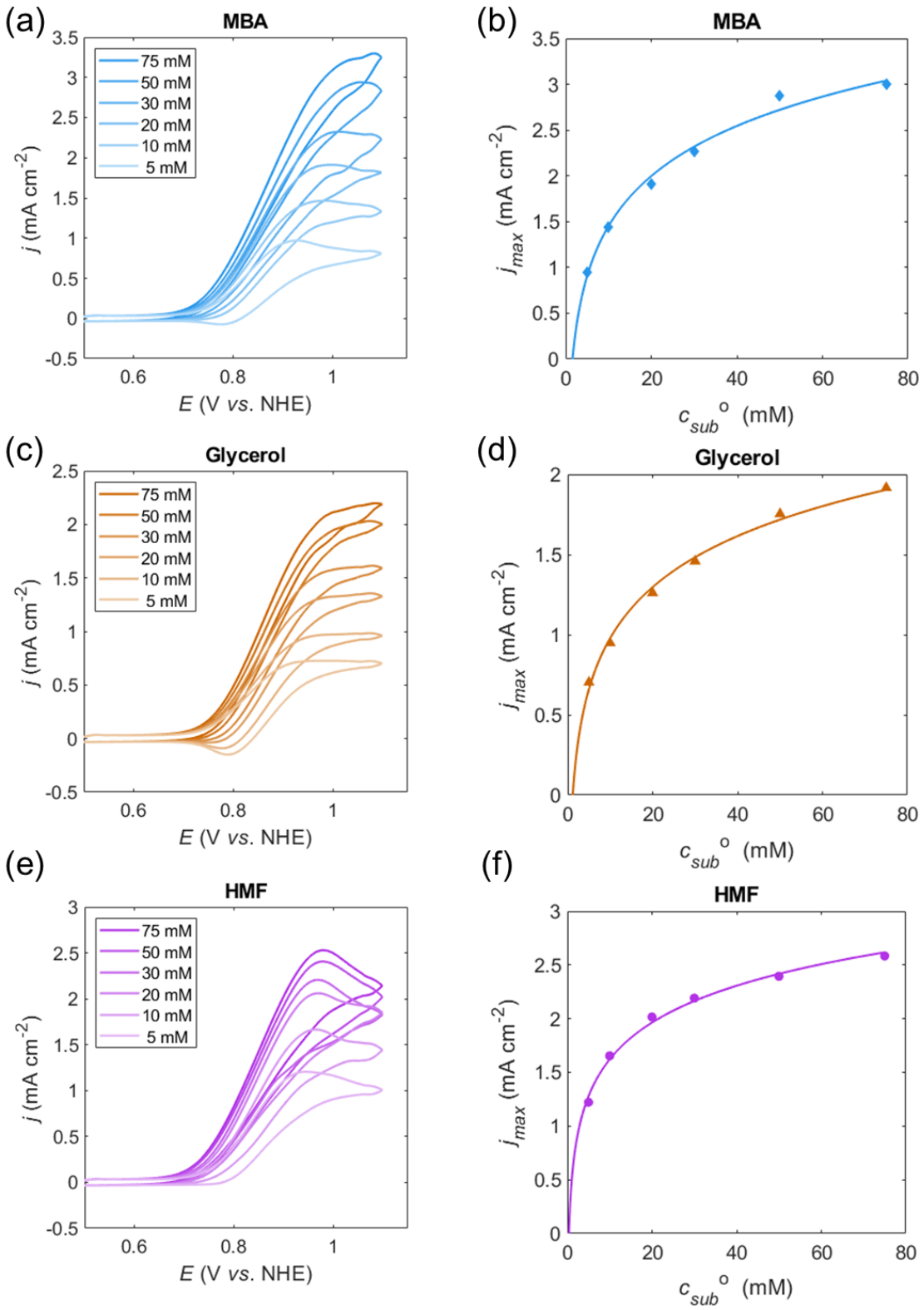

Figure 4.14: Electrochemically determined concentration profiles for representative alcohol substrates: (a) MBA, (c) glycerol, and (e) HMF, using optimised pH conditions (pH 8), aq. HCO_3^-/CO_3^{2-} (0.5 M), and $\nu = 20$ mV s^{-1}. (b), (d), and (f) shows the corresponding 'maximum current density *vs.* concentration' plots compiled for MBA, glycerol, and HMF, respectively. The trend line was fit using the equation: $j_{max} = \lambda_1 + \lambda_2 \ln(c^o_{sub})$, where λ_1 and λ_2 are substrate dependent coefficients for the fit, and c^o_{sub} denotes the initial substrate concentration.

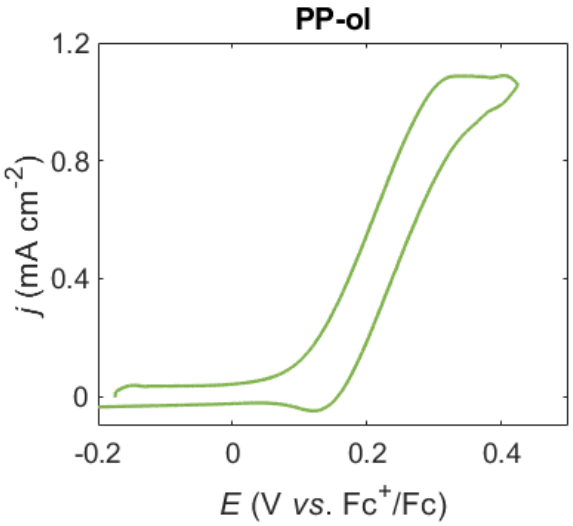

Figure 4.15: CV trace for PP-ol (20 mM), used for TOF analysis. *Conditions*: 3:2 H_2O:MeCN (0.3 M $KHCO_3$) solution, ν = 20 mV s^{-1}, N_2.

Table 4-1: TOF analysis of representative alcohol substrates.[a]

Substrate	Predicted TOF (s^{-1})
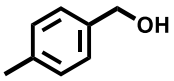	0.677
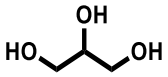	0.557
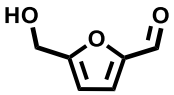	0.680
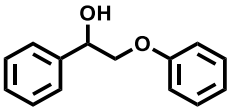	0.268

[a] Experimental conditions for TOF analysis: CV recorded under N_2, ν = 20 mV s^{-1}, c^{o}_{sub} = 30 mM, pH 8 aq. HCO_3^- /CO_3^{2-} buffer (0.5 M). For the case of PP-ol, c^{o}_{sub}= 20 mM, 3:2 H_2O:MeCN mixture, 0.3 M $KHCO_3$ electrolyte.

4.2.3 Coupled Electrolyser

Having characterised this novel anodic assembly and demonstrated the electrocatalytic compatibility of *meso*ITO|**STEMPO** with a variety of biomass representative alcohols, we turned towards applying this system within a coupled electrolyser, featuring the CP|CNT-**CoPPc** cathode assembly for complementary electroreduction of CO_2 (see Figure 4.1). To elucidate the working principle of the

coupled *meso*ITO|**STEMPO**–CP|CNT-**CoPPc** electrolyser, initial experiments were conducted using MBA as the model substrate alcohol.

Figure 4.16a and 4.16b depict catalytic responses for the *meso*ITO|**STEMPO** anode and CP|CNT-**CoPPc** cathode, respectively, recorded separately using Pt mesh as a counter electrode (CE) and Ag/AgCl reference electrode (RE) in each case. A catalytic wave for the *meso*ITO|**STEMPO** assembly in the presence of MBA (30 mM) was observed, which appeared to plateau at around 3 mA cm^{-2}, at an applied potential just above 1 V *vs.* NHE (Figure 4.16a). The CV recorded for CP|CNT-**CoPPc** under N_2 displays a broad quasi-reversible redox process (Figure 4.16b, $E_{1/2}$ ~ –0.71 V *vs.* NHE), which corresponds to the metal-centred Co^{II}/Co^{I} reduction of **CoPPc**. The surface concentration of electroactive cobalt centres, Γ_{Co}, was estimated to be 18.3 ± 1.6 nmol cm^{-2} from integration of the Co^{I}/Co^{II} oxidation wave (Figure 4.17; analogous determination to $\Gamma_{\mathbf{STEMPO}}$, c.f. Equation 4.1). This translates to 5.6 ± 0.5% cobalt sites being electrochemically accessible (see Calculations Section 4.5), which is lower compared to the reported system due to the smaller geometric surface area of the fabricated cathode in our system (~0.28 cm^2).[22]

Upon CO_2 saturation, a catalytic onset from the CP|CNT-**CoPPc** electrode was observed at a potential close to –0.84 V *vs*. NHE (Figure 4.16b). Electrocatalytic performance of the cathode was probed by stepped constant potential chronoamperometry in the range of –0.70 V to –1.00 V *vs.* NHE, with 50 mV increments and 30 min steps (Figure 4.18). Product formation was monitored via a continuous flow gas chromatography (GC) method (details provided in Experimental Section 4.4). H_2 was the only product until –0.80 V, and CO evolution was only initiated at more negative potentials (~ –0.85 V). The selectivity of the electrode towards CO increases sharply with more negative potential, with CO selectivity reaching 76% at –1.00 V *vs*. NHE (overpotential, η = 0.46 V, where $E(CO_2/CO)$ = −0.54V *vs.* NHE at pH 7.3)[47]. Within the same potential range, the blank CNT electrode did not result in the generation of any H_2 or CO, implying that the Co-based catalyst was responsible for product formation (Figure 4.18a, purple trace).

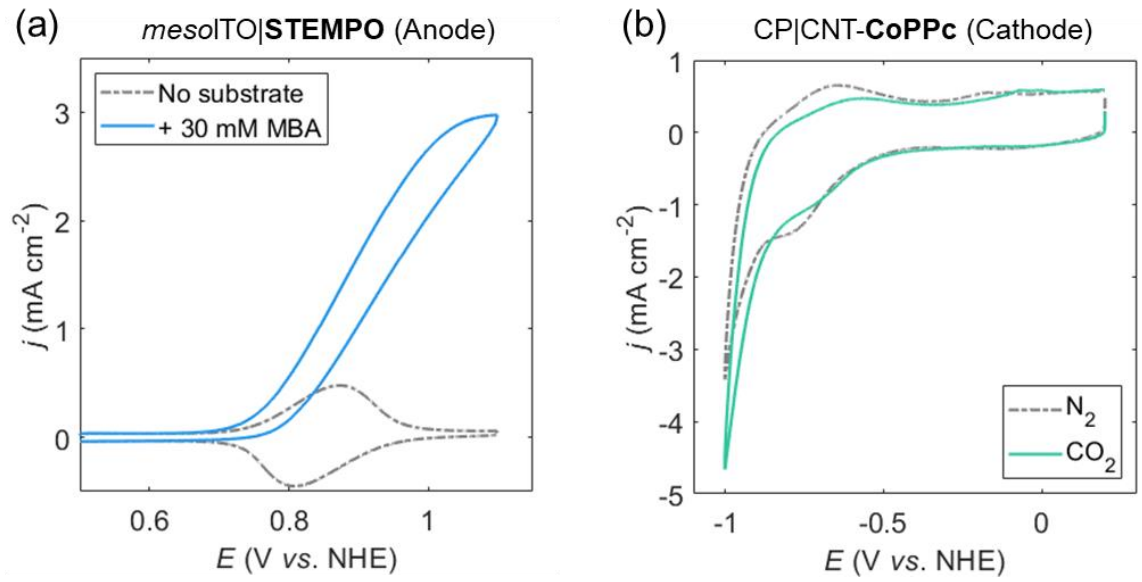

Figure 4.16: Anode and cathode CVs. (a) *meso*ITO|**STEMPO** anode, and (b) CP|CNT-**CoPPc** cathode, recorded separately in a 3-electrode setup, with Pt mesh as the CE and Ag/AgCl as RE. *Conditions*: CO_2 saturated pH 7.3 aq. HCO_3^- /CO_3^{2-} (0.5 M), ν = 20 mV s^{-1} (pH 8 for cathode N_2 trace).

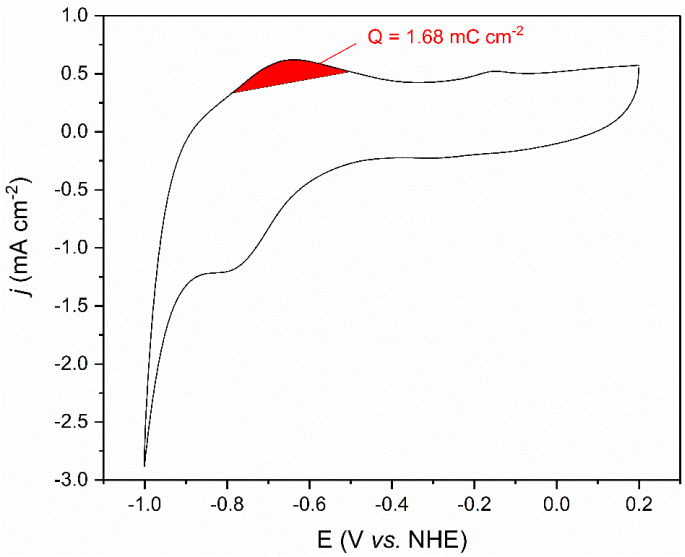

Figure 4.17: Electroactive cobalt quantification using the CV curve for CP|CNT-**CoPPc** in N_2 saturated pH 8.3 aq. HCO_3^- /CO_3^{2-} (0.5 M), ν = 20 mV s^{-1}. Electroactive Co was quantified using the reported method with the same catalyst.[22] The highlighted area shows the integration of the Co^{I}/Co^{II} anodic wave, determined using the EC-Lab software. The Γ_{Co} value reported here is the average surface concentration calculated by integration of 10 successive CV scans at 20 mV s^{-1}. (Equation 4.1 was thus applied, using this average value for Q, and the area of the cathode, where $A_{cathode}$ ~ 0.28 cm^2).

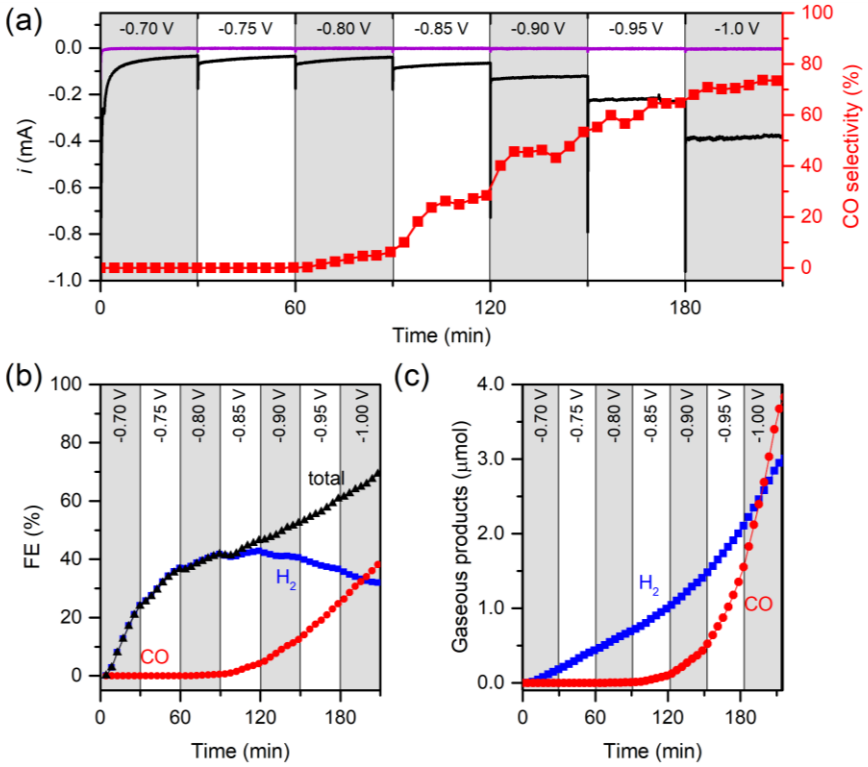

Figure 4.18: Stepped constant potential chronoamperometry result for the CP|CNT-**CoPPc** electrode (black trace) and blank CNT electrode (purple trace) under CO_2 saturated pH 7.3 aq. HCO_3^-/CO_3^{2-} (0.5 M) solution, with Pt mesh as the CE and Ag/AgCl as RE. Electrolysis was carried out in a 2-compartment cell, and the working compartment was constantly purged with CO_2 (5 sccm). Each potential step was applied for 30 min, and product formation was monitored by continuous flow GC analysis. (a) Current and CO selectivity trace as a function of the applied potential. (b) Variation in the FEs for H_2 and CO with applied potential. *Note*: low FE observed at less negative potentials (current ~0.1 mA cm^{-2}) is likely the result of gas leakage and trapped gas bubbles in carbon nanotubes, which has a more pronounced effect on the FE at lower currents. (c) Total amount of gaseous product formed during the electrolysis experiment, with CP|CNT-**CoPPc** as the WE. No H_2 and CO were detected with the blank CNT WE.

The currents were well-matched between the *meso*ITO|**STEMPO** and CP|CNT-**CoPPc** electrodes, albeit slightly lower current densities were experienced at the anode and hence, it was selected as the working electrode (WE) in the coupled electrolyser assembly while the cathode assumed the role of the CE. A two-compartment electrochemical cell was employed to conduct the coupled studies, where a Selemion-AMV anion-exchange membrane was used to separate the compartments, and a Ag/AgCl RE was placed in the working compartment.

The 3-electrode configuration was adopted prior to testing in a 2-electrode fashion to be able to control E_{app} at the WE versus a known reference, and to record the precise potential at the CE (E_{CE}) during electrolysis against the same reference, thus providing a more detailed description of the cell parameters over reaction time. For simplicity,

CO_2 saturated carbonate buffer (0.5 M) was used in both compartments, yielding a solution pH close to 7.3 which remained relatively constant throughout the experiment. Figure 4.19 depicts the results from the coupled electrolysis (3-electrode configuration) experiment, with E_{app} = 1 V *vs.* NHE at room temperature. Alcohol conversion to the corresponding aldehyde, MBAd, was quantified by HPLC, whereas CO and H_2 were quantified via the continuous flow GC method mentioned earlier. Catalytic metrics obtained for the respective anode and cathode highlight the effectiveness of the combined system. For MBA oxidation, a TON_{STEMPO} of 1515 and FE close to 90% were attained after the 3 h CPE experiment, while a cobalt-based TON for syngas generation of 1360 (TON_{CO} = 599 and TON_{H_2} = 761), with overall FEs for CO and H_2 of 35% and 45%, respectively, were achieved for the CP|CNT-**CoPPc** cathode.

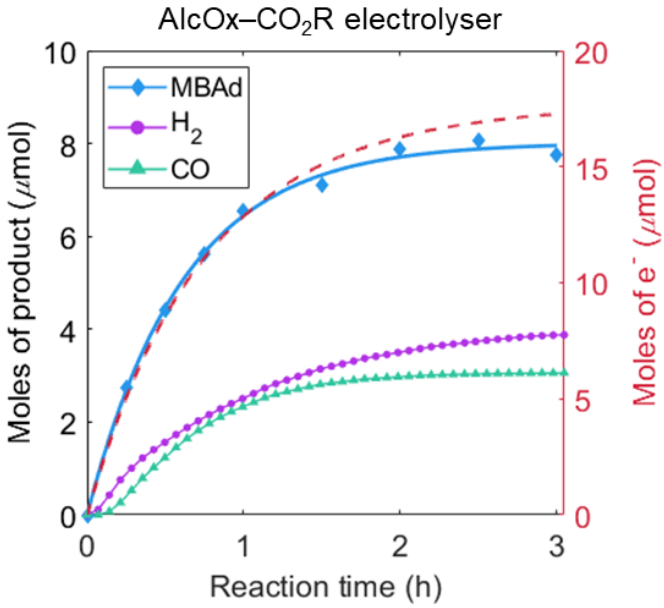

Figure 4.19: Coupled electrolyser (3-electrode setup, MBA substrate) experiment, showing moles of product (liquid and gaseous) and e^- (as recorded on the potentiostat) over reaction time. *Conditions*: 2-compartment cell fitted with anion-exchange membrane; 3-electrode configuration with *meso*ITO|**STEMPO** as WE, CP|CNT-**CoPPc** as CE and Ag/AgCl as RE; CO_2 saturated pH 7.3 aq. HCO_3^-/CO_3^{2-} (0.5 M) in both compartments; MBA substrate (30 mM) present in anodic compartment, E_{app} (anode) = 1 V *vs.* NHE, t_{CPE} = 3 h; MBAd quantified by HPLC, CO/H_2 via continuous flow GC analysis.

With these promising results at hand, we decided to substitute MBA with glycerol, on account of its aforementioned advantages as a commercially viable and abundant resource, making it a more suitable substrate for coupling with CO_2R in real-life applications. A similar setup to that used for coupled MBA oxidation was employed, except in this case, the anode compartment consisted of a carbonate buffer (0.5 M) at pH 8.3 (under N_2), whereas the catholyte was comprised of a CO_2 saturated carbonate

buffer (0.5 M) at pH 7.3 (as per the MBA experiment). This was deemed necessary for glycerol, as the **STEMPO**-mediated catalysis involving this substrate was observed to be too sluggish at the quasi-neutral pH of CO_2 saturated carbonate buffer (i.e. pH 7.3), but increased in activity under more alkaline conditions (as evidenced by the CVs recorded at pH 7.3 and pH 8.3 in the presence of glycerol, Figure 4.20).

Figure 4.21a illustrates the *reaction time plot* obtained with glycerol, rather than MBA, as the substrate, with E_{app} = 1 V *vs.* NHE. Due to the presence of primary and secondary hydroxyl groups on glycerol, this substrate can potentially be oxidised into a variety of products (Scheme 4.2).[48] However, HPLC analysis revealed that the aldose glyceraldehyde (GlyAd), stemming from primary hydroxy oxidation, was the main anodic product from the coupled electrolysis experiment. Overall, the system performed well in the presence of the glycerol substrate. The two compartments also maintained their individual pH values for the duration of the electrolysis. The $TON_{\mathbf{STEMPO}}$ and FE were found to be equal to 997 and 83%, respectively, slightly lower than for the case of MBA. This was not too surprising, given that the kinetics for glycerol oxidation are slower than for MBA (c.f. Table 4-1). In addition, although precautions were taken to minimise overoxidation and/or further reaction of GlyAd (by quenching and then freezing reaction samples), trace amounts of some side-product can potentially form (not detected by HPLC), leading to the observed ~7% drop in the FE relative to the MBA electrolyser. With regards to the cathode metrics, the cobalt-based TON was determined to be equal to 894 (TON_{CO} = 444 and TON_{H_2} = 450), while similar FEs for the gaseous products, relative to the MBA-based electrolyser, were measured (FE = 41% for CO and 41% for H_2). A side-by-side comparison of the calculated FEs for the liquid and gaseous products over reaction time, for the MBA- and glycerol-based electrolysers, is provided in Appendix A (Figure A.7).

As mentioned, use of a 3-electrode configuration allowed for E_{CE} (i.e. the potential at the CP|CNT-**CoPPc** electrode) to be monitored throughout the course of the electrolysis experiment. From the traces shown in Figure 4.21b, there is an alteration in the $CO:H_2$ ratio at the cathode over time, which seems to be a consequence of the decrease in the absolute value of E_{CE}. This decrease in the reducing potential at the cathode is itself a result of the gradual decline in activity at the anode over time. The change in the $CO:H_2$ ratio as a function of the cathodic potential is in-line with the stepped chronoamperometric experiments carried out for the CP|CNT-**CoPPc**

electrode (with Pt mesh as CE), as discussed previously (Figure 4.18). The time-lag between the minima of the E_{CE} trace and the maximum value of CO:H_2 ratio on Figure 4.21b is likely caused by the slow diffusion of CO from the porous CP|CNT-**CoPPc** electrode.

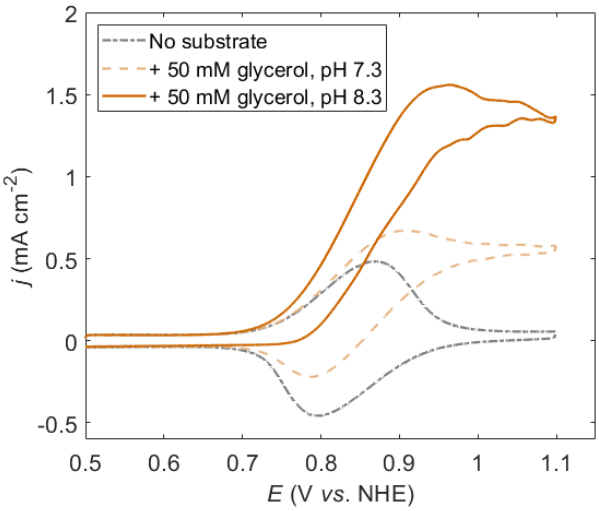

Figure 4.20: CV traces in the presence of glycerol, recorded in CO_2 saturated pH 7.3 aq. HCO_3^- /CO_3^{2-} (0.5 M) solution, and N_2 saturated pH 8.3 aq. HCO_3^- /CO_3^{2-} (0.5 M) solution. (*meso*ITO|**STEMPO** as the WE**,** glycerol (50 mM), ν = 20 mV s^{-1}).

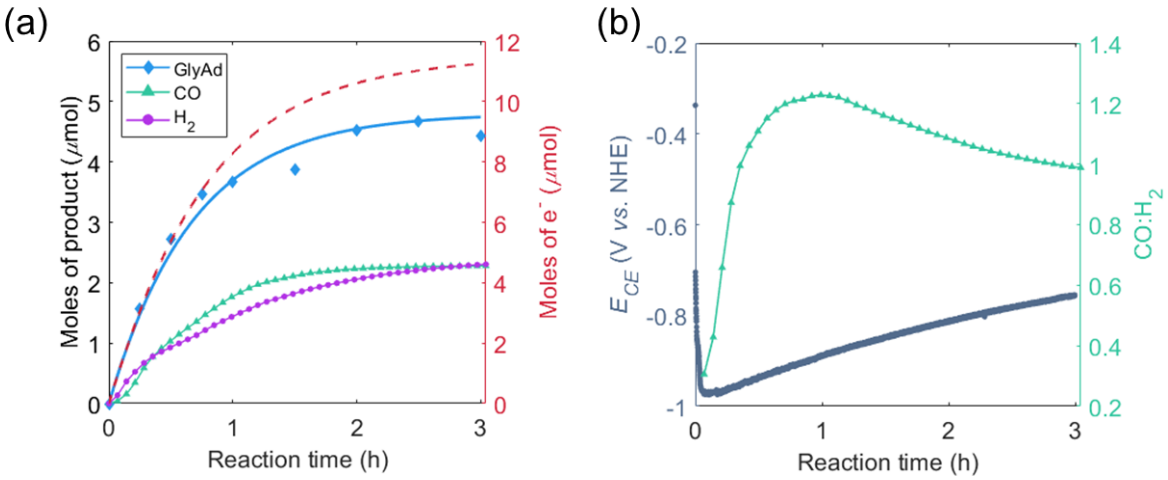

Figure 4.21: Coupled electrolyser (3-electrode setup, glycerol substrate) experiment. (a) Similar profile to Figure 4.19, but with glycerol as the substrate rather than MBA. (b) Trend in the CO:H_2 ratio and CP|CNT-**CoPPc** CE potential (E_{CE}) over reaction time. *Conditions*: 2-compartment cell fitted with anion-exchange membrane; 3-electrode configuration with *meso*ITO|**STEMPO** as WE, CP|CNT-**CoPPc** as CE and Ag/AgCl as RE; anode compartment: N_2 saturated pH 8.3 aq. HCO_3^- /CO_3^{2-} (0.5 M); cathode compartment: CO_2 saturated pH 7.3 aq. HCO_3^- /CO_3^{2-} (0.5 M); glycerol substrate (50 mM) present in anodic compartment, E_{app} (anode) = 1 V *vs.* NHE, t_{CPE} = 3 h. Glycerol oxidation and gaseous products quantified via HPLC and continuous flow GC analysis, respectively.

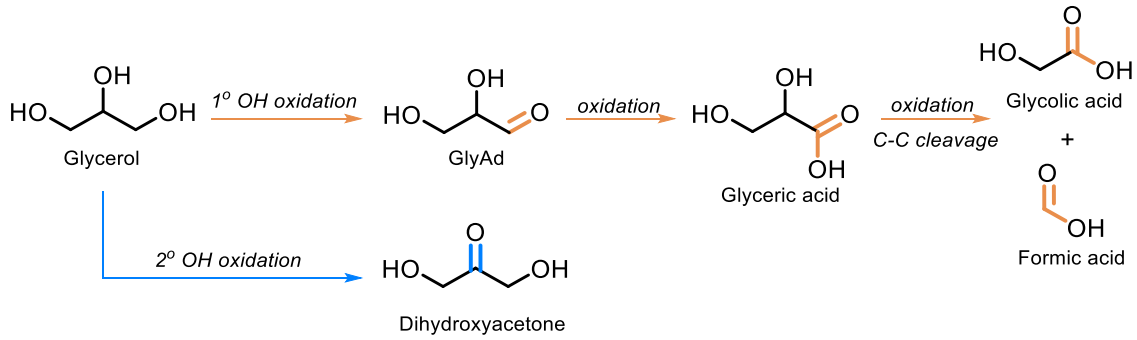

Scheme 4.2: Examples of glycerol oxidation pathways.

We furthered our investigation into coupled glycerol oxidation and CO_2R, and performed a series of experiments in a 2-electrode configuration, while varying the applied cell potential (V_{cell}). Values for V_{cell} in the range of 1.8 to 2.1 V were chosen, based on the rationale that: $|E_{cathode} - E_{anode}| \approx |\bar{E}_{CE} - E_{app}| = 1.85$ V, where $\bar{E}_{CE}$ is the average potential at the CE, over reaction time, as measured in the 3-electrode configuration (i.e. Figure 4.21b). Figure 4.22a depicts the combined FE at the cathode (for CO and H_2) and the CO:H_2 ratio, over reaction time, for V_{cell} = 2.0 V. The trends agree with those obtained for the 3-electrode setup. The increase in the maximum of the CO:H_2 ratio for the 2-electrode versus the 3-electrode configuration (shown in Figure 4.21b) could be a result of the increased driving force provided by the 2.0 V potential. This bias most likely leads to more reductive potentials at the cathode, and, in accordance with the aforementioned stepped chronoamperometry data for CP|CNT-**CoPPc** (Figure 4.18), would translate to a higher CO:H_2 ratio.

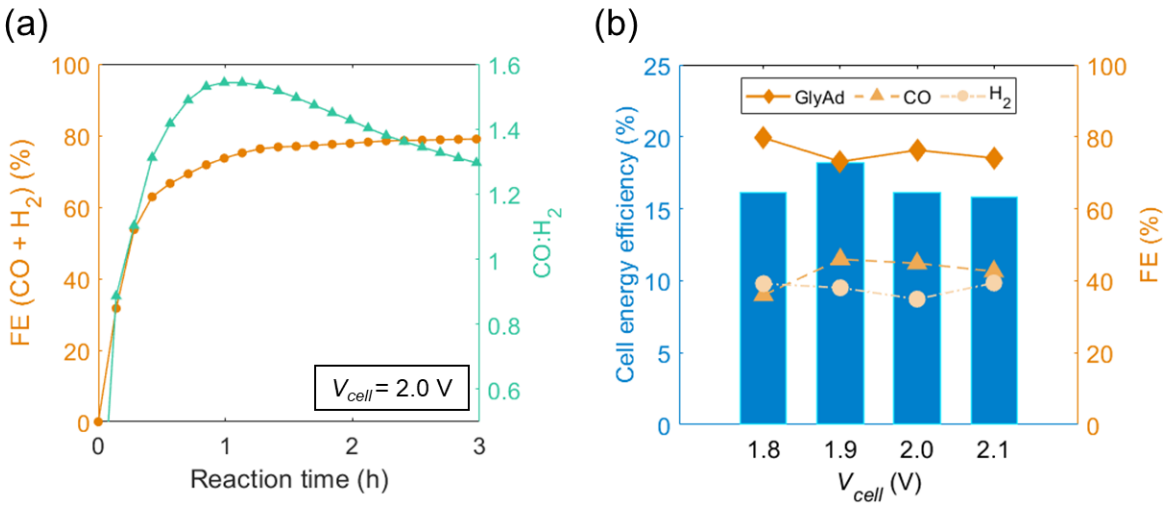

Figure 4.22: Coupled electrolyser performance in 2-electrode configuration. (a) Combined FE for CO and H_2, and corresponding CO:H_2 ratio for the 2-electrode configuration incorporating glycerol as the substrate (applied cell potential = 2.0 V). (b) Cell energy efficiency and FE plotted as a function of V_{cell} in the same 2-electrode setup. *Note*: same conditions were used for the 2- and 3-electrode configurations (see Figure 4.21 for details).

Finally, we attempted to parametrise the cell energy efficiency (ε), as a function of V_{cell}. The equation used to calculate this metric is defined in Equation 4.2:[49,50]

$$\varepsilon = \frac{|E_{cell}|}{V_{cell}} = \frac{\left|\left(FE_{H_2} \cdot E_{H^+/H_2} + FE_{CO} \cdot E_{CO_2/CO}\right) - FE_{GlyAd} \cdot E_{GlyAd/glycerol}\right|}{V_{cell}} \qquad 4.2$$

where E_{H^+/H_2}, $E_{CO_2/CO}$, and $E_{GlyAd/glycerol}$ denote the reduction potentials for H^+, CO_2, and glyceraldehyde, respectively, under non-standard conditions. A more detailed breakdown regarding the thermodynamic analysis required to compute ε is provided in Calculations Section 4.5. Figure 4.22b illustrates the FEs for the anodic and cathodic processes, along with the corresponding ε calculations, for different applied cell potentials. There is a slight improvement in the CO selectivity upon increasing from 1.8 to 1.9 V (FE_{CO} = 36 and 46%, respectively), presumably a result of the higher driving force at these applied voltages. This enhancement is met with an improvement in ε (from 16 to 18%), since the 100 mV additional bias is more than offset by the increase in FE_{CO}, as governed by Equation 4.2. However, for $V_{cell} \geq 2.0$ V, the combined effects of a largely unchanged $CO:H_2$ ratio and anodic FE, causes a corresponding drop in the cell efficiency to ~16%, similar to that obtained for V_{cell} = 1.8 V.

The cell energy efficiency values measured for our hybrid electrolyser are in accordance with those reported in the literature, where for example, an efficiency of 17%, at 1.8 V cell potential, was measured for a tandem electrolyser featuring benzyl alcohol oxidation coupled with CO_2 to CO and H_2 conversion.[12] However, the previously reported system was comprised of Ru-based molecular catalysts for the reductive and oxidative half-reactions, and additionally, only one of the catalysts was immobilised. On the other hand, we have incorporated immobilised cathodic and anodic catalysts in our electrolyser, both free of any precious-metals, and have also demonstrated the applicability of the tandem AlcOx–CO_2R device to couple the oxidation of more commercially viable alcohol substrates, such as glycerol, with CO_2-to-syngas conversion.

4.3 Conclusion

In conclusion, we have designed, fabricated and characterised a novel anode featuring the silatrane-modified TEMPO molecule on a *meso*ITO scaffold, and demonstrated, for the first time, the electrocatalytic ability of a TEMPO-based, hybrid MO system to efficiently oxidise a variety of biomass representative substrates. The siloxane anchor, formed upon hydrolysis of the silatrane cage on the MO surface, is highly robust, and we suspect that the longer-term stability of the assembly is currently limited by the amide bond in the **STEMPO** compound. Hence, the next generation of silatrane-containing catalysts for alcohol oxidation are being designed to avoid the use of this functional group. We further showed the advantages and versatility of our robust anode by coupling the alcohol oxidation half-reaction with an efficient CO_2R cathode (CP|CNT-**CoPPc**), to construct a fully molecular, precious-metal-free, AlcOx–CO_2R electrolyser, based solely on earth-abundant materials.

The functionality and performance of this coupled electrolyser was investigated using a 3-electrode configuration, first employing MBA as a model substrate, and later, using the commercially applicable substrate, glycerol. It was found that, in both cases, stoichiometric amounts of a selective oxidation product (the corresponding aldehyde) and syngas were generated at the anode and cathode, respectively. Faradaic efficiencies were typically excellent for the hybrid system, exceeding 80% for both anode and cathode. TONs were also high, approaching 1000 for *meso*ITO|**STEMPO** and 900 for CP|CNT-**CoPPc** (with glycerol as substrate). Further studies were then made using a demonstrator-type, 2-electrode setup for coupled glycerol oxidation at the anode and syngas generation at the cathode, showing similarly promising metrics as per the 3-electrode setup. Cell energy efficiency calculations also revealed the advantages of operating at lower applied potentials, with a maximum cell efficiency of 18% being measured at a cell potential of 1.9 V. This hybrid, molecular system is therefore a suitable model for the development of future AlcOx–CO_2R electrolysers based on earth-abundant materials, which can provide chemical feedstocks, for instance aldehydes and syngas, from sustainable and abundant resources, such as biomass-derived alcohols, CO_2, and renewable electricity.

4.4 Experimental Section

4.4.1 Materials

All chemicals purchased from commercial suppliers were of the highest available purity and used without further purification unless otherwise noted. ITO-coated glass substrates were purchased from Vision Tek Systems Ltd. (R = 12 Ω sq^{-1}, thickness = 1.1 mm). Ti foil (0.25 mm thick, 99.5%), 4-methylbenzyl alcohol (MBA), 4-metylbenzaldehyde (MBAd) 1,8-Diazabicyclo(5.4.0)undec-7-ene (DBU), and Carbon black (Super P® Conductive, product # H30254) were purchased from Alfa Aesar. Anhydrous ethanol (200 proof, ≥ 99.5%), triethanolamine, 5-hydroxymethylfurfural, multi-walled carbon nanotubes, and ITO nanoparticles (< 50 nm) were purchased from Sigma Aldrich. Sodium carbonate (anhydrous), potassium bicarbonate (anhydrous), 3-aminopropyl(triethoxy)silane, and thionyl chloride were purchased from Acros Organics, 1,2,4,5-tetracyanobenzene, 2-phenoxy-1-phenylethanol, glyceraldehyde (GlyAd), and DL-glyceric acid (20% in water) from Fluorochem, and 4-carboxy-TEMPO from Insight Biotechnology. Untreated carbon paper (AvCarb® MGL190) was purchased from Fuel Cell Earth. Glycerol was purchased from VWR Chemicals, and anhydrous pyridine, diisopropylethylamine, and glacial acetic acid from Fisher Scientific.

All aqueous solutions were prepared with ultrapure water (DI water; Milli-Q®, 18.2 MΩ cm). Toluene, dichloromethane (DCM), hexane, pentane, and acetonitrile (MeCN) were distilled before use.

4.4.2 Physical Characterisation

^{1}H NMR spectra were recorded on a Bruker 400 MHz or 500 MHz DCH cryoprobe spectrometer at room temperature. Chemical shifts for ^{1}H NMR spectra were referenced to residual signals from the deuterated solvent. High resolution-mass spectra (HRMS) were recorded using a Thermo Scientific Orbitrap Classic mass spectrometer. FT-IR (ATR) spectra were recorded on a Thermo Scientific Nicolet iS50 spectrometer. Raman spectra were recorded on a HORIBA LabRAM HR Evolution system with an incident laser of 633 nm. Elemental analysis was carried out by the Microanalysis Service of the Department of Chemistry, University of Cambridge, using

an Exeter Analytical CE-440 Elemental Analyser. Inductively coupled plasma optical emission spectrometry (ICP-OES) measurements were also conducted by the Microanalysis Service, on a Thermo Scientific iCAP 7400 ICPOES DUO spectrometer. The surface morphology of electrodes was analysed using a Tescan MIRA3 FEG-SEM. X-ray photoelectron spectroscopy (XPS) was carried out on an ESCALAB 250Xi Thermo Fisher Scientific spectrometer, operating in the constant analyser energy mode. An Al-Kα X-ray source was used with power of 124 W (8.5 mA and 14.55 kV), and the pass energy was set for the recorded data at 20 eV to acquire a high-resolution spectra. All spectra were calibrated, and charge compensation was applied. The spectra were referenced to 284.8 eV C_{1s} peak (adventitious carbon impurities).

4.4.3 Synthesis

Synthesis of 3-aminopropylsilatrane (1). 3-aminopropylsilatrane was synthesised according to a literature procedure.[51–53] 3-aminopropyl(triethoxy)silane (5.00 g, 22.5 mmol, 1.05 equiv.) was added to triethanolamine (3.18 g, 21.375 mmol, 1 equiv.) at room temperature in a round bottomed flask fitted with a Dean Stark apparatus under N_2. The resulting mixture was refluxed at 145 °C to remove the ethanol formed during the reaction. Once the ethanol was completely removed, the reaction mixture was allowed to cool to room temperature, and was then placed in the fridge for 1 h. A white solid was obtained which was then washed with hexane, filtered, dried under vacuum, and stored in the fridge. Characterisations were found to be similar to previously published data and the product was used in the next step without further purification.

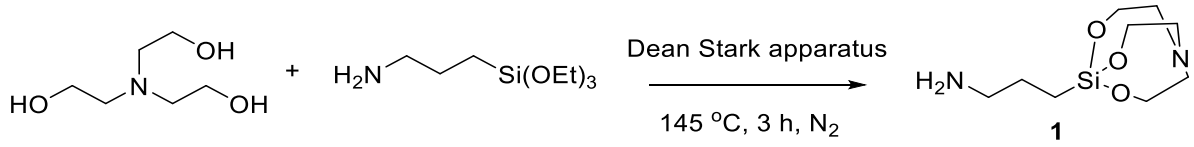

Synthesis and Characterisation of STEMPO. Pyridine (0.24 mL, 3 mmol, 2.4 equiv.) was added to a solution of 4-carboxy-TEMPO (250 mg, 1.25 mmol, 1 equiv.) in anhydrous toluene (12.5 mL) under N_2. The resulting solution was cooled to 0 °C in an ice bath and thionyl chloride (0.14 mL, 1.875 mmol, 1.5 equiv.) was added dropwise. The solution was stirred at room temperature for 1 h and an off-white precipitate was observed. The liquid layer was transferred into a round bottom flask,

and the precipitate was washed with a small amount of anhydrous toluene. The combined liquid fractions were concentrated *in vacuo* and the resulting residue dissolved in anhydrous dichloromethane (DCM) (5 mL). This crude product was added to a stirring solution of **1** (348.5 mg, 1.5 mmol, 1.2 equiv.) and *i*-Pr_2NEt (0.4 mL, 2.3 mmol, 1.8 equiv.), dissolved in anhydrous DCM (10 mL) under N_2 atmosphere. The resulting mixture was then stirred at room temperature for 1 h under N_2. The reaction mixture was concentrated, and the product was precipitated from DCM by the addition of n-pentane. The solvent was syphoned off, and the orange solid was dried under vacuum. The resultant orange powder was solubilised in DCM (30 mL) and washed successively with 1% $NaHCO_3$ water (20 mL) and brine (20 mL). The organic layer was dried over $MgSO_4$ and filtered over cotton. The solvent was evaporated under reduced pressure, and the orange powder was dried overnight under vacuum to afford **STEMPO** (70% yield). FT-IR (ATR): σ (cm^{-1}): 2972, 2929, 2878, 1646, 1547, 1456, 1178, 1123, 1086. HRMS (+ESI, m/z): calcd. for $C_{19}H_{37}O_5N_3Si_1$ $[M-H^+]^+$: 415.2502; found, 415.2496. Anal. calcd. for $C_{19}H_{36}O_5N_3Si_1$: C, 55.04; H, 8.75; N, 10.14; found: C, 55.21; H, 8.80; N, 9.69.

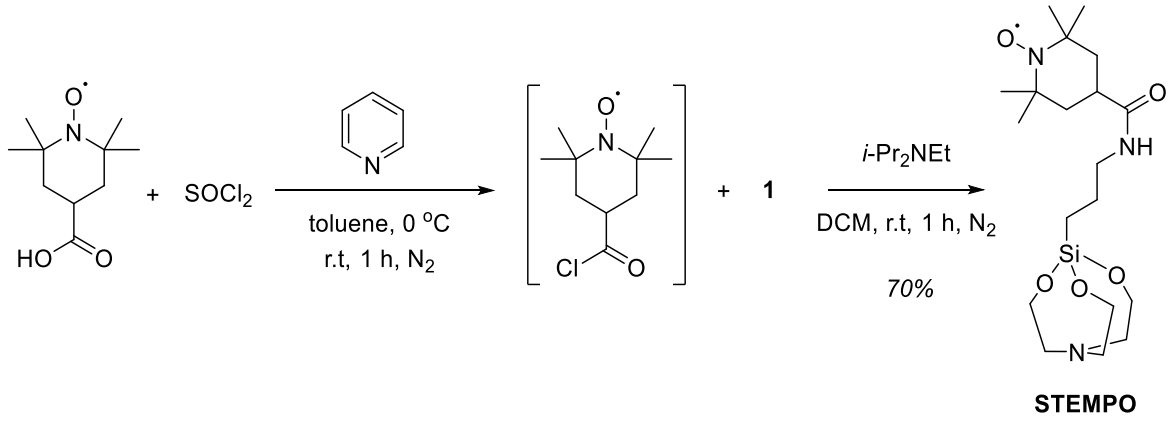

4.4.4 Assembly of Electrodes

Fabrication of *meso*ITO Electrodes. *meso*ITO electrodes were fabricated in-house following a modified literature procedure.[54,55] For *meso*ITO, 3×1 cm ITO-coated glass slides were sonicated in acetone and isopropanol for 15 min each, and then dried in an N_2 stream. A 5 wt.% mixture of ITO nanopowder in an acetic acid solution (5 M in ethanol) was sonicated for 20 min. Parafilm was used to define a constant surface area on the ITO-coated glass (0.25 cm^2), onto which, the ITO dispersion was drop-

cast. Two 5 µL aliquots were dropped onto the defined area, with an intermediate drying period (in air) of 5 min. Following the second drying period, the parafilm template was removed and the samples annealed in a Carbolite furnace, under atmospheric conditions, using the following heating programme: the slides were heated from room temperature to 450 ºC (ramp rate of 4 ºC min^{-1}), kept at this temperature for 20 min, and then slowly cooled to room temperature in the furnace chamber.

Assembly of *meso*ITO|STEMPO Electrodes. The routine followed to optimise the loading of STEMPO on the mesoITO surface was described in Section 4.2.1. For clarity, the optimised conditions used for characterising the assembly, and conducting all catalytic and coupled electrolysis experiments is summarised herein. A solution of **STEMPO** (2 mM, 2.8 mL) containing 2% v/v AcOH and 1% v/v H_2O in MeCN was prepared in a vial. The *meso*ITO electrodes were submerged in the solution; the vial was capped, and the mixture heated at 70 °C under a N_2 overpressure for a duration of 6 h.

Fabrication of CP|CNT-CoPPc Electrodes. The polymerisation of **CoPc** onto CNT fibres to form the CNT-**CoPPc** composite was carried out in accordance to a literature procedure.[22] For fabrication of the cathodes, a catalyst ink was prepared by dispersing 2 mg of the hybrid CNT-**CoPPc** material and 1 mg conductive carbon black in 0.5 mL ethanol containing 0.012 mL 10 wt% Nafion solution, followed by ultrasonication for 30 min. 0.05 mL of catalyst ink containing ~0.2 mg CNT-**CoPPc** was drop-casted onto untreated CP (1.6×0.8 cm^2) and dried under air, to yield the CP|CNT-**CoPPc** electrode assembly. The geometric area of the catalyst coverage was ~0.3 cm^2. An electric wire was connected to the CP using a conductive silver paint (RS® Components 186-3593). The electrode was encapsulated with an opaque grey epoxy adhesive (Loctite® EA 3423), leaving only the catalyst-covered area exposed (~0.28 cm^2).

Quantification of Cobalt. Cobalt loading in the hybrid CNT-**CoPPc** composite was determined by ICP-OES after digestion of the material (< 1 mg) in conc. HNO_3 (70%) (~1 mL) overnight and dilution to 10 mL with Milli-Q® water. To quantify the cobalt content of CP|CNT-**CoPPc** electrodes by ICP-OES, the catalyst powder (mixture of CNT, **CoPPc**, and carbon black) was scratched off the electrode after electrocatalysis and digested in conc. HNO_3 followed by dilution to 10 mL.

4.4.5 Electrochemical Studies

(a) General Methodology. CV and CPE measurements were performed on either an Ivium CompactStat potentiostat or a BioLogic VSP potentiostat. When investigating the oxidative or reductive half-reaction, a 3-electrode configuration was employed in an airtight, one-compartment cell (solution volume = 9 mL), with a *meso*ITO|**STEMPO** WE or CP|CNT-**CoPPc** WE respectively, a Pt mesh CE and a Ag/AgCl RE (for aqueous experiments: BASi RE-6, saturated KCl; for MeCN-water experiments: home-made RE in a solution with the same composition as the electrolyte).

For aqueous experiments, the potentials were converted from Ag/AgCl to normal hydrogen electrode (NHE) by adding +0.199 V. In MeCN-water mixtures, the reference electrode was regularly referenced against the ferrocene couple (Fc^+/Fc), and potentials were reported against Fc^+/Fc. All electrochemical experiments were carried out at room temperature (~22 °C) unless otherwise stated. The surface concentration of **STEMPO** and electroactive cobalt centres, was calculated through the integration of the oxidation wave in the CV scan (see Equation 4.1 and Figure 4.17 for details).

Unless otherwise stated, for fully aqueous conditions, a carbonate buffer (0.5 M) was employed, and pH 8, 9, and 10 solutions were titrated under ambient conditions. Solutions were purged with N_2 for 15 min prior to measurement, to remove atmospheric O_2. Purging the carbonate buffer (0.5 M) with CO_2 for 30 min resulted in a solution pH of 7.3. A 3:2 H_2O:MeCN (0.3 M bicarbonate) was used for MeCN-water mixtures.

(b) Coupled Electrolyser. For the coupled electrolyser set-up, a custom-made, airtight, two-compartment electrochemical cell was employed for all CPE measurements, where a Selemion-AMV anion-exchange membrane was utilised to separate the compartments. A 3-electrode configuration was used, with *meso*ITO|**STEMPO** as WE, CP|CNT-**CoPPc** as CE and Ag/AgCl as RE, with the WE and RE being placed in the same compartment. The solution volume of the working (anode) compartment was 7.5 mL, and the counter (cathode) compartment was 5 mL. When a two-electrode configuration was employed (by connecting the reference cable to the CE), the volume of the anode compartment was 8 mL.

Both compartments were stirred during the CPE measurement, and the duration of the CPE experiment was set to 3 h. When MBA was used as the organic substrate, both compartments contained carbonate buffer (0.5 M) and were purged with CO_2 for 30 min (pH 7.3 under CO_2 saturation). The cathode compartment was continuously purged with CO_2 (5 sccm) throughout the duration of the experiment, as required for continuous flow GC analysis (see below). When glycerol was employed as organic substrate, the anode compartment was purged with N_2 for 15 min to maintain a pH value close to 8 during the coupled CPE experiment. The cathode compartment was kept under similar conditions to those described above.

(c) Gaseous Product Analysis & Quantification. The quantification of H_2 and CO was performed with a Shimadzu Tracera GC-2010 Plus gas chromatograph equipped with a barrier discharge ionisation detector. A Hayesep D (2 m × 1/8'' o.d. × 2 mm i.d., 80/100 mesh, Analytical Columns) precolumn and a RT-Molsieve 5A (30 m × 0.53 mm i.d., Restek) main column were used to separate H_2, O_2, N_2, CH_4 and CO while blocking CO_2 and H_2O from the sensitive Molsieve column. The He (5.0, BOC) carrier gas was purified (HP2-220, VICI) prior to entering the GC. The column temperature was kept constant at 85 °C, the detector temperature was 300 °C.

The electrolyte was continuously purged with CO_2 (5 sccm) and the gas from the electrolysis cell was constantly flushed through a loop (1 mL) and injected every *ca.* 4.25 min into the GC. The GC was calibrated with a known standard for H_2, CO and CH_4 (2040 ppm H_2 / 2050 ppm CO / 2050 ppm CH_4 in balance gas CO_2, BOC, ± 2% grade) by diluting the gas with pure CO_2. The total Faradaic yield was generally observed to be below unity, which was presumably due to (i) slow release of bubbles from the porous electrode surface, and (ii) charging of the CNTs. The rates of gas evolution ($\dot{n}_{CO}$ or $\dot{n}_{H_2}$ mol s^{-1}) were calculated by means of Equation 4.3:

$$\dot{n}_{CO/H_2} = \frac{Area_{GC}}{f} \cdot \frac{\mathrm{p}}{RT} \cdot \dot{V} \qquad 4.3$$

where f is the response factor determined by GC calibration, p is the pressure in the cell (ambient pressure), R is the universal gas constant, T is the absolute temperature (298 K), and $\dot{V}$ the volumetric flow rate. The total amount of gas evolved was calculated by integrating the rate of CO and H_2 formation (mol s^{-1}) over time (s).

(d) Liquid Product Analysis & Quantification. During and after the reaction, a 50 µL aliquot of the solution was taken from the electrochemical cell and diluted with 450 µL of Milli-Q water (for experiments involving MBA) or 50 µL of a 0.55 M H_2SO_4 solution (for experiments involving glycerol), and then analysed via HPLC. Substrate conversions and yields were deduced using a Shimadzu LC-20, with an ultraviolet-visible detector (Shimadzu SPD-10AV) set at 190 nm.

Conditions for MBA oxidation: samples and standards (1 µL) were injected directly onto a 150 mm × 4.6 mm Prodigy™ 3 µm ODS-3 100 Å column purchased from Phenomenex. The mobile phase was comprised of a 1:1 MeCN/H_2O mixture with a total flow rate of 0.5 mL min^{-1} at 40 °C. Typically, a 50 µL aliquot was sampled from the reaction mixture and diluted by a factor of 10 prior to HPLC analysis.

Conditions for glycerol oxidation: samples and standards (15 µL) were injected into a configuration comprised of a Security-Guard Carbo-H cartridge and a 300 mm × 7.8 mm Rezex™ ROA-Organic Acid H+ (8%) column, both purchased from Phenomenex. A dilute sulfuric acid (2.5 mM) solution was used as the eluent, and the flow rate was set to 0.5 mL min^{-1} at 75 °C. For glycerol analysis, a 50 µL aliquot was sampled from the anode compartment and quenched with 0.55 M H_2SO_4 (50 µL), to neutralise the carbonate solution and prevent the release of CO_2 inside the HPLC column.

When conducting either analysis, one hour of column equilibration was required before the first sample injection. Initially, the starting materials and expected main products were analysed separately to identify their respective retention times on the chromatogram. This was carried out for MBA, MBAd, glycerol, and GlyAd. Standard calibration curves of the main product compounds (MBAd and GlyAd, Figure 4.23) were then produced to afford product quantification and deduce the concentration of species in the reaction aliquot.

Chromatograms for standard solutions of common oxidation products from glycerol oxidation (namely: dihydroxyacetone, glyceric acid, and glycolic acid; c.f. Scheme 4.2) were also compiled, but these compounds were not observed during analysis of the experimental (CPE) reaction aliquots. Exemplary chromatograms from the coupled CPE experiments (when using MBA and glycerol as the substrate) are presented in Figure 4.24.

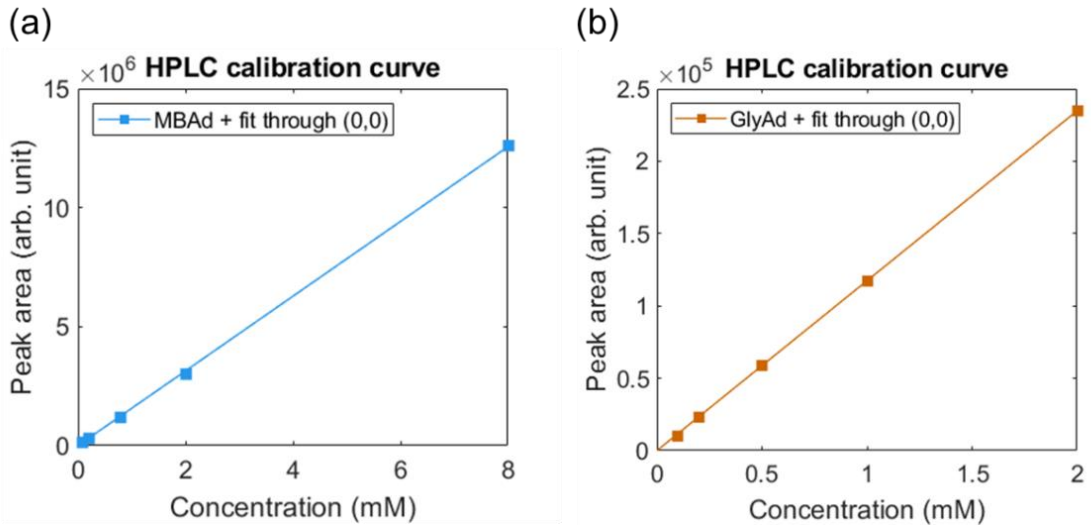

Figure 4.23: HPLC calibration curves for (a) MBAd, and (b) GlyAd, produced using a UV-Vis detector set at 190 nm.

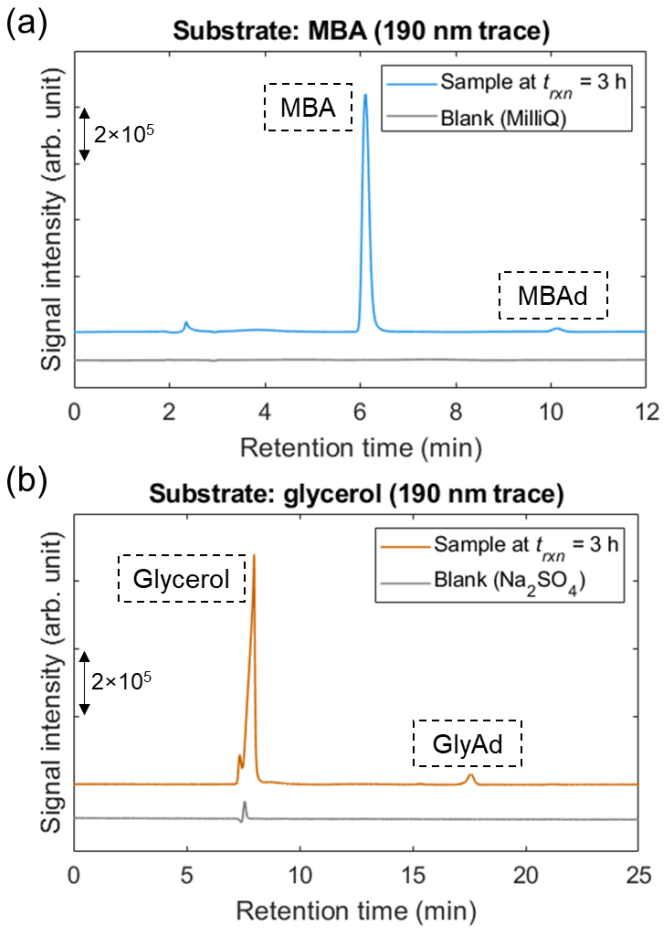

Figure 4.24: HPLC chromatograms (190 nm trace), corresponding to the 3 h time-point, for the coupled three-electrode CPE experiment (*meso*ITO|**STEMPO** as WE, CP|CNT-**CoPPc** as CE and Ag/AgCl as RE), invoking (a) MBA, and (b) glycerol, as the substrate. Such chromatograms were measured at regular time intervals to afford the time trace depicted in Figure 4.19 and Figure 4.21a, respectively.

4.4.6 EPR and FE-EPR Spectroscopy

(a) Electrochemical Measurement. 'Cylindrical *meso*ITO' (*C-meso*ITO) electrodes were prepared following a previously published protocol.[37] Electrochemical experiments were carried out using the standard 3-electrode configuration consisting of the *C-meso*ITO electrode as the WE, teflon-insulated Ag wire as pseudo-RE, and bare Pt wire as CE. All electrochemical experiments were performed in an anaerobic glovebox (MBraun, < 0.05 ppm O_2) in buffer (20 mM Na_2CO_3, adjusted to pH 8) at room temperature. In the potentiometric titration, nine *C-meso*ITO|**STEMPO** electrodes were poised at different potentials until a stable current was reached, which occurred in less than 5 min, before the sample was flash frozen in a dry ice/acetone bath. The *C-meso*ITO structure was found to be unstable to repeated freeze-thaw cycles. A new electrode was therefore assembled for each spectroelectrochemical measurement, given that such measurements had to be conducted on frozen samples. All redox potentials are quoted against NHE, where $E_{NHE} = E_{Ag\ wire} + 0.220$ V. The reference electrode (pseudo Ag wire) was calibrated using the redox potential of ferricyanide (pH 7) against a saturated calomel electrode (SCE).

(b) EPR Spectroscopic Measurements and Analysis. Low-temperature EPR measurements were performed in the Centre for Advanced ESR (CAESR) located in the Department of Chemistry of the University of Oxford, using an EMXmicro X-band CW spectrometer (Bruker BioSpin GmbH, Germany), equipped with a helium flow cryostat (ESR900, Oxford instruments) and a rectangular resonator module with 10 mm sample access (X-band Super High Sensitivity Probehead, ER 4122SHQE). Room-temperature EPR measurements were carried out in the MRSH at Imperial College, using a Bruker EMX WinEPR CW spectrometer operating at X-band frequencies and equipped with rectangular resonator module with 10 mm sample access (X-band Super High Sensitivity Probehead, ER 4122SHQE). EPR measurements were conducted under non-saturating conditions with 2 mW microwave power, 9 scans, 100 kHz modulation frequency and 2 G modulation amplitude.

The spectra of the empty resonator and of samples containing only buffer (including only the glass tube) were found to be identical. For CW measurements, the Q value, as reported by the built-in Q indicator in the Xepr programme (typically

Q = 1500 ± 100), was used as a guide to position each sample in the same location in the resonator. All data analysis was carried out using EasySpin.[56] To obtain the potentiometric titration curve, the area of each EPR spectrum was obtained through double integration, and plotted against its corresponding potential. The experimental data points were then fitted to the 1 e^- Nernst equation.

4.5 Calculations

1. Laviron Analysis

The two equations employed to carry out the Laviron analysis for the *meso*ITO|**STEMPO** assembly are as follows:[36]

$$\Delta E_{p,a} = \frac{-2.3RT}{(1-\alpha)zF}\log\left(\frac{(1-\alpha)zF}{RTk_{app}}\right) - \frac{2.3RT}{(1-\alpha)zF}\log(\nu) \qquad 4.4a$$

$$\Delta E_{p,c} = \frac{-2.3RT}{\alpha zF}\log\left(\frac{\alpha zF}{RTk_{app}}\right) - \frac{2.3RT}{\alpha zF}\log(\nu) \qquad 4.4b$$

where $\Delta E_{p,a}$ and $\Delta E_{p,c}$ denote the difference between the potential of the anodic peak (subscript *a*) and the formal redox potential ($E°'$), and that of the cathodic peak (subscript *c*) and $E°'$, respectively. $E°'$, for *meso*ITO|**STEMPO,** was obtained by averaging the anodic and cathodic potentials at low scan rates, ν. *z* is the number of electrons transferred, α is the electron-transfer coefficient, and k_{app} the apparent rate constant for electron-transfer.

To apply the Laviron analysis, a linear trend was fitted to the anodic and cathodic regions of the trumpet plot portrayed in Figure 4.9c, for values of $\Delta E_{p,a}$, $\Delta E_{p,c} > 100$ mV. $(1-\alpha)$ and α were determined from the gradients of the anodic and cathodic trends, respectively, while $k_{app,a}$ and $k_{app,c}$ were deduced from the *y*-intercept of the corresponding plots. A value for k_{app} was afforded by taking the average of the two rate constants. The critical scan rate, ν_c, was obtained from the *x*-intercept, by extrapolating the linear portions of the trumpet plot in both regions to $\Delta E_p = 0$. As per k_{app}, ν_c was then calculated based on the average between the anodic and cathodic values.

2. Catalyst Metrics

The turnover number (TON) was calculated using:

$$\textit{Anode}: \mathrm{TON}_{\mathbf{STEMPO}} = \frac{n_{\mathrm{Aldehyde}}(\mathrm{HPLC})}{n_{\mathbf{STEMPO}}\,(\mathrm{EC})} \qquad 4.5a$$

$$\textit{Cathode}: \mathrm{TON}_{\mathrm{Co}} = \frac{n_{\mathrm{CO+H_2}}(\mathrm{GC})}{n_{\mathrm{Co}}\,(\mathrm{EC})} \qquad 4.5b$$

while the Faradaic efficiency (FE) was obtained using:

$$\textit{Anode}: \mathrm{FE\ (Aldehyde)} = \frac{n_{\mathrm{Aldehyde}}(\mathrm{HPLC})}{Q_{CPE}/_{2F}} \qquad 4.6a$$

$$\textit{Cathode}: \mathrm{FE\ (CO + H_2)} = \frac{n_{\mathrm{CO+H_2}}(\mathrm{GC})}{Q_{CPE}/_{2F}} \qquad 4.6b$$

where the moles of catalyst, $n_{\mathbf{STEMPO}}$ for the anode and n_{Co} for the cathode, were determined electrochemically (EC) (see Equation 4.1 and Figure 4.17), while the moles of liquid product (n_{Aldehyde}) was determined via HPLC, and moles of gaseous product ($n_{\mathrm{CO+H_2}}$) via continuous flow GC. Q_{CPE} signifies the charge passed during the CPE experiment, and the factor of '2' in the FE equation denotes a 2 e^- process.

3. ICP Data

Table 4-2: ICP-OES measurements for quantification of the Co loaded onto the surface of CP|CNT-**CoPPc** electrodes. Loadings are given per geometric surface area.

Sample [a]	Weight (mg)	[Co] (ppm)	Total Co (mg)	Total Co (μmol) [b]	Average Co loading (nmol cm^{-2})
CNT-**CoPPc**	0.63	6.29	0.0629	-	-
CP|CNT-**CoPPc** (i)	-	0.54	0.0054	0.091	327±5
CP|CNT-**CoPPc** (ii)	-	0.54	0.0054	0.092	
CP|CNT-**CoPPc** (iii)	-	0.55	0.0055	0.093	
CP|CNT-**CoPPc** (iv)	-	0.53	0.0053	0.089	

[a] CP|CNT-**CoPPc** (i)-(iv) denote four separate electrodes from a single batch.

[b] Total Co loading on the CP|CNT-**CoPPc** electrode ($A_{cathode}$ = 0.28 cm^2).

For cathode assembly:

$$\%\ \text{electroactive Co} = \frac{\Gamma_{\text{Co}}(\text{EC})}{\text{Co loading (ICP)}} = \frac{18.3 \pm 1.6}{327 \pm 5} = 5.6 \pm 0.5\% \qquad 4.7$$

4. TOF Analysis

The turnover frequency (TOF) analysis for the heterogeneous catalytic system, *meso*ITO|**STEMPO**, in the presence of different alcohol substrates, was carried out using the rationale outlined by Costentin and Savéant.[46] The model of interest as described therein is applicable to a well-defined molecular catalyst with a well-defined standard potential, where the catalyst is deposited on the electrode surface – immobilised **STEMPO** is thus a suitable fit. In the paper, they assumed a fast electron transfer between the electrode and catalytically active redox couple, and based on the Nernst law and substrate behaviour in the diffusion-convection layer, present a complete derivation to describe the catalyst TOF. The relevant equations required for our analysis are shown below:

$$\text{TOF}_{\textbf{STEMPO}} = \frac{k_r c^{\circ}_{sub}}{1 + \exp\left[{}^{F}/_{RT}\left(E - E^{\circ}_{\text{ST}^+/\text{ST}^{\bullet}}\right)\right]} \qquad 4.8a$$

$$\frac{i_{max}}{A_{anode}F} = \frac{2k_r c^{o}_{sub}\Gamma_{\mathbf{STEMPO}}}{1 + \exp\left[{}^{F}/_{RT}\left(E - E^{o}_{ST^{+}/ST\bullet}\right)\right]} \Rightarrow \mathrm{TOF}_{\mathbf{STEMPO}} = \frac{i_{max}}{2A_{anode}F\,\Gamma_{\mathbf{STEMPO}}} \qquad 4.8b$$

where c^{o}_{sub} is the initial substrate concentration, k_r the apparent rate constant for the catalytic reaction, i_{max} the catalytic maximum current, $\Gamma_{\mathbf{STEMPO}}$ the surface concentration of **STEMPO**, and $E^{o}_{ST^{+}/ST\bullet}$ the standard potential of the **STEMPO** ('ST') redox couple. Hence, as shown in Equation 4.8b, a value for the TOF can be calculated based on empirical data. It is worth noting that, as discussed, for the case of **STEMPO**, the apparent electron transfer kinetics are sluggish. To circumvent this issue, experimentally derived CVs were recorded using a slightly low scan rate (20 mV s^{-1}), to ensure maximal oxidation of the **STEMPO** surface species. This yields a Nernstian response, which can be fitted with a sigmoidal function in accordance with Equation 4.8 (c.f. Figure 4.14 and Figure 4.15). Variation of the i_{max} was also less pronounced for c^{o}_{sub} > 30 mM, and hence, 30 mM was chosen as the substrate concentration for the TOF analysis (c.f. maximum current density *vs.* concentration plots in Figure 4.14). 20 mM PP-ol was selected due to the solubility issues of this substrate at higher concentrations in the mixed solvent. The results obtained from the TOF analysis for the four alcohol substrates were summarised in Table 4-1.

5. Cell Energy Efficiency

The following thermodynamic analysis was carried out in order to calculate ε, the cell energy efficiency, as defined by Equation 4.2. The cathode and anode half-reactions can be expressed by the following:

$$\textit{Anode}: C_3H_8O_3 + 2OH^- \rightarrow C_3H_6O_3 + 2H_2O + 2e^- \qquad 4.9a$$

$$\textit{Cathode}: CO_2 + H_2O + 2e^- \rightarrow CO + 2OH^-$$
$$2H_2O + 2e^- \rightarrow H_2 + 2OH^- \qquad 4.9b$$

Using the standard potentials (E^o) available in the literature, the reduction potentials under the operating conditions of the coupled electrolyser (E) were calculated (see Table 4-3). Where necessary, the standard Gibbs free energy change for the reaction of intertest, ΔG^{o}_{rxn}, was related to E^o through:

$$\Delta G^{o}_{rxn} = -zFE^{o} \quad 4.10$$

The Nernst law was also utilised for the thermodynamic calculation, where the shift in E^{o} with pH is given by:

$$E = E^{o} - 0.059 \cdot \mathrm{pH} \quad 4.11$$

Table 4-3: Reduction potential calculations under operating conditions of the 2-electrode configuration.

Reduction potential, E (V *vs.* NHE)	Calculation	Reference values [a]
E(GlyAd/glycerol)	$\Delta G^{o}_{rxn} = \Delta G^{o}_{f}$(glycerol) $- G^{o}_{f}$(GlyAd) $= -77.38$ kJ mol^{-1} $E = 0.4$ V $- (0.059 \times 8.3) = -0.0897$	ΔG^{o}_{f}(glycerol) $= -478.6$ kJ mol^{-1} [57] ΔG^{o}_{f}(GlyAd) $= -401.2$ kJ mol^{-1} [50]
E(CO_2/CO)	$E = -0.106$ V $- (0.059 \times 7.3) = -0.537$	E^{o} (CO_2/CO) $= -0.106$ V *vs.* RHE [47]
E(H^+/H_2)	$E = 0$ V $- (0.059 \times 7.3) = -0.431$	

[a] Values for glycerol and GlyAd reported under standard conditions of 1 bar and 298 K.

4.6 References

1 P. De Luna, C. Hahn, D. Higgins, S. A. Jaffer, T. F. Jaramillo and E. H. Sargent, *Science*, 2019, **364**, eaav3506.

2 P. Kang, Z. Chen, A. Nayak, S. Zhang and T. J. Meyer, *Energy Environ. Sci.*, 2014, **7**, 4007–4012.

3 C. C. L. McCrory, S. Jung, I. M. Ferrer, S. M. Chatman, J. C. Peters and T. F. Jaramillo, *J. Am. Chem. Soc.*, 2015, **137**, 4347–4357.

4 M. W. Kanan and D. G. Nocera, *Science*, 2008, **321**, 1072–1075.

5 I. Roger, M. A. Shipman and M. D. Symes, *Nat. Rev. Chem.*, 2017, **1**, 0003.

6 H. G. Cha and K.-S. Choi, *Nat. Chem.*, 2015, **7**, 328–333.

7 B. You, X. Liu, N. Jiang and Y. Sun, *J. Am. Chem. Soc.*, 2016, **138**, 13639–13646.

8 E. J. Horn, B. R. Rosen, Y. Chen, J. Tang, K. Chen, M. D. Eastgate and P. S. Baran, *Nature*, 2016, **533**, 77–81.

9 T. Li, Y. Cao, J. He and C. P. Berlinguette, *ACS Cent. Sci.*, 2017, **3**, 778–783.

10 T. Li, T. Kasahara, J. He, K. E. Dettelbach, G. M. Sammis and C. P. Berlinguette,

Nat. Commun., 2017, **8**, 390.

11 C. Huang, Y. Huang, C. Liu, Y. Yu and B. Zhang, *Angew. Chem. Int. Ed.*, 2019, **58**, 12014–12017.

12 Y. Wang, S. Gonell, U. R. Mathiyazhagan, Y. Liu, D. Wang, A. J. M. Miller and T. J. Meyer, *ACS Appl. Energy Mater.*, 2019, **2**, 97–101.

13 K. L. Materna, R. H. Crabtree and G. W. Brudvig, *Chem. Soc. Rev.*, 2017, **46**, 6099–6110.

14 B. J. Brennan, A. E. Keirstead, P. A. Liddell, S. A. Vail, T. A. Moore, A. L. Moore and D. Gust, *Nanotechnology*, 2009, **20**, 505203.

15 C. L. Frye, G. A. Vincent and W. A. Finzel, *J. Am. Chem. Soc.*, 1971, **93**, 6805–6811.

16 B. J. Brennan, D. Gust and G. W. Brudvig, *Tetrahedron Lett.*, 2014, **55**, 1062–1064.

17 K. E. Dalle, J. Warnan, J. J. Leung, B. Reuillard, I. S. Karmel and E. Reisner, *Chem. Rev.*, 2019, **119**, 2752–2875.

18 X. Zhang, Z. Wu, X. Zhang, L. Li, Y. Li, H. Xu, X. Li, X. Yu, Z. Zhang, Y. Liang and H. Wang, *Nat. Commun.*, 2017, **8**, 1–8.

19 M. Wang, K. Torbensen, D. Salvatore, S. Ren, D. Joulié, F. Dumoulin, D. Mendoza, B. Lassalle-Kaiser, U. Işci, C. P. Berlinguette and M. Robert, *Nat. Commun.*, 2019, **10**, 3602.

20 Y. Liu and C. C. L. McCrory, *Nat. Commun.*, 2019, **10**, 1–10.

21 E. Boutin, M. Wang, J. C. Lin, M. Mesnage, D. Mendoza, B. Lassalle-Kaiser, C. Hahn, T. F. Jaramillo and M. Robert, *Angew. Chem. Int. Ed.*, 2019, **58**, 16172–16176.

22 N. Han, Y. Wang, L. Ma, J. Wen, J. Li, H. Zheng, K. Nie, X. Wang, F. Zhao, Y. Li, J. Fan, J. Zhong, T. Wu, D. J. Miller, J. Lu, S. T. Lee and Y. Li, *Chem*, 2017, **3**, 652–664.

23 S. Roy and E. Reisner, *Angew. Chem. Int. Ed.*, 2019, **58**, 12180–12184.

24 K. L. Materna, B. Rudshteyn, B. J. Brennan, M. H. Kane, A. J. Bloomfield, D. L. Huang, D. Y. Shopov, V. S. Batista, R. H. Crabtree and G. W. Brudvig, *ACS Catal.*, 2016, **6**, 5371–5377.

25 B. J. Brennan, M. J. Llansola Portolés, P. A. Liddell, T. A. Moore, A. L. Moore and D. Gust, *Phys. Chem. Chem. Phys.*, 2013, **15**, 16605–16614.

26 K. L. Materna, B. J. Brennan and G. W. Brudvig, *Dalt. Trans.*, 2015, **44**, 20312–20315.

27 K. L. Materna, J. Jiang, R. H. Crabtree and G. W. Brudvig, *ACS Appl. Mater. Interfaces*, 2019, **11**, 5602–5609.

28 C.-J. Huang and Y.-Y. Zheng, *Langmuir*, 2019, **35**, 1662–1671.

29 Z. Chen, J. J. Concepcion, J. F. Hull, P. G. Hoertz and T. J. Meyer, *Dalt. Trans.*,

2010, **39**, 6950.

30 N. M. Muresan, J. Willkomm, D. Mersch, Y. Vaynzof and E. Reisner, *Angew. Chem. Int. Ed.*, 2012, **51**, 12749–12753.

31 P. Louette, F. Bodino and J.-J. Pireaux, *Surf. Sci. Spectra*, 2007, **12**, 133–138.

32 A. J. Bard and L. R. Faulkner, *Electrochemical Methods: Fundamentals and Applications*, Wiley, New York, 2nd edn., 2001.

33 A. F. Loftus, K. P. Reighard, S. A. Kapourales and M. C. Leopold, *J. Am. Chem. Soc.*, 2008, **130**, 1649–1661.

34 J. Zhao, X. Zhu, T. Li and G. Li, *Analyst*, 2008, **133**, 1242.

35 E. Laviron, *J. Electroanal. Chem.*, 1979, **101**, 19–28.

36 C. M. Hanna, C. D. Sanborn, S. Ardo and J. Y. Yang, *ACS Appl. Mater. Interfaces*, 2018, **10**, 13211–13217.

37 K. Abdiaziz, E. Salvadori, K. P. Sokol, E. Reisner and M. M. Roessler, *Chem. Commun.*, 2019, **55**, 8840–8843.

38 M. M. Haugland, E. A. Anderson and J. E. Lovett, in *Electron Paramagnetic Resonance*, 2017, vol. 25, pp. 1–34.

39 C. Tansakul, E. Lilie, E. D. Walter, F. Rivera, A. Wolcott, J. Z. Zhang, G. L. Millhauser and R. Braslau, *J. Phys. Chem. C*, 2010, **114**, 7793–7805.

40 D. P. Hickey, R. D. Milton, D. Chen, M. S. Sigman and S. D. Minteer, *ACS Catal.*, 2015, **5**, 5519–5524.

41 A. Das and S. S. Stahl, *Angew. Chem. Int. Ed.*, 2017, **56**, 8892–8897.

42 W. F. Bailey, J. M. Bobbitt and K. B. Wiberg, *J. Org. Chem.*, 2007, **72**, 4504–4509.

43 D. P. Hickey, D. A. Schiedler, I. Matanovic, P. V. Doan, P. Atanassov, S. D. Minteer and M. S. Sigman, *J. Am. Chem. Soc.*, 2015, **137**, 16179–16186.

44 M. Rafiee, K. C. Miles and S. S. Stahl, *J. Am. Chem. Soc.*, 2015, **137**, 14751–14757.

45 X. Wu, X. Fan, S. Xie, J. Lin, J. Cheng, Q. Zhang, L. Chen and Y. Wang, *Nat. Catal.*, 2018, **1**, 772–780.

46 C. Costentin, S. Drouet, M. Robert and J. M. Savéant, *J. Am. Chem. Soc.*, 2012, **134**, 11235–11242.

47 A. J. Bard, R. Parsons and J. Jordan, Eds., *Standard Potentials in Aqueous Solution*, New York, 1985.

48 A. C. Garcia, M. J. Kolb, C. Van Nierop Y Sanchez, J. Vos, Y. Y. Birdja, Y. Kwon, G. Tremiliosi-Filho and M. T. M. Koper, *ACS Catal.*, 2016, **6**, 4491–4500.

49 D. T. Whipple and P. J. A. Kenis, *J. Phys. Chem. Lett.*, 2010, **1**, 3451–3458.

50 S. Verma, S. Lu and P. J. A. Kenis, *Nat. Energy*, 2019, **4**, 466–474.

51 S. G. Wan, X. Y. Yang, Y. Yu and C. Liu, *Phosphorus, Sulfur Silicon Relat. Elem.*, 2005, **180**, 2813–2821.

52 R. Singh, J. K. Puri, V. K. Chahal, R. P. Sharma and P. Venugopalan, *J. Organomet. Chem.*, 2010, **695**, 183–188.

53 A. M. C. Dumitriu, M. Cazacu, S. Shova, C. Turta and B. C. Simionescu, *Polyhedron*, 2012, **33**, 119–126.

54 P. G. Hoertz, Z. Chen, C. A. Kent and T. J. Meyer, *Inorg. Chem.*, 2010, **49**, 8179–8181.

55 M. Kato, T. Cardona, a W. Rutherford and E. Reisner, *J. Am. Chem. Soc.*, 2012, **134**, 8332–8335.

56 S. Stoll and A. Schweiger, *J. Magn. Reson.*, 2006, **178**, 42–55.

57 R. P. V. Faria, C. S. M. Pereira, V. M. T. M. Silva, J. M. Loureiro and A. E. Rodrigues, *Ind. Eng. Chem. Res.*, 2013, **52**, 1538–1547.

Chapter 5

Conclusions

5.1 Summary

The aim of this thesis was to adopt photo- and electrocatalytic techniques in order to design and implement sustainable devices for conducting substrate oxidation reactions, which can be used as a synthetic tool in a multi-step flow sequence or replace the OER within a conventional CO_2R electrolyser.

Over the past decade, material modification processes of conventional carbon nitride have had a profound effect on its photocatalytic ability and performance, and such materials have found applications in solar fuel generation (including water splitting and CO_2 reduction), along with visible light mediated organic transformations. Continuous flow chemistry offers numerous advantages over batch reactors and is particularly appealing for *heterogeneous photocatalytic* applications, where the solid catalyst can be immobilised in such a way as to maximise: (i) the interfacial area in a multiphase reaction, and (ii) the *SA*-to-*V* ratio of the photoreactor for enhanced light absorption. Conceptually, combining the benefits of continuous photochemistry and carbon nitride catalysis therefore seemed like a highly attractive option – one which could provide an efficient, low-cost, and sustainable platform for organic oxidative chemistry. In the thesis section on flow photocatalysis, two different modified carbon nitride materials were utilised, namely cyanamide-functionalised carbon nitride ($^{NCN}\mathbf{CN_x}$), and mesoporous carbon nitride (**mpg-CN$_x$**).

A prototype thin channel flow device incorporating $^{NCN}\mathbf{CN_x}$ as a stationary phase was first modelled and assembled, in order to conduct a parametric study and begin gathering preliminary experimental data regarding the feasibility of such a material towards photocatalysed alcohol oxidation under continuous flow conditions. In this proof-of-concept study, with MBA as the model substrate, moderate conversions were

obtained (~17%), primarily a consequence of the short channel length of the photoreactor. Attempts to use a serpentine shaped polydimethylsiloxane (PDMS) microfluidic device, to increase the effective length of the channel, was unsuccessful, this being due to the uneven photocatalyst sheet which prevented efficient binding of the PDMS device to the ^{NCN}**CN$_x$** coated glass. Despite moderate MBA conversion, this work demonstrated the effectiveness of the thin channel design, as a potential means to utilise immobilised carbon nitrides for continuous flow photocatalysis.

Having established the limitations of the thin channel approach, an alternative strategy was employed, this time featuring a packed column photoreactor (**PCP**). It was observed that the morphology of the heterogeneous photocatalyst had a drastic effect on its ability to allow for stable gas–liquid permeation through the packed column, hence why the mesoporous carbon nitride was selected in place of bulk carbon nitrides (**b-CN$_x$**). For instance, when either ^{NCN}**CN$_x$** or **b-CN$_x$** was incorporated within the **PCP**, the resultant back-pressures during operation where too high, thereby preventing the successful flow of substrate through the column.

A triphasic **PCP** employing **mpg-CN$_x$** and aerobic O_2 was then successfully assembled to operate under continuous flow conditions. The applicability and performance advantages of this flow approach compared to conventional batch photochemistry were demonstrated via the selective aerobic oxidation of benzylic alcohols and amines, to the corresponding aldehydes and dibenzylic secondary (*E*)-imines, respectively. The reactor design also allowed for facile downstream processing and reusability for multiple flow cycles, and hence from a practical sense, was also more appealing for conducting this kind of chemistry in relation to batch.

The other method that was explored for substrate, and particularly alcohol, oxidation was based on a TEMPO-mediated electrocatalytic cycle. Here, a novel anodic assembly was fabricated, which featured a silatrane-modified TEMPO electrocatalyst (**STEMPO**) covalently immobilised on a *meso*ITO scaffold, for implementation within a coupled alcohol oxidation – CO_2R electrolyser. This approach was incentivised by the need to find an alternative anodic reaction to the OER, in order to lower the cell potential requirements for driving electrochemical CO_2R, and also improve the economics of the overall process by generating value-added chemical feedstocks at both the anode and the cathode. The novel hybrid, which was the first example of a

TEMPO-based compound directly wired to a metal oxide (MO) interface, performed well in mildly basic conditions, as required to enhance the TEMPO-mediated rate of alcohol oxidation. Turnover frequency (TOF) analysis revealed the anode's ability to efficiently oxidise a variety of biomass representative substrates, such as glycerol and HMF.

The use of silatrane chemistry for anchoring molecular components to MO electrodes in the field of photoelecto- and electrocatalysis is still greatly underexplored. The conditions required to promote surface hydrolysation of the protected anchor, and the hybrid's ability to perform well under oxidative and basic conditions, is testament to the importance of investigating and implementing these robust functionalities for attaching molecules to MO surfaces. The final demonstrator device, featuring the *meso*ITO|**STEMPO** anode and the CP|CNT-**CoPPc** cathode, is the first example of a fully molecular, precious-metal-free, immobilised electrolyser for coupling value-added oxidative transformations to fuel-generating reductive chemistry. Using glycerol, one of the top biomass-derived platform chemicals, as the substrate alcohol, we demonstrated the performance of the electrolyser to generate stoichiometric amounts of glyceraldehyde and syngas over a 3-hour electrolysis period.

Despite the fact that the two approaches described in this thesis are quite different from one another, both the **mpg-CN$_x$**-based flow photoreactor and the coupled *meso*ITO|**STEMPO**–CP|CNT-**CoPPc** electrolyser exhibit a number of similarities in terms of their advantages. Firstly, both can be classified as *sustainable* approaches to conducting oxidative chemistry, wherein the former uses visible light, which in effect can be provided by natural sunlight, while the latter offers an attractive pathway to converting excess renewable electricity into value-added chemical feedstocks (on both the reductive and oxidative side). Additionally, both systems were based on earth-abundant materials, that were both low-cost and nontoxic, thus further promoting the sustainability aspect. Secondly, the two systems make use of a full redox cycle, without involving any sacrificial components. In the flow photoreactor, the electrons sourced from alcohol or amine oxidation are essentially used for terminal oxygen reduction, to afford the superoxide species which facilitates the rate of reaction by acting as a co-oxidant. In the electrochemical setup, the electrons from **STEMPO**-mediated alcohol oxidation were employed by the CO_2R catalyst, to stoichiometrically convert CO_2 into a mixture of CO and H_2.

5.2 Outlook

Both themes explored over the course of this PhD present great scope for continual development and further application. Carbon nitride has emerged as one of the most promising heterogeneous photocatalysts, but its integration within flow photoreactors is still largely underexplored. In Chapters 2 and 3, we demonstrated (i) the versatility of immobilisation techniques for carbon nitrides, and (ii) the ability to tailor certain material properties and the design of the reactor, in order to influence the overall performance of the photocatalytic system. More broadly, it would be beneficial to bridge the gap between material design and organic synthesis, such that the modification of structural and photophysical properties could be conducted in light of targeted organic transformations. In addition, continuous flow techniques can offer certain enhanced reaction environments which are not practical or achievable within a batch system, and thus should complement the exploration of visible-light-mediated organic reactions. These will therefore be important subject areas to consider, as research efforts into the use of carbon nitrides for photoredox catalysis continue to develop.

A schematic of the next generation flow setup that we are currently investigating in the lab is shown in Figure 5.1, where $^{NCN}\mathbf{CN}_x$ is being used as the photocatalyst. In this system however, the carbon nitride material is not held in a stationary or immobilised state. Rather, upon ultrasonication in water, $^{NCN}\mathbf{CN}_x$ forms a *quasi-solution* that is stable for up to several hours, and can be pumped through the flow reactor without precipitating. This observation is likely due to the anionic cyanamide defect sites (charge-compensated by K^+ ions) which can be stabilised in the aqueous (polar protic) environment. Although this property may not be so essential in a batch reactor (since the mixture is constantly being stirred), it is highly advantageous when considering a continuous flow operation. The approach thus shares some similarities with the serial micro-batch reactor (SMBR, as introduced in Section 1.6.2),[1] but completely circumvents the need to use ionic liquids in order to disperse the carbon nitride within the micro suspension, thus greatly simplifying downstream processing. Operable under both aerobic and inert conditions, it will hopefully serve as an effective, versatile platform to pursue the discovery of new photocatalysed organic transformations.

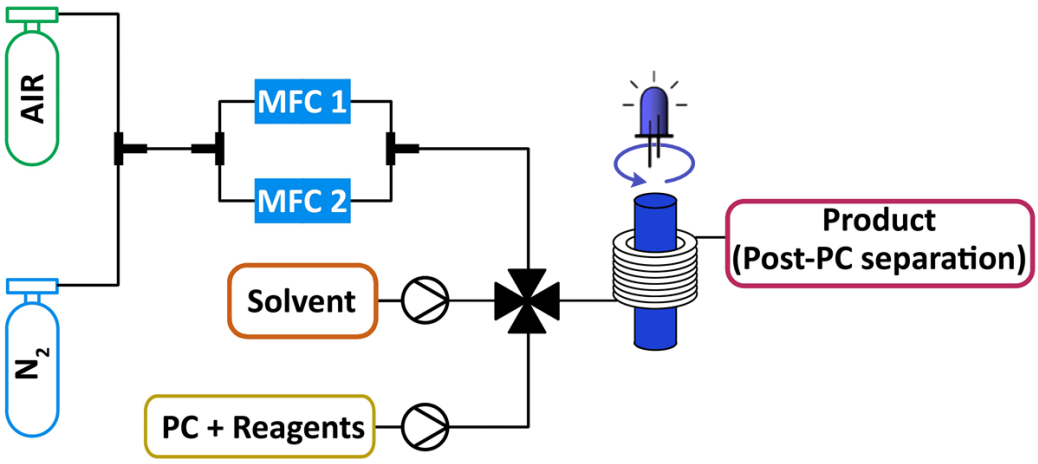

Figure 5.1: Schematic diagram of an alternative flow photoreactor design, incorporating ultrasonicated $^{NCN}\mathbf{CN_x}$ as a *quasi-solution*. The photocatalyst (PC) is effectively pumped into the reactor along with the reagents and forms a segmented flow pattern when it reaches the 3-way valve, and mixes with the gas flow; the gas and mass flow controller (MFC) must be pre-selected, and the gas-type can either be comprised of pure N_2 or air. 'MFC 1' and 'MFC 2' have different cut-off flow rates, with $\dot{V}_{MFC1} \geq 0.5$ sccm, and $\dot{V}_{MFC2} < 0.5$ sccm, thus expanding the range of achievable residence times within the reactor.

The **STEMPO** experiments described in Chapter 4 were based on the *meso*ITO|**STEMPO** assembly. Evidence suggests that the decrease in stability of the hybrid anode with increasing pH, stems from the hydrolysation of the amide bond currently utilised to link the silatrane cage to the TEMPO moiety within **STEMPO**. Thus, improvement in the lifetime of the assembly, and hence the overall coupled AlcOx – CO_2R electrolyser, could possibly be achieved via incorporation of a more robust functionality to connect the anchor to the catalytically active site.

Going forward, the hybrid anode can also be used to explore the oxidation of other abundant, low-cost and sustainable resources. The lignin polymer for example, is a major constituent of nonedible biomass and represents the largest source of naturally occurring (renewable) aromatics.[2] The aliphatic ethers that connect the aromatic groups in the polymer chain often feature functional groups which are susceptible to oxidation, such as primary or secondary alcohols. The most prevalent fragment is the β-O-4 unit, which features a benzylic secondary alcohol and a primary aliphatic alcohol.[3] Several oxidation methods and reagents have already been reported for the chemoselective oxidation of a single alcohol in the β-O-4 unit.[4–8] For either case, the resultant oxidation products were shown to undergo facile cleavage of C–C and/or C–O bonds of the aliphatic ether linker, in order to afford monomeric aromatic compounds of an increased commercial value relative to the starting lignin polymer.

Coupling such a lignin oxidation and valorisation process at the anode to the generation of syngas on the cathode-side, would make for a highly appealing and sustainable closed redox system, further extending the applicability of the *meso*ITO|**STEMPO**–CP|CNT-**CoPPc** electrolyser.

It will also be important to study the immobilisation of **STEMPO** on other MO electrodes. TiO_2, a n-type semiconductor, has been used extensively as a photoanode material within dye-sensitised photoelectrochemical cells (DSPEC).[9] In the photoanodic assembly, molecular dyes harvest sunlight and inject photoexcited electrons into the conduction band of TiO_2. The oxidised dye can then be regenerated by means of an oxidation catalyst. In a conventional DSPEC, a water oxidation catalyst typically assumes the role of the latter. However, replacing this half-reaction with the **STEMPO**-mediated substrate oxidation cycle would present an attractive alternative. In this case, besides the lower energy penalty required to drive substrate oxidation in relation to water oxidation, the photovoltage gained through dye excitation could lower the external applied bias required to drive the **STEMPO** electrocatalyst. TEMPO relies on sufficient thermodynamic driving force to reach a catalytically active state; therefore, the selection must be rationalised with respect to an 'energetically compatible' molecular dye. The kinetics of electron transfer from **STEMPO** to the dye govern the efficiency and is thus an important criterion to bear in mind when designing the photoanode. These factors, in addition to the co-immobilisation strategy employed for anchoring both the photosensitiser and catalyst to the MO surface, will play a key role in the development of **STEMPO**-based photoanode assemblies.

5.3 References

1 B. Pieber, M. Shalom, M. Antonietti, P. H. Seeberger and K. Gilmore, *Angew. Chem. Int. Ed.*, 2018, **57**, 9976–9979.

2 X. Wu, X. Fan, S. Xie, J. Lin, J. Cheng, Q. Zhang, L. Chen and Y. Wang, *Nat. Catal.*, 2018, **1**, 772–780.

3 J. Zakzeski, P. C. A. Bruijnincx, A. L. Jongerius and B. M. Weckhuysen, *Chem. Rev.*, 2010, **110**, 3552–3599.

4 A. Rahimi, A. Azarpira, H. Kim, J. Ralph and S. S. Stahl, *J. Am. Chem. Soc.*, 2013, **135**, 6415–6418.

5 A. Rahimi, A. Ulbrich, J. J. Coon and S. S. Stahl, *Nature*, 2014, **515**, 249–252.

6 W. Schutyser, J. S. Kruger, A. M. Robinson, R. Katahira, D. G. Brandner, N. S. Cleveland, A. Mittal, D. J. Peterson, R. Meilan, Y. Román-Leshkov and G. T. Beckham, *Green Chem.*, 2018, **20**, 3828–3844.

7 A. Das, A. Rahimi, A. Ulbrich, M. Alherech, A. H. Motagamwala, A. Bhalla, L. Da Costa Sousa, V. Balan, J. A. Dumesic, E. L. Hegg, B. E. Dale, J. Ralph, J. J. Coon and S. S. Stahl, *ACS Sustain. Chem. Eng.*, 2018, **6**, 3367–3374.

8 M. Rafiee, M. Alherech, S. D. Karlen and S. S. Stahl, *J. Am. Chem. Soc.*, 2019, **141**, 15266–15276.

9 D. L. Ashford, M. K. Gish, A. K. Vannucci, M. K. Brennaman, J. L. Templeton, J. M. Papanikolas and T. J. Meyer, *Chem. Rev.*, 2015, **115**, 13006–13049.

Appendix A

Appendix to Chapter 4

A.1 Supplementary Figures

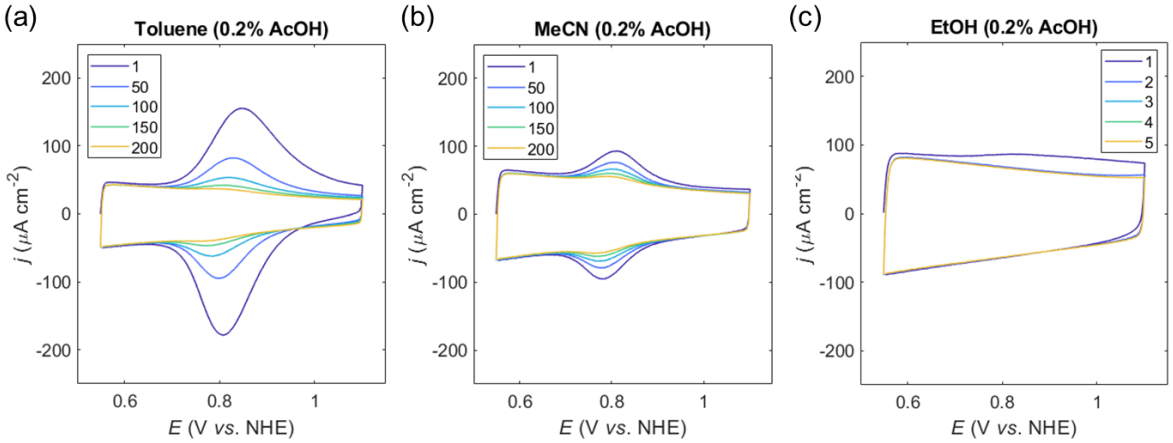

Figure A.1: Effect of solvent on *meso*ITO|**STEMPO** assembly. Multi-scan CVs for *meso*ITO|**STEMPO**, assembled using different solvents: (a) toluene, (b) acetonitrile (MeCN), and (c) ethanol (EtOH), in the presence of 0.2% v/v acetic acid (AcOH). The data was used to compile Figure 4.5. *Conditions*: pH 8 aq. HCO_3^- /CO_3^{2-} (0.2 M), $\nu = 50$ mV s^{-1}, N_2, r.t (the legend denotes scan number).

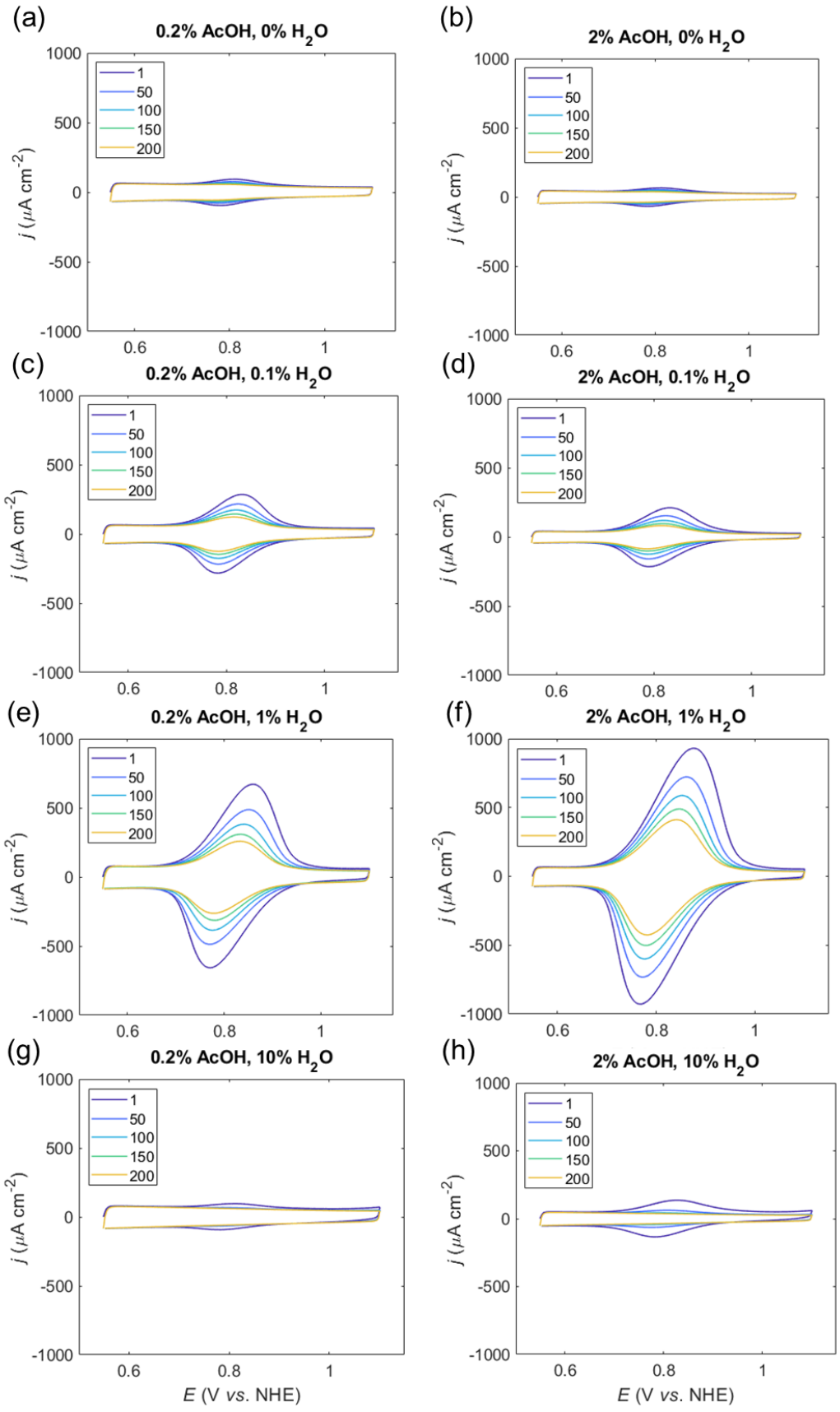

Figure A.2: Effect of AcOH and H_2O % on *meso*ITO|**STEMPO** assembly, using MeCN as solvent. The data was used to compile Figure 4.6. *Conditions*: pH 8 aq. HCO_3^- /CO_3^{2-} (0.2 M), ν = 50 mV s^{-1}, N_2, r.t (the legend denotes scan number).

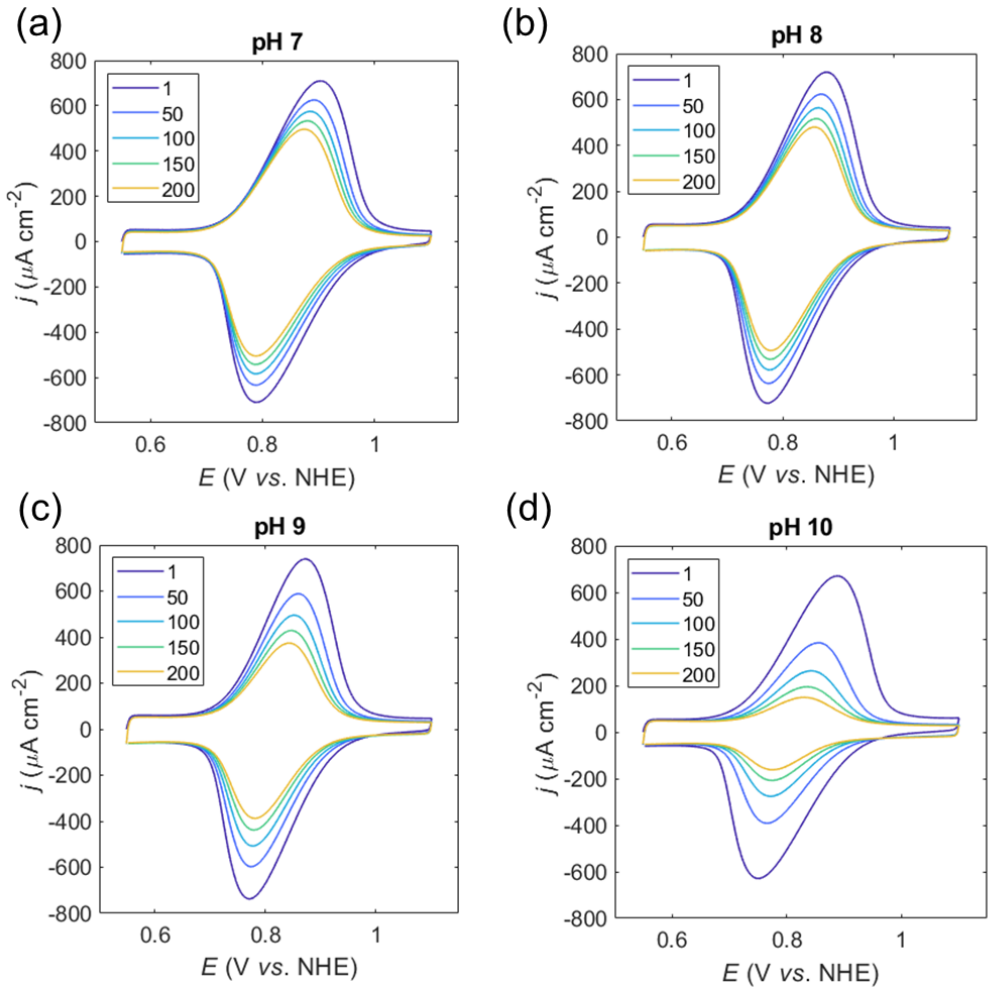

Figure A.3: Effect of pH on *meso*ITO|**STEMPO** stability. Multi-scan CVs for *meso*ITO|**STEMPO** assembly, recorded under different pH values: (a) pH 7 aq. Na_2SO_4 (0.1 M), (b), pH 8 aq. HCO_3^-/CO_3^{2-} (0.2 M), (c) pH 9 aq. HCO_3^-/CO_3^{2-} (0.2 M), (d) pH 10 aq. HCO_3^-/CO_3^{2-} (0.2 M). The data was used to compile Figure 4.11. *General conditions*: ν = 50 mV s^{-1}, N_2, r.t. (the legend denotes scan number).

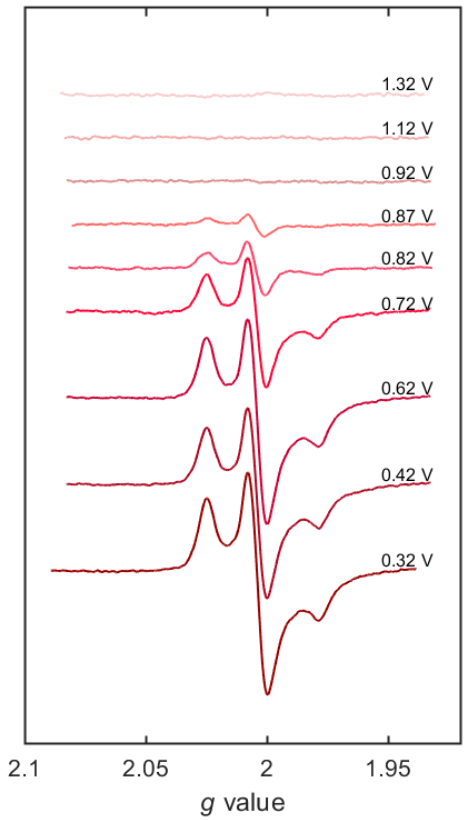

Figure A.4: Full range of EPR spectra recorded for the *C-meso*ITO|**STEMPO** assembly, poised at different potentials (as specified on the plot); *EPR conditions*: temperature = 100 K, 2 mW microwave power, 9 scans, and 2 G modulation amplitude.

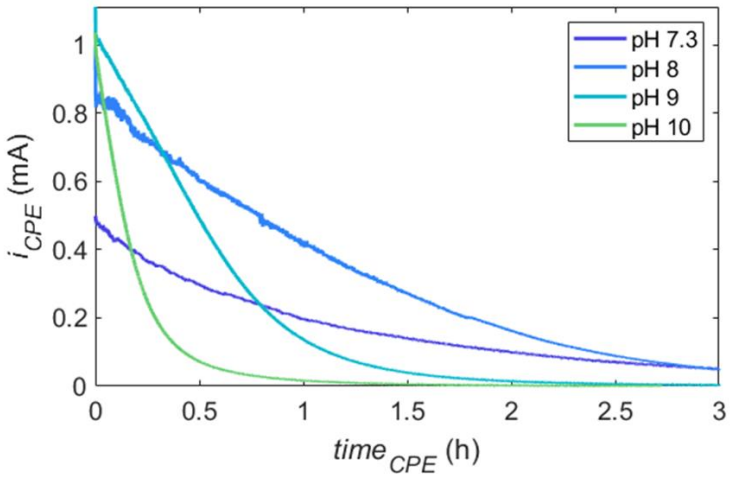

Figure A.5: Chronoamperometric profiles as a function of the pH, using *meso*ITO|**STEMPO** as the WE, in a standard 3-electrode configuration with Pt as CE, and Ag/AgCl as RE. *Controlled potential electrolysis (CPE) conditions*. pH 7.3: CO_2 saturated aq. HCO_3^-/CO_3^{2-} (0.5 M); pH 8 – 10: aq. HCO_3^-/CO_3^{2-} (0.5 M) titrated under ambient conditions to the correct pH; E_{app} = 1 V *vs.* NHE, t_{CPE} = 3 h, MBA (30 mM), r.t.

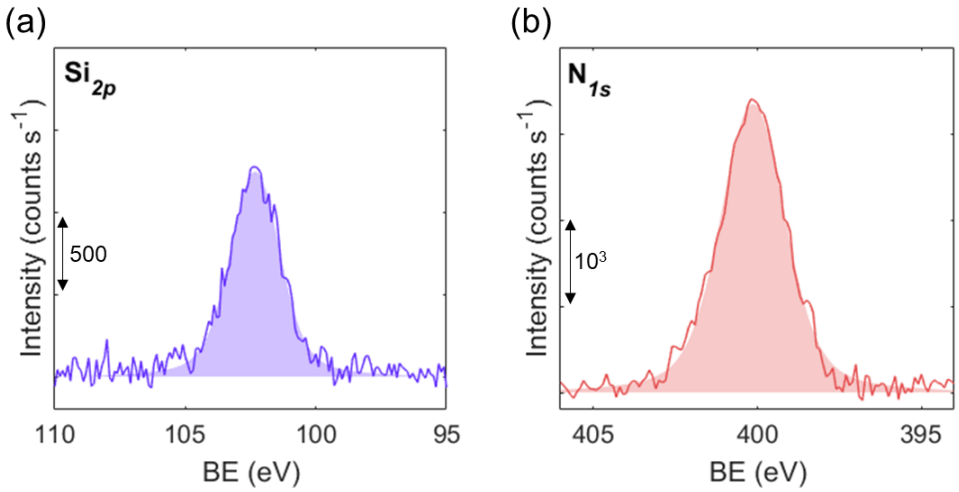

Figure A.6: Post-CPE XPS measurements on *meso*ITO|**STEMPO**, for (a) Si_{2p} region and (b) N_{1s} region. (*CPE conditions*: as per Figure A.5, using pH 8 aq. HCO_3^-/CO_3^{2-} (0.5 M) solution).

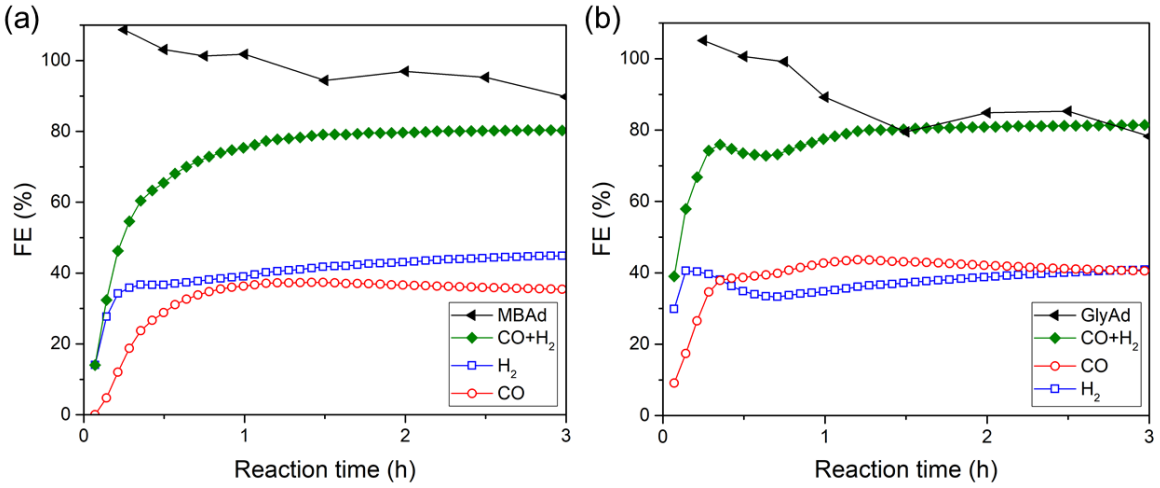

Figure A.7: FE traces over reaction time, for the oxidation and reduction products, measured for the 3-electrode configuration with *meso*ITO|**STEMPO** as WE, CP|CNT-**CoPPc** as CE and Ag/AgCl as RE; (a) MBA was used as the alcohol substrate (30 mM), and (b) glycerol (50 mM).